Quantum chemical investigations of the photophysical properties of Cu(I) and Zn(II) carbene complexes

Inaugural-Dissertation

zur

Erlangung des Doktorgrades der

Mathematisch-Naturwissenschaftlichen Fakultät

der Heinrich-Heine-Universität Düsseldorf

vorgelegt von

Nora Lüdtke

aus Düsseldorf

Düsseldorf, Dezember 2022

aus dem Institut für Theoretische Chemie und Computerchemie
der Heinrich-Heine-Universität Düsseldorf

Gedruckt mit der Genehmigung
der Mathematisch-Naturwissenschaftlichen Fakultät der
Heinrich-Heine-Universität Düsseldorf

Berichterstatter:

1. Univ.-Prof. Dr. Christel M. Marian
2. Univ.-Prof. Dr. Andreas Steffen

Tag der mündlichen Prüfung: 23.03.2023

Eidesstattliche Erklärung:

Ich versichere an Eides Statt, dass die Dissertation von mir selbständig und ohne unzulässige fremde Hilfe unter Beachtung der "Grundsätze zur Sicherung guter wissenschaftlicher Praxis an der Heinrich-Heine-Universität Düsseldorf" erstellt worden ist. Die Dissertation wurde weder in dieser, noch in ähnlicher Form bei anderen Prüfungsbehörden vorgelegt. Es wurden keine früheren erfolglosen Promotionsversuche unternommen.

Düsseldorf, den 22.12.2022

Summary

In recent years, the interest in organic light emitting diodes (OLEDs) as new display technology has strongly increased. While the interest was at first mostly academic, OLEDs are now widely used in displays of mobile phones or TVs. With OLEDs that emit via phosphorescence or TADF, an internal quantum yield of up to 100 % can be achieved. In this thesis, different Cu(I) and Zn(II) complexes were investigated with regard to their photophysical behavior as emitter. To validate the quantum chemical methods of this work, a (DPEPhos)Cu(PyrTet) complex was chosen as first complex, for which the photophysical properties were determined experimentally. On the example of CAAC-Cu complexes different solvation effects were investigated. The calculations with an explicit THF molecule showed that an exciplex is formed with the CAAC-Cu-Cl complex. The solvation effect on the dimeric CuCAAC_2^+ complex is significantly smaller and no covalent bond between the complex and the THF molecule was found. The comparison with other Cu(I) complexes revealed that low lying LLCT states are required for TADF. With lower lying MLCT states, the SOC is increased, but the complexes are rather phosphorescent. Low lying LC states lead to radiationless deactivation processes and the complexes are dark.

Although, Zn(II) has a similar d^{10} electron configuration as Cu(I), only few phosphorescent Zn(II) complexes were reported. Among the few groups of Zn(II)-complexes for which phosphorescence was reported to occur are $\mathrm{Zn(4\text{-}X\text{-}PhS)_2(phen)}$ complexes (with X=Cl,Me). To the energetic scheme reported in literature, rISC and therefore TADF could be added.

In similar manner as the Cu(I) complexes, different Zn(II)-carbene complexes and their suitability as TADF emitters were investigated. The complexes can be divided into two groups. The first group carries a 1,2-dithiolbenzene (dtb) or 1,2-diolbenzene (dob) ligand and the second group has a carbazolate ligand. For the dtb complexes, high ISC rate constants of about 10^5-10^9 s^{-1} and rISC rate constants of 10^3-10^8 s^{-1} were found at 298 K. A significant decrease of the (r)ISC was observed for the complexes with a perpendicular orientation of the dtb or dob ligand towards the carbene plane compared to the complexes with a parallel orientation. The rotation of the dtb ligand only has a small energy barrier. In experiments, the Zn-dtb complexes dimerize. As one example the dimeric CAAC-Zn-dtb complex was regarded. The dimerization leads to a rigidification and the rotation of the dtb ligand is avoided. Although a similar vertical S_1 excitation energy at the ^{1}LLCT geometries of the monomer and the dimer was found, the calculated fluorescence rate constant of the dimer is significantly lower.

The carbazolate ligand of the other group of Zn(II) carbene complexes is sterically more demanding. Therefore, the rotation of the ligand is hindered. For the investigated CAAC-Zn-carbazolate, the calculated rate constants are smaller than for the comparable CAAC-Zn-dtb complex, but do as well indicate the occurrence of TADF in addition to prompt fluorescence.

Kurzzusammenfassung

In den letzen Jahren ist das Interesse an organischen Licht emittierenden Dioden (OLEDs) als neue Display Technologie stark gestiegen. Während das Interesse zunächst eher auf die akademische Forschung begrenzt war, finden OLEDs jetzt in vielen Displays von Alltagsgegenständen wie Fernsehern oder Handys Verwendung. Mit OLEDs, die Phosphoreszenz oder thermisch aktivierte verzögerte Fluoreszenz (TADF) emittieren, kann theoretisch eine interne Quantenausbeute von bis zu 100 % erhalten werden. In dieser Arbeit werden verschiedene Cu(I) und Zn(II) Komplexe hinsichtlich ihres photophysikalischen Verhaltens als Emitter untersucht. Zunächst wurden Rechnungen an dem aus der Literatur bekannten (DPEPhos)Cu(PyrTet) Komplex durchgeführt, für den die photophysikalische Eigenschaften auch experimentell untersucht wurden, um die quantenchemischen Methoden zu validieren. Anhand der CAAC-Cu-Komplexe wurden verschiedene Lösungsmitteleffekte untersucht. Die Rechnungen mit einem explizitem THF-Molekül zeigen, dass der CAAC-Cu-Cl-Komplex ein Exziplex bildet, während der $\mathrm{Cu(CAAC)}_2^+$-Komplex deutlich weniger durch das Lösungsmittel beeinflusst wird und keine kovalente Bindung zum THF ausbildet. Der Vergleich der beschriebenen mit weiteren Cu(I)-Komplexen zeigt, dass energetisch niedrige Ligand-zu-Ligand-Charge-Transfer (LLCT)-Zustände vorliegen müssen, damit TADF beobachtet werden kann. Durch niedrigere Metall-zu-Ligand (ML)CT-Zustände wird die Spin-Bahn-Kopplung (SOC) verstärkt, aber die Komplexe zeigen eher Phosphoreszenz. Niedrige lokale Anregungen führen dazu, dass die Komplexe dunkel sind. Obwohl Zn(II) Komplexe ebenfalls eine d^{10}-Elektronenkonfiguration aufweisen, gibt es nur wenige Komplexe, für die in der Literatur berichtet wird, dass sie phosphoreszieren. Eine der Gruppen, für die Phosphoreszenz berichtet wird, sind $\mathrm{Zn(4\text{-}X\text{-}PhS)_2(phen)}$-Komplexe (mit X=Cl,Me). Zu dem in der Literatur berichteten Energie-Schema konnte RISC und dadurch TADF als Emissionsweg ergänzt werden.

In ähnlicher Weise wie die Kupfer-Komplexe wurden auch die Zink-Komplexe hinsichtlich ihrer Eignung als TADF-Emitter untersucht. Dabei wurden zwei Gruppen von Zink-Carben-Komplexen ausgewählt, von denen eine einen 1,2-Dithiolbenzol(dtb)- or 1,2-Diolbenzol(dob)-Liganden und die andere einen Carbazolat-Liganden trägt. Für die dtb-Komplexe wurden bei 298 K ISC-Ratenkonstanten zwischen 10^5-10^9 s^{-1} und rISC-Ratenkonstanten zwischen 10^3-10^8 s^{-1} gefunden. Bei einer vertikalen Anordnung des dtb- oder dob-Liganden gegenüber der Carben-Ebene sind die (r)ISC-Ratenkonstanten im Vergleich zu den Komplexen mit einer parallelen Anordnung stark abgesenkt. Die Rotation des dtb-Liganden zeigt nur eine kleine Energiebarriere. Im Experiment wurde festgestellt, dass es zur Dimierisierung der Zn-dtb-Komplexe kommt. Als Beispiel wurden Rechnungen am Dimer des CAAC-Zn-dtb-Komplexes durchgeführt. Durch die Dimerisierung wird der Komplex steifer und die Rotation des dtb-

Liganden gehemmt. Obwohl die vertikalen S_1-Anregungsenergien an den ^{1}LLCT-Geometrien des Monomers und Dimers übereinstimmen, ist die berechnete Fluoreszenzratenkonstante für das Dimer deutlich niedriger als für das Monomer.
Der Carbazolat-Ligand der zweiten Gruppe der Zn(II)-Carben-Komplexe ist sterisch anspruchsvoller. Dadurch ist die Rotation des Liganden eingeschränkt. Obwohl die (r)ISC-Ratenkonstanten des CAAC-Zn-Carbazolat-Komplexes niedriger sind als für den entsprechenden dtb-Komplex, wird neben der prompten Fluoreszenz auch TADF erwartet.

List of publications included in this thesis

Paper I

Understanding the luminescence properties of Cu(I) complexes: a quantum chemical perusal.
Nora Lüdtke, Jelena Föller and Christel M. Marian,
Phys. Chem. Chem. Phys., **2020**, 22, 23530–23544.
Own contribution: calculations on the (DPEPhos)Cu(PyrTet) complex, Carbene-Cu(I)-chlorides and its exciplex, first draft of introduction, methods and computational details and parts about (DPEPhos)Cu(PyrTet), Carbene-Cu(I)-chlorides and exciplex formation, all figures concerning these complexes, Supporting Information

Paper II

Revisiting LLCT Phosphorescence Emission from Zinc(II) Diimine Bis-Thiolate Complexes: It Actually TADF.
Nora Lüdtke, Julia Kuhnt, Tabea Heil, Andreas Steffen and Christel M. Marian,
ChemPhotoChem, **2022**, e202200142.
Own contribution: calculations and first draft of the paper, figures concerning the computational investigations, computational part of the Supporting Information

Paper III

Finding design principles of OLED emitters through theoretical investigations of Zn(II) carbene complexes.
Nora Lüdtke, Andreas Steffen and Christel M. Marian,
Inorg. Chem., **2022**, *online.*
Own contribution: all calculations, first draft of the paper, all figures, Supporting Information

Paper IV

An Air- and Moisture-stable Zinc(II) Carbene Dithiolate Dimer Showing Fast TADF and Dexter Energy Transfer Catalysis.
Ondřej Mrózek, Mousree Mitra, Benjamin Hupp, Andrey Belyaev, Nora Lüdtke, Dorothee Wagner, Cui Wang, Oliver S. Wenger, Christel M. Marian and Andreas Steffen,

Chem. Eur. J., **2022**, accepted.
Own contribution: calculations on $Zn_2(\mu - bdt)_2(^{Me}CAAC)_2]$ and $Zn(bdt)(^{Me}CAAC)$, Supporting Information part regarding Computational Details

Danksagung

Zunächst möchte ich mich bei meiner Doktormutter Christel Marian für die Betreuung meiner Doktorarbeit bedanken. Vielen Dank für die Möglichkeit zu diesem interessanten Thema forschen zu können und dabei zu wissen, dass sie hinter mir steht und ich mich bei Fragen jederzeit an sie wenden konnte.
Desweiteren möchte ich auch Andreas Steffen für die Kooperation auf der diese Arbeit beruht und die Übernahme des Zweitgutachtens und die Kooperation danken, durch die ich auch immer einen experimentellen Bezug hatte.
Vielen Dank auch an Christian Ganter für die Übernahme der Rolle als Mentor.

Ein großer Dank geht auch an den Arbeitskreis der theoretischen Chemie für die netten Gespräche. Besonders danken möchte ich Mario Bracker, für die immer wieder interessanten und aufmunternden Gespräche in unserem gemeinsamen Büro und die gemeinsamen Läufe außerhalb.

Meiner Familie und meinem Freund, die mich immer unterstützt haben und mich in Zeiten, in denen viel los war, immer weiter motiviert haben. Ein besonderer Dank nochmal an Justina und Marius für das Korrekturlesen.

Contents

List of Figures

List of Tables

1. Introduction

1.1. OLEDs

1.1.1. History of OLEDs

In recent years, the importance of organic light emitting diodes (OLEDs) in lighting and display technology has strongly increased. [3, 4, 5] The possibility of producing thin and flexible OLEDs with low power drain makes them attractive for application as displays in portable devices. Despite enormous progress since the creation of the first practical OLED three decades ago, [6] the demand for efficient OLEDs with high operational stability remains to be an important issue. The first fully flexible OLED based on a polymer was presented by Gustafsson et al. in 1992. [7] While the interest in OLEDs was mainly academic at first, they have found their way in our everyday lives and are widely used in TV and mobile displays. They have several advantages over liquid crystal displays, such as their self-luminescence, high resolution, high flexibility, high electroluminescence efficiency, wider viewing angles, high contrast colors and faster response time.[4, 8] With OLEDs it is also possible to achieve a "true black" and thinner and lighter displays than before. Of course, OLEDs also have some disadvantages. The lifetime of OLEDs is still lower than that of LCD displays. In many OLED displays, the different colors show a difference in their aging and image sticking occurs. [9]

The OLED emitters previously used in displays or lightning devices can mainly be divided into three generations. These generations can be distinguished by the way they emit light. The first generation of OLEDs was based on fluorescence and used fluorescent metal chelate complexes such as 8-hydroxyquinoline aluminum (Alq_3) as emitters. [6] While these types of OLEDs typically exhibit high operational stability, internal quantum efficiencies are limited to 25% at most because singlet and triplet excitons are created statistically at a ratio of 1:3 and only the former ones contribute to the luminescence in these devices.

To achieve higher electroluminescence quantum yields, the second generation of OLEDs was based on intersystem crossing (ISC) and phosphorescence to harvest singlet as well as triplet excitons. [10] These phosphorescent OLEDs have been widely used for the first commercial

OLED displays. To obtain the requested high ISC rate constants, organo metal complexes of heavy elements such as Ir or Pt were used, which have a high spin-orbit coupling but are costly. [11, 12, 13, 14, 15, 16, 17] Another major concern is the low operational stability of phosphorescent OLEDs which is caused by the long residence time of the emitter in the excited triplet state and the concomitant high susceptibility for side reactions. While red and green phosphorescent emitters have become standard dopants in commercial applications, the lack of stable phosphors emitting in the blue spectral region created incentives to search for new types of electroluminescent emitters that do not rely on phosphorescence. For the third generation of OLEDs, thermally activated delayed fluorescence (TADF) is used in addition to prompt fluorescence to harvest singlet and triplet excitons. The TADF process is discussed in detail in section 1.2. As TADF emitters, mostly purely organic donor–acceptor compounds or coinage metal complexes have been used. [18, 19, 20] Prerequisites for TADF are a small energy gap between the first excited singlet and triplet states and sufficiently large spin–orbit coupling (SOC) to enable reverse intersystem crossing (rISC) from the triplet to the singlet state.[21] In addition, vibronic interactions were found to play an essential role in the (r)ISC process. [22] This work focuses on transition metal complexes with d^{10} occupation on the metal center in electronic ground state, for which metal-centered d-d excitations are excluded.

1.1.2. Architecture and working principle of OLEDs

OLEDs consist of different organic semiconductor layers. The whole OLED is typically thinner than 100 nm. To improve the performance of the OLED, several layers are used. For simplification, the working principle of OLEDs is explained here by limiting to the basic processes and the layers are limited to an electron transport layer, a hole transport layer and an emitting layer. The layers are sandwiched by a cathode and an anode, of which at least one has to be transparent, so that the generated light can exit the device. If anode and cathode are both transparent, the light can exit on both sides of the device and the whole device can be transparent, when turned off. Often the anode is made of indium-tin oxide (ITO), which is conducting and transparent. The anode is followed by hole injection and the cathode by an electron injection layer. Next to the injection layers are the transport layers. In the middle of the OLED is the emission layer, which often consists of two or three different materials. The anode can be applied either on flexible or rigid substrates. The resulting OLEDs can therefore be used for different flexible and inflexible applications.

The working principle of OLEDs is similar to that of LEDs. If a voltage is applied to the OLED, the processes occurring can be divided into four different steps: 1) injection, 2) charge-carrier transport, 3) binding of charge-carrier pairs (to form excitons), 4) recombination of the excitons and emission of light. If a voltage is applied to the electrodes, electrons are injected from the cathode side to the LUMO of the organic material. Meanwhile electrons are extracted from the HOMO of the organic material at the anode side. Due to the electric field, the electrons are transported to the anode and the resulting holes are transported to the cathode. When the electrons and holes of the organic material come close to each other, they form an electron-hole pair, the exciton. If the exciton decays radiatively, a photon is created and visible light can be detected. [23]

1.2. TADF

Of particular large interest are OLED emitters based on thermally activated delayed fluorescence (TADF). As the name "thermally activated delayed fluorescence" suggests, TADF complexes emit from the S_1 state and a high fluorescence rate and efficient reverse intersystem crossing from the T_1 to the S_1 state are needed. The rISC mainly depends on two factors: the electronic spin-orbit coupling (SOC) and the energy gap ΔE_{ST} between the S_1 and the T_1 states. With a sufficiently small energy gap ΔE_{ST} between the T_1 and the S_1, after thermal activation of low vibrational states of the T_1, reverse intersystem crossing between the T_1 and the S_1 states can occur. The repopulated singlet state can deactivate via delayed fluorescence. [24, 25, 26] With increasing ΔE_{ST}, the probability for efficient rISC decreases. For singlet and triplet-coupled open-shell configurations, the energy difference depends on the exchange interaction of the unpaired electrons. [27] This is particularly small if the density distribution of the orbitals that are involved in the excitation only overlap slightly. Small energy gaps also occur in molecular systems in which the electron clouds of the half-occupied orbitals are not very far apart, but their greatest electron density lies on different atoms and is therefore bipartite. For reasons of symmetry, the electronic SOC is canceled out between singlet and triplet configurations with the same occupation of the spatial orbitals. Consequently, the SOC is only weak between singlet and triplet CT states but may be enhanced by vibronic interactions. [22, 28] Due to the close degeneracy of d orbitals with different magnetic quantum numbers, the SOC for transition metal complexes with excited metal-to-ligand charge-transfer (MLCT) states can be higher. [27] Since both rISC and phosphorescence occur from the triplet state, both are in competition with one another. If the energy difference is large and/or the lifetime of the T_1 state is too short, phosphorescence is more likely than rISC. By using TADF, triplet excitons can be harvested by bypassing the spin-forbidden T_1-S_0 transition. Accordingly, if the ΔE_{ST} is small enough, efficient TADF can be achieved for complexes with small SOC, while for phosphorescent emitters a high SOC is crucial.

The TADF process does not lead to a full repopulation of the S_1 state in all cases. In many Cu(I) complexes, the SOC leads to a high ISC rate constant and the T_1 state is populated very quickly. The repopulation of the T_1 state via rISC is significantly slower. Therefore, phosphorescence and TADF can be observed simultaneously. [29] As TADF emitters, mostly purely organic donor–acceptor compounds or coinage metal complexes have been used. [18, 19, 20] Among the latter, copper(I) complexes have been established as highly interesting emitter materials.

1.3. Aims of this work

The overall aim of this work was the development of new design principles of OLED emitters. Due to the potentially high internal quantum yield, especially emitters based on TADF are of interest. Already at the beginning of this work, a lot of investigations have focused on Cu(I) emitters. One of the few complexes, which showed TADF and for which experimental ISC and rISC rate were reported, was the (DPEPhos)Cu(PyrTet)complex of the Bräse group. [1, 19] This complex was chosen as a reference to validate the quantum chemical methods to describe the photophysical properties of transition metal complexes. The CAAC-Cu complexes synthesized by the Steffen group [30], were reported to be phosphorescent. In comparison with other investigated complexes, a systematic was searched whether a Cu(I) complex is dark, phosphorescent or shows TADF. In literature, some experiments showed a red-shift of the emission upon temperature increase, which was assigned to the formation of an exciplex for the CAAC-Cu-Cl complex in THF. Calculations with different solvent models should clarify, whether an CAAC-Cu-Cl-THF exciplex is formed and how the photophysical properties are affected by solvation.

Finding new emitters based on more earth abundant was demanded for the SPP 2102 Light-controlled reactivity of metal complexes, which financially supported this work. The results on the copper complexes should be used to investigate Zn(II) complexes, which have a similar d^{10} electron configuration, while they are more earth abundant.

1.4. State of the art

This work focusses on transition metal complexes with carbene ligands as OLED emitters and d^{10} occupation of the metal center in the electronic ground state. Accordingly, a brief overview of the state of the art of copper(I) and zinc(II) complexes and the selected carbene ligands with regard to their application in OLEDs is given here. In the last five years, the interest in this field has increased significantly, which is revealed by the high number of new publications regarding copper complexes. Since the first TADF emitter based on Zn(II) was reported in 2015, [31] the number of publications of Zn(II) complexes has remained small and only a few more complexes have been reported since then.

1.4.1. Copper complexes

Of the luminescent metal compounds based on a relatively abundant element, Cu(I) complexes and clusters form the largest class.[32, 33, 34] Accordingly, many investigations focused on Cu(I) complexes with regard to their suitability as OLED emitters. [13, 35, 36, 37, 38, 39, 40, 41] Due to the d^{10} configuration of copper(I) complexes, metal-centered (MC) dd^* transitions are absent and copper(I) complexes have been established as highly interesting emitter materials. dd^* transitions can lead to premature non-radiative decay, a prominent problem for d^6 Ir(III) or d^8 Pt(II)-based emitters. [13, 32, 42] Another advantage of the d^{10} configuration is the flexibility of the coordination geometry and with this a higher tunability of the photophysical properties compared to other metal complexes, which are limited to octahedral (d^6 metal complexes) or squareplanar (d^8 metal complexes) arrangements. [40] Most of the investigated Cu(I) complexes are trigonally or tetragonally coordinated, while the number of linear complexes is rather low. [30, 39, 43, 44] A large number of mononuclear 4-coordinated bis-phosphine Cu(I) complexes exhibit TADF. [18, 19, 1, 45, 46, 47, 48, 49] With rigidifying ligands as in Cu(N^N)(P^P) complexes, the nonradiative deactivation can be reduced and therefore the emission quantum yield can be increased. [41] For 4-coordinated copper complexes such as $Cu(N\^{}N)_2$, a fast flattening of the structural change upon photoexcitation was found, which can be attributed to a pseudo-Jahn-Teller (PJT) distortion in the MLCT-excited states. [50, 51, 52, 53, 54] Many of the trigonally coordinated Cu(I) complexes carry a sterically demanding monodentate N-heterocyclic carbene (NHC) ligand and a heterocyclic bidentate (N^N) ligand. [41] Depending on the relative orientation of the ligands, the complexes emit via phosphorescence or TADF. [55, 56, 57, 58] Due to PJT distortions of the 3-coordinated complexes, the Cu center is coordinated in a T-shape in the excited state in liquid solution. [36, 55] For the linearly coordinated complexes sterically demanding cyclic alcyl(amino)carbenes (CAACs) [20, 30, 40, 59, 60, 61, 62, 63, 64, 65, 66] or, more rarely, N-heterocyclic carbenes (NHCs) [67] are chosen. [41] The carbene ligands are further described in section 1.4.3. Linearly coordinated CAAC-Cu(I)-halogenide complexes were studied in some detail, both experimentally and theoretically.[30, 59, 60, 61] They showed microsecond lifetimes and high luminescence quantum yields with values ranging up to 0.96. Although Bochmann and Romanov first reported the occurrence of prompt fluorescence — which is rather untypical for this class of complexes — they corrected their interpretation[59, 68] and now agree with Hamze et al. and Gernert et al. who predict phosphorescence as the main emission channel.[30, 61] To corroborate their analysis of the experimental results, Gernert et al. performed time-dependent density functional (TDDFT) calculations on the Cu(CAAC)X (CAAC = 1-(2,6-diisopropylphenyl)-3,3,5,5-tetramethyl-2-pyrrolidine-ylidene, X = Cl, Br, I) complexes in vacuum, whereas the absorption had been measured in tetrahydrofuran(THF).[30] The emission spectra of Hamze et al. in solution showed a red-shift of the emission maximum when the temperature rises from 77 K to 298 K[61], which is absent for the emission in solid phase. They suspect that this shift may be caused by the formation of an exciplex with THF. Many of these linear copper complexes are phosphorescent with microsecond lifetimes typical of platinum or iridium complexes. [30, 59, 61, 63, 66, 67] While large SOCMEs between the two types of MLCT excitations lead to strong multiplicity mixing, configuration interaction with close-by LC states lends intensity to the phosphorescence emission. [39, 64] PJT interactions in the MLCT excited states manifest themselves in large-amplitude bending distortions. [69] Therefore, although photoluminescence quantum yields (PLQYs) of copper complexes can be high in the solid state, the efficiency markedly decreases in fluid solution. [70] Although the phosphorescence lifetimes of the reported linear Cu(I) complexes are faster than the ones of many other Cu(I) complexes and quantum yields of 0.33-0.65 could be achieved [30], the phosphorescence lifetimes are longer than the radiative lifetimes of typical fluorescent emitters. With longer lifetimes, the probability of side effects like efficiency roll-off effects, which are highly unpleasant for OLED emitters, increases. [13] A way to avoid side effects and achieve high quantum yields, is the usage of TADF. Among the linearly coordinated coinage metal complexes, several carbene metal amides (CMAs) with electrophilic carbenes as acceptors and electron-rich amides as strong electron donors have been shown to be efficient TADF emitters in the solid state. [20, 40, 64, 65, 66, 71]

1.4.2. Zinc emitters

Zinc(II) is used in OLEDs in different ways and in different layers. Formerly investigated zinc complexes mainly showed prompt fluorescence. The heavy-atom effect for zinc is negligible and thus the SOC of Zn(II) complexes is small as well. Therefore, phosphorescence was only observed for a few complexes. [72, 73, 74, 75, 76, 77, 78, 79, 80, 81] Among the complexes, for which phosphorescence was reported are Zn porphyrins, the phosphorescence and ISC of which are known to be vibronically induced. [82] A bright-blue phosphorescence with quantum yields of 0.07-0.11 and short emission lifetimes of 89-74 ns were reported by Oyler et al. for the hemicaged Zn bipyridyl complexes. [75] Another group of complexes, for which phosphorescence has been reported are Zn diimine bis-arylthiolate complexes [76, 77, 78, 79, 80, 81] and a Zn diimine dithiolate complex involving the dianion of the dithiosquaric acid. [83] Accordingly, Zn(II) complexes were mostly investigated as fluorescent emitters or hosts for fluorescent and phosphorescent dopants.[17, 84, 85, 86]

With the growing interest in new OLED emitters, the research on TADF-based Zn(II) emitters was strongly promoted. Even though Zn(II) complexes exhibit a d^{10} configuration like Cu(I), only few complexes have been investigated regarding their photophysical properties as OLED emitters. For copper complexes, MLCT admixtures to the emitting states are crucial. Due to the higher oxidation state of Zn(II) compared to Cu(I), the MLCT states are higher in energy. [87] Nonetheless, some investigations were carried out on Zn(II) complexes regarding their potential as TADF emitters as well. In 2015 Sakai et al. observed TADF in two complexes with phenylbenzoxazole ligands, which were stabilized by zinc (II). The complexes exhibit intra-ligand charge transfer characteristics and a high external quantum efficiency of nearly 20%. [31]. Three years later, a proton-transfer system of dichlorinated zinc with a 2-[6-(3,5-dimethyl-1H-pyrazol-1-yl)- pyrimidin-4-yl]phenol ligand was investigated by Berezin et al., which has excitation-wavelength-dependent emission and revealed TADF as well. [88] The dinuclear Zn(II) complexes with donor-acceptor ligands Zn(PhOPy)-PXZ (PXZ=phenoxazine) and Zn(PhOPy)-DMAC (DMAC=9,9-dimethyl-9,10-dihydroacridine) were presented to show TADF by Xiong et al. in 2020. [89] The most recent occurrence of TADF was presented by Goswami et al. for Zn(II) complexes with iminophosphonamide ligands. Of the three examined complexes, one showed TADF, while the other two showed prompt fluorescence. [90]

With their low cost and lower toxicity compared to other metal complexes, NHC-Zn complexes are used as catalysts in iminehydrogenation, CO_2 reductive amination, CO_2 hydrosilylation, alkene/alkyne hydrosilylation, allylic alkylation and cyclic ester/carbonate polymerization. [91] Although many Zn(II) complexes are known, which are stabilized by NHC coordination, none of the Zn(II) complexes that show TADF carried carbene ligands.

1.4.3. Carbene ligands

As briefly described before, many Cu(I) complexes, which showed TADF, have carbene ligands. Cu(I) carbene complexes have already been investigated regarding their suitability as OLED emitters. Since only few Zn (II) complexes were considered as phosphorescence or TADF emitters in general, Zn (II) carbene complexes have so far only been considered with regard to

their catalytic properties. [91]
The choice of the carbene can strongly influence the photophysical properties of the complex. In the investigated complexes, N-heterocyclic carbenes (NHCs), cyclic (alkyl)(amino) carbenes (CAACs) and cyclic (amino)(aryl) carbenes (CAArCs) were used. Their structure motives are shown in Figure 1.

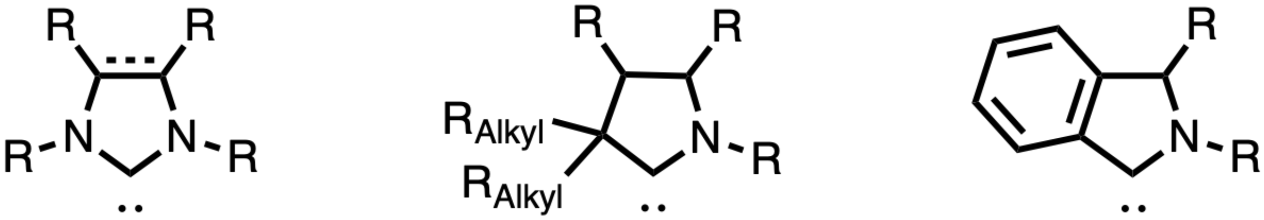

Figure 1.: Structure motives of the NHC (left), CAAC (middle) and CAArC (right) ligands.

Several Cu(I) complexes with NHC ligands are known to show high emission efficiencies. [39, 56, 57, 58, 92] With different ligands on the backbone of the NHC, the steric demand and the σ-donor strength can be tuned. [57]
CAACs were first synthesized by Bertrand and coworkers.[93, 94] Their structures closely resemble those of NHCs. While for NHC diamino groups are used, in CAACs one of the σ-withdrawing and π-electron donating amino groups is replaced by two σ-donating alkyl groups. [95] This leads to a higher σ-donor strength than in NHCs. [96] In addition, CAAC ligands are much stronger π-acceptors. [97] Because of these properties, CAACs seem to be more efficient ligands than NHCs. [98] In many cases, the resulting complexes are storable at room temperature. Like NHC complexes, CAAC complexes can be used for catalytic as well as chromophoric purposes. For Cu(I) complexes with a CAAC ligand, recent investigations have shown highly efficient emission. [20, 30, 70, 60]
In cyclic (amino)(aryl)carbenes (CAArCs) the alkyl substituents of the CAACs are replaced by an aryl substituent.[40, 95, 99, 100, 101, 102] In CAArCs the carbene center is even more electrophilic and as nucleophilic as in CAACs. This leads to an increase of the electrophilic character, while retaining a similar σ-donor strength as CAACs.

2. Theory and methods

2.1. DFT

For the optimization of the ground state geometries, density functional theory (DFT) was used. As the name suggests, DFT uses the electron density instead of the wave functions to calculate the energies. While for the calculation of a system with N electrons via wave function methods $3N$ variables are needed, the calculations with the electron density only require the three room coordinates to describe all N electrons. DFT is based on the Hohenberg-Kohn theorems. The first theorem says that for each ground state electron density exactly one clearly determinable external potential and one clearly determinable ground state energy function exists. The electronic energy of the ground state is completely determinable with the one-electron density.
The second Hohenberg-Kohn theorem shows that a variation principle exists for the exact density functional $E_0[\rho]$. Let ρ be the exact density and $\tilde{\rho}$ a test density. According to the second Hohenberg-Kohn theorem the following applies:

$$E[\tilde{\rho}] \geq E_0[\rho]] \, .(1)$$

The exact density functional $E_0[\rho]$ is unknown, however. To derive an approximate expression, the electronic energy of a multi-electron system is partitioned into the sum of the different contributions.

$$E[\rho] = F[\rho] + \int V_{ext}(\vec{r})\rho(\vec{r})d\vec{r} \tag{2}$$

The kinetic energy $T[\rho]$ and the electron-electron interaction energy $V_{ee}[\rho]$ are collected in:

$$F[\rho] = T[\rho] + V_{ee}[\rho] \, . \tag{3}$$

The last term is based on the one-to-one correspondence between the external potential $V_{ext}(\vec{r})$ and the density $\rho(\vec{r})$.

The optimal density $\rho(\vec{r})$ of the ground state cannot be determined with the variational principle without knowing the functional forms of $T[\rho]$ and $V_{ee}[\rho]$. To solve this problem, Kohn and Sham defined a reference system of N fermions with no mutual interactions. The pseudo-electrons do not have a spin or charge, but respect the Pauli principle. The reference system is called the Kohn-Sham system and has the same ground state density as the original system. The ground state wave function of the reference system consists of only one Slater determinant of N one-electron functions $\psi_k(\vec{r_i})(k = 1, \cdots, N)$ (Kohn-Sham orbitals). For this system, the ground state density is defined as

$$\rho(\vec{r}) = \sum_{k=1}^{N} e|\psi_k(\vec{r})|^2 \tag{4}$$

and is, according to the premises, the same as the ground state density of the system with interacting electrons.

In the Kohn-Sham system the kinetic energy is given by:

$$T_s[\rho] = \sum_{k=1}^{N} \int \psi_k^*(\vec{r_i})[-\frac{\hbar^2}{2m_e}\nabla_i^2]\psi_k(\vec{r_i})d\vec{r_i}\,. \tag{5}$$

Using this expression, the functional of the kinetic energy can be calculated from the Kohn-Sham orbitals for arbitrary charge distributions. But $T_s[\rho]$ is only an approximation to $T[\rho]$. Its small error is corrected at some other place. The Coulomb part of the electron interaction can be described as

$$J[\rho] = \frac{1}{2}\sum_{k=1}^{N}\sum_{\substack{l=1\\ l\neq k}}^{N} \int\int \psi_k^*(\vec{r_i})\psi_l^*(\vec{r_j})\frac{e^2}{r_{ij}}\psi_k(\vec{r_i})\psi_l(\vec{r_j})d\vec{r_i}d\vec{r_j} \tag{6}$$

in a usual manner as well.

With these definitions, equation 3 can be written as

$$F[\rho] = T_s[\rho] + J[\rho] + E_{XC}[\rho]\,. \tag{7}$$

The parts which are not included in explicit formulas are part of the exchange-correlation functional:

$$E_{XC}[\rho] = (T[\rho] - T_s[\rho]) + (V_{ee}[\rho] - J[\rho])\,. \tag{8}$$

The energy functional is given as

$$E[\rho] = T_s[\rho] + J[\rho] + E_{XC}[\rho] + \int V_{ext}(\vec{r})\rho(\vec{r})d\vec{r}\,. \tag{9}$$

The Kohn-Sham orbitals minimize the energy functional via the electron density. They can be determined by solving the one-electron eigenvalue equations (Kohn-Sham equations).

$$\left\{-\frac{\hbar^2}{2m_e}\nabla_i^2 + V_{eff}(\vec{r}_i)\right\}\psi_k(\vec{r}_i) = \epsilon_k\psi_k(\vec{r}_i) \tag{10}$$

with

$$V_{eff}(\vec{r}_i) = V_{ext}(\vec{r}_i) + \int \frac{e\rho(\vec{r}_j)}{r_{ij}} d\vec{r}_j + V_{XC}(\vec{r}_i) \tag{11}$$

The Kohn-Sham equations are solved in formal analogy to the Hartree-Fock formalism:

$$\left\{-\frac{\hbar^2}{2m_e}\nabla_i^2 - \sum_{a=1}^{K}\frac{Z_a e^2}{r_{ai}} + \sum_{\substack{l=1\\ l>k}}^{N}\int \frac{e^2\psi_l^*(\vec{r}_j)\psi_l(\vec{r}_j)}{r_{ij}} d\vec{r}_j + V_{XC}(\vec{r}_i)\right\}\psi_k(\vec{r}_i) = \epsilon_k\psi_k(\vec{r}_i)\,. \tag{12}$$

The Hartree-Fock equation includes an explicit term for the exchange operator but no correlation contributions. In the Kohn-Sham equation, the exchange is included implicitly for the exchange and correlation parts. The electron of the Kohn-Sham orbital moves in an effective potential V_{eff} of equation 11. Without external fields, this effective potential consists of the classical potentials of the electron-core interaction and the Coulomb part of the electron interaction as well as of the non-classical exchange-correlation potential.

Based on the Hohenberg-Kohn theorem, DFT is an exact theory. The Kohn-Sham version can in principle be exact as well. The solution of the Kohn-Sham equation gives a one-electron function, of which the exact ground state exchange determinant is determined. A prerequisite for this is the knowledge of the exact exchange-correlation energy or the exchange-correlation potential. Both are unknown and approximations have to be made. Therefore, DFT calculations can only approximate ground state densities or ground state energies.

In general, the solution of the Kohn-Sham equation 10 can only be done iteratively, since the effective potential V_{eff} contains the Kohn-Sham orbitals. V_{eff} is formed with a given set of variation functions $\psi_1^0, \psi_2^0, \cdots, \psi_N^0$ and the equation 10 is solved. Of the resulting functions $\psi_1^1, \psi_2^1, \cdots$ the N functions with the lowest orbital energies are selected. With the selected functions a new V_{eff} is generated and the equation is solved again until self-consistence is achieved. The functions with the N lowest orbital energies are the sought-after Kohn-Sham orbitals. In application, the Kohn-Sham orbitals are devised after a basis of atomic orbitals (LCAO-MO method). For this, the Kohn-Sham equation is transferred into a secondary system of equations, in which the coefficients are optimized. The DFT calculation is formally similar to a Roothaan-Hall calculation. The computational effort of a DFT calculation is comparable to the one of a Hartree-Fock calculation, but (approximately) includes the electron correlation. With a suitable approximation for the exchange-correlation potential, the DFT has become a routine method. Finding improved exchange-correlation functionals was and still is one of the main concerns of the research on DFT.

For the calculations of this work, the hybrid functionals PBE0 and BH-LYP were chosen. The exchange terms of the BH-LYP functional are based to one half on the Hartree-Fock and to one half on the local spin density approximation (LSDA) with Becke88 (B88) [103] correction. The correlation terms are described by the LYP correlation of Lee, Yang and Parr. [104] The exchange-correlation of the BH-LYP functional is given by: [105]

$$E_{XC}^{BH-LYP} = 0.5E_X^{HF} + 0.5E_X^{LSDA} + 0.5E_X^{B88}\,. \tag{13}$$

The PBE0 functional [106] is the hybrid version of the PBE functional by Perdew, Burke and Ernzerhof. [107, 108] For PBE0 the exchange-correlation energy is

$$E_{XC}^{PBE0} = 0.75E_X^{PBE} + 0.25E_X^{HF} + E_C^{PBE}\,. \tag{14}$$

For the DFT/MRCI method the hybrid functional BH-LYP is used.

2.2. TD-DFT

While DFT is restricted to the calculation of ground states, the time-dependent DFT method is its extension for excited states. It is based on the Runge-Gross theorem of 1984 and is a time-dependent analogon to the Hohenberg-Kohn theorem. The time-dependent electron density $\rho(\vec{r},t)$ is determined by the time-dependent external potential $V(\vec{r},t)$ and a time-dependent function $C(t)$. For the time-dependent system, no minimum principle is available and a stationary point has to be found. This is done via the action integral [109]

$$A[\rho] = \int_{t_0}^{t_1} dt \langle \Psi[\rho](\vec{r},t)| i\frac{\delta}{\delta t} - \hat{H}(\vec{r},t)|\Psi[\rho](\vec{r},t)\rangle\,. \tag{15}$$

With the Euler equation

$$\frac{\delta A[\rho]}{\delta \rho(\vec{r},t)} = 0 \tag{16}$$

the exact electron density $\rho(r,t)$ can be obtained.[109] In analogy to the time-independent Kohn-Sham equations, a time-dependent reference system with the external one-particle potentials $v_s(r,t)$ exists. The electron density of the reference system $\rho_S(r,t)$ is the exact electron density of the real interacting system $\rho(r,t)$.[110]

$$\rho(r,t) = \rho_S(r,t) = \sum_i^N |\phi_i(r,t)|^2 \tag{17}$$

The time-dependent Kohn-Sham equations are then given by

$$i\frac{\delta}{\delta t}\phi_i(r,t) = \left(-\frac{1}{2}\nabla_i^2 + v(r,t) + \int d^3r' \frac{\rho(r',t)}{|r-r'|} + \frac{\delta A_{XC}[\rho]}{\rho(r,t)}\right)\phi_i(r,t) \tag{18}$$

or

$$i\frac{\delta}{\delta t}\phi_i(r,t) = \hat{F}^{KS}\phi_i(r,t)\,. \tag{19}$$

They are single particle equations and the electrons are treated individually in the field of all others.[110] Therein $-\frac{1}{2}\nabla_i^2$ describes the kinetic energy. The exchange and correlation effects are given as $\frac{\delta A_{XC}[\rho]}{\rho(r,t)}$. Since the exact time-dependent exchange-correlation action functional (xc kernel) is unknown, an approximated functional has to be used. The first approximation made is called the adiabatic local approximation (ALDA). Since the electron density is only slowly changing, the time-dependent xc kernel of the ALDA is replaced by a time-independent one. Therefore, the xc potential of the ground state can be used for TDDFT. The time-dependent Kohn-Sham equation can be written in a matrix notation as

$$i\frac{\delta}{\delta t}\mathbf{C} = \mathbf{F^{KS}}\mathbf{C}\,, \tag{20}$$

where $\mathbf{F^{KS}}$ is the matrix representation of the time-dependent Kohn-Sham operator in the given basis and matrix $\mathbf{C}$ contains the time-dependent expansion coefficients of $\phi_i(r,t)$. Via multiplication from left with $\mathbf{C}^\dagger$ and subtraction of the Hermitian transpose, the Dirac form of the Kohn-Sham equation in matrix form is obtained:

$$\sum_q F_{pq}P_{qr} - P_{pq}F_{qr} = i\frac{\delta}{\delta t}P_{pr}\,. \tag{21}$$

In first-order (linear) response, an oscillatory perturbation leads to a change in the density matrix

$$P_{pq} = P_{pq}^{(0)} + P_{pq}^{(1)} \tag{22}$$

and to a change in the Kohn-Sham Hamiltonian

$$F_{pq} = F_{pq}^{(0)} + F_{pq}^{(1)}\,. \tag{23}$$

Substituting equations 22 and 23 into equation 21 and neglecting second-order terms gives

$$\sum_q F^{(0)}_{pq} P^{(1)}_{qr} - P^{(1)}_{pq} F^{(0)}_{qr} + F^{(1)}_{pq} P^{(0)}_{qr} = i \frac{\delta}{\delta t} P^{(1)}_{pr} \,. \tag{24}$$

The first-order Kohn-Sham Hamiltonian consists of two parts. The first is the perturbation g_{pq} with the one-electron operator f_{pq}:

$$g_{pq} = \frac{1}{2}[f_{pq} e^{-iwt} + f^*_{pq} e^{-iwt}] \,. \tag{25}$$

The second part is the two-electron contribution of $F^{(0)}_{pq}$ to the change of the density matrix with d_{pq} as density of the perturbation:

$$P^{(1)}_{pq} = \frac{1}{2}[d_{pq} e^{-iwt} + d^*_{pq} e^{-iwt}] \,. \tag{26}$$

The TD-DFT equation can then be simplified to a non-Hermitian eigenvalue equation:

$$\begin{bmatrix} \mathbf{A} & \mathbf{B} \\ \mathbf{B}^* & \mathbf{A}^* \end{bmatrix} \begin{bmatrix} \mathbf{X} \\ \mathbf{Y} \end{bmatrix} = \omega \begin{bmatrix} \mathbf{1} & \mathbf{0} \\ \mathbf{0} & -\mathbf{1} \end{bmatrix} \begin{bmatrix} \mathbf{X} \\ \mathbf{Y} \end{bmatrix} \,. \tag{27}$$

For hybrid functionals such as BH-LYP, the matrix elements A and B are given by: [110]

$$A_{ai,jb} = \delta_{ij}\delta_{ab}(\epsilon_a - \epsilon_i) + (ia|jb) - c_{HF}(ij|ab) + (1 - c_{HF})(ia|f_{xc}|jb) \tag{28}$$

and

$$B_{ai,jb} = (ia|bj) - c_{HF}(ib|aj) + (1 - c_{HF})(ia|f_{xc}|bj) \,. \tag{29}$$

The orbital energies are given by ϵ and the exchange-correlation kernel by f_{xc}. The indices i and j correspond to the occupied and a and b to the unoccupied orbitals.

Based on TD-DFT the Tamm-Dancoff approximation was developed, in which the matrix **B** is neglected, giving

$$\mathbf{AX} = \omega \mathbf{X} \tag{30}$$

with the same matrix elements of matrix **A** as in equation 28. Since the magnitudes of the amplitudes of **Y** and the elements of matrix **B** are usually small, they are less important and TDA is usually a good approximation to TDDFT.[110] One exception are the transition dipole moments, for which the small contributions of the amplitudes are important. TDDFT is size consistent and is in principle an exact theory in the Kohn-Sham formalism. The only approximations are the modulation of the exchange-correlation functional, which is not exactly known, and the restriction to linear response and thus single excitations.

2.3. DFT/MRCI

An other method to describe excited state properties is the multi-reference configuration interaction (MRCI) method. Herein, the correlated wave function is described as linear combination of different configurations: [105]

$$|\phi_0\rangle = c_0|\Phi_0\rangle + \sum_{ar} c_a^r|\Phi_a^r\rangle + \sum_{a<b,r<s} c_{ab}^{rs}|\Phi_{ab}^{rs}\rangle + ... \tag{31}$$

The different excitations and the ground state are included by individual summands and weighted by the coefficients c$_i$. For a full CI, all excitations are included and the correct correlation energy can be calculated. Since this involves a very large computational effort, a full CI is only possible for very small molecules. In most cases, the MRCI only includes single and double excitations to reduce the computational effort.

With the MRCI method, the static correlation effects are well described even with short expansions. In contrast to that, the dynamic correlations are only poorly described. Therefore, the DFT/MRCI method combines the DFT and the MRCI methods to use the advantages of both. It uses DFT for the calculation of short-ranged dynamic correlation effects and short MRCI developments to determine the long-range static correlation effects. [111] To avoid the double counting of the dynamic effects, a few global but empiric parameters are included in the DFT/MRCI Hamiltonian.

The DFT/MRCI Hamiltonian matrix is built on a basis of configuration state functions (CSFs) using the Kohn-Sham orbital basis. Starting from a Hartree-Fock basis, in second quantization any CI matrix element can be expressed as the difference from the HF ground state energy E$_{HF}$. For this $\bar{w}_i$ is the occupation number of the i-th molecular orbital, $(ij|kl)$ is a two-electron integral in Mulliken notation and E$_i^j$ an excitation operator: [105]

$$\begin{aligned}\hat{H} - E^{HF} = &-\sum_i \bar{w}_i F_{ii}^{HF} - \frac{1}{2}\sum_{ij}\bar{w}_i\bar{w}_j(V_{ijij} - \frac{1}{2}V_{ijji}] + \sum_{ij} F_{ij}^{HF} E_i^j \\ &- \sum_{ijk}(V_{ikkk} - \frac{1}{2}V_{ikkj})\bar{w}_k E_i^j + \frac{1}{2}\sum_{ijkl} V_{iljk}(E_i^j E_k^l - \delta_{jk}E_i^l)\end{aligned} \tag{32}$$

with

$$F_{ij}^{HF} = h_{ij} + \sum_k \bar{w}_k (V_{ikjk} - \frac{1}{2} V_{ikkj}) \tag{33}$$

and

$$E^{HF} = \sum_i \bar{w}_i F_{ii}^{HF} - \frac{1}{2} \sum_{ij} \bar{w}_i \bar{w}_j V_{ijij} - \frac{1}{2} V_{ijj}) \,. \tag{34}$$

The DFT/MRCI Hamiltonian matrix can be divided into different groups of diagonal and off-diagonal elements. The diagonal matrix elements in DFT/MRCI can be described by:

$$\begin{aligned} \langle \omega w | \hat{\mathcal{H}}^{DFT} - E^{DFT} | \omega w \rangle = \langle \omega w | \hat{H} - E^{HF} | \omega w \rangle &- \sum_{i \epsilon c}^{n_{exc}} (F_{ii}^{HF} - F_{ii}^{KS}) \\ &+ \sum_{i \epsilon a}^{n_{exc}} (F_{ii}^{HF} - F_{ii}^{KS}) + \Delta E_{coul} - \Delta E_{exch} \end{aligned} \tag{35}$$

with

$$F_{ii}^{HF} = h_{ii} + \sum_k \bar{w}_k (V_{ikik} - \frac{1}{2} V_{ikki}) \tag{36}$$

and

$$E^{HF} = \sum_i \bar{w}_i F_{ii}^{HF} - \frac{1}{2} \sum_{ik} \bar{w}_i \bar{w}_k (V_{ikik} - \frac{1}{2} V_{ikki}) \,. \tag{37}$$

Here, n_{exc} is the excitation class relative to the anchor configuration, the indices a and c describe annihilated and created electrons and the Kohn-Sham orbital energies replace the Hartree-Fock-like orbital energies. [111]

In the original description of Grimme and Waletzke, the two-electron terms are described by:

$$\Delta E_{coul}^{orig} - \Delta E_{exch}^{orig} = \frac{1}{n_{exc}} \sum_{i \epsilon c}^{n_{exc}} \sum_{j \epsilon a}^{n_{exc}} (p_j V_{ijij} -^{m} p N_o] V_{ijji}) \,. \tag{38}$$

The redesigned two-electron term is given by:

$$\begin{aligned} \Delta E_{coul}^{red} - \Delta E_{exch}^{red} = p_j &\left(-\sum_{\substack{i,j \epsilon c \\ i>j}}^{n_{exc}} V_{ijij} - \sum_{\substack{i,j \epsilon a \\ i>j}}^{n_{exc}} V_{ijij} + \sum_{i \epsilon c}^{n_{exc}} \sum_{j \epsilon a}^{n_{exc}} V_{ijij} + \sum_{i \epsilon s}^{n_{single}} \frac{1}{2} V_{iiii} |\Delta w_i| \right) \\ - p_x &\left(\frac{1}{2} \sum_{i \epsilon c}^{n_{exc}} \sum_{j \epsilon a}^{n_{exc}} V_{ijji} - \sum_{\substack{i,j \epsilon c \\ j \epsilon s}}^{n_{exc}} V_{ijji} - \sum_{\substack{i,j \epsilon a \\ j \epsilon s}}^{n_{exc}} V_{ijji} + \sum_{\substack{i,j \epsilon o \\ i>j}}^{N_o} V_{ijji} \eta_{ij}^{ji} \right) \,. \end{aligned} \tag{39}$$

The calculation of the off-diagonal matrix elements with same space parts and different CSFs uses the unmodified CI Hamiltonian in the original DFT/MRCI.

$$\langle \omega w|\hat{\mathcal{H}}^{DFT}|\omega^{'} w\rangle = \langle \omega w|\hat{\mathcal{H}}^{CI}|\omega^{'} w\rangle \tag{40}$$

For the redesigned Hamiltonians, a scaling factor is introduced to maintain a consistent energy splitting between the CSFs. [111]

$$\langle \omega w|\hat{\mathcal{H}}^{DFT}|\omega^{'} w\rangle = \langle \omega w|(1-p_x)\hat{\mathcal{H}}^{CI}|\omega^{'} w\rangle \tag{41}$$

To avoid a double counting of the dynamic electron correlation, a damping function is introduced for off-diagonal elements with different space and different spin parts, which damps the interaction of configurations with large energy separation. These configurations are already included in the DFT description. For the original approach, the off-diagonal elements are given by:

$$\langle \omega w|\hat{\mathcal{H}}^{DFT}|\omega^{'} w^{'}\rangle = \langle \omega w|\hat{\mathcal{H}}^{CI}|\omega^{'} w^{'}\rangle p_1 e^{-p_2 \Delta E^4_{ww'}} \; . \tag{42}$$

For the redesigned Hamiltonians R2016 and R2017, the modification of the damping and scaling functions leads to:

$$\langle \omega w|\hat{\mathcal{H}}^{DFT}|\omega^{'} w^{'}\rangle = \langle \omega w|\hat{\mathcal{H}}^{CI}|\omega^{'} w^{'}\rangle \frac{p_1}{1+(p_2\Delta E_{ww'})^5 arctan(p_2\Delta E_{ww'})^5} \; . \tag{43}$$

The redesigned damping of the R2018 Hamiltonian is again closer to the original damping, but depends with higher exponent on the energy difference between the diagonal elements of the involved CSFs $\Delta E_{ww'}$.

$$\langle \omega w|\hat{\mathcal{H}}^{DFT}|\omega^{'} w^{'}\rangle = \langle \omega w|\hat{\mathcal{H}}^{CI}|\omega^{'} w^{'}\rangle p_1 e^{-p_2 \Delta E^6_{ww'}} \tag{44}$$

2.4. Spin-orbit coupling

The spin-orbit coupling (SOC) is a relativistic effect and a result of the interaction of the spin and the orbital angular momentum. The SOC leads to a splitting of the energy levels and enables the transition between states of different spin multiplicity. Without SOC, processes like intersystem crossing (ISC) or phosphorescence would be spin-forbidden. With SOC, the electronic states are no longer pure spin states and ISC or phosphorescence can occur.

For light and heavy atoms, the SOC behaves differently. In light atoms, the SOC is small compared to the Coulomb interaction. The electron spins s_i and the orbital angular momenta

l_i couple to the total momenta $\mathbf{L} = \sum_\mathbf{i} \mathbf{l_i}$ and $\mathbf{S} = \sum_\mathbf{i} \mathbf{s_i}$. Together, S and L couple to the total angular moment $\mathbf{J} = \mathbf{L} + \mathbf{S}$. The interaction between the quantum numbers L and S is called Russell-Saunders coupling (LS-coupling).

In heavy atoms, the interaction of single electrons is small compared to the SOC. In the relativistic theory, the spin momentum **s** and the orbital angular momentum **l** cannot be treated separately. For each particle i the spin momentum $\mathbf{s_i}$ and the orbital angular moment $\mathbf{l_i}$ are summed up to the total angular momentum $\mathbf{j_i} = \mathbf{l_i} + \mathbf{s_i}$. The total angular momentum is then given by $\mathbf{J} = \sum \mathbf{j_i}$ (jj-coupling).

For the investigation of spin-orbit effects a spin-orbit operator has to be introduced. One possibility is the Breit-Pauli spin-orbit operator. The Breit-Pauli Hamiltonian is given by:

$$\begin{aligned}\hat{\mathcal{H}}_{SO}^{BP} = \frac{e^2}{2m_e^2c^2}\Bigg\{&\sum_i \left(-\vec{\nabla}_i \left(\sum_I \frac{Z_I}{\hat{r}_{iI}}\right) \times \vec{\hat{p}}_i\right) \cdot \vec{\hat{s}}_i \\ &+ \sum_i \sum_{j \neq i} \left(\vec{\nabla}_i \left(\frac{1}{\hat{r}_{ij}}\right) \times \vec{\hat{p}}_i\right) \cdot \vec{\hat{s}}_i \\ &+ \sum_i \sum_{j \neq i} \left(\vec{\nabla}_j \left(\frac{1}{\hat{r}_{ij}}\right) \times \vec{\hat{p}}_j\right) \cdot \vec{\hat{s}}_i \\ &+ \sum_i \sum_{j \neq i} \left(\vec{\nabla}_i \left(\frac{1}{\hat{r}_{ij}}\right) \times \vec{\hat{p}}_i\right) \cdot \vec{\hat{s}}_j \, .\end{aligned} \tag{45}$$

Here, i and j are labels of the electrons, Z the charge of the nucleus I, e the charge of an electron, m_e the mass of an electron and c the speed of light. The two first terms are referred to as the spin-same-orbit part. The third and fourth term are the spin-other-orbit terms and describe the coupling between the spin magnetic moment of electron i and the orbital magnetic moment of electron j. [112] To lower the computational effort, the mean-field approximation can be used for heavy elements. For this purpose, the orbitals close to the nuclei are frozen (frozen core), and the two-electron interactions of the valence orbitals are averaged over α- and β-spin orientations. The resulting spin-orbit mean-field (SOMF) hamiltonian is based on the one- and two-electron BP Hamiltonians and is given by:

$$\begin{aligned}\langle i(1)|\hat{\mathcal{H}}_{SO}^{mf}|j(1)\rangle = \langle i(1)|\hat{h}_{SO}^{BP}(1)|j(1)\rangle \\ &+ \frac{1}{2}\sum_k n_k\{2\langle i(1)k(2)|\hat{\mathcal{H}}_{SO}^{BP}(1,2)|j(1)k(2)\rangle \\ &- 3\langle k(1)i(2)|\hat{\mathcal{H}}_{SO}^{BP}(1,2)|j(1)k(2)\rangle \\ &- 3\langle i(1)k(2)|\hat{\mathcal{H}}_{SO}^{BP}(1,2)|k(1)j(2)\rangle\} \, .\end{aligned} \tag{46}$$

For the atomic mean-field integral approximation (AMFI) [113], the multicenter SOC terms are neglected, which strongly reduces the computational effort with a small error of less than 5 %.

2.4.1. Relativistic effective core potentials

For the calculations of the Cu(I) and Zn(II) complexes in this work, relativistic effective core potentials (ECPs) are used. By using them, SO relativistic effects can be included, while the computational cost is reduced, since the core electrons and their interactions with valance atoms are not treated separately. [114] As claimed by Pitzer and Winter [115], the spin-dependent terms of an atomic ECP can be described as follows:

$$\begin{aligned}\hat{\mathcal{H}}^{SO}(r) &= \sum_{l=1}^{l_{max}} \frac{2\Delta V_l(r)}{2l+1} \vec{l} \cdot \vec{s} \sum_{m_l=-l}^{+l} |l, m_l\rangle\langle l, m_l| \\ &= \sum_{l=1}^{l_{max}} \xi_l(r) \vec{l} \cdot \vec{s} \sum_{m_l=-l}^{+l} |l, m_l\rangle\langle l, m_l| \,.\end{aligned} \tag{47}$$

For the multi-configuration Dirac-Hartree-Fock (MCDHF) ECPs of this work, a semi-local ansatz was used to eliminate radial nodes in valance orbitals,

$$V_{ECP}(\vec{r}) = -\frac{Q}{r} + \sum_{l,j} V_{lj} \mathcal{P}_{ij} \tag{48}$$

where V_{lj} is a local radial potential, $\mathcal{P}_{ij}$ is a projector and l and j are the angular-momentum quantum numbers. The computational cost can be lowered further by using the detailed form of the pseudo-orbitals ϕ_{lj} in the core region. In terms of Gaussians this leads to the following short-range potential V_{lj}: [116]

$$V_{lj}(r) = \sum_{k} B_{lj,k} exp(-\beta_{lj,k} r^2) \,. \tag{49}$$

The parameters $B_{lj,k}$ and $(-\beta_{lj,k}$ were adjusted to minimize the difference of the calculated energies with the all-electron method and the ECPs.

2.5. Intersystem-crossing

Of great importance for the description of the photophysical properties of a complex – especially with regard to its qualification as TADF emitters – are the ISC and rISC rate constants. According to Fermi's golden rule, the ISC rate constant for a nonradiative transition from an initial state i to a final state f can be calculated by:

$$k = \frac{2\pi}{\hbar} \sum_f |\hat{\mathcal{H}}_{if}^{(1)}|^2 \delta(E_i - E_f)\,. \tag{50}$$

$|\hat{\mathcal{H}}_{if}^{(1)}|$ is the first-order perturbed Hamiltonian. In this golden rule approximation, the initial state is coupled to a set of final states by a perturbation of first order. For the golden rule approximation to be valid, the interaction between the initial and the final state has to be small compared to the adiabatic energy gap of the two states. The density of final vibrational states (VDOS) at the energy of the initial state has to be high. [117] In Condon approximation, the electronic and the vibronic parts of the ISC rate constant can be separated. [118] Assuming a Boltzmann population of the vibrational levels in the initial state, the ISC and rSIC rate constants can be determined by:

$$\begin{aligned} k_{\mathrm{(r)ISC}} &= \frac{2\pi}{\hbar Z g} \sum_\alpha |\langle T_b^\alpha | \hat{\mathcal{H}}_{\mathrm{SO}} | S_a \rangle|^2 \\ &\times \sum_{j,k} e^{-(E_{bj}-E_{b0})/k_B T} |\langle v_{ak} | v_{bj} \rangle|^2 \delta(E_{bj} - E_{ak}) \end{aligned} \tag{51}$$

and

$$\begin{aligned} k_{\mathrm{rISC}} &= \frac{2\pi}{3\hbar Z} \sum_\alpha |\langle T_b^\alpha | \hat{\mathcal{H}}_{\mathrm{SO}} | S_a \rangle|^2 \\ &\times \sum_{k,j} e^{-(E_{ak}-E_{a0})/k_B T} |\langle v_{ak} | v_{bj} \rangle|^2 \delta(E_{bj} - E_{ak})\,. \end{aligned} \tag{52}$$

g is its spin multiplicity and Z is the canonical partition function for vibrational motion,

$$Z = \sum_j e^{-\beta E_j}\,, \tag{53}$$

where E_j is the energy of the vibrational level of the electronic state and with β=1/k_BT.

2.6. Radiative transitions

Like the ISC and rISC rate constants, the rate constants of fluorescence and phosphorescence can be calculated using perturbation theory. Starting from Fermi's golden rule, the rate constants for spontaneous emission $k_o(\omega_\alpha)$ of an atom in free space results as follows:

$$k_o(\omega_\alpha) = \frac{\mu^2 \omega_\alpha^3}{3\pi\hbar\varepsilon_0 c^3} \,. \tag{54}$$

Here, μ is the transition dipole moment matrix element and ω_α is the transition frequency. Accordingly, the fluorescence and phosphorescence rate constants can be determined by:

$$k_{\text{rad}} = \frac{1}{3\pi\varepsilon_0\hbar^4 c^3}(E_i - E_f)^3 \left|\langle\Psi_f|\hat{\vec{\mu}}|\Psi_i\rangle\right|^2 \,. \tag{55}$$

For fluorescence, $|i\rangle$ is the wave function of the initial state S_1 and $|f\rangle$ the one of the final ground state. The transition dipole moment is given by $\vec{\mu}_{fi}$. For phosphorescence, the individual T_1 sublevels are used as initial states $|i\rangle$. At high temperatures, the phosphorescence rate constant can be averaged over all three individual triplet components. In this case, the zero-field splitting is small and the phosphorescence rate constant can be described as:

$$k_{\text{ph}^{av}} = \frac{1}{\tau_p^{av}} = \frac{1}{3}(k_{p,x} + k_{p,y} + k_{p,z}) \,. \tag{56}$$

2.7. Solvation effects

A molecule in solution can be influenced by the solvent in many different ways. Especially the polarity of the solvent, which is often described by the dielectric constant, plays an important role. Depending on the molecule and solvent polarity, the molecule is stabilized or destabilized by the solvent. In polar solvents, polar states with high dipole moments are stabilized by the solvent. As a consequence, if a molecule has a small dipole moment in the ground state and a high dipole moment in the excited state, the excited state is stabilized by the solvent, which leads to a redshift of the excitation energies (positive solvatochronism). If, however, the dipole moment in the ground state is larger than in the excited state, for these states an increase of the polarity of the solvent leads to a blueshift of the absorption and emission energies (negative solvatochronism).[119]

2.7.1. Continuum solvation models

In this work, solvation effects were described by implicit solvent models. Within the bulk of the dielectric continuum, the molecule is placed in a cavity. The continuum is polarized by the electric field of the dissolved molecule. The resulting screening charges on the interface can be described by the interaction of the polarization of the continuum and the solvated molecule. For this work, the integral equation formalism of the polarizable continuum model (IEFPCM)[120, 121, 122] and the conductor-like screening model (COSMO)[123] were used. In both models, the solvent is described by a dielectric continuum with dielectric constant ϵ, which is polarized by the molecule.

The first dielectric continuum model based on apparent surface charge (ASC) was the polarizable continuum model (PCM), which was using the exact dielectric boundary condition and is referred to as DPCM. [124] With COSMO, a conductor was used, which lead to a simplification of the boundary conditions.[123] To obtain the charge density, a scaling function was introduced, for which an empirical scaling factor x is used.

$$f_s(\epsilon) = \frac{\epsilon - 1}{\epsilon + x} \tag{57}$$

With COSMO, a reduction of errors of the outlying charges could be achieved. A similar approach based on a conductor was introduced in PCM as CPCM.[125] In IEFPCM, the advantages of the dielectric exactness of DPCM and the reduced outlying charge sensitivity of COSMO were combined. [126]

In both models, in IEFPCM and in COSMO, only the electronic ground state of the solute is described. Since IEFPCM is the default method used in gaussian, it is referred to as PCM in the following.

2.7.2. cLR

When describing solvent polarization, a distinction can be made between a dynamic and an inertial part of the solvent. The dynamic part is fast and can describe the polarization of the electronic charge, while the inertial component is rather slow and can mimic the slow contributions of the nuclei. With the vertical excitation, the initial equilibrium is perturbed. The vertical excitation can be separated into two steps: at first, the molecule is electronically excited, while the solvent polarization is frozen to the ground state. In a second step, the dynamic part of the solvent can rearrange towards the new charge distribution of the solute, while the inertial part stays frozen to the ground state. For the PCM model, two comparable frameworks can be used for the description of the solvent polarization with the reaction field kept frozen in the ground state ω_{0i}^{0}: the linear response (LR) and the state-specific (SS) approach. [127]

$$\omega_{0i}^{LR} = \omega_{0i}^{0} + \langle i^{(0)}|\hat{V}|0\rangle\langle 0|\hat{Q}_{dyn}|i^{(0)}\rangle = \omega_{0i}^{0} + R_{dyn}^{LR}(P_{0i}^{T}) \tag{58}$$

$$\omega_{0i}^{SS} = \omega_{0i}^{0} + \frac{1}{2}[\langle i^{(0)}|\hat{V}|i^{(0)}\rangle - \langle 0|\hat{V}|0\rangle][\langle i^{(0)}|\hat{Q}_{dyn}|i^{(0)}\rangle - \langle 0|\hat{Q}_{dyn}|0\rangle] = \omega_{0i}^{0} + R_{dyn}^{SS}(P_{0i}^{\Delta}) \tag{59}$$

Here, $\hat{V}$ is the molecular electrostatic potential operator, $|i^{(0)}\rangle$ is the i-th electronic state obtained in the presence of the reaction field of the ground state $|0\rangle$ and $\hat{Q}_{dyn}$ is the dynamical apparent charge operator. For the ground state description, LR and SS approaches lead to comparable results. But while the LR approach uses the transition density P_{0i}^{T}, the SS approach uses the difference of the electron densities of the initial and the final states P_{0i}^{Δ} to determine the response of the dynamic solvent polarization towards the excitation. Therefore, the LR and the SS approaches show strong deviations when the densities of ground and excited states show large changes. [127] The PCM model is suitable to describe the short time delay of an excitation of a molecule in rigid polar environment. For longer time delays and less rigid environments, the PCM model fails and a different model has to be chosen. The SS approach is based on the explicit calculation of the excited-state wave function. With the corrected linear response (cLR) model, SS corrections are introduced to the LR approach, to combine the TDDFT framework with PCM in the SS formulation. [128] The description of the solvation effects of the cLR model is based on the integral equation formalism (IEF) of the PCM model. The first-order perturbation theory ansatz is used to describe the non-linear character of the problem of TDDFT. For an accurate description of the different processes of the solute in solvation, different calculations are carried out one after the other in cLR.

Starting from the ground state, where solute and solvent are in full equilibrium, the excitation and relaxation process can be divided into a 6-step cycle (Figure 2): 1) The cycle starts with the electronic excitation of the solute and only the dynamic part of the solvent rearranges to the new charge distribution of the solute. Solute and solvent are no longer in equilibrium. 2) The second step is the complete relaxation of the solvent towards the excited state charge distribution. The geometry of the solute is still the same as in the ground state. 3) As a third step, the geometry of the solute rearranges to the excited state and a new excited state equilibrium of solute and solvent results. 4) The fourth step is the relaxation of the solute towards its electronic ground state. The dynamic part of the solute rearranges to the ground state as well. 5) At step five, the solute geometry stays the same as in the excited state, while the solvent relaxes to the ground state. 6) The final step is the complete relaxation of the solute to the ground state equilibrium of solute and solvent, which was the starting point. [128] According to this cycle,

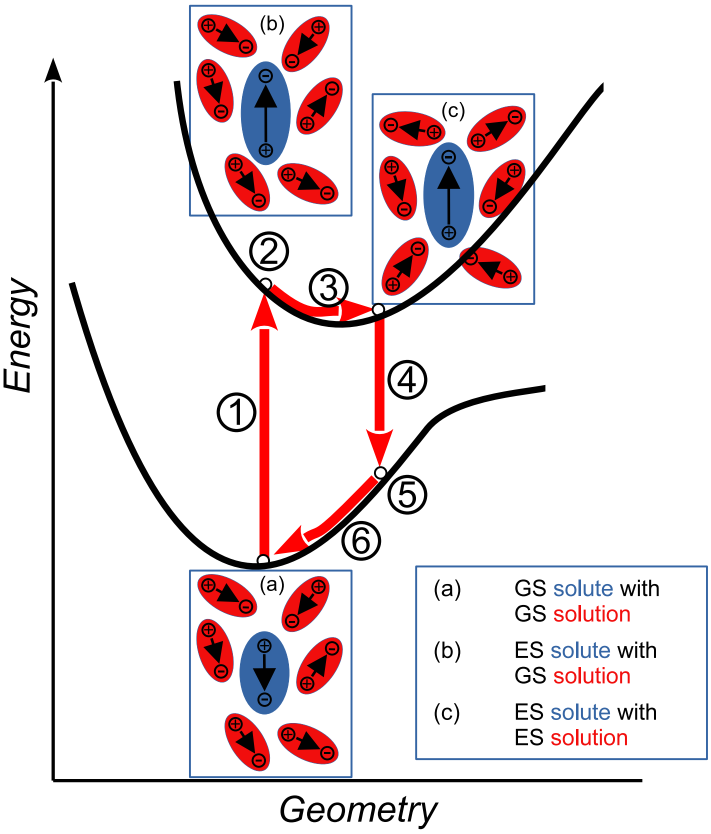

Figure 2.: Cycle of steps of the cLR model.

the descriptions of the solute and solvent can be divided into equilibrium and nonequilibrium descriptions. The description of the equilibrium is the same for the TDDFT PCM and the cLR approaches. They differ in the further description of the polarization charges of the solvent. For the cLR model, the solvent is divided into an electronic (dynamic) and an orientational (inertial) part. The two contributions are calculated separately, since the dynamic contribution rearranges much faster than the inertial contribution. The polarization charges of the inertial part are the same for the excited state and the ground state. The dynamic charges are the sum of the dynamic charges of the ground state and an additional charge for the change between the ground state and the excited state:

$$\mathbf{q}_K = \mathbf{q}_{GS} + \mathbf{q}_\Delta \,. \tag{60}$$

A TDDFT scheme with a non-Hermitian eigensystem similar to equation 27 is used. The eigenvalue ω_K^0 cannot account for the polarization of the wave function, but it can represent the excitation energy in the presence of a PCM reaction field that remains frozen in its ground state situation and is therefore a good approximation to ΔE_{GS}^{K0}.[128] With this approximation, no distinction between the equilibrium and nonequilibrium wave functions can be made. With $\Delta E_{GS}^{K0neq} = E_{GS}^{K} = \omega_K^0$, the equilibrium and nonequilibrium free energies for the excited state K become:

$$G_K^{eq} = G_{GS} + \omega_K^0 + \frac{1}{2}\sum_i V(s_i; \mathbf{P}_\Delta) q_\Delta(s_i; \mathbf{P}_\Delta) \tag{61}$$

and

$$G_K^{neq} = G_{GS} + \omega_K^0 + \frac{1}{2}\sum_i V(s_i; \mathbf{P}_\Delta^{neq}) q_\Delta^{dyn}(s_i; \mathbf{P}_\Delta^{neq}) \, . \tag{62}$$

With analytical energy gradients as extension of the TDDFT, the relaxation part of the density and the corresponding charges can be obtained. With the Z-vector approach, which is used, and the unrelaxed density matrix in terms of the eigenvectors $|X_K, Y_K\rangle$ of the TDDFT system, the unknown density matrix $\mathbf{P_\Delta}$ can be calculated for each state K.

$$\mathbf{P}_\Delta = \mathbf{T}_K + \mathbf{Z}_K \tag{63}$$

With $\mathbf{P_\Delta}$, the corresponding charges can be obtained with x=GS,K by:

$$\mathbf{q}_\Delta^x = \mathbf{Q}(\epsilon_x) + \mathbf{V}(\mathbf{P}_\Delta^x) \, . \tag{64}$$

The TD-DFT equation can then be simplified to a non-Hermitian eigenvalue equation [128]

$$\begin{bmatrix} \mathbf{A} & \mathbf{B} \\ \mathbf{B}^* & \mathbf{A}^* \end{bmatrix} \begin{bmatrix} X_K \\ Y_K \end{bmatrix} = \omega_K^0 \begin{bmatrix} \mathbf{1} & \mathbf{0} \\ \mathbf{0} & -\mathbf{1} \end{bmatrix} \begin{bmatrix} X_K \\ Y_K \end{bmatrix} \, . \tag{65}$$

For the calculations at the ground state geometry, the solvent polarization is completely equilibrated to the ground state polarization of the solute. To describe the excitation (and relaxation) process, a distinction between equilibrium and nonequilibrium has to be drawn. The nonequilibrium can be separated into two steps as well. In the first step after electronic excitation of the solute, the polarization of the solvent stays frozen to the ground state. The polarization of the solvent can be distinguished in a dynamic, fast part, which describes the electronic charge, and an inertial, slow part, which can mimic the contributions of the nuclear and molecules. After the electronic excitation of the solute, the dynamic part can rearrange first, while the initial part stays frozen to the ground state. With rearrangement of the initial part, a new equilibrium in the excited state is achieved.

3. Results

3.1. Copper complexes

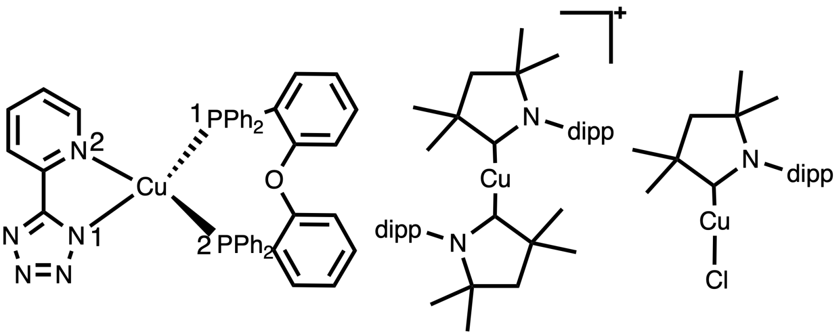

Figure 3.: Structures of the investigated copper complexes.

During the last years, the interest in OLEDs and therefore the number on publications about the photophysical properties of Cu(I) complexes has strongly increased, and some design criteria for efficient d^{10} metal complexes were found. [129] At the beginning of this work, there were only a few publications which gave reliable data of the photophysical properties to validate the quantum chemical methods. One of the few literature known complexes which shows TADF and for which lifetimes and (r)ISC rate constants were experimentally determined, was the (DPEPhos)Cu(PyrTet) complex shown in Figure 3.1. Theoretical studies with B3LYP and TD-B3LCP methods were carried out on this complex by Gao et al. [130], too. Hence, this complex is an optimal candidate to compare the results of our calculations to the experiment and other calculations to obtain an idea of how well the applied methods can represent them. In addition to this, the Cu(I) complexes were also examined in order to find a systematic for whether the complexes are dark, or show TADF, or phosphorescence. The CAAC-Cu-Cl and the $\mathrm{Cu(CAAC)}_2^+$ complexes have been experimentally investigated by the group of Steffen et al. and have been reported to be phosphorescent. [30, 129] For a similar CAAC-Cu-Cl complex with an ethyl group instead of a methyl group the emission spectra showed a strong redshift in solution by increasing the temperature from 77 K to 298 K. In solid phase, no temperature dependance of the emission was observed. Calculations with an explicit THF molecule should clarify if an exciplex is formed.

The results of the calculations on the (DPEPhos)Cu(PyrTet) and the CAAC-Cu-Cl complexes were published in paper I and are summarized in the following sections. The results of the $Cu(CAAC)_2^+$ complex have not been published yet.

3.1.1. (DPEPhos)Cu(PyrTet) (Paper I)

Of high interest for the qualification as OLED emitter are the ISC rate constants of a complex. Even though many investigations on copper (I) complexes have been carried out, the number of complexes for which the ISC rate constants were determined is limited. One of the complexes for which detailed experimental data has been reported is the [(bis(2-(diphenylphosphino)phenyl)ether) Cu(5-(2-pyridyl)tetrazolate)] (=(DPEPhos)Cu(PyrTet) complex, which was first synthesized by Bergmann et al. [1] This neutral, mononuclear metal complex shows TADF and the kinetics of the excited-state processes are known. Not only the experimental data in solution [2] and solid phase [19], but also extensive TD-DFT studies are available. [130] Accordingly, the (DPEPhos)Cu(PyrTet) complex is ideal to validate the calculation methods of this work for the calculation of photophysical processes in transition metal complexes.

Franck-Condon region

The copper atom of the (DPEPhos)Cu(PyrTet) complex is tetragonally coordinated by the ligands. The ligands show a high conformational flexibility, which leads to several ground state minimum geometries. The minimum geometry obtained by the optimization with the crystal structure as starting point is the most suitable for the comparison with the experiment and was used for further investigations. The optimized structure of the ground state in vacuum is in good agreement with the crystal structure, with changes of less than 0.04 Å in the bond lengths and less than 5° in the bond angles.

The experimental absorption spectra were measured in neat film [19] or in dichloromethane (DCM) solution [1] at room temperature. For a description in solution, the implicit DCM environment with COSMO was used. Different DFT/MRCI Hamiltonians and configuration selection thresholds were tested. As visible in Figure 4 , the calculated absorption maximum is redshifted when calculated in vacuum towards that calculated in DCM. These shifts occur in the short wavelength regime between 300-250 nm. In this region, the contribution of intraligand charge-transfer (ILCT) excitations on the PyrTet ligand is increased. These excitations

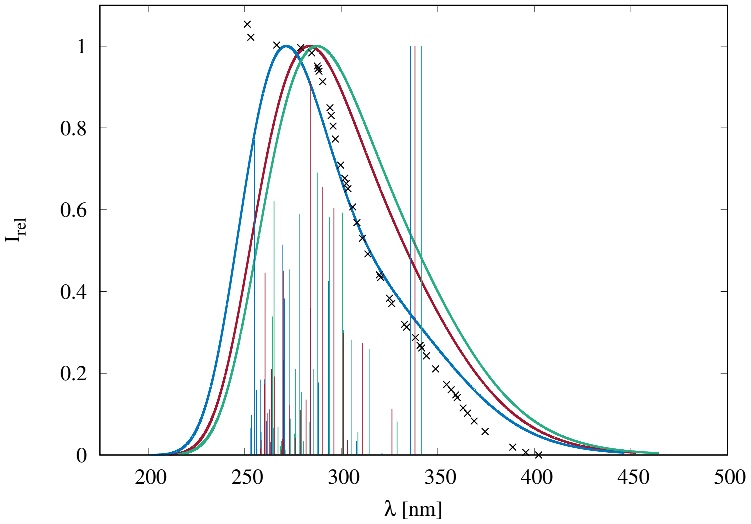

Figure 4.: Calculated absorption spectra in vacuum (with R2016 Hamiltonian in green, R2018 Hamiltonian in red) and in DCM (with the R2018 Hamiltonian in blue) of the (DPEPhos)Cu(PyrTet)complex in comparison to the experimental spectrum in DCM (black). The line spectra were broadened by a Gaussian function with 2700 cm^{-1} FWHM.

are less infected by solvation effects. For the photophysic of the complex, the long wavelength regime, where the S_1 and T_1 excitation take place, is of importance. The S_1 state absorption in vacuum shows a small blueshift from 342 nm to 338 nm by changing from the R2016 to R2018 Hamiltonian. The solvent effect on the S_1 absorption is very small and the transition wavelength is only slightly blueshifted to 336 nm (Figure 4). This is in agreement with the experiments, which describe only minor differences for the absorption in different solvents [2] and only a small blueshift of the absorption in THF compared to those in the gas phase and in a crystalline state [130]. With regard to the photophysics of the complex, the calculations in vacuum are expected to be sufficient and all further calculations were carried out in vacuum to decrease the computational effort. As Hamiltonian, the R2018 Hamiltonian with tight parameters was chosen, for which the calculations are significantly faster than for the R2016 Hamiltonian.

Between 315 and 340 nm a small shoulder can be found in the experimental absorption spectrum, which was assigned to MLCT excitations. The calculated S_0-S_1 excitation at 3.67 eV (338 nm) is in excellent agreement with the shoulder and reported experimental absorption maximum of 341 nm.[1] This excitation is mainly a transition from the highest occupied molecular orbital (HOMO) to the lowest unoccupied molecular orbital (LUMO) (66.9 %). The HOMO and the LUMO are shown in Figure 5. The HOMO is mostly located on the copper and the phosphorus atoms, while the LUMO is located on the PyrTet ligand. The calculation confirms that this absorption is due to an MLCT transition.

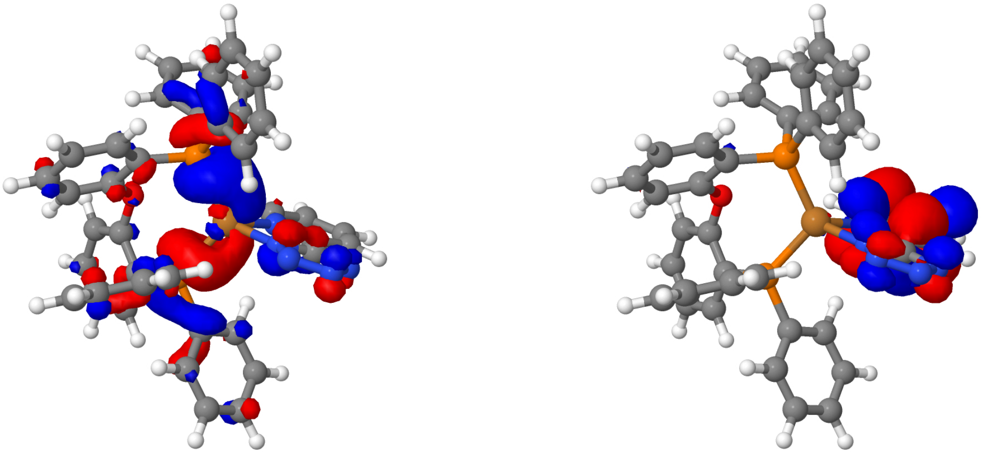

Figure 5.: HOMO (left) and LUMO (right) of the (DPEPhos)Cu(PyrTet) complex at the ground-state geometry in vacuum.

Excited state geometries

Starting from the crystal structure, an S_1 and a T_1 minimum geometry were found. The S_1 and T_1 excitations at the excited-state geometries have a similar MLCT character as the ones at the ground state geometry. The two excited state geometries differ only slightly with changes of less than 6° in their bond angles. In contrast to that, especially the bond angles containing nitrogen and phosphorus atoms show strong changes compared to the ground-state geometry. These N-N-P-P dihedral angles of the S_1 and T_1 geometries show changes of up to 30° compared to the ground state geometry. The comparison of the optimized S_0 and S_1 state geometries shows that the N-N-P-P plane of the complex is flattened in the excited state due to PJT distortion (see Figure 6). The calculated N-N-P-P-dihedral angles are shown in Table 1. A similar flattening distortion (FD) was described by Gao et al.[130] Because of the lower flexibility of the copper coordination and the hindered large-amplitude FD, the experimental emission of the (DPEPhos)Cu(PyrTet) complex in neat film (535 nm)[19] and in powder (510 nm)[1] are strongly blueshifted compared to the emission in DCM at 610 nm.[2]

With the described huge changes between the geometries of the optimized ground and excited states, no meaningful emission spectra could be calculated. Nevertheless, the vertical excitation energies can be compared to the emission maxima. With 608 nm (2.04 eV), the vertical S_0-S_1 excitation energy at the S_1-geometry is much smaller than the emission maximum of 510 nm

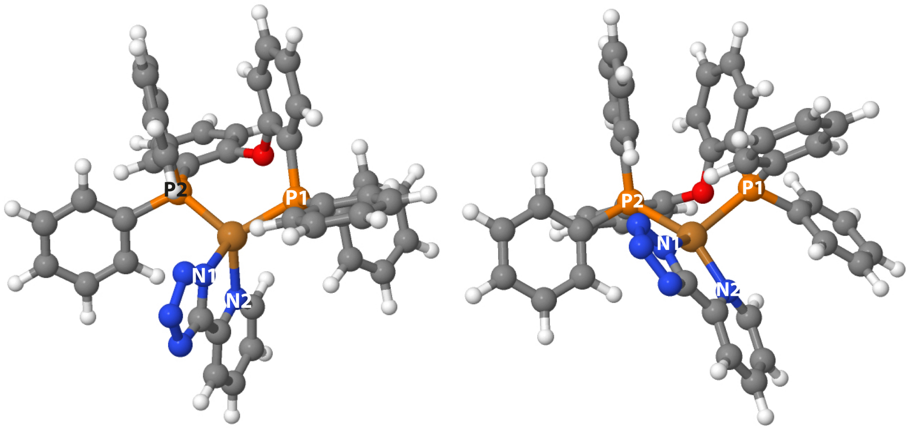

Figure 6.: S_0 (left) and S_1 state geometries (right) of the (DPEPhos)Cu(PyrTet) complex in vacuum.

Table 1.: N-N-P-P dihedral angles of the (DPEPhos)Cu(PyrTet) complex the crystal structure in comparison to the optimized geometries in vacuum.

dihedral angle	crystal structure	S_0	S_1	T_1
N1-N2-P1-P2	-70.6	-70.9	-47.5	-49.9
N1-N2-P2-P1	79.5	78.4	107.2	103.3
N2-N1-P2-P1	-72.8	-75.3	-51.3	-54.7
N2-N1-P1-P2	81.4	79.9	112.2	108.0

in the solid-state experiment, but it is in excellent agreement with the experimental emission maximum of 610 nm in DCM (Figure 7). The calculated vertical S_0-S_1 and S_0-T_1 excitation energies in vacuum are blueshifted by 0.1 eV and 0.04 eV, respectively, compared to those Gao et al. calculated in the gas phase. [130] In contrast to the strong changes of the emission maxima in solid phase and in solution, different solvents only have a small effect on the emission maxima. This is in agreement with the described FD. In solution as well as in gas phase, FD can occur, while in solid phase, the molecules are more rigid and FD is avoided. Accordingly, the calculations are comparable to the experiments in solution.

The calculated adiabatic S_1-S_0 energy of 2.98 eV (416 nm) is in good agreement with the experimental emission onset at 300 K (Figure 7). At lower temperatures, rISC and therefore TADF are unlikely to occur. Hence, the emission at 77K is mainly phosphorescence. The onset of the emission at 77 K is in good agreement with the adiabatic T_1-S_0 energy (2.76 eV, 449 nm), too.

Figure 8 shows the calculated radiative and non-radiative rate constants of the

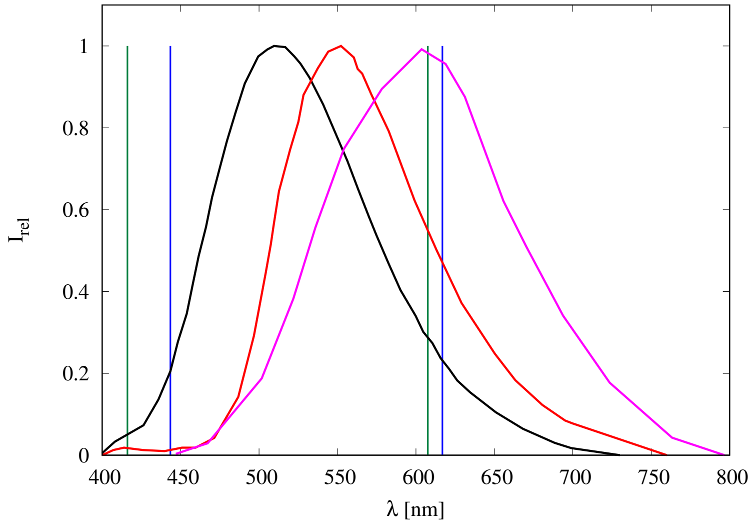

Figure 7.: Experimental emission spectra of (DPEPhos)Cu(PyrTet) as amorphous powder at room temperature (black) and at 77K (red).[1] The experimental emission of the complex in DCM at room temperature is shown in magenta.[2] The calculated adiabatic and vertical excitation energies of the S_1 (green) and T_1 states (blue) are shown as impulses.

Table 2.: Vertical excitation energies of the (DPEPhos)Cu(PyrTet)complex in vacuum.

	$\Delta E(S1-S0)$ [eV]	$\Delta E(S1-S0)$ [nm]	$\Delta E(T1-S0)$ [eV]	$\Delta E(T1-S0)$ [nm]	$\Delta E(S1-T1)$ [eV]
at S_0	3.67	338	3.53	351	0.14
at S_1	2.04	608	1.93	643	0.11
at T_1	2.14	578	2.01	617	0.13

(DPEPhos)Cu(PyrTet) complex in vacuum at room temperature. The ISC rate constant is three orders of magnitude higher than the fluorescence rate constant. The experimental ISC rate constants in DCM [2] and in neat film [1] are in the same order as the calculated ISC rate constant in vacuum. The averaged phosphorescence is even four orders of magnitude smaller than the rISC rate constant (see Figure 8). This is in agreement with the experiment as well, where no phosphorescence was observed and the rISC rate constant was estimated to be smaller than 5×10^8 s^{-1}. [131] Accordingly, the calculated rate constants suggest TADF as main emission pathway, which is in agreement with the experiment.

The calculated ISC and fluorescence rate constants are in excellent agreement with the experimental rate constants [19, 2] and the ones calculated by Gao et al. [130]. Our calculated rate constants agree with the experimental findings of delayed rather than prompt fluorescence as

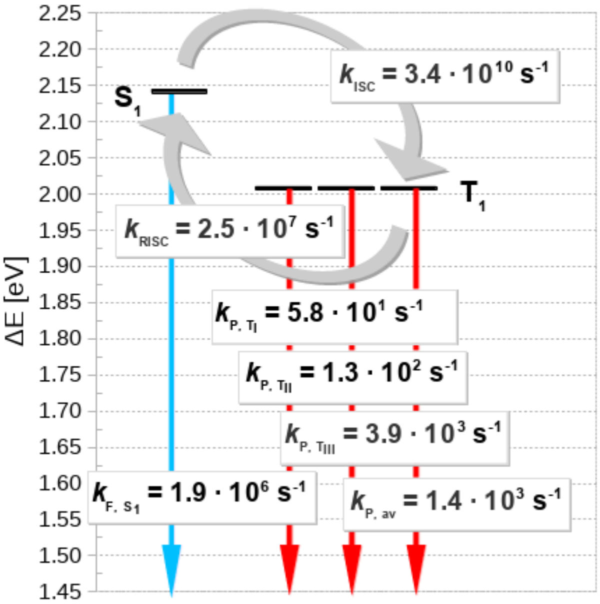

Figure 8.: Calculated rate constants of the (DPEPhos)Cu(PyrTet) complex in vacuum at room temperature.

main emission pathway. A large difference was found between the experimentally determined S_1-T_1 energy gap of 693 cm^{-1} and the calculated adiabatic energy gap between the S_1 and T_1 state of 1485 cm^{-1}. The calculated S_1-T_1 0-0 energy gap of 1503 cm^{-1} is slightly bigger than the adiabatic energy. The experimental energy gap was determined by a fitting to the emission decay times at different temperatures. The adiabatic energy gap between the S_1 and T_1 state of 0.18 eV is similar to the measured shift of the emission maxima at 300K and 77K of 0.18 eV. For the gas phase and in solution Gao et al. calculated an adiabatic S_1-T_1 energy of 0.18 eV as well. Since the crystal is much more rigid, flattening distortion is hindered in the crystal. In the calculations of Gao et al. the S_1-T_1 energy is reduced to 0.15 eV (1210 cm^{-1}) in crystal form. Therefore, the huge difference between the calculated and experimentally determined energy gap is probably mostly due to the different determination methods.

All in all, the methods used for the calculation of the photophysical properties are suitable for this complex and the calculated rate constants in good agreement with the experiment. The major challenge of the calculations is the adequate description of the geometries. The potential energy surface of the S_1 state is much flatter than the one of the ground state. Hence, small changes of the S_1 geometry lead to big changes in the excitation energy.

3.1.2. Carbene-Cu(I)-chlorides (Paper I)

One group of linear Cu(I) complexes, which has been described in literature, are CAAC-Cu-Cl complexes. The CAAC-Cu-Cl complex, on which the further investigations focus, was first synthesized by Gernert et al.[30] To investigate the influence of the carbene, the CAAC ligand was replaced by a NHC and a DAC for calculations at the ground state geometry (Figure 9). The calculations at the excited state geometries were only carried out for the CAAC complex. Since the formation of exciplexes has been found for Cu(I) systems with strong Lewis bases such as THF [132], some calculations with an explicit THF molecule were done, too.

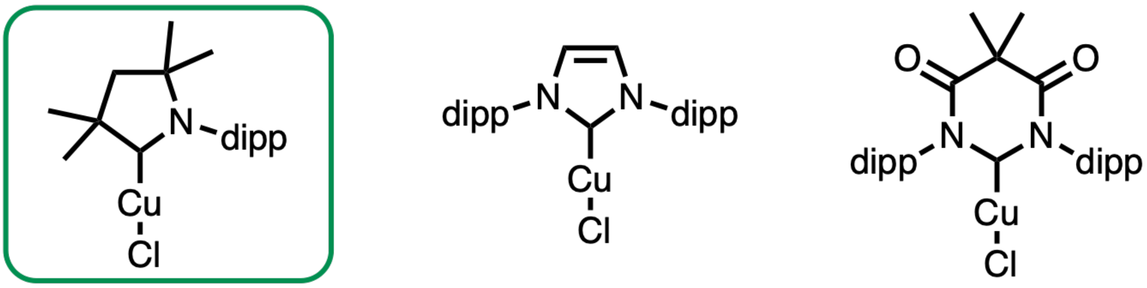

Figure 9.: Structure of the investigated Carbene-Cu(I)-chloride complexes. As carbenes a CAAC (left), a NHC (middle) and a DAC (right) ligand were chosen.

Ground-state geometry

To investigate the influence of the carbene, carbene ligands with different σ-donor and π-acceptor strength were chosen. The NHC ligand has weaker π-acceptance and a lower σ-donor strength than the CAAC ligand. This leads to an increase of the excitation energies of the MLCT and XMLCT excitations, in which the electron density is transferred from the chloride (X) and the copper (M) to the carbene ligand. With the diamidocarbene (DAC) ligand, the π-acceptor strength is further increased and the σ-donor capabilities are maintained compared to the CAAC ligand. By changing the carbene ligand from a CAAC ligand to a DAC ligand, the MLCT excitation energies are strongly redshifted by more than 0.6 eV. The NHC and the DAC ligands each have two dipp groups. The LC(dipp) states are localized on both of the dipp ligands. The CAAC ligand only has one dipp group, resulting in a small increase of less than 0.2 eV of the LC(dipp) states. With the low lying ^{3}LC states of the NHC-Cu-Cl complex, no emission is expected to occur. The comparison of the luminescence properties of different Cu(I) complexes has shown that the energy gap between S_1 and T_1 states with LLCT character is small enough to emit via TADF. Although MLCT contributions increase the SOCMEs, complexes with S_1 and T_1 states of MLCT states show phosphorescence. For the CAAC-Cu-Cl complex, the experiments showed phosphorescence as main emission pathway. [30] For the DAC-Cu-Cl complex, a redshifted phosphorescence is expected. The experimental absorption spectrum of the CAAC-Cu-Cl complex in THF shows three major bands in the region between 200 nm and 500 nm. The long wavelength band is of lower intensity. The most intense peak can be found in the lower-wavelength regime and has a small shoulder. The calculated absorption spectrum in implicit THF is in good agreement in its shape and intensities with the experimental spectrum. The first absorption maximum in the calculated absorption spectra can be assigned to the S_0-S_1 excitations, which have MLCT character, where the electron density is transferred from the copper to the carbene ligand. For the calculated absorption spectrum in vacuum, a significant redshift of the first two bands is found. In contrast to that, the absorption maximum at about 200 nm is the same in vacuum, in implicit THF and in the experiment. The optimized geometries of the complex in vacuum and in THF show only marginal changes. The differences in the absorption spectra are therefore mainly due to electronic effects. The ground state has a dipole moment of 10 D in vacuum and of 12 D in THF. In solution, the solvent molecules strongly stabilize the ground state of the molecule. With charge transfer excitations, the dipole moment is strongly decreased. Since the solution environment is not reorientated to the excited state, the excitation energies of the CT states in THF are blueshifted compared to the molecule in vacuum. The dipole moments of the LC states show only small changes and accordingly, the excitation energies show smaller changes in vacuum and in THF as well. The calculations in vacuum show strong deviations from the experiment of Gernert et al.[30], while the calculations of the FC region in implicit THF is in good agreement with the experiment. Therefore, the implicit THF solvation is chosen for further calculations.

Excited state geometries

At the optimized S_1 and T_1 geometries, the lowest singlet and triplet excitations have MLCT character. At the ground state geometry, the C-Cu-Cl bond angle is close to 180°. The C-Cu-Cl bond angle of the S_1 minimum geometry is only slightly reduced to 173°, while the T_1 geometry shows a strong bending to 132°.

To mimic the excited state THF environment, the PCM and the cLR model were used. In the PCM description, the situation shortly after excitation in solution can be described. The molecular geometry of the solute is relaxed towards the excited state, but the solvent environment is still adapted to the charge distribution of the electronic ground state. In the cLR description, a reorganization of the solvent polarization to the new charge distribution occurred, which reduces the excitation energy. For the vertical emission energies of the S_1 state, a redshift from

2.89 eV with PCM to 2.68 eV with cLR can be found. A similar shift from 2.09 eV to 1.93 eV can be found for the PCM and cLR descriptions of the T_1 excitation energies.

In the experiment of Gernert et al., the luminescence of the CAAC-Cu-Cl complex in liquid THF solution is only weak.[30] This is often the case for complexes with small radiative transition rates, which compete with the collisions of solvent molecules with the solute at the microsecond time scale. The calculations do not include explicit THF molecules and therefore no coordinative interaction of solvent and solute molecules. The experiments showed a strong temperature dependance of the emission in polymethyl methycrylate (PMMA) matrices and a comparable emission of the CAAC-Cu-Cl complex in solid phase and doped into a host of polyspirobifluorene copolymer SPB-02T with a blueshift of 1880 cm^{-1}.

Another problem for the comparison is the high flexibility of the chlorine atom. The chlorine atom only has a small steric demand and can freely rotate or bend in all directions. The calculation of emission spectra and ISC rate constants is based on the harmonic oscillator model. Since the potential energy surface of the excited states is not harmonic, this model fails for the CAAC-Cu-Cl complex. Similar problems were described by Lin et al.[133] The methods they use for the treatment of vibrational overlaps resemble those used for this work. They describe large nonadiabatic couplings and a fast non-radiative decay in liquid solution due to the large-amplitude C-Cu-Cl and Cu-C-N bending motions of the complex. Their model suggests that aggregation leads to a hinderance of the non-radiative channels and gives a strong fluorescence, which is in contrast to the experiments.

Exciplex formation

For some Cu(I) complexes it has been shown that they can form exciplexes with Lewis bases like THF, acetone or pyridine. In the literature, McMillin et al.[132] describe a quenching of MLCT emission for CAAC-Cu-Cl complexes, while Romanov et al. observed a redshift of more than 130 nm of the emission in coordinating solvents.[59] To investigate whether exciplexes are formed with THF or not, calculations with an explicit THF molecule were carried out for the CAAC-Cu-Cl complex.

In the ground state, no formation of bonds was found. The absorption spectra with and without explicit THF molecule show only a small redshift for the CT excitations, while the LC excitations are not shifted. Upon optimization of the S_1 and T_1 states of the CAAC-Cu-Cl complex in the presence of an explicit THF molecule, a covalent bond is formed between the copper atom of the CAAC-Cu-Cl complex and the oxygen atom of the THF molecule, which leads to the formation of exciplexes. Due to the new Cu-O bond, the C1-Cu-Cl bond is strongly bent and the Cu-C1 and Cu-Cl bonds are extended. The S_1 and the T_1 excitations at the exciplex geometries have MLCT/XLCT character, similar to the excitations without the THF molecule. The lone pairs of the THF molecule contribute to the HOMO, while the LUMO is nearly unaffected. The additional bond of the exciplex leads to an increased rigidity of the complex. Accordingly, the geometries of the S_1 and the T_1 states show only small changes and for the exciplex ISC and rISC rate constants can be calculated. The calculated ISC rate constant at 298 K is four orders of magnitude higher than the fluorescence rate constant. By lowering the temperature to 77 K, the ISC rate constant is only lowered by one order of magnitude and no fluorescence is expected to occur. The S_1-T_1 energy gap of 2400 cm^{-1} is higher than in typical TADF emitters. Accordingly, the rISC rate constant at 298 K of 4.9×10^3 s^{-1} is much lower than the ISC rate constant, but still slightly higher than the averaged phosphorescence rate of 4.2×10^3. At 77 K, the rISC is slowed down further and phosphorescence is more likely. The vertical excitation energy of the T_1 is strongly redshifted from 594 nm to 723 nm by formation of the exciplex.

Table 3.: Vertical emission wavelength λ [nm], spin component-averaged S_1-T_1 SOC [cm^{-1}] and radiative as well as non-radiative rate constants k [s^{-1}] of the MLCT states of CAAC-Cu-Cl-THF exciplex.

	S_1			T_1			Temp.		
	λ_F	k_F	SOC	λ_P	k_P	SOC	T [K]	k_{ISC}	k_{rISC}
1	618	7.9×10^5	21.4	723	4.2×10^3	19.0	298	8.9×10^9	4.9×10^3
							77	8.9×10^8	5.3×10^1

While the reported emission of Gernert et al. [30] was measured in solid phase, Hamze et al. [61] measured the emission of a similar CAAC-Cu-Cl complex with a ethyl group instead of the methyl group on the CAAC ligand in 2-MeTHF. Hamze et al. find a strong redshift of the emission maximum from 420 nm to 600 nm by increasing the temperature from 77 K to 298 K. [61] This is in good agreement with the calculated shift for the calculations with and without the explicit THF molecule and confirms the formation of an exciplex in solution at room-temperature.

Summary and conclusion

By substituting the CAAC ligand with other carbenes of different σ-donor and π-acceptor strength, the energy of the low-lying MLCT excitations can be reduced (DAC) or increased (NHC). The comparison of the experimental absorption spectrum of the CAAC-Cu-Cl complex to the calculated spectra in vacuum and in implicit THF, demonstrates the importance of the solvation effects on this complex. The calculations with an explicit THF molecule showed that a covalent bond between the oxygen atom of the THF and the copper atom of the CAAC-Cu-Cl molecule is formed. The THF molecule of the exciplex has only a small contribution to the S_1 and T_1 excitations. Therefore, the S_1 and T_1 states of the CAAC-Cu-Cl complex and its exciplex have similar MLCT/XLCT character and phosphorescence is expected to be the main emission channel. The formation of the exciplex leads to a red shift of the emission compared to the emission of the complex without THF.

3.1.3. Cu(CAAC)$_2^+$ (unpublished)

The Cu(CAAC)$_2^+$ complex was already investigated by Gernert et al. in 2017. [30] In their experiments, the Cu(CAAC)$_2^+$ complex has shown a very fast emission assigned to stem from the T_1 state [30]. The complex differs in two major aspects from the CAAC-Cu-Cl complex described before. It carries two bulky substituents with large steric requirements and is (approximately) inversion symmetric, resulting in a near-zero intrinsic dipole moment. With the bigger CAAC ligand instead of a chlorine atom, the calculation time for one calculation increases, but due to its more rigid structure, the bending of the ligands is restricted. Investigations of the smaller CAAC-Cu-Cl complex showed that the formation of an exciplex is possible in solution. [41] With the bulkier ligands and the non-bended structure, the formation of exciplexes is more difficult in the Cu(CAAC)$_2^+$ complex. The counter anion of the cationic complex was neglected in all calculations. In contrast to the chloride complex, the calculations of the cationic complex in vacuum and in implicit THF suggest only small solvent effects on the photophysics of the complex. The absorption spectra are nearly unaffected and the bond angles show changes of less than 0.2°. Therefore, like for the (DPEPhos)Cu(PyrTet) complex, all further calculations were carried out in vacuum. The comparison of the calculated absorption spectrum to the experimental one shows a similar shape with a redshift of the calculated peak positions. The SOC quasi-degenerate perturbation theory (SOC-QDPT) level absorption is only slightly different from the spin-orbit free absorption spectrum. In the spectral range up to 200 nm, all bands are dominated by MLCT transitions.

Due to the higher steric demand, the change in the geometries of the ground and the excited states is much lower than for the CAAC-Cu-Cl complex and the FC emission spectra could be calculated. Figure 10 shows the calculated S_1-S_0 and T_1-S_0 emission spectra in comparison to the digitalized experimental emission spectrum at 298K.

The emission spectrum in solid phase at 295 K has an emission maximum at about 398 nm. Variable-temperature emission spectroscopy (297 K-77 K) in PMMA film showed nearly no

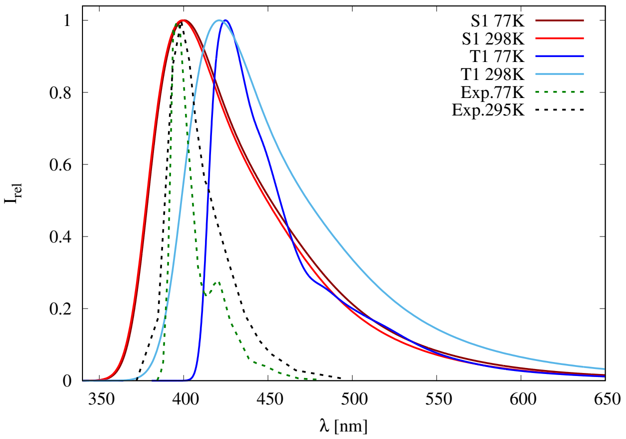

Figure 10.: Calculated S_1-S_0 (red) and T_1-S_0 (blue) emission spectra of the $Cu(CAAC)_2^+$ complex in vacuum in comparison to the experimental spectra in solid state at 298K (black) and 77 K (green).

effect on the emission maximum, while the emission intensity increases and the half-width decreases with lower temperatures. In solid phase, the emission spectrum at 77 K shows an additional emission maximum with lower intensity at about 420 nm, which is absent in the spectrum in PMMA film. [30] Like the experimental spectrum at 295 K, the calculated S_1-emission spectrum at 298 K has only one emission peak, but this peak has a broader rise and a bigger half-width. The harmonic oscillator model was used for the calculation of the spectra and the displacements in vibrational modes lead to a broadening of the emission spectra. The calculated S_1-emission at 77 K is nearly identical to the emission at 298 K. The experimental emission maximum at 398 nm is in good agreement with the calculated S_1 emission maximum at 400 nm, while the T_1 emission is slightly redshifted to 420 nm at 298 K and to 425 nm at 77 K. This redshift is similar to the redshift which was found for the calculated absorption spectrum compared to the experimental spectrum. By lowering the temperature, the spectrum of the T_1 emission becomes less broad and a small shoulder occurs at about 485 nm in the spectrum at 77 K, which is in agreement with the additional peak of the experiment at 77 K.

To decide whether S_1 or T_1 emission is more likely to occur, the rate constants have to be taken into account, too. The calculated radiative and non-radiative rate constants at 298 K can be found in Table 8.

At 298 K, the ISC rate constant is four orders of magnitude higher than the fluorescence rate constant and thus prompt fluorescence is not likely to occur. With a rISC rate constant, which is one order of magnitude higher than the calculated phosphorescence rate constant, a repopulation to the S_1 state is possible. Nevertheless, the depopulation of the T_1 via rISC and

Table 4.: Vertical emission wavelengths λ [nm], spin component-averaged S_1-T_1 SOC [cm^{-1}] and radiative as well as non-radiative rate constants k [s^{-1}] of the MLCT states of the Cu(CAAC)$_2^+$ complex.

	S_1			T_1			Temp.		
	λ_F	k_F	SOC	λ_P	k_P	SOC	T [K]	k_{ISC}	k_{rISC}
1	418	7.0×10^6	9.3	486	1.7×10^4	1.8	298	2.5×10^{10}	4.9×10^5
							77	2.9×10^9	2.4×10^{-2}

phosphorescence is rather slow compared to the population via ISC. Hence, phosphorescence is expected to be the main emission pathway at 298 K. With lowering the temperature to 77 K, the ISC rate constant is reduced by one order of magnitude to 2.9×10^9 s^{-1}. Due to the high energy gap, the rISC rate constant is very low at 77 K (2.4×10^{-2} s^{-1}) and phosphorescence is faster than rISC. The calculated phosphorescence rate constant is slightly smaller but still in the same order of magnitude as the experimental radiative rate constant of 9.4×10^4 s^{-1}, which is obtained by taking the measured quantum efficiency of 65% into account with the measured triplet lifetime of 6.9 μs of Gernert et al.[30] Even though the calculations indicate a repopulation of the S_1 state to be possible at 298 K, the calculated ISC rate constant is larger to such an extend that emission still occurs from the T_1 state. Therefore, the calculations and the experiment both expect phosphorescence to be the main emission pathway.

3.2. Zinc complexes

While many copper complexes have already been shown to have photophysics suitable for OLEDs, less attention has been payed to zinc complexes. However, since Zn(II) has a d^{10} electron configuration that prevents MC states, it seems promising to explore whether zink complexes can serve as alternative to copper complexes. This chapter deals with zinc as phosphorescent or TADF emitter. First, the Zn(4-X-PhS)$_2$(phen) complexes, which have already been described as phosphorescent in the literature, were considered (Paper II). By changing the carbene ligands, criteria for the design of new OLED emitters based on zinc carbene complexes were examined by using carbene-Zn(II)-dithiolate (Paper III + IV) and carbene-Zn(II)-carbazolate complexes.

3.2.1. Zn(4-X-PhS)$_2$(phen) complexes (Paper II)

One group of the few phosphorescent zinc(II) complexes described in literature are the Zn(4-X-PhS)$_2$(phen) complexes. They were first described in the mid 1980s by Crosby et al. and several investigations were carried out in the following years. [77, 76, 76, 80, 78, 81, 134]
For the different Zn(4-X-PhS)$_2$(phen) complexes, a dual luminescence was observed at low temperatures in rigid matrices and in the crystalline state. [77, 79, 80] The longer wavelengths luminescence with a broad structureless emission was assigned to an LLCT state, while the long-lived emission at shorter wavelength was expected to be phosphorescence from an ^{3}LC state on the (phen) ligand.

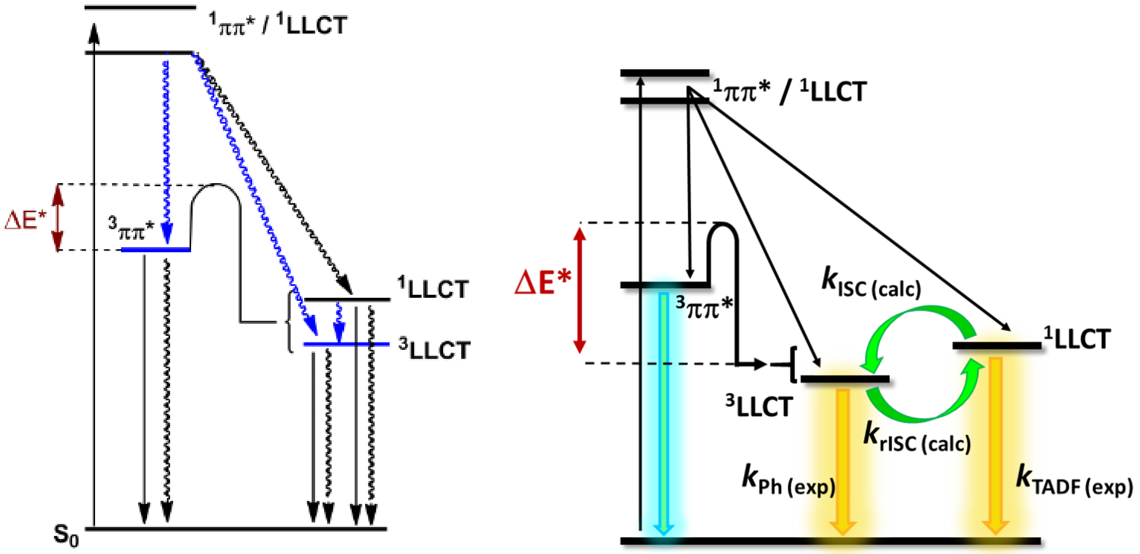

Scheme 1: Excited-state decay mechanism upon photoexcitation of [Zn(SC$_6$H$_4$-4-R)$_2$(phen)] (R = H, Me, Cl, OMe) as proposed by Crosby [79, 80] (left) and the new mechanism proposed in Paper II[135] (right).

Highland et al. proposed an energy scheme for the complexes.[79, 80] In that energy scheme, the high energy ^{1}LLCT and $^1\pi\pi^*$ (phen) states are populated first, which could be extended by new investigations (see Scheme 1).[135] With vibrational relaxation the energetically lower ^{1}LLCT, ^{3}LLCT and ^{3}LC (phen) states are populated. The ^{3}LC (phen) minimum and the lowest S_1 and T_1 states with LLCT character are separated by a thermally surmountable barrier. A repopulation of the ^{3}LC (phen) from the LLCT minima is unlikely. But instead, the reverse intersystem crossing from the ^{3}LLCT to the ^{1}LLCT state, which are nearly degenerated, is interesting for the occurrence of TADF.
Different crystal structures, which mostly differ in the orientation of the thiol ligands, were reported to have different photophysical properties. [134, 78] Jordan et al. found a monoclinic

and an orthorhombic crystal structure of a $Zn(PhS)_2$(2,9-Me_2phen) complex. For both complexes, a broad emission, expected to stem from LLCT states, was found, which is more intense and blueshifted from 660 nm to 565 nm in the monoclinic crystal structure. At temperatures lower than 77 K, a high-energy emission, assigned to $^3\pi\pi^*$ states, was observed, which is absent in the orthorhombic spectra.

For the Zn(4-Me-PhS)$_2$(phen) complex, Galin et al. measured an emission maximum at 571 nm (17513 cm^{-1}, 2.17eV) in glassy isobutyronitrile at 77 K.[81] The steady-state emission spectrum of the crystalline Zn(4-Me-PhS)$_2$(phen) at 6.5 K shows a maximum in this region as well.[80] The thermally modulated emission spectroscopy (TME) shows the occurrence of a band at about 16000 cm^{-1} (1.98 eV, 625 nm), which is assigned to the LLCT state.[80] This new band is less intense than the emission assigned to the LC state.

The LLCT emission of Zn(4-Cl-PhS)$_2$(phen) still dominates even at low temperatures such as 6.5 K, as it has been shown in TME experiments. Contradictory, the emission maximum of the crystalline Zn(4-Cl-PhS)$_2$(phen) complex of Highland et al. from 1985 [79] at 16700 cm^{-1} is much lower than the emission maximum of Highland et al. from 1986 [80] at 17600 cm^{-1}. In both cases the temperature is varied and no shift of the emission maximum was found. Since only the digits are reversed, this might be a typo. The experimental emission maximum of the Zn(4-Cl-PhS)$_2$(phen) complex in organic glass (chloroform:ethanol 1:19) of 17000 cm^{-1} lies between the other two experimental values.

In addition to these experimental studies, the photophysical properties were examined with theoretical methods. For the calculations of the Zn(4-X-PhS)$_2$(phen) complexes as ligand on the thiol ligand, a chloride and a methyl group were chosen. In literature three different crystal structures were described for the Zn(4-Me-PhS)$_2$(phen) complex. Accordingly, calculations for three different conformers were carried out, to investigate the impact of conformational changes. By replacing the methyl group at the 4-position of the thiophenol by a chlorine atom, substitution effects were taken into account, too. The different conformers of the investigated complexes are shown in Figure 11.

Ground-state properties

For complex **1**, one open **1A** and one folded **1B** conformer were investigated. For complex **2**, an additional conformer is considered, of which the degree of folding is between those of conformers **2A** and **2B**. As starting points for the geometry optimizations, the different crystal structures described in the literature were chosen. [136, 79, 78, 137] The open conformers with a face-to-face orientation of the thiol groups are the most stable conformers. Calculations of the Zn(4-X-PhS)$_2$(phen) complexes in vacuum showed [138] that calculations in vacuum are not

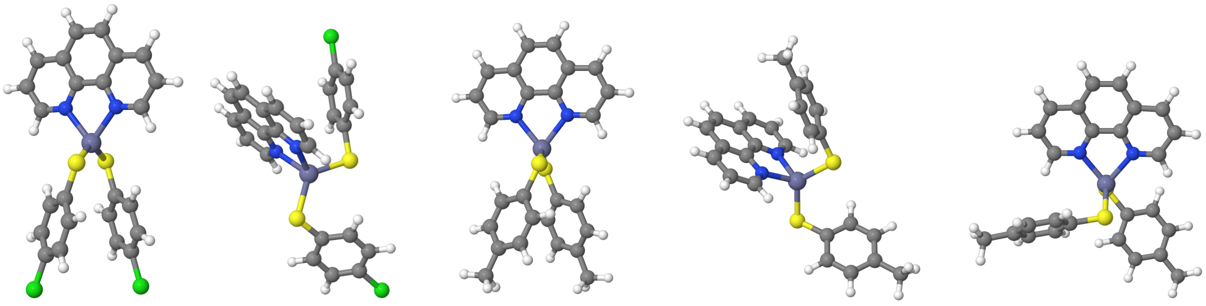
(a) **1A** (b) **1B** (c) **2A** (d) **2B** (e) **2C**

Figure 11.: Investigated conformers of the Zn(4-Cl-PhS)$_2$(phen) (**1**) and Zn(4-Me-PhS)$_2$(phen) (**2**) complexes.

sufficient for describing either solid phase nor the complexes in solution. Therefore, an implicit ethanol environment was chosen for all calculations. The dipole moments of the ground states are higher than 10 D for all conformers. Due to this, the electrostatic solvent-solute interaction is expected to be strong and the implicit ethanol environment is expected to be suitable for the description in solution as well as in crystalline phase. The changes of the ground state energies of the different conformers are rather low, with about 0.1 eV difference between conformers **A** and **B** (see Table 5). For the conformer with a degree of folding between conformers **2A** and **2B**, the ground state energy is 0.06 eV higher than that of conformer **2B**. Therefore, the formation of conformers **1B**, **2B** and **2C** is not excluded.

Table 5.: Adiabatic DFT/MRCI excitation energies (ΔE/eV) of the conformers **1A**, **1B**, **2A**, **2B** and **2C** in ethanol at their respective ground state geometries. The DFT/MRCI energy of the S_0 state at the DFT-optimized S_0 minimum geometry of conformers **1A** and **2A** serve as common origin.

conformer	S_0	S_{LLCT}	T_{LLCT}	$T_{LC(phen)}$
1				
1A	0.00	3.44	3.38	3.34
1B	0.13	3.69	3.61	3.50
2				
2A	0.00	3.28	3.23	3.38
2B	0.11	3.49	3.42	3.38
2C	0.17	3.52	3.45	3.48

When comparing the absorption spectra of different conformers, a more remarkable difference was found only for low energy regimes, while different conformers in high energy regimes absorb at similar intensities. For all conformers, the calculated absorption spectra show the highest absorption maximum between 250 and 260 nm. This is in good agreement with the experimental absorption maximum of Truesdell et al.[76] at 265 nm. The strongest absorption of the recent experiments on complex **1** of Steffen et al. shows a small redshift to 273 nm.[135] The states with the highest oscillator strengths possess LC character on the thiol or the phen ligands. Since the phen ligand is the same for regarded complexes, the LC(phen) excitations only show small variations between the different conformers. The calculated transitions in the wavelength regime between 300 and 400 nm are much weaker than in the shorter wavelength region and are in good agreement with the very broad experimental absorption of Steffen et al. at 320 - 425 nm. [135] Depending on the conformer and compound, the lowest ^{1}LC excitation is the S_5 or the S_6 state at about 310 nm. For all calculated conformers, the S_1 state has LLCT character. The electron density is transferred from the thiol ligands to the phen ligand. But while in conformers **1A**, **1B**, **2A** and **2B** both thiol ligands contribute to the excitation, for the S_1 and the S_2 state of conformer **2C** the electron density is transferred only from the bended thiol ligand to the phen ligand. Accordingly, the ^{1}LLCT absorption of conformer **2C** is spread over the S_1 and the S_2 absorption. The oscillator strength of the ^{1}LLCT absorption of conformer **2C** is more than two times stronger than in conformers **1B** and **2B** and more than 10 times higher than in conformers **1A** and **2A**. The electron transfer of the LLCT excitations leads to a strong reduction of the dipole moments. The implicit environment stabilizes the strongly polar molecules in the ground state. The excited LLCT states are much less stabilized in the implicit ethanol environment than the ground state and a strong blueshift of the LLCT excitations is visible in the calculated absorption spectra. The LC states retain a high dipole moment with excitation. Therefore, it could be shown that the LC states are equally stabilized as the ground state and the LC excitation energies are only slightly different in vacuum and in ethanol.

The calculated ^{1}LLCT absorption of conformer **1B** at 355 nm (f=0.020) and conformer **1A** at 362 nm (f=0.006) fit well to the weak shoulder, which was found in the experimental absorption spectrum of complex **1** in solution (19:1 ethanol-chloroform) at room-temperature at about 28000 cm^{-1} (357 nm). [76] For complex **2**, a small absorption maximum was found at 365 nm in isobutyronitrile, [81] which fits best to the S_1 absorption of conformer **2B** at 367 nm (f=0.028). The S_1 absorption of conformer **2A** is weaker (f=0.005) and redshifted to 378 nm.

In literature, a decay scheme was suggested. From the experiment, ^{3}LLCT and ^{3}LC(phen) states are expected in vicinity of the ^{1}LLCT state (see Scheme 1). In the calculations, at least one ^{3}LLCT and one ^{3}LC(phen) state close to the ^{1}LLCT state were found. The electron density distributions of the ^{3}LLCT states are very similar to the ones of the corresponding ^{1}LLCT states.

While the zinc atom does not contribute to the low-lying excitations, the sulfur lone pair orbitals participate in the ^{1}LLCT, ^{3}LLCT and ^{3}LC excitations. Due to the small energy gaps between these states and the heavy-atom effect caused by the sulfur atoms, a singlet-triplet mixing in the absorption region seems possible and could explain the branched triplet population kinetics.

Excited states and emission properties

For all optimized geometries, the S_1 state exhibits LLCT character. The electron transfer of the LLCT excitations leads to a strong reduction of the dipole moments compared to the large dipole moment of the ground state. The LLCT states are therefore less stabilized in a polar environment than the LC states. ^{3}LLCT and ^{3}LC(phen) states could be found by optimizing the T_1 state. The electronic and nuclear structures of the S_{LLCT} and T_{LLCT} states are very similar. This is in agreement with the expectations of the experiments. [77, 79, 80] For the open forms (**1A** and **2A**) of the complexes an additional T_1 minimum with ^{3}LC character, localized on the thiol ligands, was found, which is higher in energy than the other minima.

The optimized ^{3}LC(phen) geometries have nearly pure local $^3\pi\pi^*$ character. Since the phen ligand is the same for all compounds, the adiabatic excitation energies show only minor changes. The onset of the ^{3}LC band was reported to occur at 21800 cm^{-1} in complex **1** and at 21200 cm^{-1} in complex **2**. [80] This fits well with the calculated 0-0 energies of the ^{3}LC states of conformers **1A**, **2A** and **2B** of 21900 cm^{-1} , 21600 cm^{-1} , and 21500 cm^{-1}, respectively.

The vertical excitation energy of the $^3\pi\pi^*$ state at the relaxed ^{3}LC geometry is about 20100 cm^{-1} (2.5 eV) for all calculations and shows changes of less than 230 cm^{-1} between the different conformers of the two $Zn(4\text{-}X\text{-}PhS)_2(phen)$ complexes. With exception of conformer **2C**, the optimized LC geometries only show small changes towards the ground state geometries. Surprisingly, the optimized ^{3}LC geometry of conformer **2C** shows significant changes in the dihedral angles of up to 20° compared to the ground-state geometry. With the large-amplitude displacement of the dithiolate ligands, no meaningful phosphorescence spectrum could be calculated. At the optimized ^{3}LC geometry of conformer **2C**, the planes of both thiol ligands are nearly perpendicular to the phenanthroline plane. A similar orientation is described by Jordan et al. for the orthorhombic crystal phase of the $Zn(4\text{-}Me\text{-}PhS)_2(phen)$ complex.[78] For this crystalline phase, no $^3\pi\pi^*$ emission was found. In the calculated spectra of conformers **1A**, **2A** and **2B**, the most intense peak can be found at about 20100 cm^{-1} and they are in good agreement in their shape and position with the experiment.[76, 80] The ^{3}LC(phen) band of the spectrum of the Steffen group[135] is less intense than the other bands and in good agreement in its shape and position with the calculated ^{3}LC(phen) emission of complex **1B**. The calculated component-averaged phosphorescence lifetimes for compounds **1** and **2** of the ^{3}LC(phen) states of 0.32 s to 0.43 s are in good agreement with the experimental lifetimes at 6.5 K of 0.34 s for complex **1** and 0.39 s for complex **2**.[80]

The optimized ^{1}LLCT and ^{3}LLCT geometries of complex **2** are similar and nearly degenerated. At the LLCT states of conformer **2B**, the electron density is transferred from both thiol groups to the (phen) ligand. For conformers **2C** and **2A**, the electron density of the LLCT excitations is donated only by the thiol ligands bended towards the phen ligand. For conformer **2A**, the contribution of only one of the thiol ligands to the LLCT excitation leads to a strong change in the geometry. The donor thiol ligand is bent towards the phen ligand and is no longer oriented parallel to the other thiol ligand. The Zn-S bond of the optimized LLCT states is strongly elongated and the bond can be considered broken. A similar change, with broken Zn-S bond, was found for conformer **1A**. The complexes show a high conformational freedom and even the different calculated conformers show strong deviations between their ground state and excited state geometries. With these strong geometry changes between the ground state and the excited state, neither ISC rate constants nor emission spectra could be calculated for the LLCT states of complexes **1A**, **2A** and **2C**. In crystalline phase or in organic glass, the motion of the thiol ligands is expected to be much smaller. In accordance with that, the calculated vertical excitation energies strongly deviate from the experimental emission maxima. Therefore, a comparison of the onset of the emission to the adiabatic excitation energies is more meaningful.

In experiments of Highland et al.[80], the emission is measured in rigid glass, where the large-amplitude motions of the thiol ligands are hindered. The adiabatic energies are still expected to be comparable to the experimental onsets, since the potential energy surfaces are very shallow and torsion or bending of the thiol ligands of the complexes only lead to small changes in energy. The new emission spectra of complex **1** in solid phase at 6.5 K by the Steffens group[135] show the ^{3}LLCT and ^{3}LC(phen) bands that have been reported by Crosby et al., in particular the weak ^{3}LC(phen) band between 455 - 480 nm, the broad and structureless ^{3}LLCT band with a maximum at 587 nm, and one additional band between 365 - 450 nm. The additional band was assigned to prompt fluorescence from the ^{1}LC(phen) state. With increasing temperature, the intensity of the LLCT bands increases, while the LC bands decrease in intensity. In contrast to the LC band, the LLCT bands of complexes **1** and **2** show a significant shift. The onset of the LLCT band of complex **1** was found between 2.36-2.48 eV (19000-20000 cm^{-1}) and is redshifted to 2.11-2.23 eV (17000-18000 cm^{-1}) for complex **2**. [80, 135] Although the experiments of Highland et al. [80] describe a strong blueshift between the onsets of complexes **1** and **2**, this does not confirm with the calculated adiabatic LLCT energies, which only show marginal shifts between conformers **1A** and **2A** and are in good agreement with the experimental onset for complex **2** (Table 6). The calculated LLCT energies of conformers **2B** and **2C** are redshifted towards the other conformers, which indicates a greater importance in the orientation of thiol ligands than of the substitution (see Section 3.2.1).

Table 6.: Adiabatic DFT/MRCI excitation energies (ΔE/eV) of the conformers **1A**, **1B**, **2A**, **2B** and **2C** in ethanol. The DFT/MRCI energy of the S_0 state at the DFT-optimized S_0 minimum geometry in a polarizable ethanol environment serves as common origin. 0–0 energies including zero-point vibrational energy corrections are given in parentheses.

conformer	S_{LLCT}	T_{LLCT}	$T_{LC(phen)}$
1A	2.25 (**2.17**)	2.35 (**2.24**)	2.84 (**2.68**)
1B	2.11 (**2.05**)	2.05 (**1.99**).	2.82 (**2.66**)
2A	2.21 (**2.15**)	2.20 (**2.13**)	2.87 (**2.71**)
2B	1.93 (**1.87**)	1.87 (**1.81**)	2.84 (**2.67**)
2C	2.14(**2.07**)	2.09 (**2.03**)	2.89 (**2.73**)

At temperatures of 77 K and lower, only emission from prompt fluorescence and phosphorescence is expected to occur, because rISC from T_{LLCT} to S_{LLCT} states is too slow. Fluorescence rate constants of 3.4 μs were calculated for complex **1B** and 4.3 μs for complex **2B**, which are typical for the CT emission of donor-acceptor molecules and are in good agreement with the observed radiative lifetime of 2.9 μs of the Steffen group. [135]
At 77 K, the Steffen group measured a radiative rate constant of k_r of $7.7\times10^4 s^{-1}$ and a quantum yield Φ_{em} of 0.34. In the experiments of the Steffen group, only quantum yields for temperatures of 77 K and higher could be determined. This leads to a "35%"-scenario, where the quantum yield remains the same, and a "50%"-scenario, with an increase of the quantum yield up to 0.5 for the estimation of $\Delta E(S_1\text{-}T_1)$, $\tau_r(S_1)$ and $\tau_r(T_1^{I,II,III})$. These estimations lead to a $\tau_r(S_1)$ of about 4-58 ns. From the S_{LLCT} equilibrium states, fluorescence lifetimes of about 10 ns were calculated for conformer **2A** and of about 100 ns for conformer **2B**, which is in good agreement with the experiments. The $S_{LLCT} \rightarrow T_{LLCT}$ ISC is the only process that may compete with the fluorescence. At cryogenic temperatures, LLCT phosphorescence lifetimes of 0.7-7 ms were calculated, which fit well to the experimental $\tau_r(T_1^{I,II,III})$ of about 1 ms.

Interconversion paths between the ^{3}LC and LLCT states

Based on the TME measurements, an energy barrier of about 140 cm^{-1} between the ^{3}LC and the LLCT states was estimated. [80] For the determination of an upper bound of the energy

Table 7.: Vertical emission wavelength λ [nm], spin component-averaged $\mathrm{S_{LLCT}}$-$\mathrm{T_{LLCT}}$ SOC [$\mathrm{cm^{-1}}$] and radiative as well as non-radiative rate constants k [$\mathrm{s^{-1}}$] of the LLCT states of compounds **1** and **2**.

	$\mathrm{S_{LLCT}}$			$\mathrm{T_{LLCT}}$			Temp.		
	λ_F	k_F	SOC	λ_P	k_P	SOC	T [K]	k_ISC	k_rISC
1B	721	2.9×10^5	0.26	748	1.1×10^2	0.30	298	2.0×10^7	1.3×10^7
							77	2.8×10^7	1.6×10^4
							35	2.8×10^7	3.1×10^0
							10	1.1×10^7	—
2B	752	2.3×10^5	0.38	773	1.5×10^2	0.64	298	7.1×10^5	2.8×10^5
							77	5.3×10^6	2.4×10^3
							35	2.9×10^5	0.1×10^0
							10	2.9×10^5	—

barrier, a linearly interpolated path between the optimized ^{3}LC(phen) and ^{3}LLCT minima was calculated for conformers **1A** and **2A**. With this, upper limits of 350 $\mathrm{cm^{-1}}$ for **1A** and of 225 $\mathrm{cm^{-1}}$ for **2A** were determined, which are somewhat larger than the experimentally estimated 140 $\mathrm{cm^{-1}}$ but still in the right order of magnitude.

The intrinsic reaction coordinates of the transformation from T_{LC} to T_{LLCT} were analyzed, to find possible ways to affect the barrier height by chemical substitution.

The complexes **1** and **2** differ in their substitution on 4-position of the thiol ligand. For the geometry and excitation energy of the T_{LC} state, the change from methyl to a chloride group only has a small effect. At the T_{LLCT} geometries, the LLCT excitations to an electron transfer only from the thiol ligands bended towards the phen to phen ligand, while the other thiol ligand does not contribute to the excitations. Along the reaction path from the ^{3}LC to the ^{3}LLCT minimum, the strongest geometry change can be found for the dihedral angles of the thiol ligands.

With regard to the energy, the influence of the substituents in 4-position of the thiol ligands is small, but not negligible. The change from the Cl to Me ligand leads to a small shift of the crossing between LC and LLCT states. The +I-effect of the methyl group leads to a positive shift of the T_{LC} excitation energy and a small reduction of the T_{LLCT} excitation energy compared to the complex with a chloride ligand. The crossing of the methyl complex is slightly closer to the T_{LC} minimum and the energy barrier is 75 $\mathrm{cm^{-1}}$ smaller than in the chlorinated complex. Nevertheless, the effect of the substitution on the energy path is rather small. The impact of the orientation of the thiol group on the energy is much stronger than the impact of the substitution.

A deviation of the theoretical and experimental results was found for the energy gap between the ^{3}LC and the LLCT states. Highland et al. estimated this gap to be smaller than 1500 cm^{-1} for complexes **1** and **2**. [80] The calculated adiabatic energy gaps with ZPVE corrections of 4100 cm^{-1} for **1A**, 4900 cm^{-1} for **1B**, 4500 cm^{-1} for **2A**, and 6450 cm^{-1} for **2B** are significantly bigger than the estimation. Consequently, some errors in the experimental estimation and/or the computational model must have occurred. One possible source of errors is the broad LLCT band, which overlaps with the ^{3}LC (phen) band. This complicates the precise determination of the origin of the LLCT emission, on which the experimental estimation is based. Since the calculated ^{3}LC (phen) phosphorescence emission spectra are in excellent agreement with the experimental spectra, errors in the calculation are more likely to be found for the calculations of the LLCT states. Presumably, the computed LLCT excitation energies are somewhat too low. The ground states and locally excited states of complexes **1** and **2** are highly polar and interact with a polar environment, while the LLCT states have small dipole moments. In polar but rigid environments, the environment cannot reorganize after excitation and the LLCT transitions are strongly hypsochromically shifted. This effect may be underestimated in the model of implicit solvation used for the calculations. The good agreement between our computed and the experimental absorption spectra in the low-energy regime, in conjunction with the relocation of the thiol ligands in the LLCT states, points towards a different explanation: The rigidity of the next neighborhood prevents large geometric displacements of the flexible ligands in frozen glasses and the crystalline state whereas the thiol ligands can move nearly unhindered in our implicit solvent model. In order to mimic a solid-state environment, combined quantum mechanical and molecular mechanical (QM/MM) would have to be performed which is possible but beyond the scope of our current theoretical work.

Summary and conclusion

The calculations on the literature known complexes **1** and **2** resulted in a much longer investigation with higher effort than originally intended. For both complexes, the ^{1}LLCT, ^{3}LLCT and $^3\pi\pi^*$ states, which were described in literature, were found. The difference between the excitation energies of complexes **1** and **2** is very small. In contrast to that, the orientation of the dithiolate ligands, which is represented by the different conformers, is of great importance. The strong dependence on the photophysical properties of the orientation of the dithiolate ligands leads to problems with the correct description of the complexes in the solid phase. One possibility to achieve more accurate results could be the use of a QM/MM model for the calculations.

The high flexibility of the dithiolate ligands leads to a large amplitude motion in the LLCT states and a very broad emission spectrum. The strong folding of one of the dithiolate ligands towards the phen ligand with population of the LLCT states leads to an elongation of the Zn-S bond. One way to avoid the back folding and to obtain a less broad emission is to use bidentate dithiolate ligands instead of the two monodentate ones.

The calculations of this work confirm a very small energy gap between the $^3\pi\pi^*$ and the LLCT states. With these small energy gaps, very fast ISC and rISC rate constants were calculated. The calculated rate constants of conformers **1B** and **2B** suggest that TADF is likely to occur at room temperature and even possible at 77 K. Therefore, the originally proposed kinetic scheme of Crosby et al. [76, 77, 78, 79, 80] can be extended by adding efficient rISC from the ^{3}LLCT to the ^{1}LLCT state.

3.2.2. Zn-complex design

In analogy to the investigations of the copper complexes, different Zn(II) carbene complexes were investigated with regard to finding new design criteria for their suitability as TADF emitters. Although Zn(II) complexes offer a high flexibility in their configurational geometries, this scan focusses on trigonally coordinated Zn(II) carbene complexes. As carbene ligands, a CAAC, a NHC and a CAArC and a thiazolcarbene ligand were chosen. The different properties of the carbene ligands have been described in 1.4.3. The investigated complexes can be divided into two groups depending on the second ligand. For the first group, a 1,2-dithiolbenzene (dtb) ligand, which was modified, was chosen. The second group has a carbazolate ligand. The investigated complexes are shown in Figures 12 and 17. The findings of the dtb complexes are described first, followed by those of the carbazolate complexes.

Zn-dithiolbenzene complexes (Paper III)

As a first group of zinc(II) carbene complexes, which was investigated to find new design criteria, a 1,2-dithiolbenzene (dtb) ligand was chosen as second ligand. For this group, the influence of the carbene was investigated by varying the σ-donor and π-acceptor-strengths. The Zn(4-X-Ph-S)$_2$(phen) complexes described above showed a high contribution of the sulfur atoms to the LLCT excitations. To investigate the influence of the sulfur atoms on the photophysic of the complexes, for complex **3** the dtb ligand was substituted by a 1,2-diolbenzene (dob) ligand (Figure 12).

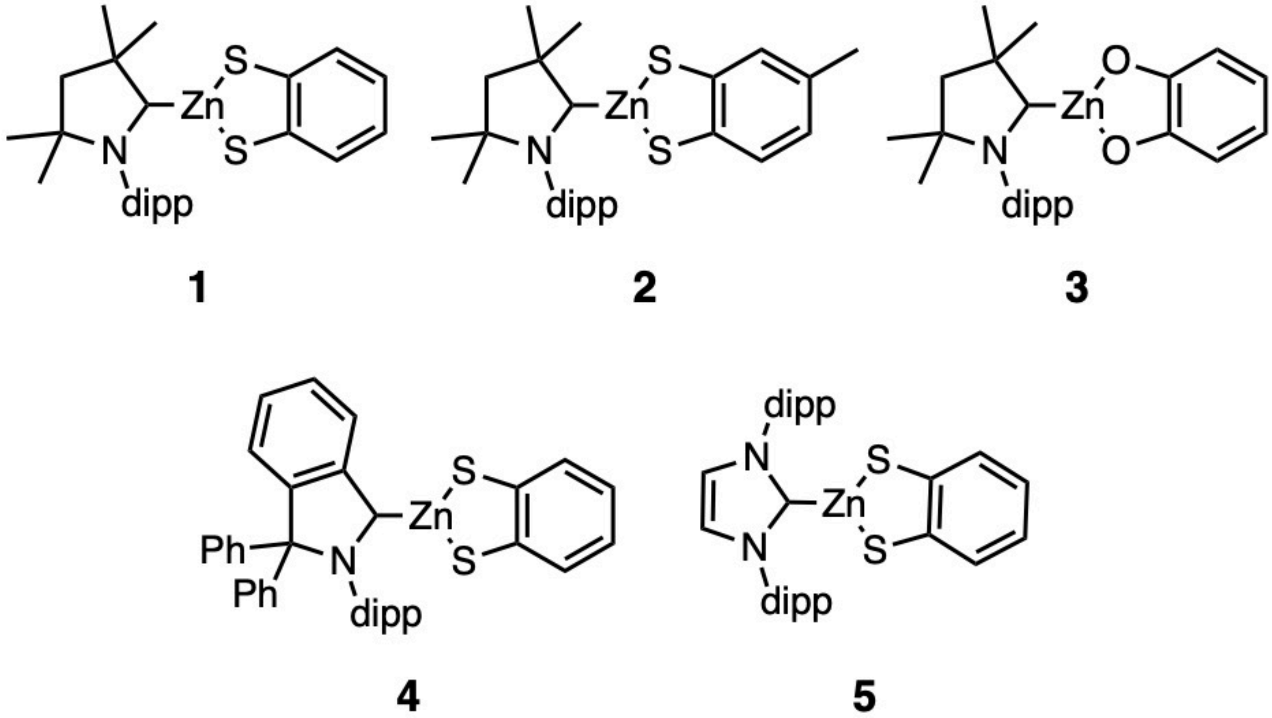

Figure 12.: Structures of the investigated Zn(II) complexes with a 1,2-dithiolbenzene or 1,2-diolbenzene ligand.

Ground-state geometries

For a first comparison, the excited state properties at the ground state geometries of the complexes were regarded. For complexes **1** - **4**, the lowest excited singlet and triplet states have LLCT character at the ground state geometry. The electron density is transferred from the π orbitals of the dtb and dob ligands to the π^* orbitals of the carbene ligands. The S_1-T_1 energy gap of 0.075 eV is very small for complex **1**. With the methylation of the dtb ligand, a small redshift of the excitation energies of complex **2** with remaining order of states as for complexes **1** was found (see Figure 13). Stronger redshifts with accompanied changes in the order of states were achieved by substituting the sulfur atoms by oxygen (compound **3**) and by replacing the CAAC ligand by a CAArC ligand (compound **4**). The order and character of the excited states of complex **5** differs from the other complexes. For this complex, two different conformers were found. The two conformers differ mostly in the orientation of the dtb ligand. For the first conformer, the dtb ligand is nearly perpendicularly orientated towards the plane of the NHC five-membered ring (conformer $\mathbf{5}^{\perp}$). In the other conformer, the dtb plane is nearly parallel to the plane of the five-membered ring of the NHC (conformer $\mathbf{5}^{\parallel}$). The NHC ligand is a weaker π acceptor than the CAAC and the CAArC ligand. Accordingly, the LLCT excitation energies of complex **5** are higher than for the other complexes. In both conformers of **5**, the S_1 state has ^{1}LLCT and the T_1 state has ^{3}LC(dtb) character, but the perpendicular orientation of the dtb ligand towards the NHC ligand leads to a significant increase of the energy of the LLCT states. Therefore, the S_1 energy of conformer $\mathbf{5}^{\perp}$ is 0.24 eV higher than the one of conformer $\mathbf{5}^{\parallel}$, while the T_1 state of conformer $\mathbf{5}^{\perp}$ is only 0.05 eV higher than the one of conformer $\mathbf{5}^{\parallel}$. At the ground state geometries of all regarded complexes, the zinc atom

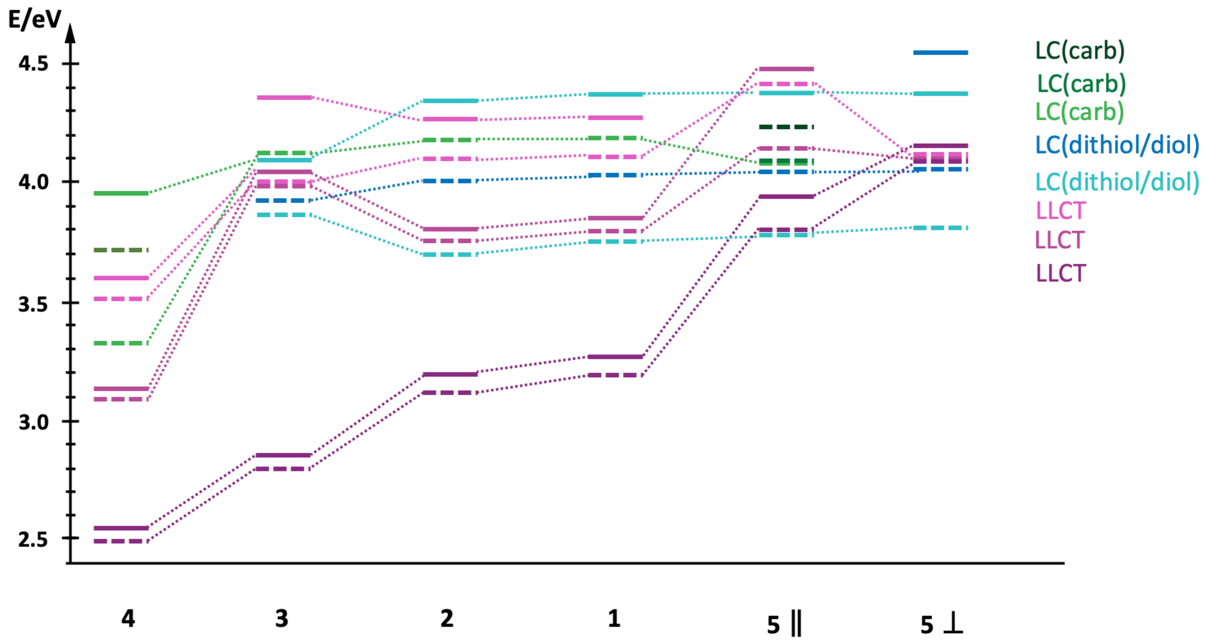

Figure 13.: Vertical excitation energies of the screened Zn(II) complexes **1-5** in THF calculated with DFT/MRCI at the respective ground state geometries. Dashed lines represent triplet states and solid lines represent singlet states. The following color codes have been used: violet and pink LLCT ($\pi_{\text{dtb/dob}} \rightarrow \pi^*_{\text{carb}}$), green LC ($\pi_{\text{carb}} \rightarrow \pi^*_{\text{carb}}$) and blue LC ($\pi_{\text{dtb/dob}} \rightarrow \pi^*_{\text{dtb/dob}}$).

mostly has a stabilizing function and only has a minor contribution to the electronic excitations. The ligand centered $\pi\pi^*$ excitations on the dtb and dob ligands are similar for all complexes. Accordingly, absorption maxima at around 225 nm were found for complexes **1-3** and complex **5**, which originate from LC excitations at the dtb or dob ligands. For complex **4** the 30 lowest singlet roots were calculated. Therefore, no excitations with energies lower than 250 nm were calculated, but it can be assumed to find a strong absorption of the LC(dtb) states of complex **4** at about 225 nm, too. The absorption intensity of the LLCT states is much lower than that of the LC states for all complexes.

Excited state geometries

For complex **1**, the optimized S_{LLCT} and T_{LLCT} geometries only show small deviations towards each other, but changes of up to 27° in the dihedral angles compared to the ground state geometry. They are lower in energy than the optimized ^{3}LC geometries. The changes in the dihedral angles are due to a bending and rotation of the dtb ligand. Nevertheless, the calculated ISC and rISC rate constants are very high and suggest TADF as main emission pathway. The calculated rate constants are shown in Table 8. The methylated dtb ligand of complex **2** results mostly in a small shift of the excitation energies without changing the character of the excitations. Therefore, similar results as for complex **1** were found for complex **2**. For complexes **3** and **4**, the optimized ^{3}LLCT geometries show a rotation of the dob or dtb ligand compared to the ground state geometry as well. Starting from the ground state geometry and the ^{3}LLCT geometry, two different ^{1}LLCT minima were found for both complexes. Like for the ground state conformers of complex **5**, the optimized S_{LLCT} minima can be distinguished by their orientation of the dtb or dob ligand towards the five-membered ring plane of the carbene ligand. One of the ^{1}LLCT geometries is close to the S_0 geometry, where the dtb and dob ligands are rotated out of the carbene plane. These states are referred to as $S^{\perp}_{LLCT}$ states. While a $T^{\perp}_{LLCT}$ geometry was optimized for complex **4**, only a saddle point was found by optimizing a perpendicular T_{LLCT} geometry for complex **3** . The other ^{1}LLCT geometries are close to the ^{3}LLCT geometry, where the dtb and dob ligand are nearly parallel to the carbene plane. These states are referred to as $S^{\|}_{LLCT}$ states. Since the displacements are large between the $S^{\perp}_{LLCT}$ and $S^{\|}_{LLCT}$ minima, the FC and harmonic oscillator approximations are not reasonable and for complex **3** only (r)ISC rate constants for the parallel minima could be determined. For complex **4** (r)ISC rate constants could be calculated for the perpendicular arrangements, too. While the calculated ISC rate constants have the same order of magnitude for the parallel and perpendicular states, the rISC and fluorescence rate constants are lowered for the perpendicular geometries of complex **4** (see Table 8). Therefore, the parallel orientation is favourable and a rotation of the ligands should be avoided for efficient TADF.

In crystal phase the orientation of the dtb and dob ligands is rigidified and has to be considered in the design of the complexes. In the calculations in implicit THF environment, the dtb and dob ligands show only a small steric hinderance and can rotate nearly freely. Using complex **4** as an example, a relaxed scan was carried out, to determine the energy barrier of the rotation of the dtb ligand, which can be described by the C_{carb}-Zn-S-C dihedral angles. By changing the C-C_{carb}-Zn-S dihedral angle between 90° and 180°, the energy of the S_1 state changes by less than 0.1 eV. Accordingly, the rotation of complex **4** is not hindered and a similarly low

Table 8.: Vertical emission wavelengths λ [nm], spin component-averaged S_{LLCT}-T_{LLCT} SOC [cm^{-1}] and radiative as well as non-radiative rate constants k [s^{-1}] of the LLCT states of compounds **1** - **4**. For complex **5**, the S_{LMCT} and T_{LMCT} geometries were selected.

	S_{LLCT}			T_{LLCT}			T		
	λ_{F}	k_{F}	SOC	λ_{P}	k_{P}	SOC	[K]	k_{ISC}	k_{rISC}
1	629	1×10^{7}	2.66	654	1×10^{1}	2.37	298	7×10^{9}	5×10^{8}
							77	6×10^{9}	5×10^{6}
2	645	1×10^{7}	3.21	673	7×10^{0}	3.21	298	4×10^{9}	1×10^{8}
							77	2×10^{9}	1×10^{5}
3$^{\parallel}$	1063	9×10^{6}	0.42	1134	3×10^{-1}	0.43	298	9×10^{7}	4×10^{7}
							77	2×10^{8}	2×10^{6}
3$^{\perp}$	970	5×10^{6}	2.54						
4$^{\parallel}$	783	8×10^{6}	1.65	828	9×10^{0}	1.55	298	1×10^{9}	7×10^{7}
							77	5×10^{8}	2×10^{5}
4$^{\perp}$	771	4×10^{6}	3.31	799	$2{\times}10^{5}$	3.60	298	1×10^{9}	8×10^{6}
							77	4×10^{8}	$2{\times}10^{2}$
5$^{\parallel}$	566	3×10^{6}	3.56	597	4×10^{2}	3.56	298	2×10^{7}	1×10^{6}
							77	2×10^{5}	6×10^{4}

energy change during the rotation is expected for the other complexes as well. The comparison of the parallel and orthogonal orientation has shown that the ISC rate constants for the parallel orientated molecules are significantly higher. Therefore, for efficient TADF the rotation of the dithiolate ligands has to be avoided. Two different ways are possible to avoid the rotation: 1) increasing the steric demand of the dithiolate ligands by bulkier ligands or 2) a dimerization of the complexes. The methylation of the dtb ligand only leads to small redshifts and no changes in the order of states. By using bulkier groups, a slightly further redshift is expected with remaining high rate constants. The NHC complex **5** is the only complex for which a contribution of the zinc atoms is found in the excitations. For complex **5** one S_1 geometry and three different T_1 geometries were optimized. For two of the T_1 minimum geometries the T_1 state has LC character, for one localized on the NHC ligand and for the other one localized on the dtb ligand. The S_1 minimum and the third T_1 minimum are mixed ligand-to-metal (LM)CT/LLCT states. The T_1 energy at the LMCT/LLCT geometry is more than 0.35 eV lower than at the LC geometries. At the ^{3}LMCT/LLCT geometry no rotation but a bending of the dtb ligand is found. The calculated fluorescence rate constant is one order of magnitude lower than for complex **1** and nearly the same order of magnitude as the calculated ISC rate constants. For the bended configuration, prompt and delayed fluorescence is expected to occur.

With a hindered bending of the dtb ligand like in the solid phase, the ^{3}LC(dtb) state forms the lowest T_1 minimum and the complex is probably non-emissive.

Dimer (Paper IV)

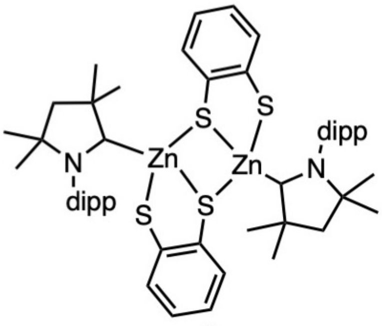

6

Figure 14.: Structure of the investigated CAAC-Zn(II)-dtb dimer.

As an example, some calculations were done for the dimer of complex **1** (see Figure 14). In experiment, the complex was found as μ-bridged dimer.[139] The dithiolate ligands in this complex **6** are strongly bent. Since the calculations indicated efficient TADF for the monomeric complex **1** to occur, a comparison of the monomeric and the dimeric complex is of high interest. As for complex **1**, the S_1 and the T_1 states of complex **6** both have LLCT character at the ground state geometry. The electron density is transferred from both dithiolate ligands to both CAAC ligands. For the monomeric as well as for the dimeric complex, the S_1 state absorbs at 380 nm. Due to the inversion symmetry of complex **6**, the excited states can be separated in gerade and ungerade states. The $S_0 \rightarrow S_2$ and the $S_0 \rightarrow S_3$ excitations are both $^1A_g \rightarrow {}^1A_u$ excitations and have LLCT character. This leads to significantly higher oscillator strengths (0.02 and 0.05, respectively) than for the $S_0 \rightarrow S_1$ excitation, which is a dark $^1A_g \rightarrow {}^1A_g$ excitation. Therefore, a blueshift from 380 nm to about 340 nm is found for the lowest absorption maximum of complex **6** compared to that of complex **1**. The observed shift of the low energy absorption maximum from 401 nm in toluene to 374 nm in DCM may indicate the break-up of the dimer into two monomers. Like for the monomeric complex, the dimeric complex **6** has an absorption maximum with high intensity between 250 nm and 300 nm.

For complex **1**, the strong absorption was due to local excitations. The highest oscillator strength of the dimeric complex **6** was found for the S_{12} state (276 nm) and the S_{14} state (272 nm), which both have a mixed LC/LLCT character. The local excitation is localized on the thiol ligand. In the excitations of the S_{12} and S_{14} states, the electron density is mostly donated by the n-orbitals of the sulfur atoms. For the monomeric complex **1** the contribution of the sulfur atoms is much lower for all regarded excitations.

As for the Zn(4-X-Ph-S)$_2$(phen) complexes, the positively charged dithiolate ligands lead to repulsion and therefore to a break of the symmetry at the optimized geometries of the S_1 and the T_1 state. Due to the broken symmetry, the excitations at the excited state geometries are localized on only one CAAC-Zn-dtb moiety.

At the optimized S_1 geometry, the S_1 state has LLCT character, where the electron density is mostly transferred from one of the dtb ligands to one of the CAAC ligands. The vertical S_1 energy of complex **6** of 1.83 eV (676 nm) is 0.14 eV lower than for the monomeric complex **1** (1.97 eV, 628 nm). By optimization of the T_1 state geometry of complex **6**, two different minima with different character of the T_1 state were found. At the first minimum, the T_1 state has LC(dithiol) character, while the T_1 state at the second has a mixed LLCT/LC character. At both T_1 geometries, the S_1 state has LLCT character similar to the one at the S_1 geometry. Although, the adiabatic T_1 energy of 2.75 eV at the ^{3}LLCT/LC geometry of complex **6** is significantly lower than at the ^{3}LC geometry (3.15 eV), the adiabatic excitation energy of the T_1 state at the ^{1}LLCT geometry, which is a pure ^{3}LLCT state, is the lowest (2.44 eV). This indicates that a ^{3}LLCT minimum close to the ^{1}LLCT minimum exists, which could not be optimized. The adiabatic energy gap of 0.085 eV between the S_1 and the T_1 states at the ^{1}LLCT geometry of complex **6** is very small, thermally surmountable and in good agreement with the experimental energy gap of 0.079 eV. A similar shift of 0.07 eV (from 577 nm to 558 nm) was found in experiment for the emission in PMMA, when the temperature is lowered from 297 K to 77 K.

The calculated averaged phosphorescence rate constants at the ^{3}LLCT/LC and ^{3}LC geometries of complex **6** of 7 s^{-1} and 46 s^{-1} respectively, are very small. Although the calculated fluorescence rate constant of complex **6** (5.31×10^5 s^{-1}) is significantly larger than the calculated phosphorescence rate constant, the fluorescence rate constant of complex **1** is two orders of magnitude larger.

Although the rotation of the dtb ligands is hindered in the dimeric complex **6** and TADF can be expected, too, the monomeric complex **1** is preferable due to its significantly faster fluorescence.

Solvation models

As already mentioned, the choice of the solvent model has a major impact on the accuracy of the description of the selected complex. On the example of complex **1** of the Zn-dithiolate complexes, the PCM model was compared to its cLR extension and some limits of the cLR model are demonstrated. For the performed DFT/MRCI calculations, the point charges of the calculations with PCM and cLR were extracted. Since only single-point calculations are possible in the cLR model, the geometries are the same as for the PCM calculations. For the calculations of complex **1**, the PCM and cLR descriptions showed highly differing vertical excitation energies.

A first impression of the effects of the solvation model can be gained by regarding the ground state geometry. For complex **1**, no experimental data are available, but the comparison of the dimeric complex **6** showed a very good agreement of the calculated absorption spectrum to the experimental spectrum (see section 3.2.2). Therefore, the description of the ground-state is expected to be suitable for complex **1**, too. The comparison of the calculated absorption spectra (Figure 15) shows a strong blueshift of the calculations with implicit THF solvation with PCM compared to those in vacuum. This shift is much stronger for the long wavelength regime, while the excitations in the region from 200-250 nm are only slightly affected by solvation. The lower wavelength absorption is dominated by local excitations on the dithiolate ligand, while the strongly blueshifted excitations have an LLCT character, where the electron density is transferred from the dtb to the CAAC ligand.

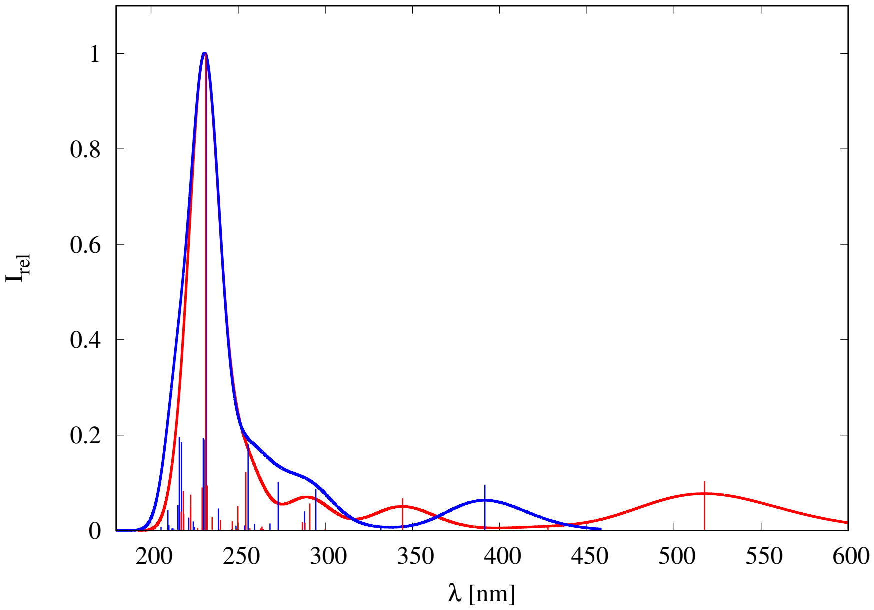

Figure 15.: Calculated singlet absorption spectra of the CAAC-Zn-dtb complex in vacuum (red) and in THF with PCM (blue).

In both environments the S_1 state has a LLCT character. Accordingly, the S_0-S_1 excitation energy is strongly affected by solvation and shows a blueshift from 2.40 eV in vacuum to 3.10 eV with PCM. While the ground state is highly polar with a dipole moment of 11.6 D in vacuum and 15.8 D in PCM, the dipole moment of the S_1 state points in another direction and is strongly reduced to 3.3 D in vacuum and 0.6 D in PCM (Figure 16).

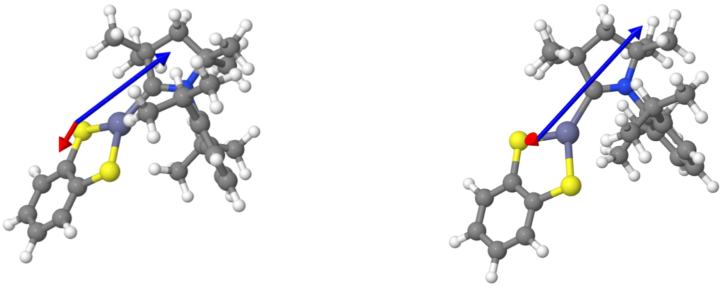

@ S_0 vacuum   @ S_0 PCM

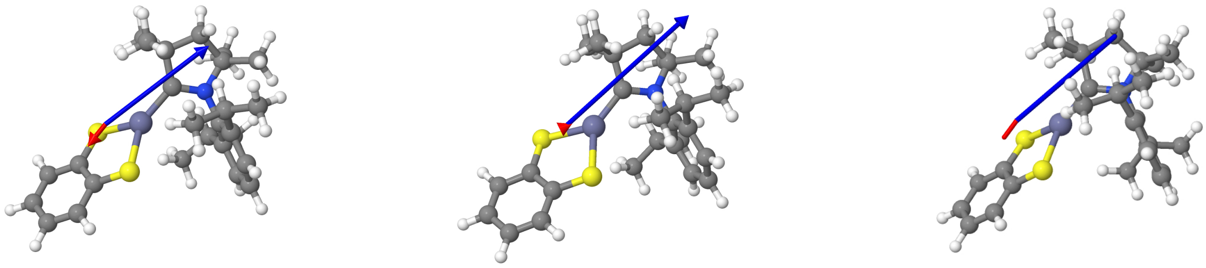

@ S_1 vacuum   @ S_1 PCM   @ S_1 cLR

Figure 16.: Dipolemoments of the S_0 (blue) and S_1 state (red) at the optimized geometries in different environments.

At the ground state geometry, the THF environment leads to stabilization of the S_0 state, while the excited state is destabilized. After excitation to the S_1 state, a reorientation of the solvent molecules towards the new electron distribution occurs. The PCM and the cLR model were used to describe different situations of the relaxation process. With PCM, the solvent molecules are still adapted to the ground state reaction field, while the solute is already excited. With the cLR model, the solvent molecules can reorientate to the excited state density and less rigid environments and longer time delays can be described. Accordingly, the S_1 state of the calculations with cLR is assumed to be stabilized compared to the calculations with PCM, while the S_0 state is expected to be strongly destabilized.

The vertical S_0-S_1 excitation energies are listed in Table 9. Since the dipole moment of the S_1

Table 9.: Vertical excitation [eV], emission wavelength λ [nm] and fluorescence rate constants in different environments.

	S_0-S_1[eV]	λ_F	k_F
vacuum	1.1118	1115	3.41×10^5
PCM	1.9680	630	3.31×10^6
cLR	1.0137	1223	1.42×10^6

state is rather small, a small stabilization of the S_1 energy is expected to occur by reorientation of the solvent molecules to the excited state density distribution. But instead of a decrease of the S_1 state energy at the S_1 geometry, an increase of the adiabatic S_1 energy from 2.51 eV with PCM to 2.75 eV with cLR is found. The difference between the PCM and the cLR model is even stronger for the S_0 energies at the S_1 geometries. The S_0 state energy is 0.53 eV higher than at the ground state equilibrium geometry for the calculations with PCM and 1.74 eV higher with cLR. This indicates a strong destabilization of the S_0 state with cLR at the excited state geometries. The strong decrease of the dipole moment and its change of direction seem to cause serious problems for the cLR model in complex **1**. The results of the cLR calculations contradict the effects expected for this complex.

A failure of the cLR model has been found for an organic terephthalonitrile-based donor-acceptor fluorophore complex, too. [140] The investigated organic complex has a small dipole moment in the ground state and a much higher dipole moment in the S_1 state. Three different solvents with different polarity were selected: hexane, ethyl acetate and dimethyl sulfoxide (DMSO). For the comparison of the calculated and the experimental absorption spectra, only COSMO and no PCM was used. Nevertheless, the results with COSMO at the ground state geometry are expected to be in a comparable range to those with PCM. The comparison of the calculated absorption spectra to the experimental ones showed small redshifts of the lower energy bands at about 410 nm. For the calculations at the excited state geometries, the cLR model was used. The vertical S_1 excitation energies in different solvents were compared to the vertical S_1 excitation energies in vacuum. Even in the unpolar hexane environment, the S_1 energy is lowered by about 0.7 eV. In ethyl acetate, the S_1 energy is lowered by about 1.4 eV with cLR. The calculated shifts in emission energy, from 675 nm in hexane to 1100 nm in ethyl acetate, are stronger than the shifts of the emission maxima in experiment (hexane: 444 nm, ethyl acetate: 572 nm), too.

Mewes et al. did calculations on the solvent effects on a Dimethylaminobenzonitrile complex. [141] They combined SS-PCM, which is comparable to the cLR approach, with algebraicdiagrammatic construction methods for the polarization propagator (ADC) of second (ADC2) and third order (ADC3). Although the SS-PCM was used in similar manner for both approaches, the results differ strongly. While the description of the locally excited states was in good agreement with the experiment for all solvent models, the CT states showed some problems. While better fluorescence energies were found with the ADC(2)/SS-PCM, the relative energies of the LE and CT states were more consistent with the experiment for the ADC3 calculation. In non-polar solvents, however, both approaches failed.

Although the calculations on Cu(I) and Au(I) carbene-metal-amide complexes with the cLR model gave meaningful results, [142] the cLR model is neither suitable for the reported organic complex [140] nor for complex **1**. The problems encountered for these complexes with strong changes of the dipole moments between the ground state and the excited states should be kept in mind regarding the choice of solvation model.

Summary and conclusion

For complexes **1** - **4** the lowest excited singlet and triplet states both have LLCT character and are energetically close. Even though the T_1 state at the two optimized ground state geometries of complex **5** has LC character, the T_1 state at the optimized ^{1}LLCT geometry is significantly lower than the T_1 state at the ^{3}LC geometry.

The calculated ISC and rISC rate constants suggest that for complexes **1** - **5** TADF is likely to occur. By changing the carbene ligand, the emission can be tuned from yellow (**5**) over orange/red (**1** and **2**) to deep red/near infrared (**4**). The substitution of the dtb ligand by a dob ligand leads to a strong redshift of the luminescence and complex **3** is expected to emit in the infrared region. For complexes **3** and **4**, two different S_{LLCT} geometries, one with a parallel orientation of carbene and dtb and dob ligand and one with the ligand twisted out of the carbene plane, were found. While for complex **3** only a $T^{\parallel}_{LLCT}$ geometry was found, for complex **4** a $T^{\perp}_{LLCT}$ geometry was optimized as well. The comparison of the rate constants with parallel and perpendicular orientation of the dtb ligand of complex **4** showed a reduction of the fluorescence and rISC rate constants. Similar effects are expected for the other complexes, too. With a relaxed scan of complex **4**, it was demonstrated that the potential energy surface of the excited S_1 state is very shallow. Due to this, the rotation of the dithiolate ligands of the monomeric complex in solution can lead to a reduction of the rISC and fluorescence rate constants. For efficient TADF, the rotation of the dithiolate ligands has to be avoided. The hindrance of the motion of the dithiolate ligand can be achieved in different ways. Two possible ways are the dimerization of the complexes or the usage of bulkier ligands. The synthesis of the proposed complex **1** by the Steffen group showed that the monomeric complex is chemically not stable and dimerizes. As an example of a dimeric complex **6**, which is the μ-bridged dimer of complex **1**, was chosen for some further calculations. The ^{3}LLCT geometry is expected to be similar to the ^{1}LLCT geometry. The energy gap of 0.07 eV of complex **6** is clearly small enough for TADF, but the fluorescence rate constant is two orders of magnitude smaller than for the monomeric complex. Hence, the monomeric complex is preferable as TADF emitter. With a methyl group at the dtb ligand, the steric demand of complex **2** is slightly higher than for complex **1**. The methylation of the dtb ligand leads to a small redshift without changing the energetic order of states and remaining the high ISC and fluorescence rate constants. With bulkier ligands on the dithiolate ligands such as tert-butyl groups instead of methyl groups, a slightly stronger redshift is assumed and the rotation is expected to be less likely. With an increased steric demand, the probability of a dimerization is decreased as well and higher quantum yields are expected to be achieved.

3.2.3. ZnCarbazolates (unpublished)

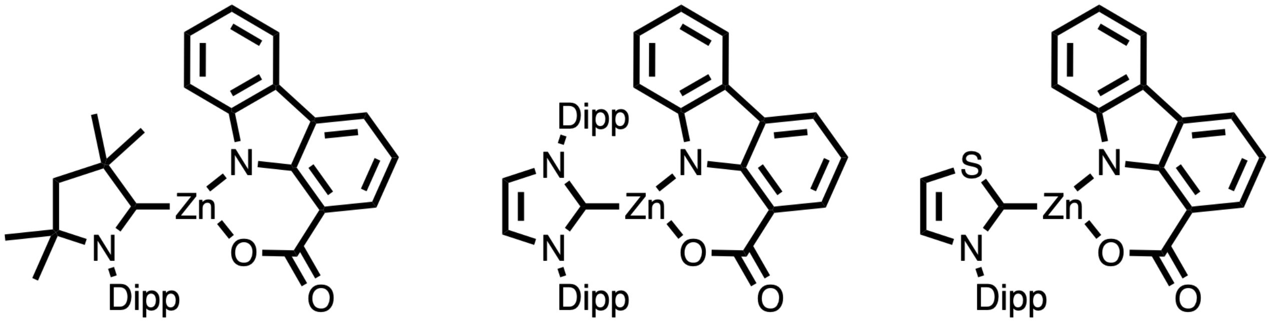

7 **8** **9**

Figure 17.: Structures of the investigated Zn(II) carbene complexes with a carbazolate ligand.

A different group of Zn(II) carbene complexes, which has been investigated for this work, are carbene-Zn(II)-carbazolate complexes. The structures of the chosen complexes are shown in Figure 17. As carbene ligands, the commonly used NHC ligand and the corresponding CAAC ligand, which has a higher σ-donor and π-acceptor strength, were chosen. As a third ligand, an aminothiocarbene was used, which has a sulfur atom instead of the second nitrogen of the NHC ligand.

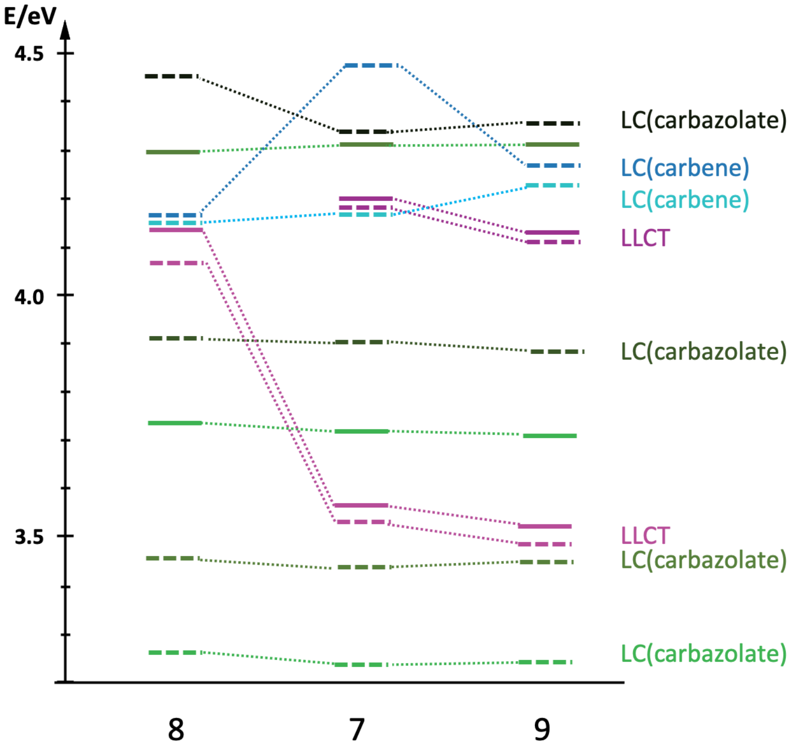

Figure 18.: Vertical excitation energies of the screened Zn(II) complexes with carbazolate ligand in THF calculated with DFT/MRCI at the respective ground state geometries. Dashed lines represent triplet states and solid lines represent singlet states. The following color codes have been used: violet and pink LLCT ($\pi_{ph} \rightarrow \pi^*_{carb}$), green LC ($\pi_{carbene} \rightarrow \pi^*_{carbene}$) and blue LC ($\pi'_{carbazolate} \rightarrow \pi^*_{carbazolate}$).

Ground state geometries

First, the ground state geometries of the three complexes were optimized with an implicit THF environment. The vertical excitation energies of states lower than 4.9 eV of the three complexes are shown in Figure 18. Between complexes **7** and **9**, only small differences of the excitation energies are found. Therefore, the further descriptions will focus on complex **8** and complex **7**, which is expected to have similar photophysical properties as complex **9**. For all carbazolate complexes, the T_1 state and the T_2 state have LC character localized on the carbazolate ligand. The energy of the LC states shows only small changes by changing the carbene ligand from NHC to CAAC. A significant difference can be found for the LLCT states. In complex **7**, the LLCT states are lowered by more than 0.5 eV compared to those of complex **8**. Similar redshifts have been found for copper complexes with NHC and CAAC ligands as well. [41]

At the ground-state geometry of complex **7**, the S_1 state has an LLCT character, where the electron density is transferred from the carbazolate ligand to the CAAC ligand. The corresponding lowest T_{LLCT} state is the T_3 state, which is 0.03 eV lower than the S_1 state. The T_1 and the T_2 state both have LC character localized on the carbazolate ligand, with different π orbital contribution.

At the ground state geometry of complex **8**, the S_1 as well as the T_1 state have LC character localized on the carbazolate ligand. The lowest S_{LLCT} state of complex **8** is the S_2 state, which is 0.4 eV higher in energy than the S_1 state.

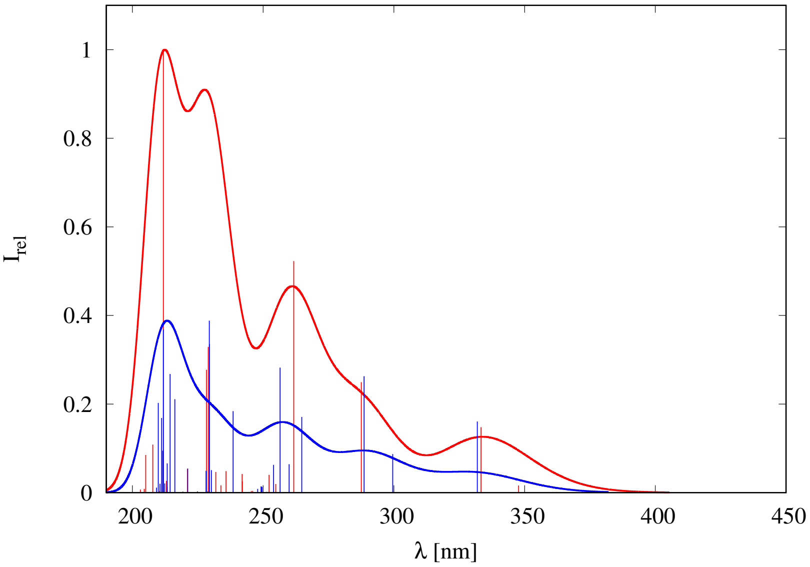

Figure 19.: Calculated singlet absorption spectra of compounds **7** (red) and **8** (blue) in THF. The intensity of the absorption is normed to the absorption maximum of complex **7**.

The absorption intensities of the LLCT states of the carbazolate complexes are low. The energy scheme of Figure 18 shows that changes of the excitation energies of complexes **7** and **8** are mainly found for the LLCT states. The strongly absorbing states have LC character localized on the carbazolate ligand. Since the carbazolate ligand is the same for both complexes, these excitations are similar in both complexes. Accordingly, a similar shape with only small shifts of the absorption maxima is found for the absorption spectra of complexes **7** and **8** (see Figure 19). The intensity of the absorption of complex **7** is slightly higher than that of complex **8**.

The energy gap between the S_{LLCT} and the T_{LLCT} state of 0.03 eV for complex **7** is very small. The same energy gap of complex **8** (0.23 eV) is significantly higher. Since the lowest S_{LLCT} and T_{LLCT} states are 0.40 eV and 0.81 eV, respectively, higher than the lowest S_{LC} and T_{LC} state, respectively, no TADF is expected to occur for complex **8**, but rather a non-radiative

Table 10.: DFT/MRCI excitation energies (ΔE/eV) of complex **7** in THF at various molecular geometries. The DFT/MRCI energy of the S_0 state at the DFT-optimized S_0 minimum geometry in a polarizable THF environment serves as common origin. 0–0 energies including zero-point vibrational energy corrections are given in parentheses.

state	optimized geometry				
	S_0	S_{LLCT}	S_{LC}	T_{LLCT}	T_{LC}
S_0	0.00	0.49	0.10	0.49	0.30
S_{LLCT}	3.57	2.74 (**2.64**)	3.56	2.74	3.85
S'_{LLCT}	4.20	3.63	4.29	3.64	4.38
S_{LC}	3.72	4.07	3.51(**3.38**)	4.07	3.72
S'_{LC}	4.31	4.62	4.24	4.62	4.18
T_{LLCT}	3.53	2.70	3.51	2.71 (**2.61**)	3.81
T'_{LLCT}	4.18	3.61	4.27	3.61	4.35
T_{LC}	3.24	3.59	3.02	3.59	2.92 (**2.77**)
T'_{LC}	3.44	4.02	3.32	4.02	3.46

relaxation.

Excited state geometries

The description of the excited states focusses on complex **7**, since complex **8** is expected to be non-emissive and complex **9** is expected to have similar luminescence properties as complex **7**. By optimizing the S_1 and the T_1 states S_{LLCT}, S_{LC}, T_{LLCT} and T_{LC} minimum geometries were found. The energies of the S_1 and the T_1 states are significantly lower at the S_{LLCT} and T_{LLCT} geometries than at the S_{LC} and T_{LC} geometries (see Table 10). The S_1 state of the S_{LC} geometry has some contribution of the CAAC ligand's n orbitals, while the T_1 of the T_{LC} geometry is a pure $\pi\pi^*$ excitation on the carbene ligand. In contrast to the Zn(4-X-PhS)$_2$(phen) and Zn-dithiolate-carbene complexes (see Section 3.2.1 and 3.2.2), the geometries of the excited states do not show a rotation or bending of the ligands with excitation. The dihedral angles of the ground-state and the LLCT geometries show changes of less than 10°. The emission spectra of the LLCT states were calculated at 298 K and 77 K and are shown in Figure 20. The calculated LLCT emission spectra have only one emission maximum and are very broad and structureless. Only a small redshift of the T_1-emission towards the S_1 emission was found. By decreasing the temperature from 298 K to 77 K, the intensity of the calculated emission spectra increases and the emission maxima show a small redshift.

The adiabatic energy gap between the S_1 and the T_1 state with LLCT character of 0.03 eV

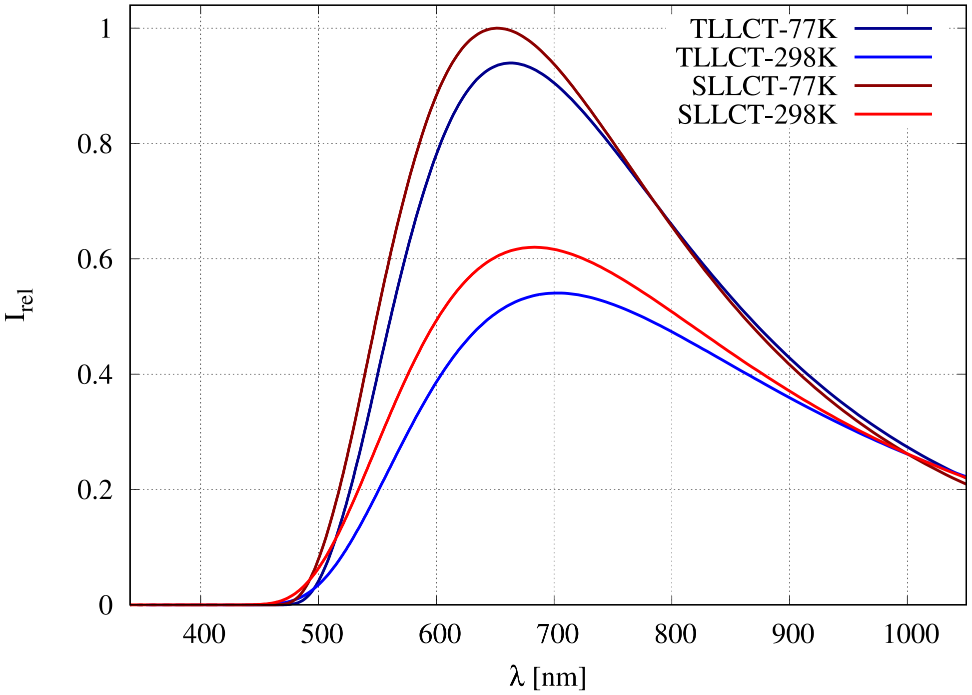

Figure 20.: Calculated emission spectra in implicit THF environment at 298 K(dark) and 77 K(light) of the optimized singlet (red) and triplet (blue) LLCT geometries complex **7**.

is very low and in the thermally surmountable region. The calculated rate constants (see Table 11) suggest that TADF occurs at 298 K. Since the phosphorescence rate constant of the T_{LLCT} state is very low, even at 77 K TADF is expected to be the main emission channel. The calculated vertical emission energies indicate the emitted light to be green. The averaged phosphorescence rate constant of the T_{LC} state is even lower with 1.78×10^{-1} cm^{-1} than for the T_{LLCT} state and the LC states can be expected to be non-emissive.

Summary and conclusion

Although the lowest excited states of all three investigated carbazolate complexes have LC character in the FC region, the energies at the optimized LLCT geometries of complex **7** are lower than at the optimized LC geometries. The calculated rate constants indicate TADF to be the main emission pathway. The S_1-T_1 energy gap of the LLCT states is very low with 0.03 eV and thermally surmountable. Even at 77 K, rISC is much faster than the very slow phosphorescence. The investigated Zn(II)-dithiolate-carbene complexes showed a strong decrease of the calculated ISC rate constants if the dithiolate ligand was rotated out of the carbene plane. The

Table 11.: Vertical emission wavelength λ [nm], spin component-averaged $\mathrm{S_{LLCT}}$-$\mathrm{T_{LLCT}}$ SOC [$\mathrm{cm^{-1}}$], and radiative as well as nonradiative rate constants k [$\mathrm{s^{-1}}$] of the LLCT states of complex **7**.

$\mathrm{S_{LLCT}}$				$\mathrm{T_{LLCT}}$		Temp.		
λ_F	k_F	SOC	λ_P	k_P	SOC	T [K]	k_ISC	k_rISC
553	1×10^6	0.38	559	8×10^1	0.26	298	3×10^7	1×10^6
						77	7×10^6	5×10^3

sterical demand of the carbazolate ligand is higher than the ligands of the Zn(4-X-PhS)$_2$(phen) and Zn(II)-dithiolate-carbene complexes. Hence, the carbazolate ligands show no bending and only a small rotation towards the carbene ligand. This is a strong advantage of the carbazolate ligands towards the dithiolate ligands. At the ground state geometry, the excitation energies of complex **9** are similar to the ones of complex **7** and similar photophysical properties are expected for the two complexes.

With the lower σ-donor and π-acceptor strength of the NHC ligand, the excitation energies of the LLCT states of complex **8** show a strong increase compared to those of complex **7**. Accordingly, the energies of the dark LC states are lower than those of the LLCT states at the optimized excited state geometries, too.

4. Summary and outlook

Based on the comparison of the calculations on the (DPEPhos)Cu(PyrTet) complex to the experimental data, the suitability of the computational methods could be examined. The calculated absorption spectra are in good agreement with the experiment and therefore the ground state description is expected to be correct. The computation of the excited states has revealed some difficulties. A flattening-distortion of the excited states was reported for the complex and is confirmed by the optimized geometries of the excited states. While the calculated rate constants and adiabatic excitation energies confirm the suitability of the computational methods, the vertical excitation energies strongly deviate from the experimental emission maxima.

The CAAC-Cu complexes were used to investigate solvent effects on the photophysical properties. The $Cu(CAAC)_2^+$ complex is more rigid and the copper center is less accessible than for the CAAC-Cu-Cl complex. Accordingly, solvent effects are small for $Cu(CAAC)_2^+$. The calculations of CAAC-Cu-Cl with and without explicit THF molecules showed that in the excited state, a covalent bond between the copper atom and the nitrogen of THF is formed, which is absent in the ground state. The formation of the exciplex leads to a strong red-shift of the emission energy. In comparison with other copper complexes, some new requirements for the occurrence of TADF in Cu(I) complexes could be reported. Low-lying LC states have to be avoided. Although MLCT states lead to an increase of SOC, they lead to phosphorescence rather than TADF. The comparison of the Cu(I) complexes showed that the lowest excited states should have LLCT character.

In literature, most of the luminescent Zn(I) complexes are phosphorescent. One group of the few Zn(I) complexes, which were reported to be fluorescent, are the $Zn(4\text{-}X\text{-}PhS)_2(phen)$ complexes.[77, 76, 76, 80, 78, 81, 134] For these complexes, an energetic scheme was proposed by Highland et al. [79, 80]. With the new investigations, TADF instead of phosphorescence is expected to be the main emission pathway.

Based on the findings of the Cu(I) complexes, a screening of different Zn(II) complexes was carried out. As for the Cu(I) complexes, low-lying LC states have to be avoided in light emitting Zn(II) complexes, too. For the Zn(II) complexes, the contribution of the zinc atom to the excitations is rather low. An increase of the SOC could be achieved by the n orbitals of sulfur atoms of the ligands. The investigated Zn(II)-dtb complexes showed high ISC and rISC constants. The calculations revealed that the dtb ligands can rotate with only a small energy barrier, but with significant impact on the ISC rate constants. Based on the findings of the screened Zn(I)-carbene complexes, a CAAC-Zn(II)-dtb complex was synthesized in the Steffen group. [139] The experimental investigations showed, that the CAAC-Zn-dtb complex dimerizes. The calculated fluorescence rate constant of the dimeric complex is two orders of magnitude lower than the one of the monomeric complex. One way to avoid the dimerization and the rotation of the dtb or dob ligands could be the introduction of bulkier ligands like *tert*-butyl on the dtb ligand.

As a third group, carbene-Zn-carbazolate complexes were investigated. For the NHC complex, no low-lying LLCT states were found in the FC region and no emission is expected for this complex. The FC region of the complexes with a CAAC ligand and an aminothiocarbene is similar. Hence, similar photophysical properties are expected for them. The carbazolate ligand is sterically more demanding than the dtb ligand and therefore, no rotation or bending was found. The calculated fluorescence rate constant is significantly higher than the phosphorescence rate constant and prompt and delayed fluorescence are expected to occur.

Therefore, both groups of Zn(I)-carbene complexes are expected to be interesting fur further investigations regarding their properties as TADF emitters.

5. Bibliography

[1] L. Bergmann, J. Friedrichs, M. Mydlak, T. Baumann, M. Nieger, and S. Bräse, "Outstanding luminescence from neutral copper(I) complexes with pyridyl-tetrazolate and phosphine ligands," Chem. Commun., vol. 49, pp. 6501–6503, 2013.

[2] M. Grupe, F. Bäppler, M. Theiß, J. M. Busch, F. Dietrich, D. Volz, M. Gerhards, S. Bräse, and R. Diller, "Real-time observation of molecular flattening and intersystem crossing in [(DPEPhos)Cu(i)(PyrTet)] via ultrafast UV/Vis- and mid-IR spectroscopy on solution and solid samples," Phys. Chem. Chem. Phys., vol. 22, pp. 14187–14200, 2020.

[3] J.-H. Jou, S. Kumar, A. Agrawal, T.-H. Li, and S. Sahoo, "Approaches for fabricating high efficiency organic light emitting diodes," J. Mater. Chem. C, vol. 3, pp. 2974–3002, 2015.

[4] C. Adachi, "Third-generation organic electroluminescence materials," Jpn. J. Appl. Phys., vol. 53, no. 6, p. 060101, 2014.

[5] S. Lamansky, , P. I. Djurovich, F. Abdel-Razzaq, S. Garon, D. L. Murphy, and M. E. Thompson, "Cyclometalated Ir complexes in polymer organic light-emitting devices," J. Appl. Phys., vol. 92, no. 3, pp. 1570–1575, 2002.

[6] C. W. Tang and S. A. VanSlyke, "Organic electroluminescent diodes," Appl. Phys. Lett., vol. 51, no. 12, pp. 913–915, 1987.

[7] G. Gustafsson, Y. Cao, G. Treacy, F. Klavetter, N. Colaneri, and A. Heeger, "Flexible light-emitting diodes made from soluble conducting polymers," Nature, vol. 357, no. 6378, pp. 477–479, 1992.

[8] G. Hong, X. Gan, C. Leonhardt, Z. Zhang, J. Seibert, J. M. Busch, and S. Bräse, "A Brief History of OLEDs– Emitter Development and Industry Milestones," Adv. Mater., vol. 33, p. 2005630, 2021.

[9] B. Geffroy, P. le Roy, and C. Prat, “Organic light-emitting diode (OLED) technology: materials, devices and display technologies,” Polym. Int., vol. 55, no. 6, pp. 572–582, 2006.

[10] M. A. Baldo, D. F. O’Brien, Y. You, A. Shoustikov, S. Sibley, M. E. Thompson, and S. R. Forrest, “Highly efficient phosphorescent emission from organic electroluminescent devices,” Nature, vol. 395, pp. 151–154, 1998.

[11] M. Thompson, “The Evolution of Organometallic Complexes in Organic Light-Emitting Devices,” MRS Bulletin, vol. 32, pp. 694–701, 2007.

[12] S. Kappaun, C. Slugovc, and E. J. W. List, “Phosphorescent organic light-emitting devices: Working principle and iridium based emitter materials,” Int. J. Mol. Sci., vol. 9, pp. 1527–1547, 2008.

[13] H. Yersin, A. F. Rausch, R. Czerwieniec, T. Hofbeck, and T. Fischer, “The triplet state of organo-transition metal compounds. Triplet harvesting and singlet harvesting for efficient OLEDs,” Coord. Chem. Rev., vol. 255, no. 21, pp. 2622–2652, 2011. Controlling photophysical properties of metal complexes: Towards molecular photonics.

[14] P. S. Wagenknecht and P. C. Ford, “Metal centered ligand field excited states: Their roles in the design and performance of transition metal based photochemical molecular devices,” Coord. Chem. Rev., vol. 255, pp. 591 – 616, 2011.

[15] T. Strassner, “Phosphorescent Platinum(II) Complexes with C^C* Cyclometalated NHC Ligands,” Acc. Chem. Res., vol. 49, pp. 2680–2689, 2016.

[16] C. Cebrián and M. Mauro, “Recent advances in phosphorescent platinum complexes for organic light-emitting diodes,” Beilstein J. Org. Chem., vol. 14, pp. 1459–1481, 2018.

[17] C. Bizzarri, E. Spuling, D. M. Knoll, D. Volz, and S. Bräse, “Sustainable metal complexes for organic light-emitting diodes (OLEDs),” Coord. Chem. Rev., vol. 373, pp. 49–82, 2018.

[18] R. Czerwieniec and H. Yersin, “Diversity of Copper(I) Complexes Showing Thermally Activated Delayed Fluorescence: Basic Photophysical Analysis,” Inorg. Chem., vol. 54, pp. 4322–4327, 2015.

[19] L. Bergmann, G. J. Hedley, T. Baumann, S. Bräse, and I. D. W. Samuel, “Direct observation of intersystem crossing in a thermally activated delayed fluorescence copper complex in the solid state,” Sci. Adv., vol. 2, no. 1, 2016.

[20] D. Di, A. S. Romanov, L. Yang, J. M. Richter, J. P. H. Rivett, S. Jones, T. H. Thomas, M. Abdi Jalebi, R. H. Friend, M. Linnolahti, M. Bochmann, and D. Credgington, "High-performance light-emitting diodes based on carbene-metal-amides," Science, vol. 356, no. 6334, pp. 159–163, 2017.

[21] H. Uoyoma, K. Goushi, K. Shizu, H. Nomura, and C. Adachi, "Highly efficient organic light-emitting diodes from delayed fluorescence," Nature, vol. 492, pp. 234–238, 2012.

[22] T. J. Penfold, E. Gindensperger, C. Daniel, and C. M. Marian, "Spin-Vibronic Mechanism for Intersystem Crossing," Chem. Rev., vol. 118, pp. 6975–7025, 2018.

[23] T. D. Schmidt and W. Brütting, Efficiency Enhancement of Organic Light-Emitting Diodes Exhibiting Delayed Fluorescence and Nonisotropic Emitter Orientation, ch. 6, pp. 199–228. John Wiley Sons, Ltd, 2018.

[24] K. Masui, H. Nakanotani, and C. Adachi, "Analysis of exciton annihilation in high-efficiency sky-blue organic light-emitting diodes with thermally activated delayed fluorescence," Org. Electron., vol. 14, no. 11, pp. 2721–2726, 2013.

[25] Y. Noguchi, H.-J. Kim, R. Ishino, K. Goushi, C. Adachi, Y. Nakayama, and H. Ishii, "Charge carrier dynamics and degradation phenomena in organic light-emitting diodes doped by a thermally activated delayed fluorescence emitter," Org. Electron., vol. 17, pp. 184–191, 2015.

[26] Y. Kitamoto, T. Namikawa, T. Suzuki, Y. Miyata, H. Kita, T. Sato, and S. Oi, "Dimesitylarylborane-based luminescent emitters exhibiting highly-efficient thermally activated delayed fluorescence for organic light-emitting diodes," Org. Electron., vol. 34, pp. 208–217, 2016.

[27] C. M. Marian, J. Föller, M. Kleinschmidt, and M. Etinski, Intersystem crossing processes in TADF emitters. Wiley-VCH: Weinheim Germany, 2018.

[28] C. M. Marian, "Understanding and Controlling Intersystem Crossing in Molecules," Annu. Rev. Phys. Chem., vol. 72, pp. 616–640, 2021.

[29] H. Yersin, R. Czerwieniec, M. Z. Shafikov, and A. F. Suleymanova, "TADF Material Design: Photophysical Background and Case Studies Focusing on CuI and AgI Complexes," ChemPhysChem, vol. 18, no. 24, pp. 3508–3535, 2017.

[30] M. Gernert, U. Müller, M. Haehnel, J. Pflaum, and A. Steffen, “A Cyclic Alkyl(amino)carbene as Two-Atom π-Chromophore Leading to the First Phosphorescent Linear CuI Complexes,” Chem. Eur. J., vol. 23, no. 9, pp. 2206–2216, 2017.

[31] Y. Sakai, Y. Sagara, H. Nomura, N. Nakamura, Y. Suzuki, H. Miyazaki, and C. Adachi, “Zinc complexes exhibiting highly efficient thermally activated delayed fluorescence and their application to organic light-emitting diodes,” Chem. Commun., vol. 51, pp. 3181–3184, 2015.

[32] A. Barbieri, G. Accorsi, and N. Armaroli, “Luminescent complexes beyond the platinum group: the d^{10} avenue,” Chem. Commun., pp. 2185–2193, 2008.

[33] X.-L. Chen, C.-S. Lin, X.-Y. Wu, R. Yu, T. Teng, Q.-K. Zhang, Q. Zhang, W.-B. Yang, and C.-Z. Lu, “Highly efficient cuprous complexes with thermally activated delayed fluorescence and simplified solution process OLEDs using the ligand as host,” J. Mater. Chem. C, vol. 3, pp. 1187–1195, 2015.

[34] E. Cariati, E. Lucenti, C. Botta, U. Giovanella, D. Marinotto, and S. Righetto, “Cu(I) hybrid inorganicrganic materials with intriguing stimuli responsive and optoelectronic properties,” Coordination Chemistry Reviews, vol. 306, p. 56614, 2016.

[35] A. Lavie-Cambot, M. Cantuel, Y. Leydet, G. Jonusauskas, D. M. Bassani, and N. D. McClenaghan, “Improving the photophysical properties of copper(I) bis(phenanthroline) complexes,” Coord. Chem. Rev., vol. 252, no. 23, pp. 2572–2584, 2008. 17th International Symposium on the Photochemistry and Photophysics of Coordination Compounds.

[36] J. Föller, M. Kleinschmidt, and C. M. Marian, “Phosphorescence or Thermally Activated Delayed Fluorescence? Intersystem Crossing and Radiative Rate Constants of a Three-Coordinate Copper(I) Complex Determined by Quantum-Chemical Methods,” Inorg. Chem., vol. 55, no. 15, pp. 7508–7516, 2016.

[37] R. Czerwieniec, M. J. Leitl, H. H. Homeier, and H. Yersin, “Cu(I) complexes - Thermally activated delayed fluorescence. Photophysical approach and material design,” Coord. Chem. Rev., vol. 325, pp. 2–28, 2016.

[38] Y. Zhang, M. Schulz, M. Wächtler, M. Karnahl, and B. Dietzek, “Heteroleptic diimine-diphosphine Cu(I) complexes as an alternative towards noble-metal based photosensitizers: Design strategies, photophysical properties and perspective applications,” Coord. Chem. Rev., vol. 356, pp. 127–146, 2018.

[39] J. Föller, C. Ganter, A. Steffen, and C. M. Marian, "Computer-aided design of luminescent linear N-heterocyclic carbene copper(I) pyridine complexes," Inorg. Chem., vol. 58, pp. 5446–5456, 2019.

[40] M. Gernert, L. Balles-Wolf, F. Kerner, U. Müller, A. Schmiedel, M. Holzapfel, C. M. Marian, J. Pflaum, C. Lambert, and A. Steffen, "Cyclic (Amino)(aryl)carbenes Enter the Field of Chromophore Ligands: Expanded π System Leads to Unusually Deep Red Emitting CuI Compounds," J. Am. Chem. Soc., vol. 142, no. 19, pp. 8897–8909, 2020. PMID: 32302135.

[41] N. Lüdtke, J. Föller, and C. M. Marian, "Understanding the Luminescence Properties of Cu(I) Complexes: A Quantum Chemical Perusal," Phys. Chem. Chem. Phys., vol. 22, pp. 23530–23544, 2020.

[42] P.-T. Chou, Y. Chi, M.-W. Chung, and C.-C. Lin, "Harvesting luminescence via harnessing the photophysical properties of transition metal complexes," Coordination Chemistry Reviews, vol. 255, no. 21, pp. 2653–2665, 2011. Controlling photophysical properties of metal complexes: Towards molecular photonics.

[43] H. Yersin, ed., Highly Efficient OLEDs: Materials Based on Thermally Activated Delayed Fluorescence. Wiley VCH, 2018.

[44] A. S. Romanov, L. Yang, S. T. E. Jones, D. Di, O. J. Morley, B. H. Drummond, A. P. M. Reponen, M. Linnolahti, D. Credgington, and M. Bochmann, "Dendritic Carbene Metal Carbazole Complexes as Photoemitters for Fully Solution-Processed OLEDs," Chem. Mater., vol. 31, no. 10, pp. 3613–3623, 2019.

[45] R. Czerwieniec, K. Kowalski, and H. Yersin, "Highly efficient thermally activated fluorescence of a new rigid Cu(I) complex $[Cu(dmp)(phanephos)]^+$," Dalton Trans., vol. 42, pp. 9826–9830, 2013.

[46] X.-L. Chen, R. Yu, Q.-K. Zhang, L.-J. Zhou, X.-Y. Wu, Q. Zhang, and C.-Z. Lu, "Rational Design of Strongly Blue-Emitting Cuprous Complexes with Thermally Activated Delayed Fluorescence and Application in Solution-Processed OLEDs," Chem. Mater., vol. 25, pp. 3910–3920, 2013.

[47] M. Osawa, I. Kawata, R. Ishii, S. Igawa, M. Hashimoto, and M. Hoshino, "Application of Neutral d^{10} Coinage Metal Complexes with an Anionic Bidentate Ligand in Delayed

Fluorescence-Type Organic Light-Emitting Diodes," J. Mater. Chem. C, vol. 1, pp. 4375–4383, 2013.

[48] C. L. Linfoot, M. J. Leitl, P. Richardson, A. F. Rausch, O. Chepelin, F. J. White, H. Yersin, and N. Robertson, "Thermally Activated Delayed Fluorescence (TADF) and Enhancing Photoluminescence Quantum Yields of $[\mathrm{Cu^I(diimine)(diphosphine)}]^+$ Complexes—Photophysical, Structural, and Computational Studies," Inorg. Chem., vol. 53, pp. 10854–10861, 2014.

[49] Q. Zhang, J. Chen, X.-Y. Wu, X.-L. Chen, R. Yu, and C.-Z. Lu, "Outstanding blue delayed fluorescence and significant processing stability of cuprous complexes with functional pyridine-pyrazolate diimine ligands," Dalton Trans., vol. 44, pp. 6706–6710, 2015.

[50] M. Iwamura, S. Takeuchi, and T. Tahara, "Substituent effect on the photoinduced structural change of Cu(i) complexes observed by femtosecond emission spectroscopy," Phys. Chem. Chem. Phys., vol. 16, pp. 4143–4154, 2014.

[51] Z. A. Siddique, Y. Yamamoto, T. Ohno, and K. Nozaki, "Structure-Dependent Photophysical Properties of Singlet and Triplet Metal-to-Ligand Charge Transfer States in Copper(I) Bis(diimine) Compounds," Inorg. Chem., vol. 42, pp. 6366–6378, 2003.

[52] G. Capano, M. Chergui, U. Röthlisberger, I. Tavernelli, and T. J. Penfold, "A Quantum Dynamics Study of the Ultrafast Relaxation in a Prototypical Cu(I)-Phenanthroline," J. Phys. Chem. A, vol. 118, no. 42, pp. 9861–9869, 2014.

[53] G. Capano, M. Chergui, U. Röthlisberger, I. Tavernelli, and T. J. Penfold, "A Quantum Dynamics Study of the Ultrafast Relaxation in a Prototypical Cu(I)-Phenanthroline," J. Phys. Chem. A, vol. 118, no. 42, pp. 9861–9869, 2014.

[54] G. Capano, U. Röthlisberger, I. Tavernelli, and T. J. Penfold, "Theoretical Rationalization of the Emission Properties of Prototypical Cu(I)-Phenanthroline Complexes," J. Phys. Chem. A, vol. 119, no. 27, pp. 7026–7037, 2015.

[55] V. A. Krylova, P. I. Djurovich, M. T. Whited, and M. E. Thompson, "Synthesis and characterization of phosphorescent three-coordinate Cu(I)-NHC complexes," Chem. Commun., vol. 46, pp. 6696–6698, 2010.

[56] V. A. Krylova, P. I. Djurovich, J. W. Aronson, R. Haiges, M. T. Whited, and M. E. Thompson, "Structural and Photophysical Studies of Phosphorescent Three-

Coordinate Copper(I) Complexes Supported by an N-Heterocyclic Carbene Ligand," Organometallics, vol. 31, no. 22, pp. 7983–7993, 2012.

[57] V. A. Krylova, P. I. Djurovich, B. L. Conley, R. Haiges, M. T. Whited, T. J. Williams, and M. E. Thompson, "Control of emission colour with N-heterocyclic carbene (NHC) ligands in phosphorescent three-coordinate Cu(i) complexes," Chem. Commun., vol. 50, pp. 7176–7179, 2014.

[58] M. J. Leitl, V. A. Krylova, P. I. Djurovich, M. E. Thompson, and H. Yersin, "Phosphorescence versus Thermally Activated Delayed Fluorescence. Controlling Singlet–Triplet Splitting in Brightly Emitting and Sublimable Cu(I) Compounds," J. Am. Chem. Soc., vol. 136, pp. 16032–16038, 2014.

[59] A. S. Romanov, D. Di, L. Yang, J. Fernandez-Cestau, C. R. Becker, C. E. James, B. Zhu, M. Linnolahti, D. Credgington, and M. Bochmann, "Highly photoluminescent copper carbene complexes based on prompt rather than delayed fluorescence," Chem. Commun., vol. 52, p. 6379, 2016. Corrected in: Romanov et al., *Chem. Commun.* **2018**, *54*, 3672.

[60] A. S. Romanov, C. R. Becker, C. E. James, D. Di, D. Credgington, M. Linnolahti, and M. Bochmann, "Copper and Gold Cyclic (Alkyl)(amino)carbene Complexes with Sub-Microsecond Photoemissions: Structure and Substituent Effects on Redox and Luminescent Properties," Chem. Eur. J., vol. 23, no. 19, pp. 4625–4637, 2017.

[61] R. Hamze, R. Jazzar, M. Soleilhavoup, P. I. Djurovich, G. Bertrand, and M. E. Thompson, "Phosphorescent 2-, 3- and 4-coordinate cyclic (alkyl)(amino)carbene (CAAC) Cu(I) complexes," Chem. Commun., vol. 53, p. 9008, 2017.

[62] B. Bertrand, A. S. Romanov, M. Brooks, J. Davis, C. Schmidt, I. Ott, M. O'Connell, and M. Bochmann, "Synthesis, structure and cytotoxicity of cyclic (alkyl)(amino) carbene and acyclic carbene complexes of group 11 metals," Dalton Trans., vol. 46, pp. 15875–15887, 2017.

[63] F. Chotard, A. S. Romanov, D. L. Hughes, M. Linnolahti, and M. Bochmann, "Zwitterionic Mixed-Carbene Coinage Metal Complexes: Synthesis, Structures, and Photophysical Studies," Eur. J. Inorg. Chem., vol. 2019, no. 39-40, pp. 4234–4240, 2019.

[64] R. Hamze, J. L. Peltier, D. Sylvinson, M. Jung, J. Cardenas, R. Haiges, M. Soleilhavoup, R. Jazzar, P. I. Djurovich, G. Bertrand, and M. E. Thompson, "Eliminating nonradiative

decay in Cu(I) emitters: >99% quantum efficiency and microsecond lifetime,” Science, vol. 363, no. 6427, pp. 601–606, 2019.

[65] R. Hamze, M. Idris, D. S. Muthiah Ravinson, M. C. Jung, R. Haiges, P. I. Djurovich, and M. E. Thompson, “Highly Efficient Deep Blue Luminescence of 2-Coordinate Coinage Metal Complexes Bearing Bulky NHC Benzimidazolyl Carbene,” Front. Chem., vol. 8, p. 401, 2020.

[66] A. S. Romanov, S. T. E. Jones, Q. Gu, P. J. Conaghan, B. H. Drummond, J. Feng, F. Chotard, L. Buizza, M. Foley, M. Linnolahti, D. Credgington, and M. Bochmann, “Carbene metal amide photoemitters: tailoring conformationally flexible amides for full color range emissions including white-emitting OLED,” Chem. Sci., vol. 11, pp. 435–446, 2020.

[67] S. Shi, L. R. Collins, M. F. Mahon, P. I. Djurovich, M. E. Thompson, and M. K. Whittlesey, “Synthesis and characterization of phosphorescent two-coordinate copper(I) complexes bearing diamidocarbene ligands,” Dalton Trans., vol. 46, pp. 745–752, 2017.

[68] A. S. Romanov, D. Di, L. Yang, J. Fernandez-Cestau, C. R. Becker, C. E. James, B. Zhu, M. Linnolahti, D. Credgington, and M. Bochmann, “Correction: Highly photoluminescent copper carbene complexes based on prompt rather than delayed fluorescence,” Chem. Commun., vol. 54, no. 29, p. 3672, 2018.

[69] T.-y. Li, D. S. Muthiah Ravinson, R. Haiges, P. I. Djurovich, and M. E. Thompson, “Enhancement of the Luminescent Efficiency in Carbene-Au(I)-Aryl Complexes by the Restriction of Renner–Teller Distortion and Bond Rotation,” J. Am. Chem. Soc., vol. 142, pp. 6158–6172, 2020.

[70] S. Shi, M. C. Jung, C. Coburn, A. Tadle, D. Sylvinson M. R., P. I. Djurovich, S. R. Forrest, and M. E. Thompson, “Highly Efficient Photo- and Electroluminescence from Two-Coordinate Cu(I) Complexes Featuring Nonconventional N-Heterocyclic Carbenes,” J. Am. Chem. Soc., vol. 141, no. 8, pp. 3576–3588, 2019.

[71] R. Hamze, S. Shi, S. C. Kapper, D. S. Muthiah Ravinson, L. Estergreen, M.-C. Jung, A. C. Tadle, R. Haiges, P. I. Djurovich, J. L. Peltier, R. Jazzar, G. Bertrand, S. E. Bradforth, and M. E. Thompson, “"Quick-Silver" from a Systematic Study of Highly Luminescent, Two-Coordinate, d10 Coinage Metal Complexes,” J. Am. Chem. Soc., vol. 141, no. 21, pp. 8616–8626, 2019. PMID: 31062972.

[72] I. Chan, W. van Dorp, T. Schaafsma, and J. van der Waals, “The lowest triplet state of Zn porphin,” Mol. Phys., vol. 22, pp. 753–760, 1971.

[73] A. Harriman, “Luminescence of porphyrins and metalloporphyrins. Part 1. – Zinc(II), nickel(II) and manganese(II) porphyrins,” J. Chem. Soc., Faraday Trans. 1, vol. 76, pp. 1978–1985, 1980.

[74] M. Pineiro, A. L. Carvalho, M. M. Pereira, A. M. d. R. Gonsalves, L. G. Arnaut, and S. J. Formosinho, “Photoacoustic Measurements of Porphyrin Triplet-State Quantum Yields and Singlet-Oxygen Efficiencies,” Chem. Eur. J., vol. 4, pp. 2299–2307, 1998.

[75] K. D. Oyler, F. J. Coughlin, and S. Bernhard, “Controlling the Helicity of 2,2′-Bipyridyl Ruthenium(II) and Zinc(II) Hemicage Complexes,” J. Am. Chem. Soc., vol. 129, pp. 210–217, 2007.

[76] K. A. Truesdell and G. A. Crosby, “Observation of a novel low-lying excited state in zinc(II) complexes,” J. Am. Chem. Soc., vol. 107, pp. 1787–1788, 1985.

[77] G. Crosby, R. Highland, and K. Truesdell, “Spectroscopic properties of $(nd)^{10}$ transition metal complexes,” Coord. Chem. Rev., vol. 64, pp. 41 – 52, 1985.

[78] K. J. Jordan, W. F. Wacholtz, and G. A. Crosby, “Structural dependence of the luminescence from bis(substituted benzenethiolato)(2,9-dimethyl-1,10-phenanthroline)zinc(II) complexes,” Inorg. Chem., vol. 30, pp. 4588–4593, 1991.

[79] R. Highland and G. Crosby, “Determination of the activation barrier to energy transfer from $^3\pi\pi^*$ to charge transfer levels via steady-state and transient luminescence measurements on bis(4-chlorothiophenol)(1,10-phenanthroline)zinc(II),” Chem. Phys. Lett., vol. 119, pp. 454 – 458, 1985.

[80] R. G. Highland, J. G. Brummer, and G. A. Crosby, “Redistribution of excitation energy between nonequilibrated electronic excited levels of zinc(II) complexes,” J. Phys. Chem., vol. 90, pp. 1593–1598, 1986.

[81] A. Galin, Y. Razskazovsky, and M. Mel’nikov, “Photophysical properties of mixed-ligand complexes (ArS)2ZnPhen with interligand charge-transfer excited states: influence of substituents in the arylthiolate ligand,” J. Photochem. Photobiol. A: Chemistry, vol. 72, no. 1, pp. 35 – 40, 1993.

[82] B. Minaev and H. Ågren, “Theoretical DFT study of phosphorescence from porphyrins,” Chemical Physics, vol. 315, pp. 215 – 239, 2005.

[83] P. Gronlund, J. Burt, and W. Wacholtz, “Synthesis and characterization of luminescent mixed ligand zinc(II) complexes containing a novel dithiol ligand,” Inorg. Chim. Acta, vol. 234, pp. 13 – 18, 1995.

[84] R. Wang, L. Deng, M. Fu, J. Cheng, and J. Li, “Novel Zn^{II} complexes of 2-(2-hydroxyphenyl)benzothiazoles ligands: electroluminescence and application as host materials for phosphorescent organic light-emitting diodes,” J. Mater. Chem., vol. 22, pp. 23454–23460, 2012.

[85] F. Dumur, “Zinc complexes in OLEDs: An overview,” Synth. Met., vol. 195, pp. 241–251, 2014.

[86] G. U. Mahoro, J. Fernandez-Cestau, J.-L. Renaud, P. B. Coto, R. D. Costa, and S. Gaillard, “Recent Advances in Solid-State Lighting Devices Using Transition Metal Complexes Exhibiting Thermally Activated Delayed Fluorescent Emission Mechanism,” Adv. Opt. Mater., vol. 8, no. 16, p. 2000260, 2020.

[87] O. S. Wenger, “Photoactive Complexes with Earth-Abundant Metals,” Journal of the American Chemical Society, vol. 140, no. 42, pp. 13522–13533, 2018.

[88] A. S. Berezin, K. A. Vinogradova, V. P. Krivopalov, E. B. Nikolaenkova, V. F. Plyusnin, A. S. Kupryakov, N. V. Pervukhina, D. Y. Naumov, and M. B. Bushuev, “Excitation-Wavelength-Dependent Emission and Delayed Fluorescence in a Proton-Transfer System,” Chem. Eur. J., vol. 24, no. 49, pp. 12790–12795, 2018.

[89] J. Xiong, K. Li, T. Teng, X. Chang, Y. Wei, C. Wu, and C. Yang, “Dinuclear ZnII Complexes Exhibiting Thermally Activated Delayed Fluorescence and Luminescence Polymorphism,” Chem. Eur. J., vol. 26, no. 30, pp. 6887–6893, 2020.

[90] B. Goswami, T. J. Feuerstein, R. Yadav, S. Lebedkin, P. J. Boden, S. T. Steiger, G. Niedner-Schatteburg, M. Gerhards, M. M. Kappes, and P. W. Roesky, “Thermally activated delayed fluorescence and phosphorescence quenching in iminophosphonamide copper and zinc complexes,” Chem. Eur. J., 2021.

[91] J.-C. Bruyere, D. Specklin, C. Gourlaouen, R. Lapenta, L. F. Veiros, A. Grassi, S. Milione, L. Ruhlmann, C. Boudon, and S. Dagorne, “Cyclic(Alkyl)(Amino)Carbene (CAAC)-

Supported Zn Alkyls: Synthesis, Structure and Reactivity in Hydrosilylation Catalysis," Chem. Eur. J., vol. 25, no. 34, pp. 8061–8069, 2019.

[92] A. Liske, L. Wallbaum, T. Hölzel, J. Föller, M. Gernert, B. Hupp, C. Ganter, C. M. Marian, and A. Steffen, "Cu-F interactions between cationic linear NHC-Cu(I)-pyridine complexes and their counterions greatly enhance blue luminescence efficiency," Inorg. Chem., vol. 58, pp. 5433–5445, 2019.

[93] V. Lavallo, Y. Canac, C. Präsang, B. Donnadieu, and G. Bertrand, "Stable Cyclic (Alkyl)(Amino)Carbenes as Rigid or Flexible, Bulky, Electron-Rich Ligands for Transition-Metal Catalysts: A Quaternary Carbon Atom Makes the Difference," Angew. Chem., vol. 117, no. 35, pp. 5851–5855, 2005.

[94] V. Lavallo, Y. Canac, A. DeHope, B. Donnadieu, and G. Bertrand, "A rigid cyclic (alkyl)(amino)carbene ligand leads to isolation of low-coordinate transition-metal complexes," Angew. Chem. Int. Ed., vol. 44, no. 44, pp. 7236–9, 2005.

[95] B. Rao, H. Tang, X. Zeng, L. L. Liu, M. Melaimi, and G. Bertrand, "Cyclic (Amino)(aryl)carbenes (CAArCs) as Strong -Donating and -Accepting Ligands for Transition Metals," Angew. Chem. Int. Ed., vol. 54, no. 49, pp. 14915–14919, 2015.

[96] V. Lavallo, Y. Canac, A. DeHope, B. Donnadieu, and G. Bertrand, "A Rigid Cyclic (Alkyl)(amino)carbene Ligand Leads to Isolation of Low-Coordinate Transition-Metal Complexes," Angew. Chem. Int. Ed., vol. 44, no. 44, pp. 7236–7239, 2005.

[97] O. Back, M. Henry-Ellinger, C. D. Martin, D. Martin, and G. Bertrand, "^{31}P NMR Chemical Shifts of Carbene–Phosphinidene Adducts as an Indicator of the π-Accepting Properties of Carbenes," Angew. Chem. Int. Ed., vol. 52, no. 10, pp. 2939–2943, 2013.

[98] M. Soleilhavoup and G. Bertrand, "Cyclic (Alkyl)(Amino)Carbenes (CAACs): Stable Carbenes on the Rise," Acc. Chem. Res., vol. 48, no. 2, p. 256, 2015.

[99] R. Jazzar, J.-B. Bourg, R. D. Dewhurst, B. Donnadieu, and G. Bertrand, "Intramolecular "Hydroiminiumation and -amidiniumation" of Alkenes: A Convenient, Flexible, and Scalable Route to Cyclic Iminium and Imidazolinium Salts," J. Org. Chem., vol. 72, no. 9, pp. 3492–3499, 2007.

[100] S. Gómez-Bujedo, M. Alcarazo, C. Pichon, E. Álvarez, R. Fernández, and J. M. Lassaletta, "Isoquinolin-1-ylidenes as electronically tuneable ligands," Chem. Commun., pp. 1180–1182, 2007.

[101] A. Magriz, S. Gómez-Bujedo, E. Álvarez, R. Fernnández, and J. M. Lassaletta, "Phthalazin-2-ylidenes As Cyclic Amino Aryl Carbene Ligands in Rhodium(I) and Iridium(I) Complexes," Organometallics, vol. 29, no. 22, pp. 5941–5945, 2010.

[102] M. B. Gildner and T. W. Hudnall, "Cyclic (aryl)(amido)carbenes: pushing the π-acidity of amidocarbenes through benzannulation," Chem. Commun., vol. 55, pp. 12300–12303, 2019.

[103] A. D. Becke, "Density-functional exchange-energy approximation with correct asymptotic behavior," Phys. Rev. A, vol. 38, pp. 3098–3100, Sep 1988.

[104] C. Lee, W. Yang, and R. G. Parr, "Development of the Colle-Salvetti Correlation-Energy Formula into a Functional of the Electron Density," Phys. Rev. B, vol. 37, pp. 785–789, 1988.

[105] S. Grimme and M. Waletzke, "A Combination of Kohn–Sham Density Functional Theory and Multi-Reference Configuration Interaction Methods," J. Chem. Phys., vol. 111, pp. 5645–5655, 1999.

[106] C. Adamo and V. Barone, "Toward Reliable Density Functional Methods without Adjustable Parameters: The PBE0 Model," J. Chem. Phys., vol. 110, pp. 6158–6170, 1999.

[107] J. P. Perdew, K. Burke, and M. Ernzerhof, "Generalized Gradient Approximation Made Simple," Phys. Rev. Lett., vol. 77, pp. 3865–3868, 1996.

[108] J. P. Perdew, M. Ernzerhof, K. Burke, and A. Savin, "On-top pair-density interpretation of spin density functional theory, with applications to magnetism," Int. J. Quantum Chem., vol. 61, pp. 197–205, 1997.

[109] E. Runge and E. K. Gross, "Density-functional theory for time-dependent systems," Phys. Rev. Lett., vol. 52, no. 12, p. 997, 1984.

[110] A. Dreuw and M. Head-Gordon, "Single-Reference ab Initio Methods for the Calculation of Excited States of Large Molecules," Chem. Rev., vol. 105, no. 11, pp. 4009–4037, 2005. PMID: 16277369.

[111] C. M. Marian, A. Heil, and M. Kleinschmidt, "The DFT/MRCI Method," WIREs Comp. Mol. Sci., vol. 9, p. e1394, 2019.

[112] C. M. Marian, "Spin–Orbit Coupling in Molecules," in Reviews in Computational Chemistry (K. Lipkowitz and D. Boyd, eds.), vol. 17, pp. 99–204, Wiley-VCH, Weinheim (2001), 2001.

[113] AMFI is an atomic spin-orbit integral program written by B. Schimmelpfennig, University of Stockholm, 1996.

[114] K. A. Peterson and C. Puzzarini, "Systematically Convergent Basis Sets for Transition Metals. II. Pseudopotential-Based Correlation Consistent Basis Sets for the Group 11 (Cu, Ag, Au) and 12 (Zn, Cd, Hg) Elements," Theor. Chem. Acc., vol. 114, pp. 283–296, 2005.

[115] R. M. Pitzer and N. W. Winter, "Electronic-structure methods for heavy-atom molecules," The Journal of Physical Chemistry, vol. 92, no. 11, pp. 3061–3063, 1988.

[116] D. Figgen, G. Rauhut, M. Dolg, and H. Stoll, "Energy-Consistent Pseudopotentials for Group 11 and 12 Atoms: Adjustment to Multi-Configuration Dirac–Hartree–Fock Data," Chem. Phys., vol. 311, pp. 227–244, 2005.

[117] C. M. Marian, "Spin-orbit coupling and intersystem crossing in molecules," WIREs Comput Mol Sci, vol. 2, no. 2, pp. 187–203, 2012.

[118] M. Etinski, J. Tatchen, and C. M. Marian, "Thermal and Solvent Effects on the Triplet Formation in Cinnoline," Phys. Chem. Chem. Phys., vol. 16, pp. 4740–4751, 2014.

[119] W. Liptay, "Electrochromism and solvatochromism," Angew. Chem., Int. Ed. in Engl., vol. 8, no. 3, pp. 177–188, 1969.

[120] E. Cancès, B. Mennucci, and J. Tomasi, "A new integral equation formalism for the polarizable continuum model: Theoretical background and applications to isotropic and anisotropic dielectrics," J. Chem. Phys., vol. 107, p. 3032, 1997.

[121] B. Mennucci, E. Cancès, and J. Tomasi, "Evaluation of Solvent Effects in Isotropic and Anisotropic Dielectrics and in Ionic Solutions with a Unified Integral Equation Method: Theoretical Bases, Computational Implementation, and Numerical Applications," J. Phys. Chem. B, vol. 101, p. 10506, 1997.

[122] E. Cancès and B. Mennucci, "New applications of integral equations methods for solvation continuum models: ionic solutions and liquid crystals," J. Math. Chem., vol. 23, no. 3, pp. 309–326, 1998.

[123] A. Klamt and G. Schüürmann, “COSMO: A New Approach to Dielectric Screening in Solvents with Explicit Expressions for the Screening Energy and its Gradient,” J. Chem. Soc., Perkin Trans. 2, vol. 5, pp. 799–805, 1993.

[124] S. Miertuš, E. Scrocco, and J. Tomasi, “Electrostatic interaction of a solute with a continuum. A direct utilizaion of AB initio molecular potentials for the prevision of solvent effects,” Chem. Phys., vol. 55, no. 1, pp. 117–129, 1981.

[125] V. Barone and M. Cossi, “Quantum Calculation of Molecular Energies and Energy Gradients in Solution by a Conductor Solvent Model,” J. Phys. Chem. A, vol. 102, no. 11, pp. 1995–2001, 1998.

[126] A. Klamt, C. Moya, and J. Palomar, “A Comprehensive Comparison of the IEFPCM and SS(V)PE Continuum Solvation Methods with the COSMO Approach,” Journal of Chemical Theory and Computation, vol. 11, no. 9, pp. 4220–4225, 2015. PMID: 26575917.

[127] C. A. Guido, D. Jacquemin, C. Adamo, and B. Mennucci, “Electronic Excitations in Solution: The Interplay between State Specific Approaches and a Time-Dependent Density Functional Theory Description,” Journal of Chemical Theory and Computation, vol. 11, no. 12, pp. 5782–5790, 2015. PMID: 26642990.

[128] M. Caricato, B. Mennucci, J. Tomasi, F. Ingrosso, R. Cammi, S. Corni, and G. Scalmani, “Formation and relaxation of excited states in solution: A new time dependent polarizable continuum model based on time dependent density functional theory,” J. Chem. Phys., vol. 124, no. 12, p. 124520, 2006.

[129] A. Steffen and B. Hupp, “Design of Efficient Emissive Materials,” in Comprehensive Coordination Chemistry III (E. C. Constable, G. Parkin, and L. Que Jr, eds.), pp. 466–502, Oxford: Elsevier, 2021.

[130] Y.-J. Gao, W.-K. Chen, Z.-R. Wang, W.-H. Fang, and G. Cui, “QM and ONIOM studies on thermally activated delayed fluorescence of copper(i) complexes in gas phase, solution, and crystal,” Phys. Chem. Chem. Phys., vol. 20, pp. 24955–24967, 2018.

[131] L. Bergmann, New Emitters for OLEDs: The Coordination- and Photo-Chemistry of Mononuclear Beiträge zur Organischen Synthese, Logos Verlag Berlin, 2016.

[132] D. R. McMillin, J. R. Kirchhoff, and K. V. Goodwin, “Exciplex quenching of photo-excitd copper complexes,” Coord. Chem. Rev., vol. 64, pp. 83 – 92, 1985.

[133] S. Lin, Q. Peng, Q. Ou, and Z. Shuai, “Strong Solid-State Fluorescence Induced by Restriction of the Coordinate Bond Bending in Two-Coordinate Copper(I)–Carbene Complexes,” Inorg. Chem., vol. 58, pp. 14403–14409, 2019.

[134] J. Burt and G. Crosby, “Barriers to energy migration in mixed-ligand zinc(II) complexes,” Chem. Phys. Letters, vol. 220, no. 6, pp. 493 – 496, 1994.

[135] N. Lüdtke, J. Kuhnt, T. Heil, A. Steffen, and C. M. Marian, “Revisiting LLCT phosphorescence emission from zinc(II) diimine bis-thiolate complexes: It’s actually TADF,” ChemPhotoChem, vol. under revision, 2022.

[136] T. L. Cremers, D. R. Bloomquist, R. D. Willett, and G. Crosby, “Structure of (1,10-phenanthroline)bis(4-toluenethiolato)zinc(II),” Acta Cryst., vol. B36, pp. 3097–3099, 1980.

[137] T.-W. Ngan, C.-C. Ko, N. Zhu, and V. W.-W. Yam, “Syntheses, Luminescence Switching, and Electrochemical Studies of Photochromic Dithienyl-1,10-phenanthroline Zinc(II) Bis(thiolate) Complexes,” Inorg. Chem., vol. 46, pp. 1144–1152, 2007.

[138] F. Becker, “Quantenchemische Untersuchung zur dualen Lumineszenz von Zink(II)-Diimin-bis-Thiolat-Komplexen.” Bachelor’s thesis, Heinrich-Heine Universität, Düsseldorf, 2020.

[139] O. Mrózek, M. Mitra, B. Hupp, A. Belyaev, N. Lüdtke, D. Wagner, C. Wang, O. S. Wenger, C. M. Marian, and A. Steffen, “An Air- and Moisture-stable Zinc(II) Carbene Dithiolate Dimer Showing Fast TADF and Dexter Energy Transfer Catalysis.,” Manuscript submitted for publication, 2022.

[140] Y. Acar, “Quantenchemische Untersuchung der photophysikalischen Eigenschaften von Terephthalnitril-basierten Donor-Akzeptor-Fluorophoren,” Master’s thesis, Heinrich-Heine Universität, Düsseldorf, 2017.

[141] J.-M. Mewes, J. M. Herbert, and A. Dreuw, “On the accuracy of the general, state-specific polarizable-continuum model for the description of correlated ground- and excited states in solution,” Phys. Chem. Chem. Phys., vol. 19, pp. 1644–1654, 2017.

[142] J. Föller and C. M. Marian, “Rotationally Assisted Spin-State Inversion in Carbene–Metal–Amides Is an Artifact,” J. Phys. Chem. Lett., vol. 8, no. 22, pp. 5643–5647, 2017.

A. Appendices

Paper I

PCCP

ROYAL SOCIETY OF CHEMISTRY

PAPER

View Article Online
View Journal | View Issue

Check for updates

Cite this: *Phys. Chem. Chem. Phys.*, 2020, **22**, 23530

Understanding the luminescence properties of Cu(I) complexes: a quantum chemical perusal†

Nora Lüdtke, Jelena Föller and Christel M. Marian *

Electronic structures and excited-state properties of Cu(I) complexes with varying coordination numbers have been investigated by means of advanced quantum chemical methods. The computational protocol employs density functional-based methods for geometry optimizations and vibrational analyses including solvent effects through continuum models. Excitation energies, spin–orbit couplings and luminescence properties are evaluated using multireference configuration interaction methods. Rate constants of spin-allowed and spin-forbidden transitions have been determined according to the Fermi golden rule. The computational results for the 4-coordinate (DPEPhos)Cu(PyrTet), the 3-coordinate $[\mathrm{IPr{-}Cu{-}Py_2}]^+$, and the linear $\mathrm{CAAC^{Me_2}{-}Cu{-}Cl}$ complexes agree well with experimental absorption and emission wavelengths, intersystem crossing (ISC) time constants, and radiative lifetimes in liquid solution. Spectral shifts on the ligand-to-ligand charge transfer (LLCT) and metal-to-ligand charge transfer (MLCT) transitions caused by the polarity of the environment are well represented by the continuum models whereas the shifts caused by pseudo-Jahn–Teller distortions in the MLCT states are too pronounced in comparison to solid-state data. Systematic variation of the ligands in linear Cu(I) carbene complexes shows that only those complexes with S_1 and T_1 states of LLCT character possess sufficiently small singlet–triplet energy gaps ΔE_{ST} to enable thermally activated delayed fluorescence (TADF). Complexes whose S_1 and T_1 wavefunctions are dominated by MLCT excitations tend to emit phosphorescence instead. Unlike the situation in metal-free TADF emitters, the presence of low-lying locally excited triplet states does not promote ISC. These states rather hold the danger of trapping the excitation with non-radiative deactivation being the major deactivation channel.

Received 3rd September 2020,
Accepted 16th September 2020

DOI: 10.1039/d0cp04654j

rsc.li/pccp

1 Introduction

Thermally activated delayed fluorescence (TADF) is looked upon as a significant emerging technology for generating highly performant electroluminescent devices for displays and lighting systems.[1–6] Many TADF-based organic light emitting diodes (OLEDs) have high internal quantum efficiencies (IQEs), but the limited operational stability of the OLED devices still represents a problem. Ideally, thermally stable dyes with a small singlet–triplet energy gap, substantial S_1–T_1 intersystem crossing (ISC) and T_1–S_1 reverse intersystem crossing (rISC), high fluorescence but minimal nonradiative decay to the electronic ground state are required. These conditions are not easily met simultaneously and often compromises have to be sought. The interplay of all the factors influencing the probability of TADF is not yet fully understood and needs further investigation. It seems to be clear, however, that a small singlet–triplet energy gap alone is not sufficient for enabling efficient TADF.

The energy difference between a singlet and triplet-coupled open-shell configuration depends on the exchange interaction of the unpaired electrons. This interaction is small when the density distributions of the orbitals involved in the excitation do not overlap substantially. Typically, this requirement is fulfilled by charge-transfer (CT) states where the unpaired electrons are far apart. Unfortunately, the overlap of orbital densities in the initial and final states plays a decisive role for the magnitude of the fluorescence rate and electronic spin–orbit coupling (SOC) as well. Electronic SOC is a fairly short-ranged interaction and SOC matrix elements (SOCMEs) between singlet and triplet configurations with equal occupation of the spatial orbitals vanish for symmetry reasons.[7] As a consequence, configuration interaction with locally excited states and/or vibronic couplings is required to enhance the ISC and rISC processes in metal-free donor–acceptor complexes.[8–12] Owing to the near-degeneracy of d orbitals with different magnetic moments, the situation is more favorable in transition metal complexes with metal-to-ligand charge-transfer (MLCT) excited states in addition to ligand-to-ligand charge-transfer (LLCT) states, provided that the emitting

---

Institute of Theoretical and Computational Chemistry, Heinrich-Heine-University Düsseldorf, Universitätsstr. 1, 40225 Düsseldorf, Germany.
E-mail: Christel.Marian@hhu.de; Fax: +49 211 8113466; Tel: +49 211 8113209

† Electronic supplementary information (ESI) available: Selected geometry parameters of ground and excited states, additional difference densities, energies, and calculated spectra of individual conformers. See DOI: 10.1039/d0cp04654j

state is not deactivated by predissociation through a metal-centered (MC) ligand-field state or trapped in a ligand-centered (LC) triplet state.[13] The presence of low-lying MC states can be avoided in organometallic complexes based on d^{10} metal ions such as Cu(I), Ag(I), Au(I) or even Zn(II).[6,14–22]

Cu(I) complexes currently constitute the largest class of luminescent transition metal compounds based on a relatively earth-abundant element. Most of the investigated complexes are trigonally or tetragonally coordinated compounds while the number of luminescent linear two-coordinate copper compounds is still small.[6] Owing to a pseudo-Jahn–Teller (PJT) distortion in the MLCT-excited d^9 state, 4-coordinate Cu(N^N)$_2$ complexes undergo a fast flattening structural change upon photo excitation.[23–27] The higher rigidity of Cu(N^N)(P^P) complexes leads to a reduction of nonradiative deactivation and thus an increase of emission quantum yield.[28] Several mononuclear 4-coordinate[28–35] bis-phosphine Cu (I) complexes were reported to show TADF. In 3-coordinate Cu(I) complexes with a sterically demanding monodentate N-heterocyclic carbene (NHC) ligand and a heterocyclic bidentate (N^N) ligand, the relative orientation of the ligands, in particular their interplanar angle, seems to decide whether TADF or phosphorescence is observed.[36–39] In addition, PJT distortion leads to a T-shaped coordination environment of the Cu center in liquid solution.[36,40] Conformational flexibility in these 3-coordinate complexes is also the key to understanding the photophysical properties of three-coordinated thiolate Cu(I) complexes that give bright blue emission at 77 K and orange emission at ambient temperature.[41] To stabilize the under-coordinated linear complexes, they mostly bear sterically demanding carbene ligands.[19,21,42–51] Many of these complexes are strongly phosphorescent with microsecond lifetimes typical of platinum or iridium complexes.[42,44,45,47,48,51] Their high ISC and phosphorescence rate constants have been traced back to the presence of low-lying MLCT states with d_π-type holes in the copper 3d shell in addition to the typical $d_\sigma \rightarrow \pi^*_{\mathrm{NHC}}$ MLCT excitation forming the T_1 state. While large SOCMEs between the two types of MLCT excitations lead to strong multiplicity mixing, configuration interaction with close-by LC states lends intensity to the phosphorescence emission.[49,52] PJT interactions in the MLCT excited states manifest themselves in large-amplitude bending distortions.[53] Therefore, although photoluminescence quantum yields (PLQYs) of copper complexes can be high in the solid state, the efficiency markedly decreases in fluid solution.[54] Of particular interest in OLED research are the TADF emitting species. Among the linearly coordinated coinage metal complexes, several carbene metal amides (CMAs) with electrophilic carbenes as acceptors and electron-rich amides as strong electron donors have been shown to be efficient TADF emitters in the solid state.[19–21,49–51]

Most experimental studies of these compounds are accompanied by Kohn–Sham density functional theory (DFT) calculations that focus on the nature of the highest occupied molecular orbital (HOMO) and the lowest unoccupied molecular orbital (LUMO). This bears some danger because the lowest electronically excited state does not necessarily originate from a HOMO–LUMO transition. Proceeding with due caution to avoid an unbalanced description of CT and LC states, it is preferable to use time-dependent density functional theory (TDDFT) or – even better – approximate coupled-cluster or multi-reference configuration interaction (MRCI) methods to characterize the excited states. In several cases, TDDFT has been employed to determine singlet–triplet energy gaps ΔE_{ST} of Cu(I) complexes and other spectral properties. Our group uses the combined DFT/MRCI approach[55,56] for computing excitation energies and excited-state properties in conjunction with geometries and vibrational frequencies from TDDFT calculations.

Quantum chemical studies that explicitly take account of SOC for determining ISC and rISC in Cu(I) complexes are scarce. In addition to a series of papers studying the emission properties of Cu(I)-bis-phenanthroline complexes,[25–27] Penfold and coworkers very recently performed quantum dynamics simulations within the framework of the multi-configuration time-dependent Hartree method to study the evolution of excited-state populations upon torsional motion of linear CMAs.[57–59] In the latter works, SOCMEs were calculated at the TDDFT level using the approach of Wang and Ziegler[60] and ISC rate constants were obtained by fitting the population decay of S_1 to an exponential function. ISC constants based on Fermi's golden rule approach were presented for linear copper carbene halogenide complexes by Lin *et al.*,[61] but the authors did not explicitly state how SOC was computed. They used TDDFT in combination with point charges from self-consistent reaction field calculations to model a liquid solvent environment and combined quantum mechanical/molecular mechanical (QM/MM) methods to mimic the crystalline state. Similar approaches were chosen by other authors to investigate the photophysics of mixed four-coordinate copper phosphine complexes.[62–64] Earlier work on spin-forbbidden radiative and non-radiative transitions of electronically excited Cu(I) complexes in our group uses a static approach for determining rate constants as well, but employs DFT/MRCI wavefunctions in conjunction with an effective spin–orbit core potential on the metal atom and an atomic spin–orbit mean field approximation on the other centers for computing the electronic SOCMEs.[21,40,52,65,66] Phosphorescence rate constants are obtained by including electron correlation and SOC on the same footing in a variational approach, the multireference spin–orbit configuration interaction (DFT/MRSOCI) method.[67]

To validate our theoretical methods for computing r(ISC) and radiative rate constants in Cu(I)-based TADF compounds, we will first investigate a complex with experimentally known kinetics of the excited-state processes. Such a complex is (DPEPhos)Cu(PyrTet) (Fig. 1) which stands for [(bis(2-(diphenylphosphino)phenyl)ether) Cu(5-(2-pyridyl)tetrazolate)]. It represents an important class of neutral, mononuclear metal complexes that show TADF.[35] The temporal evolution of its excited-state populations following photoexcitation has been determined experimentally both in the solid state[35] and in liquid solution.[68] For comparison, the results of extensive TDDFT studies are available as well.[63] We will then move on to the three-coordinate complex [IPr–Cu–Py$_2$]$^+$ (Fig. 1) which has been shown to emit phosphorescence in the solid state and in solution.[66] Finally, we investigate the influence of the ligands on the energy profiles of linear copper carbene complexes, some of which were shown to have excellent TADF performance in the solid state[19–21,49,50,54] while others are phosphorescent[42,44,45] or non-emissive.[66]

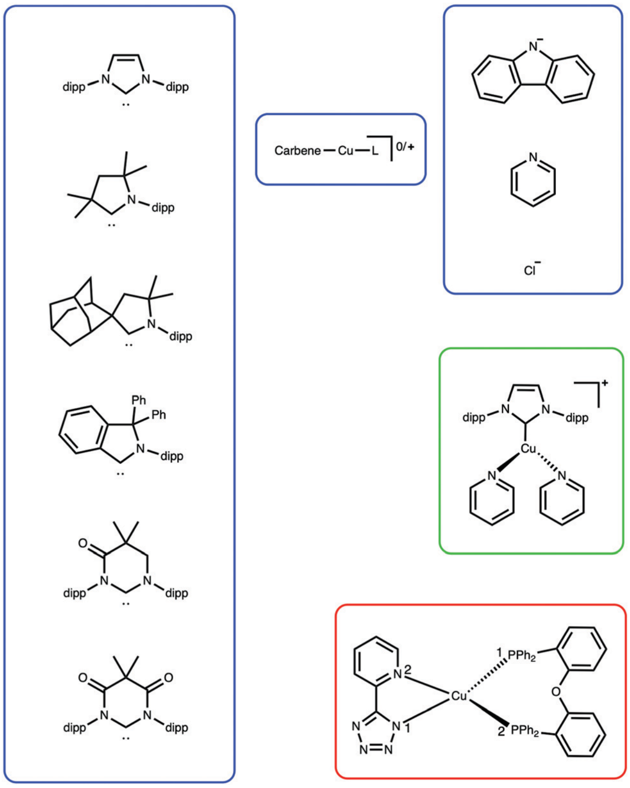

Fig. 1 Chemical structures of the Cu(I) complexes investigated in this work: the four-coordinate (DPEPhos)Cu(PyrTet) complex (red frame), the cationic three-coordinate [IPr–Cu–Py$_2$]$^+$ complex (green frame) and several linear two-coordinate carbene complexes (blue frame). The carbene ligands are denominated (from top to bottom): IPr, CAAC$^{\text{Me}_2}$, CAAC$^{\text{Ad}}$, CAArC, MAC, and DAC. Ph represents a phenyl residue and dipp stands for 2,6-diisopropylphenyl.

2 Methods and computational details

Throughout, the cc-pVDZ-PP basis set was used for the Cu atom in conjunction with the Stuttgart-Koln multi-configuration Dirac–Fock scalar relativistic effective core potential (ECP).[69,70] For the other atoms, the def-SV(P) basis set of the Turbomole library[71] was chosen. The ground-state geometries of the isolated Cu complexes were optimized with the DFT package of Turbomole[72,73] and used subsequently as starting points for optimizing the excited states with the corresponding TDDFT module.[74] Full linear response equations were solved for excited singlet states whereas the Tamm–Dancoff approximation (TDA)[75] was employed for the geometry optimization of the triplet states to avoid triplet instabilities. Unless noted otherwise, the hybrid density functional PBE0[76,77] was chosen in the optimization step. Vibrational frequency analyses of the ground and excited states were performed using either numerical (SNF[78]) or analytical second derivatives (Gaussian 16[79]).

Implicit solvent models for absorption properties and solid-state emission comprised the conductor-like screening model (COSMO)[80] and the polarizable continuum model (PCM).[81] In order to describe emission properties in liquid solution, the corrected linear response approach (cLR)[82] was chosen which takes account of solvent relaxation in the excited state. In our case, the point charges of the solvent, completely adapted to the excited state of the solute, were used. The PCM and cLR point charges were determined at the TDDFT level using Gaussian 16[79] and then imported to Turbomole to enable their use in subsequent DFT/MRCI calculations.

Electronic excitation energies and oscillator strengths of the spin-allowed transitions were calculated using the DFT/MRCI method[55,56] employing the redesigned R2016[83] or R2018 Hamiltonians[84] that are particularly well suited for multichromophore systems. DFT/MRCI is a semi-empirical multireference configuration interaction ansatz based on Kohn–Sham orbitals and orbital energies of a closed-shell BH-LYP functional[85,86] determinant. For the construction of the two-electron integrals, the auxiliary basis sets from the Turbomole library[87] were used in the resolution-of-the-identity approximation. With the computational details concerning the DFT/MRCI parameter set, the selection thresholds for including configuration in the variational space and the number of roots determined in the Davidson diagonalization procedure for each molecule can be found in the ESI.† Unless noted otherwise, line spectra were broadened with Gaussian functions of 1800 cm^{-1} full width at half maximum (FWHM).

Electronic spin–orbit coupling matrix elements (SOCMEs) were obtained with the SPOCK program.[88,89] The effective one-electron Hamiltonian comprised a relativistic SO-ECP[70] on copper and an atomic mean-field approximation of the Breit–Pauli spin–orbit operator[90,91] on all other centers. Rate constants for ISC and rISC were calculated perturbationally according to the Fermis golden rule and in Condon approximation assuming a Boltzmann population of the vibrational levels in the initial state. Furthermore, it is supposed that the rate constants are additive in the $S_1 \rightsquigarrow T_1$ case (ISC) and that they can be averaged over all triplet sublevels in the $T_1 \rightsquigarrow S_1$ case (rISC).

$$k_{(\mathrm{r})\mathrm{ISC}} = \frac{2\pi}{\hbar Z g}\left|\left\langle {}^3\phi_{\mathrm{a}}^{(0)}\middle|\hat{\mathscr{H}}_{\mathrm{SO}}\middle|{}^1\phi_{\mathrm{b}}^{(0)}\right\rangle\right|^2 \times \sum_{j,k} \mathrm{e}^{-\left(E_{\mathrm{b}j}-E_{\mathrm{b}0}\right)/k_{\mathrm{B}}T}\left|\left\langle \nu_{\mathrm{a}k}|\nu_{\mathrm{b}j}\right\rangle\right|^2\delta\left(E_{\mathrm{b}j}-E_{\mathrm{a}k}\right) \tag{1}$$

Herein, Z is the partition function of all vibrations of the initial electronic state

$$Z = \sum_j \mathrm{e}^{-\left(E_{\mathrm{b}j}-E_{\mathrm{b}0}\right)/k_{\mathrm{B}}T} \tag{2}$$

and g is its spin multiplicity. The Franck–Condon (FC) weighted density of states in expression (1) were calculated *via* a fast Fourier transformation ansatz employing the Vibes program.[92,93]

Phosphorescence lifetimes were determined variationally using the multireference spin–orbit configuration interaction (MRSOCI) method.[67] In this way, convergence problems with sum-over-states perturbation theory expressions can be avoided. Moreover, the same expressions can be used for computing fluorescence and phosphorescence probabilities.

$$k_{\mathrm{rad}} = \frac{1}{3\pi\varepsilon_0\hbar^4c^3}\left(E_{\mathrm{i}} - E_{\mathrm{f}}\right)^3\left|\langle \mathrm{f}|\vec{r}|\mathrm{i}\rangle\right|^2 \tag{3}$$

For fluorescence, $|\mathrm{i}\rangle$ is the DFT/MRCI wavefunction of the initial S_1 state, $\langle\mathrm{f}|$ is the wavefunction of the ground state and E_{i}

and E_f are the corresponding electronic energies. For phosphorescence, individual rate constants are obtained by choosing the complex-valued DFT/MRSOCI wavefunctions of the T_1 sublevels as initial states $|i\rangle$ and the spin–orbit perturbed S_0 wavefunction as the final state $\langle f|$ of the transition. While in spin-allowed transitions the length or velocity forms of the electric dipole interaction are equivalent in the limit of exact wave functions, the length form of the transition operator is the appropriate form to be used in spin-forbidden electric dipole transitions.[7] In the high-temperature limit, the individual phosphorescence rate constants can be averaged over the three triplet components as the zero-field splittings are small in comparison to room temperature (298 K). Further computational details regarding the integration schemes and damping factors for generating the FC spectra and (r)ISC rate constants may be found in the ESI.†

3 Results and discussion

3.1 The four-coordinate (DPEPhos)Cu(PyrTet) complex

Owing to its high conformational flexibiliy, several minima on the ground-state potential energy surface (PES) of (DPEPhos)-Cu(PyrTet) can be found. We report here only results that were obtained while starting the geometry optimization from the experimental crystal structure. The calculated bond distances and bond angles of the isolated complex agree well with the crystal structure (for details, see the ESI†). Test calculations with different DFT/MRCI Hamiltonians and configuration selection thresholds revealed only minor differences between the two computed absorption profiles. Both spectra are in good agreement with the experimental absorption spectra recorded for a neat film[35] or in dichloromethane (DCM) solution[34] at room temperature. In agreement with the experimental observations[68] and the results of a recent theoretical study,[63] the inclusion of a DCM environment by means of an implicit solvent model leads to a small blue shift of the absorption band only while preserving its shape (Fig. 2).

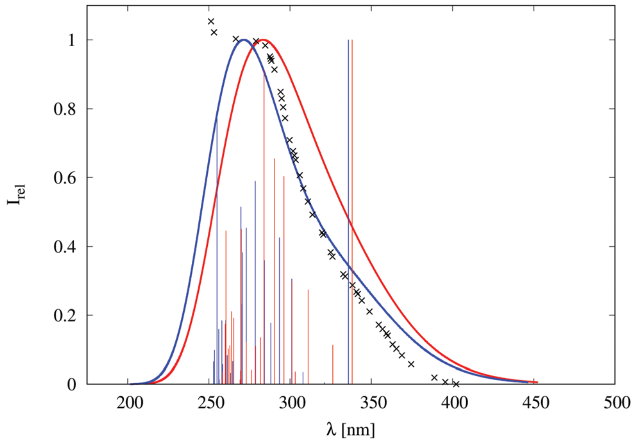

Fig. 2 Calculated absorption spectra in a vacuum (red) and in DCM (blue) of the (DPEPhos)Cu(PyrTet) complex with the R2018 Hamiltonian in comparison to the experimental spectrum in DCM (black).[34] The line spectra were broadened by a Gaussian function with 2700 cm^{-1} FWHM.

Table 1 DFT/MRCI absorption wavelength λ [nm] and state characteristics of (DPEPhos)Cu(PyrTet) in comparison with the literature results

State	Character	λ	Remarks
S_1	MLCT/PLCT/ILCT	341	DFT/MRCI, vacuum
S_6	ILCT/PLCT/MLCT	296	DFT/MRCI, vacuum
S_7	LLCT/PLCT/MLCT	290	DFT/MRCI, vacuum
S_8	ILCT/PLCT/MLCT	284	DFT/MRCI, vacuum
S_{25}	MLCT/ILCT/LLCT	256	DFT/MRCI, vacuum
S_{28}	MLCT/ILCT/LLCT	251	DFT/MRCI, vacuum
(sh)	MLCT	341	Exp., RT, DCM[34]
(sh)	LC	280	Exp., RT, DCM[34]
(max)	LC	265	Exp., RT, DCM[34]

Henceforth, all excited-state calculations on the (DPEPhos)Cu-(PyrTet) complex were performed with the R2018 Hamiltonian[84] and a tight selection threshold in a vacuum (Table 1).

In all strong transitions, intra-ligand charge-transfer (ILCT) excitations on the PyrTet ligand are involved. We also notice major contributions from PLCT excitations, shifting electronic charge from the phosphorous centers to the PyrTet ligand, in the low-energy regime (Fig. 3).

In this complex, the pronounced spectral shift of the emission maximum in a liquid solution as compared to the solid state (Table 2) is not caused by electrostatic effects. The vertical emission wavelength obtained for the S_1 state of the isolated complex agrees well with the experimental emission maxima in DCM (λ_{max} = 610 nm) and even the much more polar acetonitrile (λ_{max} = 610 nm). It is rather the reduced flexibility of the copper coordination environment in the solid state that impedes the large-amplitude flattening distortion causing changes in the N–N–P–P dihedral angles of up to roughly 30° in the S_1 and T_1 states (Table 3). This conclusion was also drawn by Gao *et al.*[63] who mimicked the crystal environment

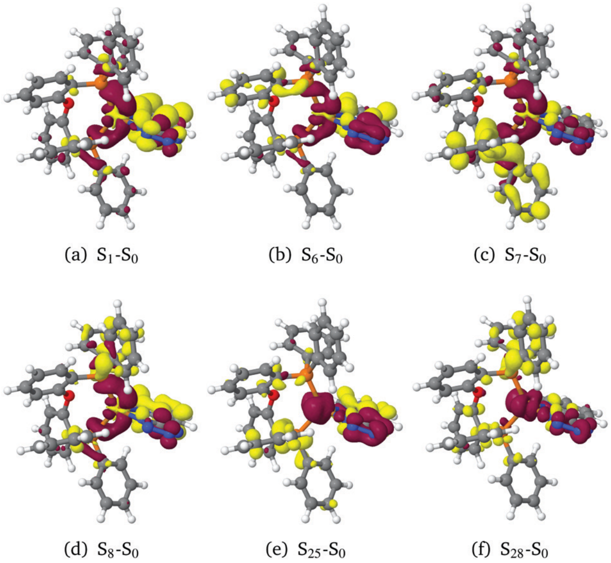

(a) S_1-S_0 (b) S_6-S_0 (c) S_7-S_0

(d) S_8-S_0 (e) S_{25}-S_0 (f) S_{28}-S_0

Fig. 3 DFT/MRCI difference densities (±0.001) of the most intensive absorption transitions in the (DPEPhos)Cu(PyrTet) complex at the ground state geometry in a vacuum. Areas losing electron density during excitation are shown in red, and areas gaining electron density are shown in yellow.

Table 2 DFT/MRCI excited-state properties of (DPEPhos)Cu(PyrTet) in comparison with the literature results: emission maxima $\lambda_{\max}$ [nm] of photoluminescence (PL), averaged radiative lifetimes $\tau_{\rm rad}$ [µs], rate constants [s^{-1}] of ISC (S_1) and rISC (T_1)

	$t_{\rm rad}$	$\lambda_{\max}$	$k_{\rm ISC}/k_{\rm rISC}$	Remarks
S_1	0.5	608	3.4×10^{10}	DFT/MRCI, 298 K, vacuum
T_1	739	617	2.5×10^{7}	DFT/MRCI, 298 K, vacuum
PL	19.9	510		Exp., 293 K, powder[34]
PL	111.5	549		Exp., 77 K, powder[34]
PL	11.5	535	3.7×10^{10}	Exp., 293 K, neat film[35]
PL	—	610	2.3×10^{10}	Exp., RT, DCM[68]
S_1	0.7	579	8.0×10^{9}	TD-B3LYP, 300 K, vacuum[63]
T_1	290	605	8.4×10^{5}	TD-B3LYP, 300 K, vacuum[63]
S_1	0.3	571	9.9×10^{9}	TD-B3LYP, 300 K, THF[63]
T_1	401	599	1.9×10^{6}	TD-B3LYP, 300 K, THF[63]
S_1	0.6	544	1.3×10^{9}	TD-B3LYP, 300 K, crystal[63]
T_1	222	564	2.1×10^{5}	TD-B3LYP, 300 K, crystal[63]

Table 3 NNPP dihedral angles of the (DPEPhos)Cu(PyrTet) complex and the crystal structure in comparison to the optimized geometries in a vacuum

Dihedral angle	Crystal structure	S_0	S_1	T_1
N1–N2–P1–P2	−70.6	−70.9	−47.5	−49.9
N1–N2–P2–P1	79.5	78.4	107.2	103.3
N2–N1–P2–P1	−72.8	−75.3	−51.3	−54.7
N2–N1–P1–P2	81.4	79.9	112.2	108.0

using a molecular mechanics force field interacting with the quantum mechanically treated complex.

Bergmann *et al.* were able to temporally resolve the ISC process in the solid state (neat film) for which they determined a rate constant of 3.7×10^{10} s^{-1}, corresponding to a time constant of 27 ps. A global analysis of recent ultrafast UV/Vis- and mid-IR spectroscopy on (DPEPhos)Cu(PyrTet) in the liquid DCM solution obtains an ISC time constant of 43 ± 6 ps,[68] corresponding to a rate constant (2.3×10^{10} s^{-1}) of comparable magnitude as in the solid state. Our computed ISC rate constant of 3.4×10^{10} s^{-1} matches these experimental values very well. With regard to the luminescence decay, Bergmann *et al.* concluded that all subsequent emission is delayed fluorescence at room temperature (RT) with an overall photoluminescence lifetime of 11.5 µs in the neat film and 19.9 µs in powder.[34,35] The results of our calculations support the conclusion that ISC is much faster than prompt fluorescence ($k_F = 1.9 \times 10^6$ s^{-1}) which will therefore be quenched and is not observable. The rate-determining step of the luminescence is reverse ISC instead. Our calculations yield a rate constant of $k_{\rm rISC} = 2.5 \times 10^7$ s^{-1} at RT in Condon approximation, in qualitative agreement with the experimentally based estimation[94] that the rISC rate constant is smaller than 5×10^8 s^{-1}. Phosphorescence is not observed experimentally, and even the much longer radiative decay time of 111.5 µs at 77 K is presumably a consequence of the slower rISC and nonradiative decay processes at these temperatures. According to our calculations, only one of the three triplet sublevels is capable of emitting phosphorescence at a reasonable time scale of about 260 µs. The value of 739 µs, listed in Table 2, results from averaging over all three triplet sublevels.

3.2 Trigonal *vs.* linear NHC–Cu(I)–pyridine complexes

Linear cationic IPr–Cu(I)–pyridine complexes, where IPr stands for 1,3-bis(2,6-diisopropylphenyl)imidazol-2-ylidene, were shown to be nonemissive at room temperature due to the presence of low-lying dark ^{3}LC states which represent the global minima on the T_1 potential energy surface.[52,66] The results of quantum chemical calculations on related compounds suggest that the quenching of luminescence can be suppressed by employing adamantyl or other alkyl substituents instead of diisopropyl (dipp) residues on the NHC.[52] Alternatively, the ^{3}MLCT transitions could be lowered in energy by introducing –I/–M substituents to the pyridine ligand.

Crystals of $[\text{IPr–Cu–Py}]^+BF_4^-$ show mechanochromism, *i.e.*, optically dark crystals start to emit sky blue luminescence upon mechanical grinding. This mechanical response was interpreted in terms of coordinative Cu–F bond formations between the under-coordinated Cu atom of the linear $[\text{IPr–Cu–Py}]^+$ cation and one or two fluorine atoms of the BF_4^- counterion. In addition to the nonluminescent linear mono-pyridine complexes, brightly luminescing trigonal bis-pyridine complexes, $[\text{IPr–Cu–Py}_2]^+BF_4^-$, can be crystallized from the tetrahydrofuran (THF) solution.[66] Here, the different behaviors of the linear and the trigonal complexes will be exemplified and explained on the basis of computational studies on the trigonal bis-pyridine complex. Test calculations (see the ESI†) revealed a minimal effect of a polar environment on the spectral properties of these complexes. Therefore, all calculations in this section were carried out for the isolated cationic complexes.

3.2.1 Ground-state geometry. The S_1 state of the linear $[\text{IPr–Cu–Py}]^+$ originates from a $d_{z^2} \rightarrow \pi^*_{\rm Py}$ MLCT excitation (the axis designation was chosen assuming that the $C_{\rm NHC}$–Cu–Py bonds lie on the *z*-axis and the *y*-axis is perpendicular to the pyridine plane). In the isolated complex, the imidazol ylidene and pyridine rings are co-planar whereas they adopt a twist angle of *ca.* 70° in the crystal due to packing effects.[52,66] While this conformational change has a large impact on the absorption wavelengths of the higher-lying singlet states (*vide infra*), the $S_1 \leftarrow S_0$ transition is nearly unaffected by the ligand twist. Four triplet states are found to lie energetically below S_1 in the DFT/MRCI calculations at the co-planar ground-state minimum in a vacuum (Table 4): T_1 and T_2 are ππ* ^{3}LC states localized on

Table 4 Vertical DFT/MRCI energies [eV] and characterization of the lowest-lying singlet and triplet states of the isolated cationic $[\text{IPr–Cu–Py}]^+$ and $[\text{IPr–Cu–Py}_2]^+$ complexes in the Franck–Condon region

	$[\text{IPr–Cu–Py}]^+$		$[\text{IPr–Cu–Py}_2]^+$	
State	Excitation	Energy	Excitation	Energy
S_1	$d_{z^2} \rightarrow \pi^*_{\rm Py}$	4.10	$d_{xz} \rightarrow \pi^*_{\rm Py}$	3.93
S_2	$\pi_{\rm dipp} \rightarrow \pi^*_{\rm dipp}$	4.55	$d_{xz} \rightarrow \pi^{*\prime}_{\rm Py}$	4.04
S_3	$\pi_{\rm dipp} \rightarrow \pi^*_{\rm dipp}$	4.56	$d_{z^2} \rightarrow \pi^*_{\rm Py}$	4.19
T_1	$\pi_{\rm dipp} \rightarrow \pi^*_{\rm dipp}$	3.74	$\pi_{\rm dipp}/d_{xz} \rightarrow \pi^*_{\rm dipp}$	3.76
T_2	$\pi_{\rm dipp} \rightarrow \pi^*_{\rm dipp}$	3.74	$\pi_{\rm dipp}/d_{xz} \rightarrow \pi^*_{\rm dipp}$	3.76
T_3	$d_{z^2} \rightarrow \pi^*_{\rm NHC}$	3.93	$d_{xz} \rightarrow \pi^*_{\rm Py}$	3.77
T_4	$d_{yz}/\pi_{\rm Py} \rightarrow \pi^*_{\rm Py}$ $\pi_{\rm NHC} \rightarrow \pi^*_{\rm NHC}$	4.07	$d_{z^2} \rightarrow \pi^*_{\rm Py}/\pi^*_{\rm NHC}$	3.87
T_5	$\pi_{\rm Py} \rightarrow \pi^*_{\rm Py}$	4.17	$d_{xz}/\pi_{\rm NHC} \rightarrow \pi^{*\prime}_{\rm Py}$	3.88

the dipp rings, T_3 has an electronic structure corresponding to S_1, and T_4 may be characterized as a ^{3}MLCT/LC state involving a $d_{yz} \rightarrow \pi^*_{Py}$ transition mixed with local excitations on the carbene and the pyridine rings.

Coordination of a second pyridine ligand to the metal center leads to a C_2-symmetric structure in the electronic ground state in which the pyridine and imidazol ylidene rings are no longer co-planar. S_1 and S_2 have MLCT character with electron density being transferred from a d_{xz}-like orbital (here, the Cu–C bond lies on the z-axis while x and z span the N_{Py1}–Cu–N_{Py2} plane) to π^* orbitals on both pyridine ligands (Fig. 4). The d_{z^2} like-orbital is involved in the S_3 MLCT excitation. Five triplet states are located below S_1 in the FC region (Table 4): T_1–T_3 states are practically isoenergetic here. The T_1 and T_2 states exhibit mixed LC/MLCT character, with the accepting orbitals being localized mainly on the dipp substituents. The T_3 state corresponds to the S_1 state. The T_4 state is also a MLCT state, but in this case the metal d contributions come from a d_{z^2}-like orbital. The electronic structure of the T_5 state resembles the one of S_2 with some additional $\pi_{NHC} \rightarrow \pi^*_{Py}$ CT contributions. The first bright singlet is S_3 at 296 nm for which the electronic structure resembles that of the T_4 state. The largest oscillator strength was calculated for the S_{12}, which lies at 252 nm and is dominated by local Cu(d_π) to Cu($4p_\pi$) with some additional CT character.

It is interesting to compare the calculated absorption spectra of the mono- and bis-pyridine complexes with experimental absorption spectra obtained when dissolving crystalline $[IPr–Cu–Py_2]^+BF_4^-$ and $[IPr–Cu–Py]^+BF_4^-$, respectively, in DCM (Fig. 5). The two experimental spectra are hardly distinguishable, presumably due to the loss of one of the pyridine ligands.[66] In addition to the absorption spectra computed for the geometry relaxed ground states, a line spectrum of the mono-pyridine complex is shown in which the interligand torsional angle has been fixed to 70°, the angle adopted in the crystalline state. Based on the intensities in the long wavelength regime, absorption spectra of the bis-pyridine and the twisted mono-pyridine complexes are a nearly perfect match whereas the NHC → Py LLCT excitation is markedly red shifted in the co-planar minimum conformation.

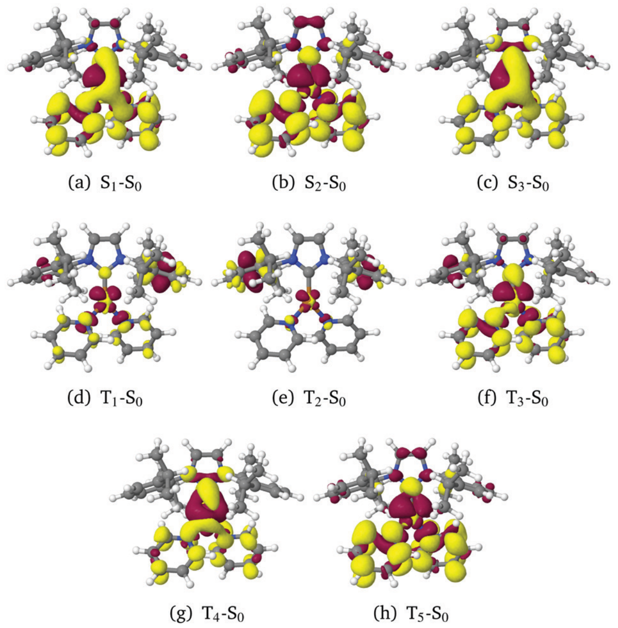

Fig. 4 DFT/MRCI difference densities of low-lying singlet and triplet states in the $[IPr–Cu–Py_2]^+BF_4^-$ complex at the ground state geometry in a vacuum. For color codes, see Fig. 3.

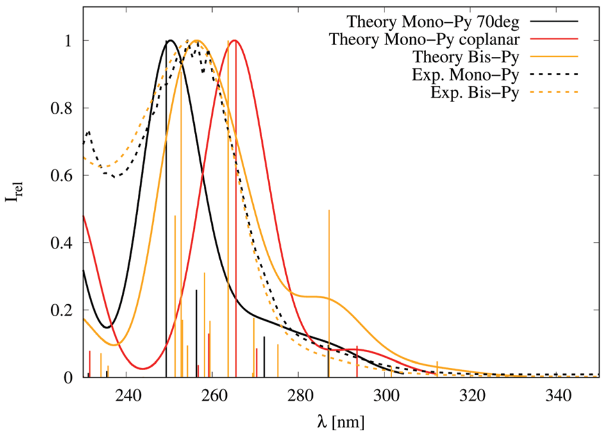

Fig. 5 Absorption spectra of $[IPr–Cu–Py_2]^+$ and $[IPr–Cu–Py]^+$ at the respective S_0 minima in comparison to the experimental absorption spectra[66] in DCM. In addition, a theoretical absorption spectrum of $[IPr–Cu–Py]^+$ is shown that was obtained by fixing the NHC–Py interplanar angle to 70°.

3.2.2 Excited-state geometries. With so many low-lying triplet states in a narrow energy range, a prediction of the states forming the lowest-lying minimum on the T_1 potential energy surface based solely on the results in the FC region is impossible. To this end, geometry optimizations of the excited states have to be performed.

In contrast to the linear Py complex, where the lowest triplet minimum corresponds to local dipp excitations, here the TDDFT optimization of the T_1 state gave a triplet minimum with mainly $d_{xz}/d_{z^2} \rightarrow \pi^*_{Py}$ character, where π^*_{Py} is localized on only one of the pyrdine ligands (E_{adia} = 3.48 eV). The optimization of the S_1 state yielded the corresponding singlet minimum (E_{adia} = 3.66 eV). At these geometries, the T_1 state is the only triplet state located energetically below the S_1 state. PJT distortion leads to an asymmetric T-shaped Cu coordination in the excited state geometries (Fig. 6): one of the C–Cu–N angles is closer to linearity than at the S_0 geometry (about 150–160° compared to 132°). The spatial symmetry of the involved d orbital is less obvious and seems to be in between d_{xz} and d_{z^2}. The T_1 and S_1 minimum nuclear arrangements differ additionally by the twist angle between the imidazol ylidene and the distal pyridine ring. At the S_1 minimum, one N_{NHC}–C_{NHC}–N_{Py}–C_{Py} dihedral angle amounts to −12° while the corresponding angle takes a value of +29° in the T_1 state. The molecular geometry has an enormous impact on the mutual T_1–S_1 SOC as exemplified by the sum over the squared SOCMEs of all cartesian components at the corresponding minimum geometries, *i.e.*, $\Sigma(\text{SOCMEs}^2)$ = 582 cm^{-2} at $S_{1,min}$, $\Sigma(\text{SOCMEs}^2)$ = 12 596 cm^{-2} at $T_{1,min}$. Although the Condon

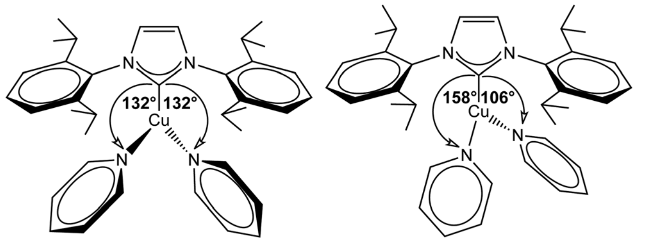

(a) S_0 state (b) S_1 state

Fig. 6 Copper coordination in the trigonal $[IPr–Cu–Py_2]^+$ complex. The PJT distortion leads to an asymmetric T-shaped structure in the excited state.

approximation is not valid under such circumstances, the computed rate constants clearly indicate that ISC ($k_{ISC}^{FC} \approx 2 \times 10^8\ s^{-1}$) dominates over fluorescence decay ($k_F^{FC} \approx 2 \times 10^6\ s^{-1}$).

The evolution of the T_1 population is not so clear-cut. The potential energy surface of the T_1 state is very shallow in the minimum region. Its energy changes by merely 0.04 eV when relaxing from the S_1 to the T_1 minimum. At the same time, the twist of the distal pyridine ring substantially increases the SOC strength and enhances the rISC probability by a factor of roughly 20 compared to the value obtained from the Boltzmann relation at the S_1 minimum. Whether TADF is possible at room temperature or not ($k_{rISC}^{FC} \approx 2 \times 10^7\ s^{-1}$ evaluated at the T_1 minimum in Condon approximation, $k_{rISC}^{FC} \approx 1 \times 10^6\ s^{-1}$ if evaluated at the S_1 minimum) will strongly depend on the ligand flexibility.

As a further complication, the T_{MLCT} minimum is not the global minimum on the T_1 potential energy surface. Optimization of the $\pi_{dipp} \rightarrow \pi^*_{dipp}$ triplet geometry succeeded when employing the BH-LYP instead of the PBE0 density functional. In the course of the optimization, the excitation localizes on one of the two dipp rings and loses the MLCT contributions found in the FC region. The adiabatic energy of the ^{3}LC state is 3.24 eV at the DFT/MRCI level of theory, that is to say, lower than that of the T_{MLCT} state with the $d_{xz} \rightarrow \pi^*$ electronic structure (3.48 eV). With a value of 1.10 eV, the vertical triplet excitation energy of the ^{3}LC state at the T_{MLCT} minimum is much higher, however, than the corresponding value of 0.38 eV in the mono-pyridine complex where a nearly barrierless path connects the two triplet minima.[52] Due to the increased reorganization energy, we do not expect fast radiationless decay to the ^{3}LC minimum to occur in the bis-pyridine complex. Nevertheless, it might be a good idea to exchange the dipp substituents of the NHC by bulky residues with higher-lying local excitations when designing Cu(I)-based luminescent pyridine complexes.

The phosphorescence rate constants of the individual triplet sublevels of the T_{MLCT} state span three orders of magnitude, varying from $3 \times 10^1\ s^{-1}$ and $3 \times 10^2\ s^{-1}$ for the degenerate $T_{1,I}$ and $T_{1,II}$ sublevels, respectively, to $5 \times 10^4\ s^{-1}$ for the upper $T_{1,III}$ level with a zero-field splitting of 9 cm^{-1}. The latter rate constant matches well with the experimental observations. The polymorphous powder emits with a maximum of 476 nm, a quantum yield of 0.76, and a bi-exponential decay with τ_1 = 16 µs (0.82) and τ_2 = 10 µs (0.18) that was interpreted as phosphorescence.[66] The calculated vertical fluorescence emission wavelength of the free complex lies at 424 nm and that of the phosphorescence at 465 nm, *i.e.*, in the violet to blue spectral range. Due to marked geometry displacements and the small 0–0 overlaps between the excited states and the ground state, the spectral FC profiles are very broad, however. Like in the tetragonal (DPEPhos)Cu(PyrTet) complex, the PJT distortion is expected to be reduced in the solid state due to steric hindrance.

3.3 Linear carbene Cu(I) complexes

In the following, we investigate the influence of the particular type of carbene on the energetic location and character of the electronically excited states of several linear carbene Cu(I) amides and halogenides. To this end, a series of carbene complexes is constructed employing a cyclic (alkyl)(amino)carbene (CAAC), a cyclic (amino)(aryl)carbene (CAArC), a monoamido-aminocarbene (MAC), and a diamidocarbene (DAC) in addition to a clasical N-heterocyclic carbene (NHC). CAACs have stronger σ-donor and π-acceptor strengths than comparable NHCs, affecting a stabilization of the carbene metal bond and a destabilization of the Cu d_σ orbital which in turn leads to a reduction of the MLCT excitation energy. CAArCs and DACs possess even higher π-accepting capacities than CAACs while maintaining their σ-donor capabilities to a large extent.[21] The electron-rich carbazolide (Cz^-) or chloride (Cl^-) anions typically act as σ- and π-donors whereas the unsubstituted neutral pyridine (Py) is a σ-donor and a weak π-acceptor. Some of these complexes were shown to have excellent TADF performance in the solid state[19–21,49,50,54] while others are phosphorescent[42,44,45] or non-emissive,[66] some just exist on paper and have been computed here to systematically investigate trends.

3.3.1 Carbene–Cu(I)–pyridine complexes. Let us begin with the cationic IPr–Cu(I)–Py complex, addressed already in Section 3.2, and substitute a CAAC^{Ad} and a DAC, respectively, for the classical NHC IPr. To our knowledge, the latter two complexes are experimentally unknown.

The π-acceptor capacities of the pyridine ligand prevail solely in the NHC complex. As may be seen from the energy profiles in Fig. 7, already CAAC^{Ad} is a stronger π-acceptor than pyridine. The MLCT($d_\sigma \rightarrow \pi^*_{CAAC}$) transition is significantly lower in energy than the corresponding transition in the NHC complex. The MLCT($d_\sigma \rightarrow \pi^*_{Py}$) excitation that had formed the S_1 state in $[Ipr–Cu(I)–Py]^+$ is blue shifted by about 0.3 eV and constitutes the S_2 state in the CAAC complex. This trend is even more pronounced in the DAC complex where the MLCT(Py) transition is not among the low-lying singlet states. In contrast to the IPr complex where the lowest-lying triplet state is a ^{3}LC excitation on the dipp, the T_1 states of the corresponding CAAC and DAC complexes have an MLCT($d_\sigma \rightarrow \pi^*_{CAAC}$) electronic structure. If the latter two complexes can be synthesized, we expect them to be phosphorescent because of the MLCT character of the S_1 and T_1 states and their substantial energy separation.

3.3.2 Carbene–Cu(I)–carbazolide complexes. The electron-rich carbazolide ligand forms highly polar CMA complexes. The inclusion of solvation effects in the quantum chemical modeling

93

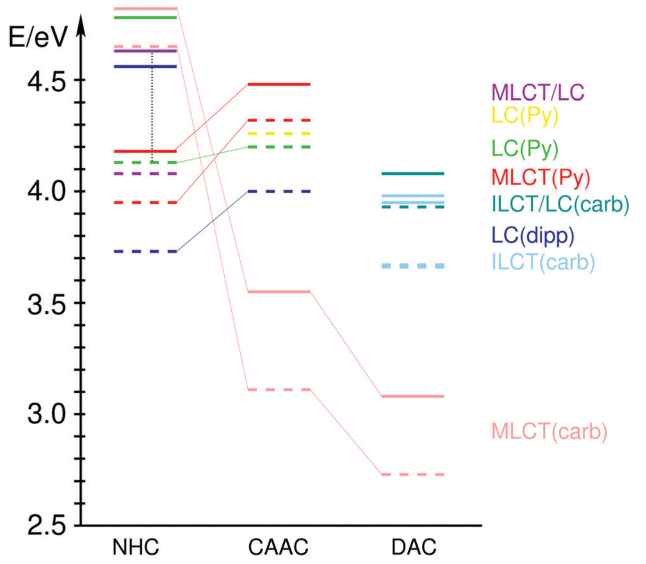

Fig. 7 Vertical excitation energies of linear carbene–Cu(I)–pyridine complexes calculated with DFT/MRCI at the respective ground-state geometries in DCM (COSMO). Solid lines represent singlet states, and dashed lines represent triplet states. The following color codes have been used: (dark blue) LC(dipp), (red) MLCT($d_\sigma \rightarrow \pi^*_{Py}$), (violet) MLCT/LC($d_\pi/\pi_{Py} \rightarrow \pi^*_{Py}$), (green) LC($\pi_{Py} \rightarrow \pi^*_{Py}$), (yellow) LC($\pi'_{Py} \rightarrow \pi^*_{Py}$), (pink) MLCT($d_\sigma \rightarrow \pi^*_{carb}$), (light blue) ILCT($\pi_{carb} \rightarrow \pi^*_{carb}$), and (cyan) ILCT/LC($\pi_{dipp}/\pi_{carb} \rightarrow \pi^*_{carb}$). Vertical dashed black lines indicate that intermediate states have been omitted.

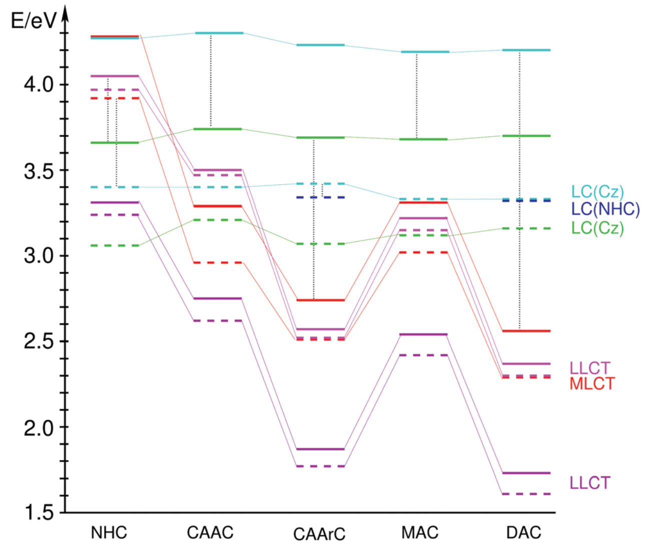

Fig. 8 Vertical excitation energies of the linear carbene copper carbazolide complexes in a vacuum calculated with DFT/MRCI at the respective ground-state geometries. Solid lines represent singlet states, dashed lines represent triplet states. The following color codes have been used: (violet) LLCT($\pi_{Cz} \rightarrow \pi^*_{carb}$), (red) MLCT($d_\sigma \rightarrow \pi^*_{carb}$), (green) LC($\pi_{Cz} \rightarrow \pi^*_{Cz}$), (magenta) LLCT($\pi'_{Cz} \rightarrow \pi^*_{carb}$), (cyan) LC($\pi'_{Cz} \rightarrow \pi^*_{Cz}$), (gold) LC($\pi''_{Cz} \rightarrow \pi^*_{Cz}$), and (dark blue) LC (carb). Vertical dashed black lines indicate that intermediate states have been omitted.

of their spectral properties is, therefore, essential. To get an idea of the environmental effects, we nevertheless first present the results of our calculations on the isolated complexes and subsequently discuss the changes brought about by the surrounding.

In the electronic ground state, the carbene and Cz ligands are oriented in co-planar fashion. In all carbene complexes studied here except for the classical NHC complex, the leading configuration of the S_1 and T_1 wave functions is an excitation from the HOMO π_{Cz} on the electron-rich Cz ligand to the LUMO comprising mainly the CN antibonding π^*_{carb} orbital of the carbene ligand. In addition to this LLCT excitation, some MLCT($d_\pi \rightarrow \pi^*_{carb}$) contributions to the S_1 and T_1 wave functions can be made out. The latter are particularly important with regard to the ability of the carbene–Cu–Cz complexes to undergo efficient ISC and rISC (*vide infra*). As noted already by Hamze *et al.*,[49] the $S_1 \leftarrow S_0$ transition is remarkably bright considering its LLCT character and the small overlap of the HOMO and LUMO density distributions. Variation of the carbene ligand leads to the expected trends on the LLCT states. The higher π-acceptor capabilities of the CAAC and MAC ligands cause marked lowerings of the LLCT excitation energies in comparison to the corresponding IPr complex. This trend is even more pronounced when a CAArC or a DAC is used as the carbene ligand instead. The energy profile of the ($d_\sigma \rightarrow \pi^*_{CAAC}$) MLCT excitations, which form the S_2 and T_2 states of the CAAC complex, follow this trend. In contrast, the type of carbene ligand affects the energetic location of the LC states involving various $\pi_{Cz} \rightarrow \pi^*_{Cz}$ excitations on the Cz moiety to a much lesser extent. In the IPr complex, where the LLCT and MLCT states lie in the violet to ultraviolet part of the spectrum in the gas phase, an ^{3}LC(Cz) excitation forms the T_1 state. An overview of the spectral energy profiles at the respective ground-state geometries is found in Fig. 8.

As mentioned before, the CMAs are very polar molecules in the electronic ground state. A polar solvent environment therefore largely stabilizes the charge distribution (Fig. 9, left) and even enhances the zwitterionic character. Experimental spectra on CAAC^{Ad}–Cu–Cz and related compounds were recorded in the solid state and in apolar to mildly polar solvents.[19,49] Upon excitation to the S_1 or T_1 state, electronic density is transferred from the carbazolide to the CAAC^{Ad} ligand. As a consequence,

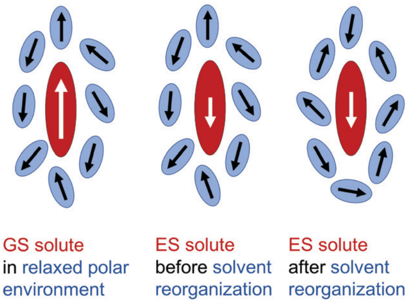

Fig. 9 Solvation schemes of a solute that is highly polar in the electronic ground state (GS, left panel) and reverses the orientation of the electric dipole moment when in the excited state (ES, middle). Systems of this type, *e.g.*, linear carbene coinage metal amides and halogenides, show strong negative solvatochromicity in polar environments. Solvent reorganization in the excited state (right panel) leads to a bathochromic shift of the emission in liquid solution in comparison to solid-state emission.

the direction of the electric dipole moment vector is reversed and its magnitude reduces to about 7–8 D in a vacuum and to about 3–4 D in chlorobenzene. Owing to this huge change of the dipole moment by about 18 D, solvation and solvent reorganization are expected to have large impact on the absorption and emission properties of this complex. A polar medium that is adapted to the zwitterionic charge distribution of the solute in the electronic ground state is a very unfavorable environment for an excited state with reversed dipole moment (Fig. 9, middle). Therefore, negative solvatochromicity of the S_1 and T_1 transition is to be expected in CAAC^{Ad}–Cu–Cz. Experimental and computational studies on a related CAAC^{Men}–Cu–Cz complex, carrying a menthyl instead of an adamantyl substituent, by Hamze *et al.*,[49] corroborate our finding that the LLCT absorption band strongly blue shifts with increasing solvent polarity.

According to our calculations, the LLCT absorption wavelengths of all CMAs experience substantial hypsochromic shifts in DCM solution (compare Fig. 8 and 10), ranging from approx. 0.6 eV in IPr–Cu–Cz to about 0.8 eV in the DAC–Cu–Cz complex. The MLCT states are affected to a lesser exent by the solvent–solute interaction causing blue shifts of the order of 0.2 eV in DCM. As may be expected, the vertical excitation wavelengths of the LC states change by less than 0.1 eV. Together with the varying amounts of exchange interactions, increasing in the order LLCT < MLCT < LC, this has the consequence that the ^{3}LLCT, ^{3}MLCT, ^{3}LC and ^{1}LLCT states are energetically very close in the CAAC and MAC complexes. Experimental observations and other theoretical studies support this conclusion. Absorption and emission properties of the MAC–Cu–Cz complex were found to be strongly solvent and temperature dependent and the underlying reason was attributed to the energetic proximity of the ^{3}Cz and ^{3}LLCT states.[54] Similar conclusions were drawn with regard to the photophysics of the CAAC^{Ad}–Cu–Cz complex.[49,58,59] It is noteworthy that the MLCT states of CAAC^{Ad}–Cu–Cz are significantly lower than the corresponding states in the CAAC^{Ad}–Au–Cz complex where the ^{3}LLCT and ^{1}LLCT states form the S_1 and T_1 states, respectively.[57,58,95] The lower propensity of Au(I) to form MLCT states leads to a smaller admixture of $d_\pi \rightarrow \pi^*_{CAAC}$ character into the S_1 and T_1 wavefunctions and the counterintuitive result that their SOCMEs are smaller than in the corresponding Cu(I) complex.[59] A similar observation has been made for other gold and copper homologues.[96] The strong π acceptor capabilities of the CAArC and DAC ligands make sure that the ILCT and MLCT states remain the lowest excited states of the CAArC–Cu–Cz and DAC–Cu–Cz complexes even in a polar environment, as confirmed by experimental studies.[21,54] In contrast, LC states with large singlet–triplet energy gaps form the S_1 and T_1 states of the classical NHC complex IPr–Cu–Cz which is therefore not expected to emit phosphorescence or TADF. Recent work by Hamze *et al.*[50] shows that the extension of the NHC backbone of IPr by a fused benzene ring lowers the LLCT state energies to an extent that they are nearly isoenergetic with the ^{3}Cz state.

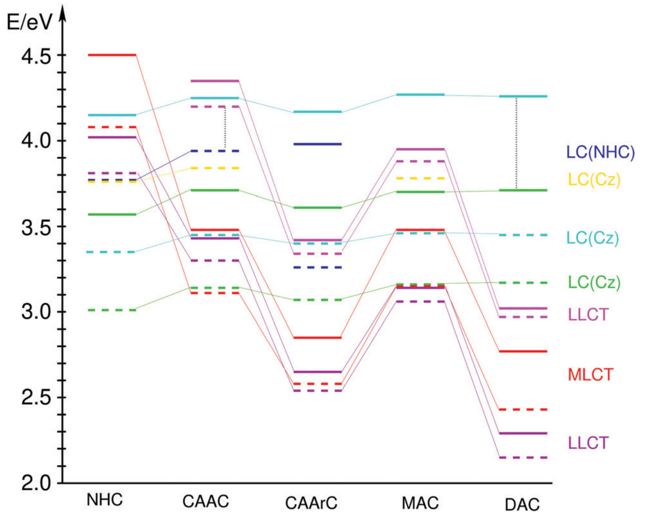

Fig. 10 Vertical excitation energies of the linear carbene copper carbazolide complexes in dichloromethane (COSMO) calculated with DFT/MRCI at the respective ground-state geometries. For line types and color codes, see Fig. 8.

With respect to solvent effects on the emission wavelength of the CMAs, two scenarios seem plausible, provided that geometry relaxation of the excited state solute is fast. At very short time delays after excitation or in rather rigid polar environments a reorientation of the surrounding has not taken place or is hindered (Fig. 9, middle). The second scenario applies to longer time delays and less rigid environments. Here, the solvent molecules can adjust to the charge distribution in the excited state of the solute (Fig. 9, right). The solvent reorganization leads to an additional stabilization of the excited state and a destabilization of the ground state. The first scenario can be simulated by PCM calculations, while for the second scenario corrected linear response (cLR) calculations have to be employed.

Except for the IPr–Cu–Cz complex, the other CMAs are TADF emitters with high IQEs in the solid state. In addition to preventing solvent reorganization, a solid state environment inhibits large-amplitude torsional motions of the Cz ligand in the S_1 state. Instead of performing an internal rotation by 90°, the Cz ligand librates about the co-planar conformation in the crystal or in a rigid host. Although the rotationally assisted spin-state inversion mechanism, proposed by Di *et al.*,[19] to explain the efficient ISC and rISC transitions, turned out to be an artefact,[95] spin-vibronic coupling is essential for the ISC and rISC dynamics.[58] The importance of a co-planar ligand orientation for absorption and emission was impressively demonstrated by Hamze *et al.*,[49] who compared the spectra of the CAAC^{Ad}–Cu–Cz complex to those of a related complex carrying methyl groups in the 2- and 9-position of the Cz ligand. These methyl groups cause the ligands to arrange in a perpendicular fashion leading to much weaker absorption and significantly lower PLQY of emission compared to the co-planar CAAC^{Ad}–Cu–Cz complex. These authors also systematically varied the alkyl substituents of the CAAC showing that their steric demand is decisive for preventing fast nonradiative decay of the emission. Most efficient in terms of the PLQY was a menthyl group (CAAC^{Men}–Cu–Cz, PLQY = 1.0), followed by adamantyl (CAAC^{Ad}–Cu–Cz, PLQY = 0.68) and diethyl (CAAC^{Et_2}–Cu–Cz, PLQY = 0.51). Least efficient was a dimethyl substitution (CAAC^{Me_2}–Cu–Cz, PLQY = 0.11).[49]

3.3.3 Carbene–Cu(I)–chlorides.

2-Coordinate carbene–Cu(I)–halogenide complexes are often utilized as intermediates in the synthesis of other carbene copper complexes, but their photophysics have recently attracted interest in their own right.[21,42–45] CAAC–Cu–Cl complexes showed microsecond lifetimes and high PLQYs with values ranging up to 0.96. Although Romanov *et al.*[43] first reported the occurrence of prompt fluorescence – which is rather untypical for this class of complexes – they later corrected their interpretation and now agree with Hamze *et al.*[44] and Gernert *et al.*,[45] who predicted phosphorescence as the main emission channel. To corroborate their analysis of the experimental results, Gernert *et al.* performed TDDFT calculations on the CAAC^{Me_2}–Cu–X (CAAC^{Me_2} = 1-(2,6-diisopropylphenyl)-3,3,5,5-tetramethyl-2-pyrrolidine-ylidene, X = Cl, Br, I) complexes in a vacuum, whereas the absorption had been measured in THF.[45] Pronounced effects of the environment polarity on the spectral properties have been encountered in linear CMAs[21,49,57–59,95] and we will show here that the same applies to carbene–Cu(I)–Cl complexes.

The S_1 and T_1 states of the CAAC^{Me_2}–Cu–Cl complex are dominated by MLCT($d_\sigma \rightarrow \pi^*_{carb}$) excited configurations (Fig. 11 and 12). The accepting orbital is the same in the S_2 and S_3 states, but the d hole has π in-plane ($\pi_\parallel$) and out-of-plane ($\pi_\perp$) character, respectively, in these states. In addition, charge is transferred from the matching Cl p orbital to the CAAC which is why we denominate these states being of XMLCT type. Because of the larger singlet–triplet energy gaps of LC states, the energetic order of the triplet states is not the same as in the singlet manifold. Rather, we find an ^{3}LC($\pi_{dipp} \rightarrow \pi^*_{dipp}$) excitation among the low-lying triplet states.

The excitation energy profile arising from the variation of the carbene ligand (Fig. 12) shows that DAC–Cu–Cl behaves very similar to CAAC^{Me_2}–Cu–Cl, albeit with strongly red-shifted phosphorescence. The corresponding IPr–Cu–Cl complex is expected to be non-emissive due to the ^{3}LC character of the T_1 state.

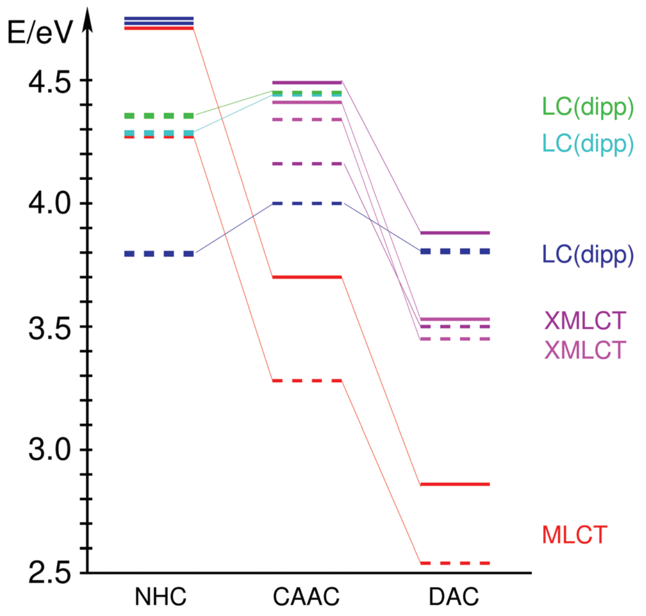

Fig. 12 Vertical excitation energies of linear carbene–Cu(I)–chloride complexes calculated with DFT/MRCI at the respective ground-state geometries in THF(PCM). Solid lines represent singlet states, and dashed lines represent triplet states. The following color codes have been used: (dark blue, cyan, green) LC($\pi_{dipp} \rightarrow \pi^*_{dipp}$), (red) MLCT($d_\sigma \rightarrow \pi^*_{carb}$), (magenta) XMLCT($p_{Cl\parallel}/d_{\pi\parallel} \rightarrow \pi^*_{carb}$), and (violet) XMLCT($p_{Cl\perp}/d_{\pi\perp} \rightarrow \pi^*_{carb}$).

Calculated line spectra and the spectral envelopes of the Gaussian broadened peaks of CAAC^{Me_2}–Cu–Cl in a vacuum and in the THF solution are shown in Fig. 13 together with the experimental spectrum as described by Gernert *et al.*[45] We distinguish 3 major bands in the spectral region between 200 and 500 nm, a weak band in the long wavelength regime followed by a medium strong band and an intense peak with a shoulder at shorter wavelengths.

The first and second absorption bands of the CAAC^{Me_2}–Cu–Cl complex experience strong hypsochromic shifts upon inclusion of a THF solvent model in the calculations whereas the strong

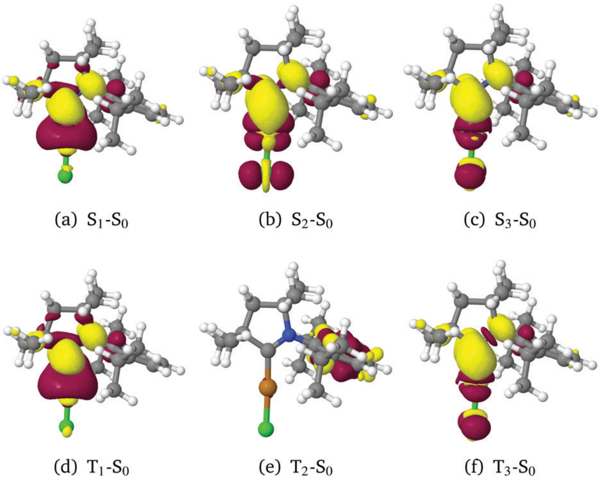

Fig. 11 DFT/MRCI difference densities of low-lying singlet and triplet transitions of the CAAC^{Me_2}–Cu–Cl complex at the ground state geometry in THF (PCM). For color codes, see Fig. 3.

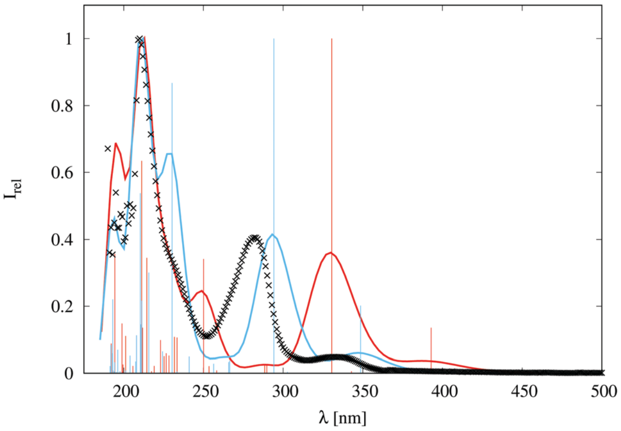

Fig. 13 Calculated absorption spectra of CAAC^{Me_2}–Cu–Cl in a vacuum (red) and in THF with PCM (blue) in comparison to the experimental spectrum in THF (black).

absorption peak in the wavelength range between 190 and 250 nm is nearly unaffected. The changes are mainly electronic in nature as the geometry parameters vary only to a small extent when the molecular cage is surrounded by a polarizable continuum model of THF. Because of the σ electron donating properties of the CAAC and the high electronegativity of the chlorine atom, CAAC^{Me_2}–CuCl exhibits a large permanent electric dipole moment in the electronic ground state (9.49 D in a vacuum) which is even enhanced by a polar solvent environment (11.92 D in THF). The shallow absorption peak with maximum at approximately 330 nm in the experimental spectrum (349 nm in THF) is due to the $S_1 \leftarrow S_0$ MLCT transition. The higher oscillator strength of the $S_3 \leftarrow S_0$ XMLCT excitation leads to a more intense peak at approximately 275 nm (294 nm in THF). In both cases, the electric dipole moment of the molecule is significantly reduced in its magnitude (to 4.00 D in the S_1 and 1.79 D in the S_3 state in a vacuum and to 5.52 D in S_1 and 4.61 D in S_3 in THF) and leads to a blue shift of the corresponding absorption peaks. Similar arguments hold true for the solvent dependence of the corresponding spin-forbidden triplet absorption. The T_1 state exhibits a static dipole moment of 4.81 D in a vacuum and 6.72 D in THF. Very weak absorption was observed in the wavelength region between 360 and 410 nm by Gernert *et al.*,[45] and assigned to the $T_1 \leftarrow S_0$ transition. The value computed for the vertical $T_1 \leftarrow S_0$ transition in PCM (388 nm) falls well within this wavelength regime. In addition to LC excitations on the CAAC ligand, the transition at *ca.* 250 nm in the vacuum comprises MLCT contributions and therefore experiences a blue shift upon solvation as well. In solution, it forms a shoulder of an intense peak that is predominantly formed by local transitions to the 4p shell of the Cu atom. The optically bright excitations in the 190–250 nm range, which jointly result in a wide, intense peak, have predominantly local character. Electrostatic effects on the position of this band are therefore small.

Geometry relaxation in the S_1 and T_1 potentials leads to a marked elongation of the C_1–N bond by 6–7 pm (see the ESI†). Also the Cu–Cl bond is elongated, but to a lesser extent. Because of the MLCT character of the excitations, the effective d orbital population on the Cu atom is close to 9 in the S_1 and T_1 states. In addition to becoming a strong Lewis acid in the excited state (see Section 3.3.4 for exciplex formation), the MLCT transition leads to a substantial deviation of the C_1–Cu–Cl coordination from linearity. In the vacuum, the C_1–Cu–Cl bending angle of S_1 is nearly 12° smaller than in the ground state, whereas the opposite trend is observed for the Cu–C_1–C_2 angle. In the THF solution, the changes are somewhat less pronounced. In the T_1 state, the Cu coordination deviates strongly from linearity. The C_1–Cu–Cl bending angle is about 43° smaller than in the ground state and 31° smaller than in the S_1 geometry. While the bond angles in the 5-membered CAAC are less distorted than in the S_1 state, the Cl–Cu–C_1–N dihedral angle is close to 110° at the T_1 minimum.

The vertical emission energies of the S_1 state shift from 2.53 eV (491 nm, vacuum) to 2.89 eV (429 nm, PCM) to 2.68 eV (463 nm, cLR). Herein, PCM applies to a situation very shortly after excitation or in rigid environments where the molecular geometry of the solute has relaxed but the solvent environment is still adapted to the charge distribution in the electronic ground state. In the cLR model, the solvent polarization is relaxed as well. The corresponding values of the T_1 state amount to 1.82 eV (681 nm, vacuum), 2.09 eV (594 nm, PCM) and 1.93 eV (643 nm, cLR). Compared to an apolar surrounding, we therefore expect an overall blue shift of the emisson whereas the transition from a frozen solution (or the solid state where the neighboring complexes cannot reorient) to a relaxed solvent environment should result in a red shift of the emission maxima.

Comparison with experimental observations is difficult for two reasons. The first relates to the experimental reference. According to Gernert *et al.*,[45] the luminescence of CAAC^{Me_2}–Cu–Cl is very weak in liquid THF solution. This is not untypical for compounds with small radiative transition rates because quenching processes due to collisions with solvent molecules become competitive at the microsecond time scale. CAAC^{Me_2}–Cu–Cl doped into a host of polyspirobifluorene copolymer SPB-02T yielded an emission spectrum comparable in width to that in the solid state, albeit red-shifted by about $\Delta = 1880\ \text{cm}^{-1}$. Measurements in polymethyl methacrylate (PMMA) matrices revealed a strong temperature dependent red shift of the phosphorescence emission maximum. The second problem derives from the theoretical model. A meaningful FC spectrum of the emission could not be obtained because the large-amplitude C_1–Cu–Cl bending motion in the excited states and the resulting double-minimum potential wells prevent the application of a harmonic oscillator model that forms the basis of the algorithms implemented in the VIBES program. For the same reason, ISC and rISC rate constants could not be calculated either for the free complex in THF solution. Lin *et al.*[61] encountered similar problems in their computational treatment of vibrational overlaps which closely resembles the methods applied in our work. They ascribe the tendency of the complex to undergo fast nonradiative decay in liquid solution to nonadiabatic coupling caused by the large-amplitude C–Cu–Cl and Cu–C–N bending motions. According to their model, confinement of these bending motions, due to aggregation, blocks the nonradiative channels and causes strong fluorescence, at variance with experimental observations. The reason for this discrepancy presumably is the unusually small ($10^2\ \text{s}^{-1}$) ISC rate constant calculated by these authors.

Gernert *et al.* measured a time constant of 26 μs for the emission of this complex in the solid state at room temperature and a photoluminescence quantum yield of 0.60, which translates into a pure radiative lifetime of 43 μs.[45] When the temperature is lowered to 77 K, the emission maximum shifts from 511 nm to 526 nm and the time constant changes to 41 μs. As the quantum yield was not determined in this temperature regime, time constants for purely radiative decay cannot be deduced from this value. It may be assumed, however, that the photoluminescence quantum yield is at least 0.60 and possibly larger at this temperature. These time constants compare well with our computed phosphorescence decay times at the T_1 minimum. The most strongly interacting triplet sublevel decays with a time constant of 48 μs according to our calculations, whereas the

97

averaged lifetime is longer by a factor of 3. It is not clear, however, whether the averaging of phosphorescence rate constants is appropriate in this case. For the averaging to be justified in these complexes, spin-relaxation among the triplet sublevels has to be fast enough to repopulate the other triplet sublevels on the time scale of the emission. Because of the large singlet–triplet energy gap ($\Delta E_{\mathrm{ST}} > 0.70$ eV in vacuum and the PCM and cLR models of a THF environment), delayed fluorescence is not expected to contribute to the luminescence.

3.3.4 Exciplex formation.

It has been shown that Lewis bases such as THF, acetone, or pyridine can form exciplexes with Cu(I) systems. While McMillin *et al.*[97] reported a quenching of the MLCT emission, Romanov *et al.*[42] found red shifts of the emission by >130 nm in coordinating solvents. Therefore, the question arises whether and how THF molecules in solution or co-crystallized with the CAAC$^{\mathrm{Me_2}}$–Cu–Cl complex actively participate in its photophysics.

In the electronic ground state, THF is only loosely bound to CAAC$^{\mathrm{Me_2}}$–Cu–Cl. THF coordination to the complex in the electronic ground state leads to a small red shift of the CT absorption bands in the long wavelength region and a loss of intensity in the 190–250 nm range.

Upon excitation to the MLCT states, the intermolecular separation decreases and a covalent bond is formed beween the copper and oxygen atoms resulting in a nearly T-shaped Cu coordination with a Cl–Cu–C$_1$ angle of approximately 160° (see the ESI†). Formation of the Cu–O bond (≈2.04 Å) leads to a marked elongation of the Cl–Cu and Cu–C$_1$ bonds (Fig. 14). Interestingly, the MLCT/XLCT character of the electronic transition is largely preserved. The lone-pair electrons of oxygen, involved in the formation of the covalent bond, contribute to the electron density of the HOMO whereas the shape of the LUMO is nearly unchanged (Fig. 14). We will therefore not speak of quenching the MLCT emission by THF coordination but rather of a strong red shift of the emission.

The coordination of the THF molecule to the CAAC$^{\mathrm{Me_2}}$–Cu–Cl complex rigidifies the copper coordination environment, *i.e.*, the optimized S$_1$ and T$_1$ minimum geometries closely resemble one another. In combination with the adiabatic energy gap of about 2400 cm^{-1} and squared SOCMEs of *ca.* 450 cm^{-2}, the nested potentials lead to substantial ISC. Prompt fluorescence at a rate of 7.9×10^5 s^{-1} cannot compete with ISC. For the latter, we predict rate constants of 8.9×10^9 s^{-1} at 298 K and 8.9×10^8 s^{-1} at 77 K. Hence, we expect all exciplexes formed in the S$_1$ state to proceed to the T$_1$ state. We compute an averaged radiative rate constant of 4.2×10^3 s^{-1}, corresponding to a phosphorescence lifetime of 240 μs and an emission wavelength of 723 nm. Reverse ISC is an order of magnitude slower at 298 K (4.9×10^3 s^{-1}) and three orders of magnitude slower at 77 K (5.3×10^1 s^{-1}). For that portion of CAAC$^{\mathrm{Me_2}}$–Cu–Cl complexes which form exciplexes with nearby THF molecules, therefore only red-shifted phosphorescence (in addition to nonradiative triplet decay) is expected. In the electronic ground state, the molecules separate again so that this decay channel is not considered destructive.

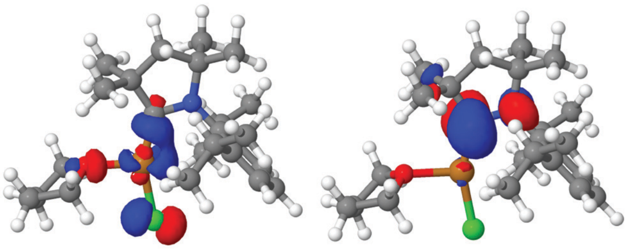

Fig. 14 HOMO (left) and LUMO (right) of the CAAC$^{\mathrm{Me_2}}$–Cu–Cl-THF exciplex at the T$_1$ state in the implicit THF solution.

4 Summary and conclusions

The computational protocol applied in this work starts with geometry optimizations and vibrational analyses at the level of (TD)DFT, followed by extensive DFT/MRCI and DFT/MRSOCI single-point calculations providing the basis for the subsequent evaluation of rate constants of spin-allowed and spin-forbidden transitions according to the Fermi golden rule approximation. Solvent effects are introduced into the calculations *via* point charges obtained from self-consistent reaction field optimizations of a continuum solvation model in the electronic ground state (COSMO or PCM) or in the excited state taking account of solvent reorganization by a corrected linear response approach (cLR). This protocol is applied to a number of Cu(I) complexes with varying coordination numbers and type of ligands. Among them are TADF and phosphorescence emitters with experimentally well-known excited-state properties such as ISC time constants, radiative lifetimes and absorption as well as emission maxima in the solid state and in liquid solution. Their data can serve as a benchmark for validating the theoretical methods. In addition, we have systematically varied the ligands in neutral and cationic linear Cu(I) carbene complexes with the aim to identify trends in their excited-state energy profiles.

The density of low-lying electronic states is high in most of the Cu(I) complexes studied in this work. We note that the S$_1$ and T$_1$ states do not necessarily originate from HOMO–LUMO excitations. To get an overview over the type and energetic order of electronically excited states, the application of excited-state quantum chemical methods is mandatory. Because of the larger exchange interaction in LC states in comparison to CT states, the contribution of locally excited configurations is typically higher in low-lying triplet states than in their singlet congeners. Regarding the luminescence properties of linear Cu(I) carbene complexes, the following pattern has emerged. Only those complexes with S$_1$ and T$_1$ states of LLCT character possess sufficiently small singlet–triplet energy gaps ΔE_{ST} to enable TADF. MLCT contributions to the LLCT wavefunctions ensure SOCMEs to be sizeable. Complexes whose S$_1$ and T$_1$ wavefunctions are dominated by MLCT excitations tend to emit phosphorescence instead because rISC cannot compete against radiative decay. Unlike the situation in metal-free TADF emitters, the presence of low-lying ^{3}LC states does not promote ISC and rISC. These states rather hold the danger of trapping the excitation with nonradiative deactivation being the major deactivation channel. In the linear carbene complexes comprising the electron-rich Cz^- ligand, the energetic position of the LLCT states is steered by the π-acceptor capability of the carbene whereas its σ-donor capability controls the energetic position of the MLCT states. The π-donor capacity of the chloride ligand is too small to make XLCT states the lowest singlet and triplet states. Except for the classical NHC complex IPr–Cu–Cl, which is predicted to be dark because of the LC character of its T_1 state, the carbene–Cu–Cl complexes exhibit MLCT S_1 and T_1 states which are energetically too far apart for TADF to prevail.

In all cases, the environment exerts substantial influence on the photophysical properties of the complexes. The LLCT states of the neutral linear carbene–Cu–Cz and carbene–Cu–Cl complexes, *e.g.*, which exhibit large dipole moments in their electronic ground states, experience hypsochromic shifts of up to 0.8 eV in mildly polar solvents such as DCM and THF. MLCT states shift to a lesser extent and LC states are nearly unaffected by the solvent–solute interactions. The electrostatic effects are well described by the solvent models, *i.e.*, COSMO or PCM in the solid state where the environment cannot reorient on the time scale of the emission and cLR for liquid solutions. The methods addressed above perform well in many cases and transition energies and rate constants are obtained in good agreement with the experiment. In contrast, pseudo Jahn–Teller distortions in MLCT excited states present technical problems. Because of the shallow excited-state potentials, even small modulations of the energy can have dramatic effects on the nuclear arrangement. In the solid state, large-amplitude motions are prevented by steric repulsions of the rigid environment. A continuum solvation model cannot mimic such effects. To properly model the impact of a solid-state environment on the photophysics of MLCT-excited Cu(I) complexes a QM/MM treatment of the molecular surrounding appears more appropriate. Work along these lines is in progress.

MLCT states of the undercoordinated linear complexes behave like Lewis acids. Unless the copper center is protected by very bulky substituents, they readily form exciplexes with coordinating solvents. Exciplex formation does not cause the MLCT emission of the $CAAC^{Me_2}$–Cu–Cl complex to be quenched. It rather rigidifies the copper coordination and leads to a red shift of the phosphorescence. The coordination of a second pyridine ligand to the $[IPr–Cu–Py]^+$ complex lowers the MLCT transition in relation to the optically dark ^{3}LC state on the dipp substituent and thus enables the emission of phosphorescence in the bis-pyridine compound $[IPr–Cu–Py_2]^+$.

Conflicts of interest

There are no conflicts to declare.

Acknowledgements

This work was supported by the Deutsche Forschungsgemeinschaft [DFG, MA 1051/17-1 and Priority Program SPP 2102 "Light-controlled reactivity of metal complexes" (MA 1051/18-1)].

Notes and references

1 H. Uoyoma, K. Goushi, K. Shizu, H. Nomura and C. Adachi, *Nature*, 2012, **492**, 234–238.

2 F. B. Dias, K. N. Bourdakos, V. Jankus, K. C. Moss, K. T. Kamtekar, V. Bhalla, J. Santos, M. R. Bryce and A. P. Monkman, *Adv. Mater.*, 2013, **25**, 3707–3714.

3 C. Adachi, *Jpn. J. Appl. Phys.*, 2014, **53**, 060101.

4 J.-H. Jou, S. Kumar, A. Agrawal, T.-H. Li and S. Sahoo, *J. Mater. Chem. C*, 2015, **3**, 2974–3002.

5 Z. Yang, Z. Mao, Z. Xie, Y. Zhang, S. Liu, J. Zhao, J. Xu, Z. Chi and M. P. Aldred, *Chem. Soc. Rev.*, 2017, **46**, 915–1016.

6 *Highly Efficient OLEDs: Materials Based on Thermally Activated Delayed Fluorescence*, ed. H. Yersin, Wiley VCH, 2018.

7 C. Marian, *Reviews In Computational Chemistry*, Wiley-VCH, Weinheim, 2001, vol. 17, pp. 99–204.

8 F. B. Dias, J. Santos, D. R. Graves, P. Data, R. S. Nobuyasu, M. A. Fox, A. S. Batsanov, T. Palmeira, M. N. Berberan-Santos, M. R. Bryce and A. P. Monkman, *Adv. Sci.*, 2016, 1600080.

9 M. K. Etherington, J. Gibson, H. F. Higginbotham, T. J. Penfold and A. P. Monkman, *Nat. Commun.*, 2016, **7**, 13680.

10 C. M. Marian, *J. Phys. Chem. C*, 2016, **120**, 3715–3721.

11 I. Lyskov and C. M. Marian, *J. Phys. Chem. C*, 2017, **121**, 21145–21153.

12 T. J. Penfold, E. Gindensperger, C. Daniel and C. M. Marian, *Chem. Rev.*, 2018, **118**, 6975–7025.

13 P. S. Wagenknecht and P. C. Ford, *Coord. Chem. Rev.*, 2011, **255**, 591–616.

14 A. Barbieri, G. Accorsi and N. Armaroli, *Chem. Commun.*, 2008, 2185–2193.

15 X.-L. Chen, C.-S. Lin, X.-Y. Wu, R. Yu, T. Teng, Q.-K. Zhang, Q. Zhang, W.-B. Yang and C.-Z. Lu, *J. Mater. Chem. C*, 2015, **3**, 1187–1195.

16 E. Cariati, E. Lucenti, C. Botta, U. Giovanella, D. Marinotto and S. Righetto, *Coord. Chem. Rev.*, 2016, **306**, 566–614.

17 R. Czerwieniec, M. J. Leitl, H. H. Homeier and H. Yersin, *Coord. Chem. Rev.*, 2016, **325**, 2–28.

18 M. J. Leitl, D. M. Zink, A. Schinabeck, T. Baumann, D. Volz and H. Yersin, *Top. Curr. Chem.*, 2016, **374**, 25.

19 D. Di, A. S. Romanov, L. Yang, J. M. Richter, J. P. H. Rivett, S. Jones, T. H. Thomas, M. Abdi Jalebi, R. H. Friend, M. Linnolahti, M. Bochmann and D. Credgington, *Science*, 2017, **356**, 159–163.

20 R. Hamze, S. Shi, S. C. Kapper, D. S. Muthiah Ravinson, L. Estergreen, M.-C. Jung, A. C. Tadle, R. Haiges, P. I. Djurovich, J. L. Peltier, R. Jazzar, G. Bertrand, S. E. Bradforth and M. E. Thompson, *J. Am. Chem. Soc.*, 2019, **141**, 8616–8626.

21 M. Gernert, L. Balles-Wolf, F. Kerner, U. Müller, A. Schmiedel, M. Holzapfel, C. M. Marian, J. Pflaum, C. Lambert and A. Steffen, *J. Am. Chem. Soc.*, 2020, **142**, 8897–8909.

22 Y. Sakai, Y. Sagara, H. Nomura, N. Nakamura, Y. Suzuki, H. Miyazaki and C. Adachi, *Chem. Commun.*, 2015, **51**, 3181–3184.

23 M. Iwamura, S. Takeuchi and T. Tahara, *Phys. Chem. Chem. Phys.*, 2014, **16**, 4143–4154.

24 Z. A. Siddique, Y. Yamamoto, T. Ohno and K. Nozaki, *Inorg. Chem.*, 2003, **42**, 6366–6378.

25 G. Capano, T. J. Penfold, U. Röthlisberger and I. Tavernelli, *Chimia*, 2014, **68**, 227–230.

26 G. Capano, M. Chergui, U. Röthlisberger, I. Tavernelli and T. J. Penfold, *J. Phys. Chem. A*, 2014, **118**, 9861–9869.

27 G. Capano, U. Röthlisberger, I. Tavernelli and T. J. Penfold, *J. Phys. Chem. A*, 2015, **119**, 7026–7037.

28 C. L. Linfoot, M. J. Leitl, P. Richardson, A. F. Rausch, O. Chepelin, F. J. White, H. Yersin and N. Robertson, *Inorg. Chem.*, 2014, **53**, 10854–10861.

29 R. Czerwieniec, K. Kowalski and H. Yersin, *Dalton Trans.*, 2013, **42**, 9826–9830.

30 X.-L. Chen, R. Yu, Q.-K. Zhang, L.-J. Zhou, X.-Y. Wu, Q. Zhang and C.-Z. Lu, *Chem. Mater.*, 2013, **25**, 3910–3920.

31 M. Osawa, I. Kawata, R. Ishii, S. Igawa, M. Hashimoto and M. Hoshino, *J. Mater. Chem. C*, 2013, **1**, 4375–4383.

32 R. Czerwieniec and H. Yersin, *Inorg. Chem.*, 2015, **54**, 4322–4327.

33 Q. Zhang, J. Chen, X.-Y. Wu, X.-L. Chen, R. Yu and C.-Z. Lu, *Dalton Trans.*, 2015, **44**, 6706–6710.

34 L. Bergmann, J. Friedrichs, M. Mydlak, T. Baumann, M. Nieger and S. Bräse, *Chem. Commun.*, 2013, **49**, 6501–6503.

35 L. Bergmann, G. J. Hedley, T. Baumann, S. Bräse and I. D. W. Samuel, *Sci. Adv.*, 2016, **2**, e1500889.

36 V. A. Krylova, P. I. Djurovich, M. T. Whited and M. E. Thompson, *Chem. Commun.*, 2010, **46**, 6696–6698.

37 V. A. Krylova, P. I. Djurovich, J. W. Aronson, R. Haiges, M. T. Whited and M. E. Thompson, *Organometallics*, 2012, **31**, 7983–7993.

38 V. A. Krylova, P. I. Djurovich, B. L. Conley, R. Haiges, M. T. Whited, T. J. Williams and M. E. Thompson, *Chem. Commun.*, 2014, **50**, 7176–7179.

39 M. J. Leitl, V. A. Krylova, P. I. Djurovich, M. E. Thompson and H. Yersin, *J. Am. Chem. Soc.*, 2014, **136**, 16032–16038.

40 J. Föller, M. Kleinschmidt and C. M. Marian, *Inorg. Chem.*, 2016, **55**, 7508–7516.

41 M. Osawa, *Chem. Commun.*, 2014, **50**, 1801–1803.

42 A. S. Romanov, D. Di, L. Yang, J. Fernandez-Cestau, C. R. Becker, C. E. James, B. Zhu, M. Linnolahti, D. Credgington and M. Bochmann, *Chem. Commun.*, 2016, **52**, 6379.

43 A. S. Romanov, C. R. Becker, C. E. James, D. Di, D. Credgington, M. Linnolahti and M. Bochmann, *Chem. – Eur. J.*, 2017, **23**, 4625.

44 R. Hamze, R. Jazzar, M. Soleilhavoup, P. I. Djurovich, G. Bertrand and M. E. Thompson, *Chem. Commun.*, 2017, **53**, 9008.

45 M. Gernert, U. Müller, M. Haehnel, J. Pflaum and A. Steffen, *Chem. – Eur. J.*, 2017, **23**, 2206–2216.

46 B. Bertrand, A. S. Romanov, M. Brooks, J. Davis, C. Schmidt, I. Ott, M. O'Connell and M. Bochmann, *Dalton Trans.*, 2017, **46**, 15875–15887.

47 S. Shi, L. R. Collins, M. F. Mahon, P. I. Djurovich, M. E. Thompson and M. K. Whittlesey, *Dalton Trans.*, 2017, **46**, 745.

48 F. Chotard, A. S. Romanov, D. L. Hughes, M. Linnolahti and M. Bochmann, *Eur. J. Inorg. Chem.*, 2019, 4234–4240.

49 R. Hamze, J. L. Peltier, D. Sylvinson, M. Jung, J. Cardenas, R. Haiges, M. Soleilhavoup, R. Jazzar, P. I. Djurovich, G. Bertrand and M. E. Thompson, *Science*, 2019, **363**, 601–606.

50 R. Hamze, M. Idris, D. S. Muthiah Ravinson, M. C. Jung, R. Haiges, P. I. Djurovich and M. E. Thompson, *Front. Chem.*, 2020, **8**, 401.

51 A. S. Romanov, S. T. E. Jones, Q. Gu, P. J. Conaghan, B. H. Drummond, J. Feng, F. Chotard, L. Buizza, M. Foley, M. Linnolahti, D. Credgington and M. Bochmann, *Chem. Sci.*, 2020, **11**, 435–446.

52 J. Föller, C. Ganter, A. Steffen and C. M. Marian, *Inorg. Chem.*, 2019, **58**, 5446–5456.

53 T.-y. Li, D. S. Muthiah Ravinson, R. Haiges, P. I. Djurovich and M. E. Thompson, *J. Am. Chem. Soc.*, 2020, **142**, 6158–6172.

54 S. Shi, M. C. Jung, C. Coburn, A. Tadle, D. Sylvinson MR, P. I. Djurovich, S. R. Forrest and M. E. Thompson, *J. Am. Chem. Soc.*, 2019, **141**, 3576–3588.

55 S. Grimme and M. Waletzke, *J. Chem. Phys.*, 1999, **111**, 5645–5655.

56 C. M. Marian, A. Heil and M. Kleinschmidt, *Wiley Interdiscip. Rev.: Comput. Mol. Sci.*, 2019, **9**, e1394.

57 S. Thompson, J. Eng and T. J. Penfold, *J. Chem. Phys.*, 2018, **149**, 014304.

58 J. Eng and T. J. Penfold, *Chem. Rec.*, 2020, **20**, 1–27.

59 J. Eng, S. Thompson, H. Goodwin, D. Credgington and T. J. Penfold, *Phys. Chem. Chem. Phys.*, 2020, **22**, 4659–4667.

60 F. Wang and T. Ziegler, *J. Chem. Phys.*, 2005, **123**, 154102.

61 S. Lin, Q. Peng, Q. Ou and Z. Shuai, *Inorg. Chem.*, 2019, **58**, 14403–14409.

62 L. Lv, K. Yuan and Y. Wang, *Org. Electron.*, 2017, **51**, 207.

63 Y.-J. Gao, W.-K. Chen, Z.-R. Wang, W.-H. Fang and G. Cui, *Phys. Chem. Chem. Phys.*, 2018, **20**, 24955–24967.

64 A. Stoïanov, C. Gourlaouen, S. Vela and C. Daniel, *J. Phys. Chem. A*, 2018, **122**, 1413–1421.

65 C. M. Marian, J. Föller, M. Kleinschmidt and M. Etinski, *Highly Efficient OLEDs, Materials Based on Thermally Activated Delayed Fluorescence*, Wiley-VCH, Weinheim, 2018, pp. 257–296, ch. 8.

66 A. Liske, L. Wallbaum, T. Hölzel, J. Föller, M. Gernert, B. Hupp, C. Ganter, C. M. Marian and A. Steffen, *Inorg. Chem.*, 2019, **58**, 5433–5445.

67 M. Kleinschmidt, J. Tatchen and C. M. Marian, *J. Chem. Phys.*, 2006, **124**, 124101.

68 M. Grupe, F. Bäppler, M. Theiß, J. M. Busch, F. Dietrich, D. Volz, M. Gerhards, S. Bräse and R. Diller, *Phys. Chem. Chem. Phys.*, 2020, **22**, 14187–14200.

69 K. A. Peterson and C. Puzzarini, *Theor. Chem. Acc.*, 2005, **114**, 283–296.

70 D. Figgen, G. Rauhut, M. Dolg and H. Stoll, *Chem. Phys.*, 2005, **311**, 227–244.

71 A. Schäfer, H. Horn and R. Ahlrichs, *J. Chem. Phys.*, 1992, **97**, 2571–2577.

72 TURBOMOLE, a development of University of Karlsruhe and Forschungszentrum Karlsruhe GmbH, 1989–2007, TURBOMOLE GmbH, since 2007; available from, http://www.turbomole.com.

73 M. Von Arnim and R. Ahlrichs, *J. Comput. Chem.*, 1998, **19**, 1746–1757.

74 F. Furche and R. Ahlrichs, *J. Chem. Phys.*, 2002, **117**, 7433–7447.

75 S. Hirata and M. Head-Gordon, *Chem. Phys. Lett.*, 1999, **314**, 291–299.

76 J. P. Perdew, K. Burke and M. Ernzerhof, *Phys. Rev. Lett.*, 1996, **77**, 3865–3868.

77 C. Adamo and V. Barone, *J. Chem. Phys.*, 1999, **110**, 6158–6170.

78 T. Weymuth, M. P. Haag, K. Kiewisch, S. Luber, S. Schenk, C. R. Jacob, C. Herrmann, J. Neugebauer and M. Reiher, *J. Comput. Chem.*, 2012, **33**, 2186–2198.

79 M. J. Frisch, G. W. Trucks, H. B. Schlegel, G. E. Scuseria, M. A. Robb, J. R. Cheeseman, G. Scalmani, V. Barone, G. A. Petersson, H. Nakatsuji, X. Li, M. Caricato, A. V. Marenich, J. Bloino, B. G. Janesko, R. Gomperts, B. Mennucci, H. P. Hratchian, J. V. Ortiz, A. F. Izmaylov, J. L. Sonnenberg, D. Williams-Young, F. Ding, F. Lipparini, F. Egidi, J. Goings, B. Peng, A. Petrone, T. Henderson, D. Ranasinghe, V. G. Zakrzewski, J. Gao, N. Rega, G. Zheng, W. Liang, M. Hada, M. Ehara, K. Toyota, R. Fukuda, J. Hasegawa, M. Ishida, T. Nakajima, Y. Honda, O. Kitao, H. Nakai, T. Vreven, K. Throssell, J. A. Montgomery, Jr., J. E. Peralta, F. Ogliaro, M. J. Bearpark, J. J. Heyd, E. N. Brothers, K. N. Kudin, V. N. Staroverov, T. A. Keith, R. Kobayashi, J. Normand, K. Raghavachari, A. P. Rendell, J. C. Burant, S. S. Iyengar, J. Tomasi, M. Cossi, J. M. Millam, M. Klene, C. Adamo, R. Cammi, J. W. Ochterski, R. L. Martin, K. Morokuma, O. Farkas, J. B. Foresman and D. J. Fox, *Gaussian 16, Revision A.03*, Gaussian Inc., Wallingford CT, 2016.

80 A. Klamt and G. Schüürmann, *J. Chem. Soc., Perkin Trans. 2*, 1993, 799.

81 S. Miertuš, E. Scrocco and J. Tomasi, *Chem. Phys.*, 1981, **55**, 117–129.

82 M. Caricato, B. Mennucci, J. Tomasi, F. Ingrosso, R. Cammi, S. Corni and G. Scalmani, *J. Chem. Phys.*, 2006, **124**, 124520.

83 I. Lyskov, M. Kleinschmidt and C. M. Marian, *J. Chem. Phys.*, 2016, **144**, 034104.

84 A. Heil, M. Kleinschmidt and C. M. Marian, *J. Chem. Phys.*, 2018, **149**, 164106.

85 C. Lee, W. Yang and R. G. Parr, *Phys. Rev. B: Condens. Matter Mater. Phys.*, 1988, **37**, 785–789.

86 A. D. Becke, *J. Chem. Phys.*, 1993, **98**, 1372–1377.

87 F. Weigend, M. Häser, H. Patzelt and R. Ahlrichs, *Chem. Phys. Lett.*, 1998, **294**, 143–152.

88 M. Kleinschmidt, J. Tatchen and C. M. Marian, *J. Comput. Chem.*, 2002, **23**, 824–833.

89 M. Kleinschmidt and C. M. Marian, *Chem. Phys.*, 2005, **311**, 71–79.

90 B. A. Heß, C. M. Marian, U. Wahlgren and O. Gropen, *Chem. Phys. Lett.*, 1996, **251**, 365–371.

91 *AMFI is an atomic spin–orbit integral program*, B. Schimmelpfennig, University of Stockholm, 1996.

92 M. Etinski, J. Tatchen and C. M. Marian, *J. Chem. Phys.*, 2011, **134**, 154105.

93 M. Etinski, J. Tatchen and C. M. Marian, *Phys. Chem. Chem. Phys.*, 2014, **16**, 4740–4751.

94 L. Bergmann, *New Emitters for OLEDs: The Coordination- and Photo-Chemistry of Mononuclear Neutral Copper(I) Complexes*, Logos Verlag Berlin, 2016.

95 J. Föller and C. M. Marian, *J. Phys. Chem. Lett.*, 2017, **8**, 5643–5647.

96 C.-W. Hsu, C.-C. Lin, M.-W. Chung, Y. Chi, G.-H. Lee, P.-T. Chou, C.-H. Chang and P.-Y. Chen, *J. Am. Chem. Soc.*, 2011, **133**, 12085–12099.

97 D. R. McMillin, J. R. Kirchhoff and K. V. Goodwin, *Coord. Chem. Rev.*, 1985, **64**, 83–92.

Electronic Supplementary Information for Understanding the Luminescence Properties of Cu(I) Complexes: A Quantum Chemical Perusal

Nora Lüdtke, Jelena Föller, and Christel M. Marian*

Institut für Theoretische Chemie und Computerchemie, Heinrich-Heine-Universität Düsseldorf, Universitätsstr. 1, 40225 Düsseldorf, Germany

E-mail: Christel.Marian@hhu.de

S1 Further Computational Details

For the calculation of the nonradiative rate constants, a time interval of 3 ps with 165536 grid points was chosen and the correlation function was damped with a Gaussian function of 10 cm^{-1} width at half maximum. The temperature was set on 77K and 298K.

S2 (DPEPhos)Cu(PyrTet)

For the (DPEPhos)Cu(PyrTet) complex, the semiempirical Grimme D3 dispersion correction was included in the calculations.[1,2] DFT/MRCI test calculations at the ground-state minimum geometry were made with the R2016 Hamiltonian and standard parameters[3] and the R2018 Hamiltonian with tight parameters.[4] They showed only minor differences (see Figure S1). For the test calculations, 24 roots were calculated with the R2016and 30 singlet and triplet roots with the R2018 Hamiltonian. For the single point calculations at the excited-state minima, only the R2018 Hamiltonian with tight parameters was used and 24 singlet and triplet roots were calculated at each geometry. For all calculations with standard parameters the selection threshold was set to 0.8 E_h in the first run, which only serves for setting up the reference space, and to 1.0 E_h for the final run. With the R2018 Hamiltonians two runs with a selection threshold of 0.8 E_h have been performed.

For the calculations in DCM, the ground state geometry was optimized with the polarizable continuum model (PCM)[5] which is implemented in Gaussian 16.[6] The resulting point charges were adapted for DFT/MRCI calculations and 24 singlet and triplet roots with the R2018 and tight parameters were computed.

The flattening distortion of the (DPEPhos)Cu(PyrTet) complex in the S_1 state is visualized in Figure S2.

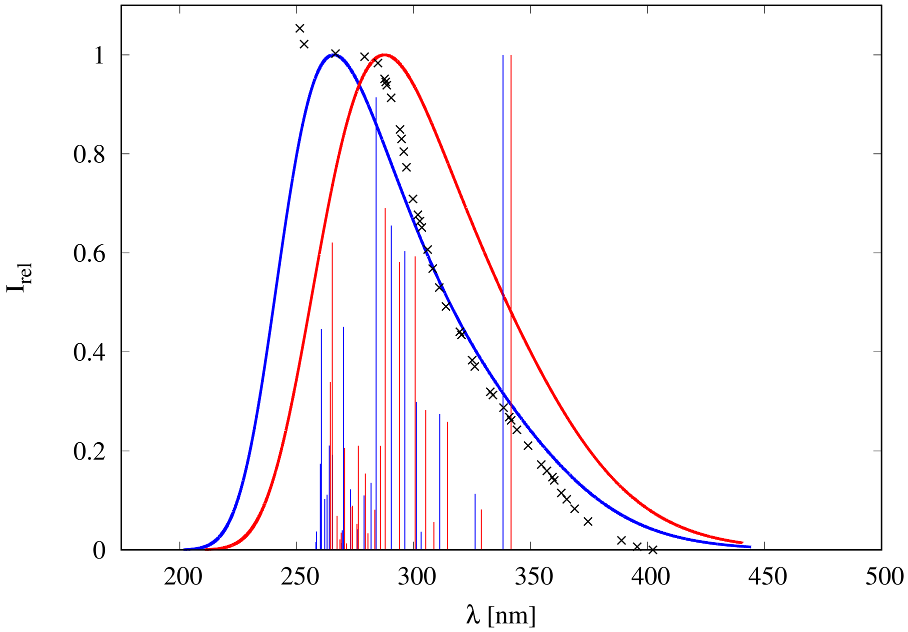

Figure S1: Calculated absorption spectra in vacuum of (DPEPhos)Cu(PyrTet) with the R2016 (red) and R2018 (blue) Hamiltonian in comparison to the experimental spectrum in CH_2Cl_2 (black).

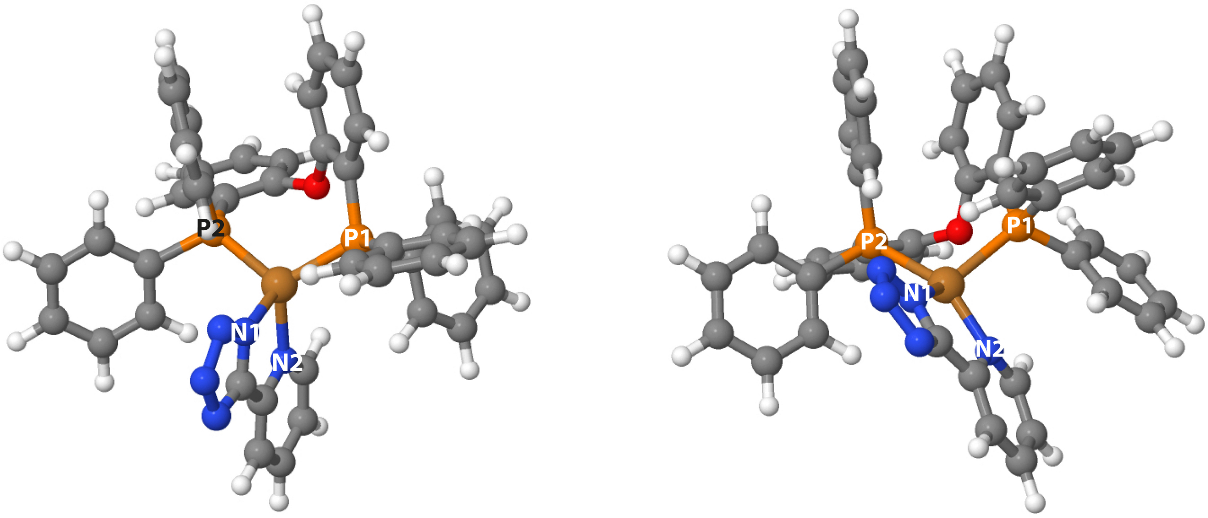

Figure S2: S_0 (left) and S_1 state geometries (right) of the (DPEPhos)Cu(PyrTet) complex in vacuum.

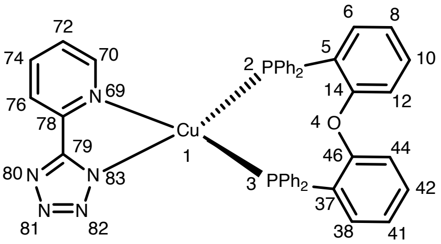

Figure S3: Structure with atom numbers of the (DPEPhos)Cu(PyrTet) complex.

Table S1: Calculated bond lengths (in Å) of the optimized (DPEPhos)Cu(PyrTet) complex in vacuum in comparison to the crystal structure.

bond	S_0	S_1	T_1	crystal structure
C5-C6	1.40	1.40	1.40	1.39
C5-C14	1.40	1.40	1.40	1.38
C6-C8	1.39	1.39	1.39	1.38
C8-C10	1.39	1.39	1.39	1.37
C10-C12	1.39	1.39	1.39	1.38
C12-C14	1.39	1.39	1.39	1.38
C37-C38	1.40	1.40	1.40	1.38
C37-C46	1.41	1.40	1.40	1.39
C38-C40	1.39	1.39	1.39	1.38
C40-C42	1.39	1.39	1.39	1.38
C42-C44	1.39	1.39	1.39	1.37
C44-C46	1.39	1.39	1.39	1.38
C58-C59	1.40	1.40	1.40	1.38
C70-C72	1.39	1.37	1.37	1.37
C72-C74	1.40	1.43	1.43	1.37
C74-C76	1.39	1.40	1.39	1.37
C76-C78	1.40	1.39	1.39	1.38
C78-C79	1.45	1.45	1.44	1.45
Cu1-N69	2.11	1.98	1.95	2.08
Cu1-N83	2.01	1.94	1.94	2.04
Cu1-P2	2.23	2.41	2.38	2.23

Continued on next page

Table S1: Calculated bond lengths (in Å) of the optimized (DPEPhos)Cu(PyrTet) complex in vacuum in comparison to the crystal structure.

bond	S_0	S_1	T_1	crystal structure
Cu1-P3	2.25	2.38	2.36	2.25
C5-P2	1.83	1.83	1.83	1.81
C37-P3	1.84	1.84	1.84	1.83
C14-O4	1.37	1.37	1.37	1.38
C46-O4	1.37	1.37	1.37	1.38
C70-N69	1.33	1.36	1.37	1.33
C78-N69	1.35	1.40	1.41	1.34
C79-N80	1.33	1.33	1.33	1.32
C79-N83	1.34	1.35	1.35	1.33
N80-N81	1.32	1.34	1.34	1.34
N81-N82	1.31	1.29	1.29	1.31
N82-N83	1.32	1.33	1.34	1.34

Table S2: Calculated bond angles (in °) of the optimized (DPEPhos)Cu(PyrTet) complex in vacuum in comparison to the crystal structure.

angle	S_0	S_1	T_1	crystal structure
C5-C6-C8	120.8	120.7	120.7	120.4
C6-C14-C12	121.4	121.3	121.3	121.7
C6-C5-C14	118.3	118.5	118.5	118.3
C6-C8-C10	119.9	119.8	119.8	120.1
C8-C10-C12	120.3	120.5	120.5	120.3
C10-C12-C14	119.3	119.2	119.2	119.2
C37-C38-C40	121.2	121.1	121.1	121.5
C37-C46-C44	121.4	121.5	121.5	121.9
C38-C37-C46	117.7	117.8	117.8	117.3
C38-C40-C42	120.0	120.0	120.0	119.7
C41-C42-C44	119.8	119.9	119.9	120.3

Continued on next page

Table S2: Calculated bond angles (in °) of the optimized (DPEPhos)Cu(PyrTet) complex in vacuum in comparison to the crystal structure.

angle	S_0	S_1	T_1	crystal structure
C42-C44-C46	119.8	119.7	119.7	119.4
C70-C72-C74	118.3	119.7	120.0	119.4
C72-C74-C76	119.3	117.3	117.3	118.9
C74-C76-C78	118.7	120.6	120.7	118.6
C76-C78-C79	123.2	125.6	125.9	123.3
C72-C70-N69	122.7	123.4	123.4	122.9
C76-C78-N69	121.7	121.7	121.7	122.7
C78-C79-N80	129.6	133.5	133.6	128.1
C78-C79-N83	119.9	117.3	117.2	119.7
C79-C78-N69	115.0	112.6	112.4	114.0
C79-N80-N81	104.8	105.2	105.2	104.1
C79-N83-N82	105.7	106.9	106.8	105.1
N80-N81-N82	110.3	111.1	111.2	110.0
N81-N82-N83	108.7	107.7	107.6	108.5
Cu1-N83-N82	141.9	138.8	139.8	141.8
Cu1-N69-C70	129.5	127.6	129.8	129.2
Cu1-N69-C78	111.3	111.9	113.2	113.3
Cu1-N83-C79	112.4	113.1	113.2	112.0
Cu1-P2-C5	111.9	115.1	114.1	107.1
Cu1-P3-C37	119.9	116.2	115.6	120.7
C6-C5-P2	123.7	124.2	124.1	123.7
C14-C5-P2	117.6	117.1	117.2	117.2
C38-C37-P2	122.5	121.4	121.3	122.8
C46-C37-P3	119.6	120.6	120.8	119.9
C5-C14-O4	116.2	115.8	115.8	115.3
C12-C14-O4	122.4	122.9	122.8	123.1
C37-C46-O4	120.1	119.7	119.8	120.1
C44-C46-O4	118.4	118.7	118.7	117.9

Continued on next page

Table S2: Calculated bond angles (in °) of the optimized (DPEPhos)Cu(PyrTet) complex in vacuum in comparison to the crystal structure.

angle	S_0	S_1	T_1	crystal structure
C14-O4-C46	119.8	120.0	119.8	118.4
N69-Cu1-P2	117.4	102.0	105.1	113.2
N69-Cu1-P3	113.9	143.9	139.8	118.1
N83-Cu1-P2	120.2	129.8	129.0	117.4
N83-Cu1-P3	107.3	95.4	94.8	109.0
N69-Cu1-N83	81.3	83.9	83.9	80.5
P2-Cu1-P3	113.0	105.8	106.6	114.4

S3 Trigonal vs. linear NHC-Cu(I)-pyridine complexes

For the $[\text{IPr-Cu-Py}]^+$ and $[\text{IPr-Cu-Pyz}]^+$ complexes the original Grimme Hamiltonian with standard parameters was used in the DFT/MRCI runs.[7] At the ground-state geometry, 21 singlet and 20 triplet roots were calculated and at the excited state geometries 11 singlet and 10 triplet roots were computed.

S4 Carbene-Cu(I)-pyridine complexes

For the -Cu-Py and DAC-Cu-Py complexes, the R2016 Hamiltonian with tight parameters was used.[3] The selection threshold was set on 0.6 E_h in the first and on 0.8 E_h in the second run. In all calculations, 30 singlet and 30 triplet roots were computed.

S5 Carbene-Cu(I)-carbazolide complexes

For all DFT/MRCI calculations of the complexes with the carbazolide ligand and for the CAAC-Cu-Py and DAC-Cu-Py complexes, the R2016 Hamiltonian with tight parameters

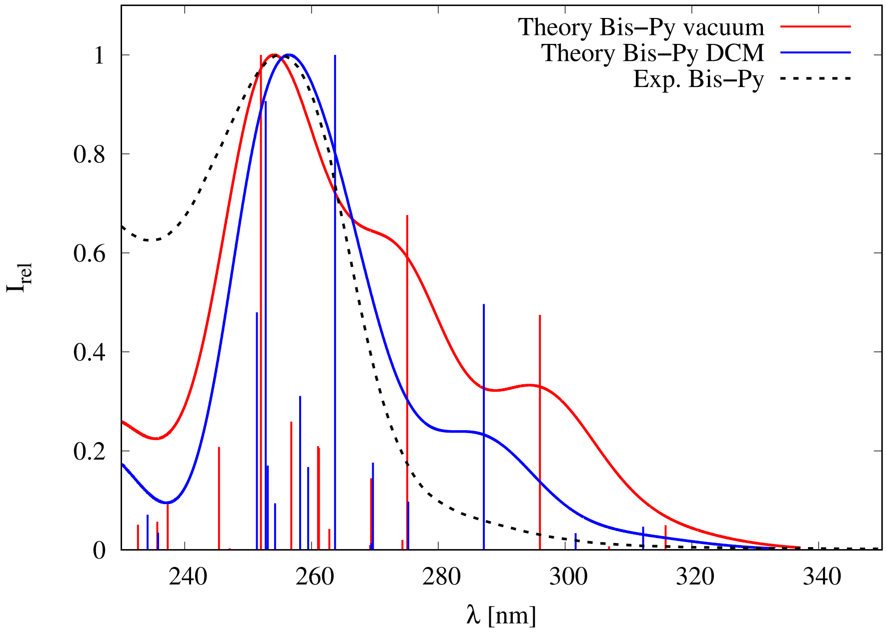

Figure S4: Calculated absorption spectra in vacuum (red) and in DCM (blue) of the [IPr-Cu-Py_2]$^+$ complex in comparison to the experimental spectrum in DCM (black).

was used.[3] The selection threshold was set on 0.6 E_h in the first and on 0.8 E_h in the second run. For the CAArC-Cu-Cz and DAC-Cu-Cz complexes 20 singlet and 20 triplet roots and for the other complexes 30 singlet and 30 triplet roots were computed.

S6 Carbene-Cu(I)-chlorides

The DAC-Cu-Cl and NHC-Cu-Cl complexes were optimized with implicit THF solvation of PCM[5] and Gaussian 16.[6] The CAAC^{Me}-Cu-Cl complex is strongly affected by solvation. Solvation effects have to be taken into account in the excited states as well. PCM was used for the ground state, while for the implicit solvation with THF of the S_1 and T_1 states, the corrected Linear Response (cLR) model was chosen.[8] The PCM and cLR point charges were generated and ulitized for DFT/MRCI calculation with the R2016 Hamiltonian and tight parameters.[3] In all DFT/MRCI calculations 30 singlet and 30 triplet roots were calculated and a selection threshold of 0.8 E_h was chosen.

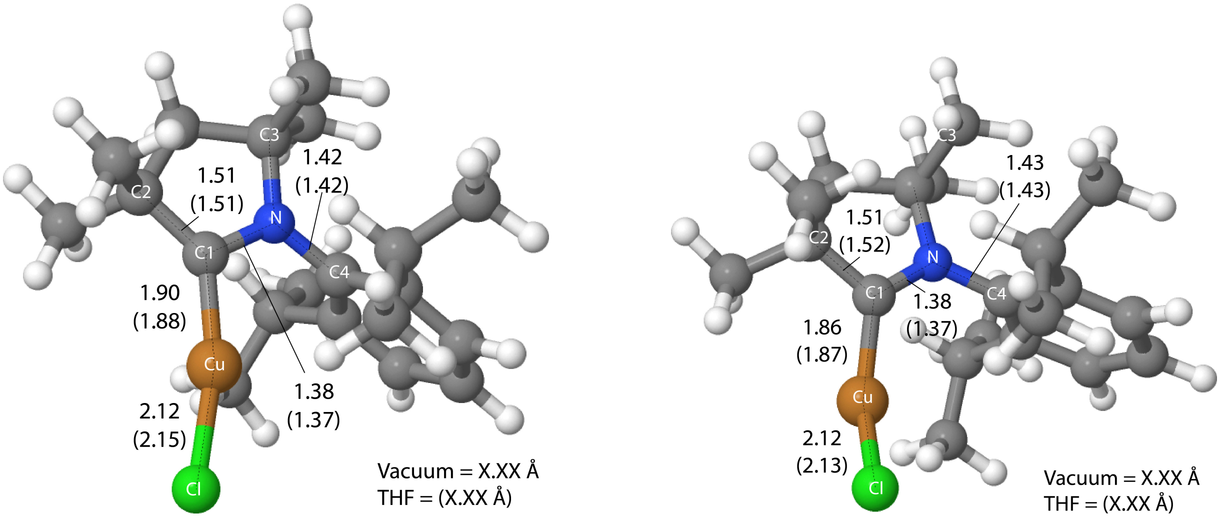

Figure S5: Singlet and triplet excited-state geometries of CAAC^{Me}-Cu-Cl in vacuum showing selected bond lengths (in Å units): Left S_1, right T_1. Corresponding values for THF solution in the cLR environment are shown in parentheses.

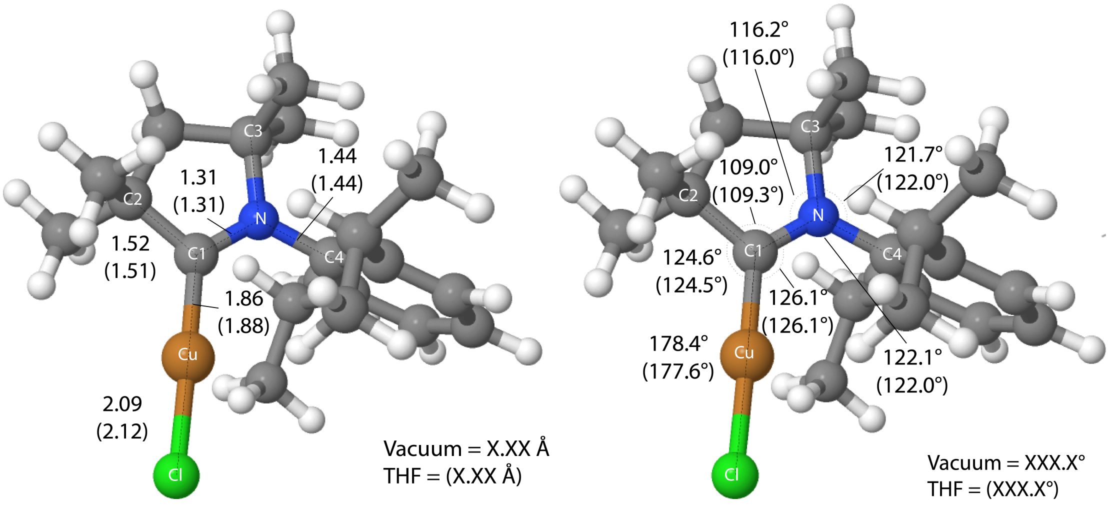

Figure S6: Ground-state geometry of CAAC^{Me}-Cu-Cl in vacuum showing selected bond lengths (left in Å units) and bond angles (right). Corresponding values for THF solution in the PCM are displayed in parentheses.

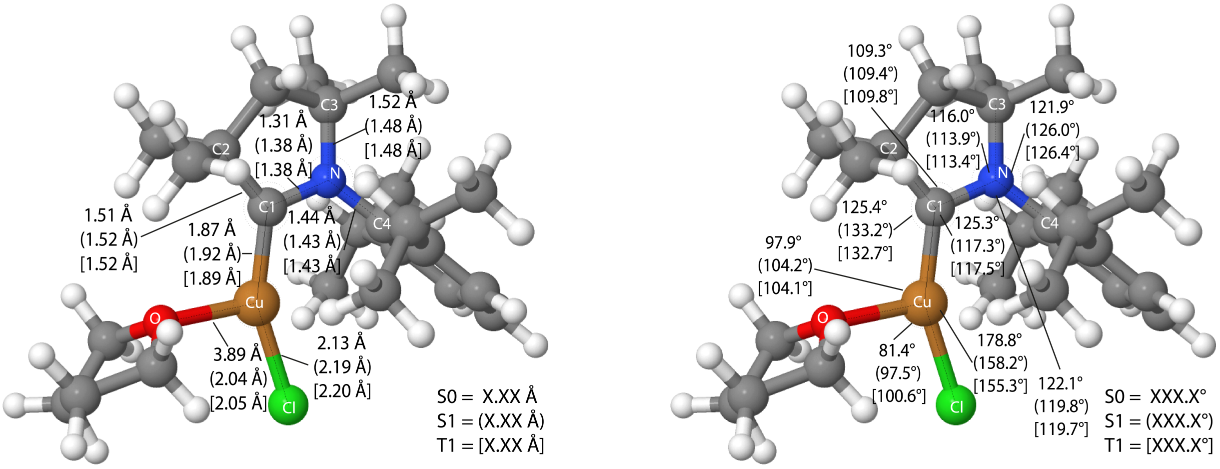

Figure S7: CAAC$^{\mathrm{Me}}$-Cu-Cl with an explicit THF molecule showing selected bond lengths (left in Å units) and bond angles (right) of the ground state and the first excited singlet and triplet states in implicit THF solution.

References

(1) Grimme, S.; Antony, J.; Ehrlich, S.; Krieg, H. A consistent and accurate ab initio parametrization of density functional dispersion correction (DFT-D) for the 94 elements H-Pu. *J. Chem. Phys.* **2010**, *132*, 154104.

(2) Grimme, S. Density functional theory with London dispersion corrections. *WIREs Comput. Mol. Sci.* **2011**, *1*, 211–228.

(3) Lyskov, I.; Kleinschmidt, M.; Marian, C. M. Redesign of the DFT/MRCI Hamiltonian. *J. Chem. Phys.* **2016**, *144*, 034104.

(4) Heil, A.; Kleinschmidt, M.; Marian, C. M. On the performance of DFT/MRCI Hamiltonians for electronic excitations in transition metal complexes: The role of the damping function. *J. Chem. Phys.* **2018**, *149*, 164106.

(5) Miertuš, S.; Scrocco, E.; Tomasi, J. Electrostatic interaction of a solute with a continuum. A direct utilizaion of AB initio molecular potentials for the prevision of solvent effects. *Chem. Phys.* **1981**, *55*, 117 – 129.

(6) Frisch, M. J. et al. Gaussian 16 Revision B.01. 2016; Gaussian Inc. Wallingford CT.

(7) Grimme, S.; Waletzke, M. A Combination of Kohnham Density Functional Theory and Multi-Reference Configuration Interaction Methods. *J. Chem. Phys.* **1999**, *111*, 5645–5655.

(8) Caricato, M.; Mennucci, B.; Tomasi, J.; Ingrosso, F.; Cammi, R.; Corni, S.; Scalmani, G. Formation and relaxation of excited states in solution: A new time dependent polarizable continuum model based on time dependent density functional theory. *J. Chem. Phys.* **2006**, *124*, 124520.

Paper II

ChemPhotoChem

Research Articles
doi.org/10.1002/cptc.202200142

Chemistry Europe
European Chemical Societies Publishing

www.chemphotochem.org

Special Collection

Revisiting Ligand-to-Ligand Charge Transfer Phosphorescence Emission from Zinc(II) Diimine Bis-Thiolate Complexes: It is Actually Thermally Activated Delayed Fluorescence

Nora Lüdtke,[a] Julia Kuhnt,[b] Tabea Heil,[b] Andreas Steffen,*[b] and Christel M. Marian*[a]

In this work we revisit and re-evaluate the photophysical behavior of the prototypical complex [Zn(SC$_6$H$_4$-4-R)$_2$(phen)] as the most in-depth studied type of Zn(II)-based triplet state emitters. Previous reports suggest population of ligand-to-ligand charge transfer (LLCT) states via phenanthroline localized ππ* states, with an energy barrier between the ^{3}ππ* and the bk;$^{1/3}$LLCT states requiring thermal activation. Besides very weak prompt fluorescence, the dominant radiative mechanism was attributed to phosphorescence. Our photophysical studies, including temperature-dependent quantum yield determination and time-resolved luminescence measurements, reveal a high radiative rate constant $k_r = 3.5 \times 10^5\ \mathrm{s}^{-1}$ at room temperature and suggest thermally activated luminescence as the major emission path. High-level DFT/MRCI calculations confirm this assignment and provide deeper insight into the excited-state kinetics, including rate constants for the (reverse) intersystem crossing processes. Thus, our study demonstrates that further optimization of the photophysical properties of this type of Zn(II) triplet exciton emitter bears great potential for future application in devices.

Introduction

Luminescent transition metal complexes play a vital role for the development of imaging agents, sensing applications, photocatalysts or as emitters in light generating devices. The latter application in particular depends on the efficiency of the luminophores to emit from triplet excited states because the excitation process leading to electroluminescence occurs via recombination of holes and electrons as charge carriers, generating 25% singlet and 75% triplet states according to spin statistics. Various strategies have been tested to harvest all excitons in electroluminescent devices, of which the two most promising appear to be the employment of phosphorescent transition metal complexes of 5d elements with high spin-orbit coupling (SOC) such as iridium or platinum, or of thermally activated delayed fluorescence (TADF) emitters.[1–3] Bypassing the spin-forbidden triplet emission via reverse intersystem-crossing (rISC) and subsequent spin-allowed luminescence from the S$_1$ state reduces the importance of SOC for triplet exciton harvesting, and even organic TADF emitters can be very attractive luminophores exhibiting high quantum yields and relatively short lifetimes of a few microseconds. It is noteworthy that a class of linearly coordinated photoactive d^{10} coinage metal complexes, designed according to a donor-acceptor motif, show particularly large radiative rate constants which can exceed $k_r > 2 \times 10^6\ \mathrm{s}^{-1}$.[4–7] A small admixture of metal-to-ligand charge transfer (MLCT) character to the S$_1$ and T$_1$ states of dominantly ligand-to-ligand (LL)CT nature in those Cu$^{\mathrm{I}}$/Ag$^{\mathrm{I}}$/Au$^{\mathrm{I}}$ carbene amide complexes enhances the SOC contribution and accelerates the spin-forbidden processes.[8–10]

In contrast to group 11 metal complexes in their d^{10} electron configuration, light-emitting Zn(II) complexes are often brightly fluorescent with the lowest-lying states originating either from ligand-centered (LC) or LLCT excitations.[11–16] Owing to the high ionization potential of the Zn^{2+} core, MLCT contributions mediating SOC are not to be expected, although there are indications that ligand-to-metal (LM)CT excitations involving the 4p shell of Zn might contribute to the wavefunctions of some complexes and thereby could enhance intersystem crossing (ISC). Consequently, electroluminescent Zn(II) complexes have mainly been employed as emitters in fluorescent OLEDs and as host materials for phosphorescent OLEDs containing iridium complexes as dopants.[17] However, Adachi and coworkers recently reported the use of a Zn(II) complex featuring $^{1/3}$intra-ligand ($^{1/3}$IL)CT states with very small singlet-triplet energy gap ΔE(T$_1$–S$_1$) for TADF-based OLEDs.[18] Mixed LLCT and ILCT transitions were also held responsible for the intense orange to deep red luminescence of triarylamine-

---

[a] N. Lüdtke, Prof. Dr. C. M. Marian
Institute of Theoretical and Computational Chemistry
Heinrich-Heine-University Düsseldorf
40204 Düsseldorf (Germany)
E-mail: Christel.Marian@hhu.de

[b] J. Kuhnt, T. Heil, Prof. Dr. A. Steffen
Faculty of Chemistry and Chemical Biology
TU Dortmund University,
Otto-Hahn-Str. 6, 44227 Dortmund (Germany)
E-mail: Andreas.Steffen@tu-dortmund.de

Supporting information for this article is available on the WWW under https://doi.org/10.1002/cptc.202200142

An invited contribution to a Special Collection on Emissive Materials for Organic Light Emitting Diodes

containing Zn(II) diimine bis-thiolate complexes, of which the authors do not define the type of emission, but we note that the quantum yield ϕ and observed lifetimes τ are indicative of fluorescence.[19]

Only a few phosphorescent Zn(II) complexes have been reported in the literature, including a hemicage Zn bipyridyl complex ZnL_3 ($L_3 = m$-(bpy(C_2H_4))$_3C_6H_3(CH_3)_3$, with bpy = 2,2′-bipyridine),[20] Zn porphyrins[21–23] and several representatives of a broader class of [Zn(thiolate)$_2$(diimine)] complexes.[24–30] Very recently, ultra-long lifetimes in the millisecond regime were reported for cyclic (alkyl)(amino)carbene (cAAC) complexes of Zn(II) halides at 77 K and shown to stem from ligand-centered triplet states.[31] While ISC and phosphorescence of Zn(II) porphyrins are known to be vibronically induced,[32] the underlying mechanisms operative in the Zn(II) diimine dithiolates are not well understood despite some very sophisticated and detailed studies conducted by Crosby and coworkers.[25,27,28] The authors observed for a series of [Zn(SC_6H_4-4-R)$_2$(phen)] complexes (phen = 1,10-phenanthroline; R=H, Cl, Me, OMe) temperature-dependent dual luminescence in organic glass and in the crystalline solid state that has been attributed to vibrationally resolved high energy phosphorescence from a ^{3}LC(phen) state with ultralong lifetimes in the millisecond regime and simultaneous broad emission from a lower energy LLCT state. Thermally modulated emission spectroscopy (TME) measurements suggest that these two luminescent states are not in thermal equilibrium and the following scheme has been proposed. Photoexcitation primarily populates high energy ^{1}LLCT and LC(phen) states, which convert via branched decay paths to vibrationally relaxed ^{1}LLCT, ^{3}LLCT, and ^{3}LC (phen) states (Scheme 1). Whether the ^{3}LLCT state is populated directly by vibrationally hot ^{1}LLCT and LC(phen) states or via the equilibrated ^{1}LLCT state remained an open question. Clear is that a path with a thermally surmountable barrier connects the energetically higher ^{3}LC(phen) minimum with the global minima of the S_1 and T_1 potentials, respectively, of LLCT type. A back transfer from the equilibrated LLCT states to the ^{3}LC (phen) state is not expected.

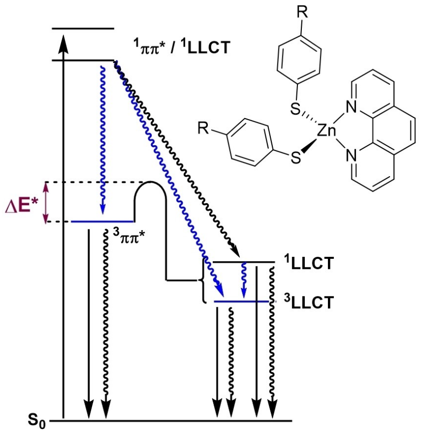

Scheme 1. Chemical structure of [Zn(SC_6H_4-4-R)$_2$(phen)] (R=H, Me, Cl, OMe) and excited-state decay mechanism upon photoexcitation as proposed by Crosby *et al.*[27,28]

Later work by Burt *et al.*[33] indicated that the barrier heights and transition probabilities might not only depend on the chemical composition of the Zn(II) complex. Specifically, luminescence studies at 5 K on structurally related [Zn(SC_6H_4-4-Cl)$_2$(2,9-Me_2-phen)] in the single crystalline solid state showed for the $P2_1/N$ phase a highly structured emission with λ_{max} at 452 nm and a broad, structureless emission with λ_{max} = 540 nm. The same general features are also found in PMMA films, but in the $P2_1/C$ crystal phase the complex exhibits only a structureless band at 570 nm. The high-energy band has been assigned to phosphorescence from a $^3\pi\pi^*$ state localized at the phen ligand, and the broader lower-energy band to LLCT transitions.[33] The authors conclude that the barrier is molecular in nature, but its height depends on the geometry determined by the packing in the crystals, which supports the original assumption by Highland *et al.*[27,28]

In conjunction with our current quest to explore Zn(II) complexes as potential TADF emitters, the probability of a further process in Scheme 1 attracts attention, namely the repopulation of the ^{1}LLCT state by rISC from the ^{3}LLCT state. Thus, the present joint theoretical and experimental study sets out to investigate the electronic structures and excited-state properties of such Zn(II) complexes to elucidate structure-property relationships for their possible application as TADF emitters.

Results and Discussion

We have chosen the previously studied complex [Zn(SC_6H_4-4-Cl)$_2$(phen)] (**1**) as model compound for an in-depth photophysical and theoretical study, and compare the findings with those obtained from further calculations for [Zn(SC_6H_4-4-Me)$_2$(phen)] (**2**) to elucidate the excited-state behavior of this general class of emitters.

Ground State and Absorption Properties

In contrast to Crosby et al., we have opted for THF as alternative solvent instead of $CHCl_3$/EtOH (1:19) to record the absorption due the higher solubility of **1** and because we experienced minor decomposition after prolonged irradiation in the original solvent combination. The appearance of the spectra at room temperature is identical to those previously reported albeit the absorption coefficients are slightly higher by a factor of ca. 1.5 (Figure 1).

The lowest energy absorption is very broad and found between λ_{abs} = 320–425 nm with low intensity (ε = 1,500 $M^{-1}cm^{-1}$), followed by a more allowed transition at λ_{abs} = 290 nm (ε = 19,000 $M^{-1}cm^{-1}$) and a high-intensity absorption with a maximum at λ_{abs} = 273 nm (ε = 60,000 $M^{-1}cm^{-1}$). Our concentration dependent measurements demonstrate that no ligand dissociation, aggregation or decomposition occurs that might interfere with the analysis of the photophysical data of the molecular species. The solid absorption shows the same general bands, although the infinite concentration results in

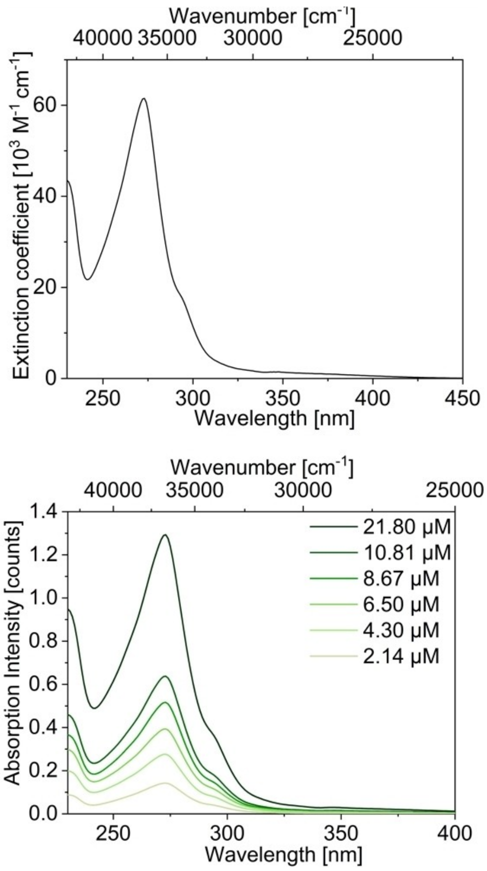

Figure 1. Concentration-dependent absorption spectra of [Zn(SC$_6$H$_4$-4-Cl)$_2$(phen)] (**1**) recorded in THF at room temperature.

significant vibrational broadening (Figure S4). However, it is important to note that in contrast to well-established photoactive Cu(I) phenanthroline complexes of the type [Cu(phen)(N^N/P^P/P$_2$)] (N^N=diimine, P^P=chelating phosphines, P=monodentate phosphines), which typically exist in only one conformation due to the steric bulk of the ligand sphere, the solution spectra represent an average over all conformers that can arise from rotation of the arylthiolate ligands, which also influence the luminescence behavior (*vide infra*).

Indeed, our calculations, using ethanol as solvent in the PCM implicit solvation model to account for the expected strong electrostatic solvent-solute interactions (see Methods), identified two major conformers in the ground state. One conformation is an open form with the arylthiolates arranged face-to-face and pointing away from the phen ligand (**1 A**/**2 A**) (Figure 2), as previously found for **1** in the single crystalline solid state by Cremers et al.[34] In the second conformer one of the arylthiolate ligand is backfolded towards the phenanthroline (**1 B**/**2 B**) which slightly destabilizes this nuclear arrangement in the electronic ground state by ca. 0.10 eV and should thus be accessible in the liquid phase. Due to the favorable Coulomb interaction between the donor and acceptor moieties after CT, the backfolded structures are preferred over the straight ones in the LLCT states, however (*vide infra*). Crystal structures of backfolded 1,10-phenanthroline zinc(II) bis(thiolate) complexes and methylated derivatives thereof were reported by Jordan et al.[26] and Scheins et al.[35] The X-ray analysis of single crystalline samples of **1** (Figure S3 of the Supporting Information) confirms a backfolded molecular structure in our solid-state experiments as well.[71]

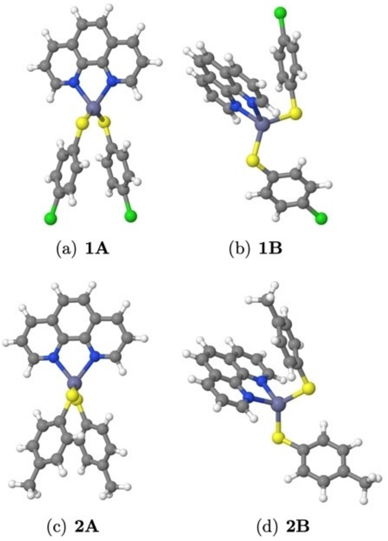
(a) **1A** (b) **1B**

(c) **2A** (d) **2B**

Figure 2. Computationally investigated conformers of complexes **1** and **2**.

Figure 3 shows the calculated absorption spectra of the two conformers of **1**. Corresponding spectra of **2** are displayed in

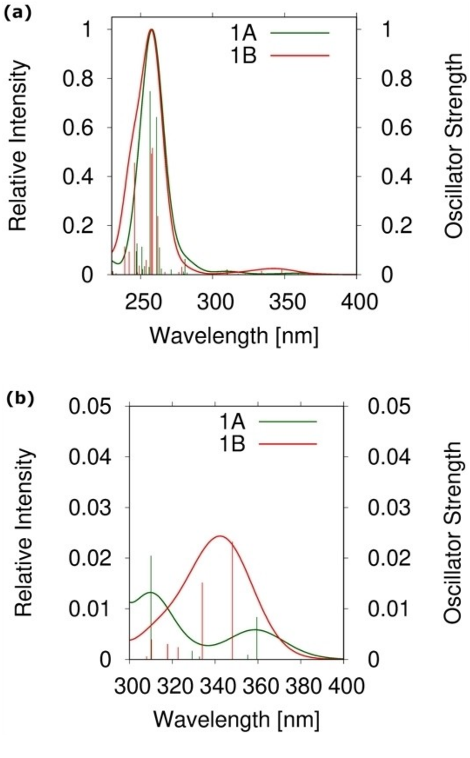

Figure 3. a) Calculated absorption spectra in implicit ethanol environment of conformers **A** (green) and **B** (red) of [Zn(SC$_6$H$_4$-4-Cl)$_2$(phen)] (**1**). b) Zoom in the low energy region.

Figure S8 of the ESI. Their envelopes were obtained by broadening the line spectra with Gaussians of 1000 cm^{-1} width and normalizing the intensity to the height of the peak in the 250–260 nm wavelength region. To get an impression of the intensity variations between the open forms **1 A** and **2 A** on the one hand and the backfolded conformers **1 B** and **2 B** on the other hand, the oscillator strengths of the spectral lines were left unscaled.

For all considered conformers, a broad peak in the short wavelength regime with a maximum at about 250–260 nm is found (Figures 3(a) and S8(a) of the ESI), which coincides well with the experimental results in solution (Figure 1 and Ref. [24]). The strongly absorbing states exhibit primarily LC character localized either on the phen or the thiolate ligands.

Their electron density differences are depicted for compound **1 A** in Figure 4 as S_{13} and S_{17}, respectively. Because the phen ligand is the same for all considered structures, the excitation wavelengths of its LC states vary only slightly among the compounds. The thiol-localized states are more sensitive with respect to the substituent in 4-position of the arene ring. For example, the most intense LC(thiolate) transition in **1 A** is bathochromically shifted with respect to the corresponding state in **1 B** by 0.16 eV and has only half the oscillator strength of the latter. CT contributions from sulfur lone-pair orbitals to the phen or thiolate π systems are found in nearly all transitions whereas contributions involving the Zn atom are negligible.

Much weaker transitions occur in the longer wavelength regime (Figure 3(b), Figure S8(b) in the Supporting Information). The maximum of the lowest-lying LC(phen) state, S_5 or S_6 depending on the specific compound and conformer (Figure 4), is rather constant at 305–310 nm. Interestingly, its oscillator strength is very conformation-dependent and one order of magnitude higher in the open form **1 A**/**2 A** than in the backfolded conformation **1 B**/**2 B**. In contrast, the position of the $S_1 \leftarrow S_0$ excitation of ^{1}LLCT nature is more ligand dependent and possesses a 3–5 times lower oscillator strength in the open forms **1 A** ($\lambda = 359$ nm, $f = 0.008$) and **2 A** ($\lambda = 378$ nm, $f = 0.005$) than in the backfolded conformers **1 B** ($\lambda = 348$ nm, $f = 0.023$) and **2 B** ($\lambda = 367$ nm, $f = 0.028$). These low-energy transitions agree nicely with the very weak and broad absorption band of $[Zn(SC_6H_4\text{-}4\text{-}Cl)_2(phen)]$ (**1**) in THF solution between 320–425 nm (Figure 1), which has also been found in other solvents and for other derivatives. Despite the good overall agreement between theory and experiment that supports the presence of conformers in solution and in the solid state, this comparison is not conclusive with regard to the population ratios of open **A** vs. folded **B**.

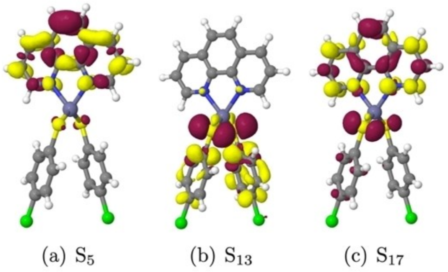
(a) S_5 (b) S_{13} (c) S_{17}

Figure 4. DFT/MRCI difference densities of the most prominent singlet LC excitations of compound **1 A** at the S_0 geometry in ethanol. Areas losing electron density in comparison to the electronic ground state are shown in red (isovalue −0.001), areas gaining electron density in yellow (isovalue +0.001).

According to our analysis, at least one ^{3}LLCT state and one ^{3}LC (phen) state are found in the vicinity of the lowest ^{1}LLCT state in the FC region (see Tables 1 and 2). The electron density distributions of the ^{3}LLCT states are very similar to their singlet counterparts, as exemplified for compound **1 A** in Figure 5. Difference densities for the most relevant excited states of the

Table 1. DFT/MRCI excitation energies (ΔE/eV) of **1 A** in ethanol at various molecular geometries. The DFT/MRCI energy of the S_0 state at the DFT optimized S_0 minimum geometry in a polarizable ethanol environment serves as common origin. 0-0 energies including zero-point vibrational energy corrections are given in parentheses.

State	Optimized geometry			
	S_0	S_{LLCT}[a]	T_{LLCT}[a]	$T_{LC(phen)}$
S_0	0.00	0.39	0.53	0.35
S_{LLCT}	3.44	2.25 (**2.17**)	2.50	3.64
S'_{LLCT}	3.48	2.93	3.14	3.66
T_{LLCT}	3.38	2.17	2.35 (**2.24**)	3.60
T'_{LLCT}	3.43	2.89	3.06	3.63
T_{LC}	3.34	–	3.71	2.84 (**2.68**)
T'_{LC}	3.58	–	3.81	3.58

[a] Structure with one strongly elongated Zn-thiolate bond.

Table 2. DFT/MRCI excitation energies (ΔE/eV) of **1 B** in ethanol at various molecular geometries. The DFT/MRCI energy of the S_0 state at the DFT optimized S_0 minimum geometry in a polarizable ethanol environment serves as common origin. 0-0 energies including zero-point vibrational energy corrections are given in parentheses. The ground state of conformer **1 B** lies 0.11 eV above conformer **1 A** in implicit ethanol solution

State	Optimized geometry			
	S_0	S_{LLCT}	T_{LLCT}	$T_{LC(phen)}$
S_0	0.00	0.39	0.39	0.36
S_{LLCT}	3.56	2.11 (**2.05**)	2.11	3.78
S'_{LLCT}	3.71	2.82	2.82	3.94
T_{LLCT}	3.48	2.05	2.05 (**1.99**)	3.74
T'_{LLCT}	3.72	2.78	2.78	3.90
T_{LC}	3.37	3.59	3.59	2.82 (**2.66**)
T'_{LC}	3.58	3.66	3.66	3.56

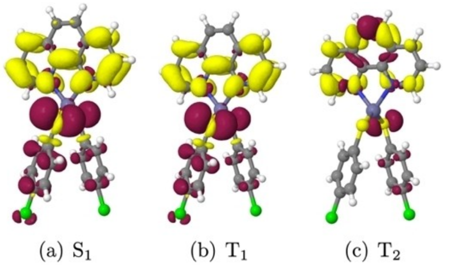
(a) S_1 (b) T_1 (c) T_2

Figure 5. DFT/MRCI difference densities of the low-lying singlet and triplet excitations of compound **1 A** in ethanol at the S_0 geometry. For color codes and isovalues, see Figure 4.

other compounds are found in Figures S9-S14. The Zn ion does not appear to be involved in these low-lying excitations.

Note that the ^{3}LC (phen) wave function exhibits marked sulfur→phen CT contributions in the FC region, with consequences for its SOC ability (see below). The heavy-atom effect caused by the participation of the sulfur lone pair orbitals in the excitation of the ^{1}LLCT, ^{3}LLCT and ^{3}LC (phen) states in conjunction with their close energetic proximity opens the chance for substantial singlet-triplet mixing in the absorption region and could explain the branched triplet population kinetics. Indeed, we observe very strong SOC between different LLCT states in the FC region, designated by unprimed and primed symbols in Tables 1 and 2 (see also Tables S4 and S5 in the Supporting Information). In the open forms **1 A** and **2 A**, for example, the S_{LLCT} and T'_{LLCT} states are nearly degenerate. With values of 20.8 and 18.5 cm^{-1}, respectively, their mutual spin-component averaged SOCMEs are large enough to cause substantial mixing of singlet and triplet character. SOCMEs of similar magnitudes (21.6 and 19.0 cm^{-1}) are found for the S'_{LLCT} and T_{LLCT} pair of states.

Emission Properties

The emission spectrum of **1** in the solid state at 6.5 K shows three bands that vary in intensity in dependence of the temperature (Figure 6). A vibrationally resolved high energy band is observed between $\lambda_{em}=365$–450 nm that has not been reported by Crosby et al., which we assign to residual fluorescence from a ^{1}LC (phen) state due to its very short lifetime of $\tau \ll 15$ ns. We exclude the presence of free 1,10-phenanthroline being responsible for this emission on the basis of our analytical characterization and the fact that its fluorescence would yield a much longer lifetime on the nanosecond timescale at such low temperatures. Also, the relative intensities of the fluorescence progressions compared to free phen at 13 K is significantly different (see Figure S5). Furthermore, very weak ^{3}LC (phen) emission occurs with $\lambda_{em}=$ 455–480 nm and an additional very intense, broad and structureless band with an emission maximum at $\lambda_{em}=587$ nm originates from a ^{3}LLCT state. While the intensity of the $^3\pi\pi^*$ band decreases between 6.5 K and 23 K, the ^{3}LLCT emission becomes more pronounced in that temperature range, which confirms that the higher energy ^{3}LC state thermally populates the lower energy state when an activation barrier is surmounted. At higher temperatures $T>23$ K, the phenanthroline ligand phosphorescence is absent and enhanced non-radiative decay also reduces the emission intensity of the CT band. In contrast, Crosby et al. describe an increase in intensity of the ^{3}LLCT emission from 3 K to 35 K, but the difference might be explained as follows.

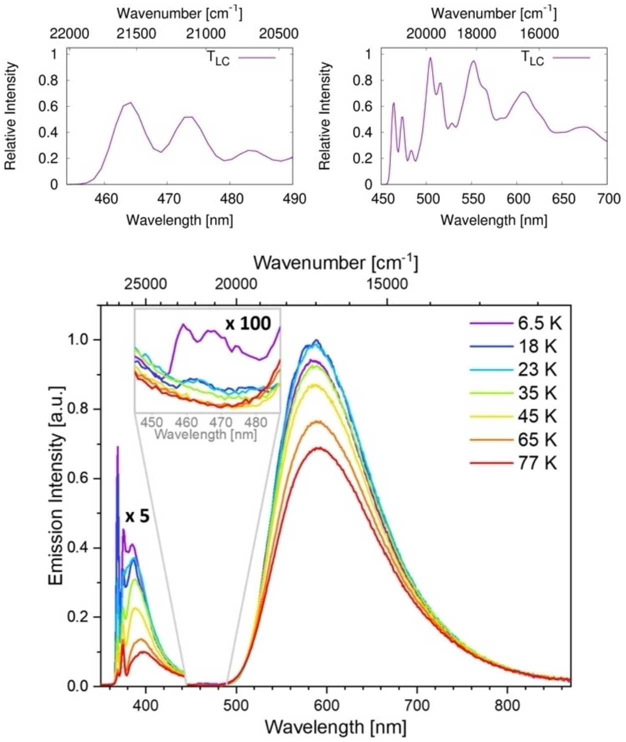

Figure 6. Bottom: Temperature-dependent emission spectra ($\lambda_{Ex}=320$ nm) of a powdered sample of [Zn(SC$_6$H$_4$-4-Cl)$_2$(phen)] (**1**) recorded at 6.5–77 K, including expanded portions of the short-lived emission band emanating from the phen ligand and on the $^3\pi\pi^*$ band. Top: Computed $^3\pi\pi^*$ phosphorescence emission spectrum of conformer **1 A** (right) and expanded portion of the first major peak (left).

A comparison between measurements in rigid glass and crystals of the zinc(II) complexes revealed a different temperature-dependent behavior of the $^3\pi\pi^*$ band depending on the sample preparation: While the $^3\pi\pi^*$ band is still visible at 77 K in the rigid glass, it is completely quenched at 35 K in the crystal. As mentioned in the introduction, the different emission properties of a related complex in *P*2$_1$/*N* vs. *P*2$_1$/*C* crystal phases had led to the conclusion that geometrical restriction is a crucial factor effecting the energy barrier connecting LC and LLCT states (Scheme 1).[26,33] The most significant difference between the two crystal structures is the relative orientation of the thiolate ligands. Analysis of the reaction paths connecting the T_{LC} and T_{LLCT} minima (*vide infra*) furthermore suggest that large amplitude motion of one thiolate ligand promotes the internal conversion. Thus, assuming weaker geometrical restrictions in the powdered sample as a result of a less rigid environment, a faster population of the $^{1/3}$LLCT states and increase in intensity would be expected first. However, more facile non-radiative processes should then become dominant in the powder at lower temperatures than in the crystalline samples, which is what we observe. For further discussion of the emission process, it is important to note that neither the emission onset nor the offset shift when the temperature is raised to 77 K.

^{3}LC Emission

Time-resolved luminescence measurements reveal for the ^{3}LC emission at 6.5 K a tri-exponential decay with a shorter lifetime of $\tau_{av}=274$ ms than the earlier value of the mono-exponential $\tau=390$ ms, but the intensity was too low to reliably determine the lifetime for higher temperatures although Crosby et al. reported a lifetime of 40–45 ms even at 23 K. The short lifetime component is presumably due to tunneling through the barrier connecting the ^{3}LC and LLCT potentials (*vide infra*).

Vibronic ^{3}LC phosphorescence spectra of **1 A** are displayed in Figure 6 top. Very similar spectra are obtained for **1 B**, **2 A** and **2 B** (see Figures S15–S17). Their 0-0 energies range between 2.67 and 2.71 eV (21,500–21,900 cm^{-1}), in excellent agreement with experiment. Highland et al.[28] assumed the first vibrational peak to be the band origin and reported onsets of 21,800 cm^{-1} and 21,200 cm^{-1} for the $^3\pi\pi^*$ luminescence of **1** and **2**, respectively. According to our calculations, the pronounced vibrational progressions can predominantly be associated with a stretching vibration of the C_5-C_6 bond of the phenanthroline backbone ($\nu = 1{,}760$ cm^{-1} in the S_0 state) and a bending vibration of the N_1–Zn–N_{10} bite angle ($\nu = 441$ cm^{-1} in the S_0 state). The highest maxima in the calculated phosphorescence spectra are the second peaks at about 20,000 cm^{-1}. Both, the shapes and peak positions, match very well with a low-temperature luminescence spectrum of the [$ZnCl_2$(phen)] complex where the LLCT states are absent.[28] Computed component-averaged radiative lifetimes of the ^{3}LC(phen) phosphorescence range from about 3 s for **1 A** and **1 B** to about 2 s for **2 A** and **2 B**. These are typical values for a pure $^3\pi\pi^*$ emission, but they are about an order of magnitude larger than the experimentally determined lifetimes of the blue-green emission at 6.5 K. One explanation for the difference between measured and computed lifetimes is the FC approximation applied in the calculations. Coupling between vibrational and electronic degrees of freedom is known to enhance the probability of weak spin-forbidden transitions.[62–65] Another explanation takes account of the fact that the energy barrier for the $^3\text{LC} \rightsquigarrow {}^3\text{LLCT}$ internal conversion is very low suggesting that the measured lifetimes entail contributions from non-radiative deactivation channels.

On the basis of TME experiments, Highland et al. estimated a barrier height of ≈140 cm^{-1} for the migration from the $^3\pi\pi^*$ to the LLCT potentials.[28] Qualitatively, our calculations support the conclusions that a thermally surmountable barrier exists between the ^{3}LC and ^{3}LLCT potentials. An upper bound for the energy barrier of the open forms was obtained by calculating energy profiles along linearly interpolated paths connecting the optimized $^3\pi\pi^*$ (phen) and LLCT geometries (Figures 7 and S18 of the Supporting Information). The electronic energy differences between the intersections of the triplet potentials and the respective ^{3}LC minima yields barrier heights of 350 cm^{-1} for **1 A** and 225 cm^{-1} for **2 A**. Both values are somewhat larger than the experimentally estimated energy barrier of 140 cm^{-1}, but still in the right ballpark.

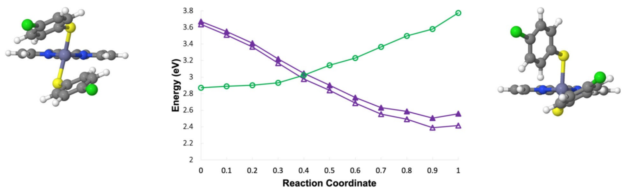

Figure 7. DFT/MRCI energy profiles of **1 A** (middle) in implicit ethanol environment along a linearly interpolated path connecting the connecting the T_{LC} minimum (reaction coordinate 0) with the T_{LLCT} minimum (reaction coordinate 1). Filled symbols: singlets, unfilled symbols triplets, violet: LLCT, green: LC $^3\pi\pi^*$ (phen). Orientation of the thiolate ligands at the T_{LC} minimum geometries (left) and at the intersection between the T_{LC} and T_{LLCT} potentials (right).

To get an idea how the barrier height could possibly be manipulated by chemical substitution, we analyzed the intrinsic reaction coordinate of this transformation. A detailed list of geometry parameters can be found in Tables S4–S9 of the Supporting Information. With regard to the energy, the influence of the substituents in 4-position of the thiol ligands is small, but not negligible. The +I-effect of the Me group leads to slight shifts of the T_{LC} and T_{LLCT} excitation energies in comparison to the chlorinated compound. These shifts have the effect that the crossing between the LC $^3\pi\pi^*$ (phen) state and the LLCT lies in closer proximity to the T_{LC} minimum and that the energy barrier is marginally lower in complex **2 A** than in complex **1 A** (compare Figure 7 and Figure S18). All in all, the effect of the substitution on the energy paths is rather small, however. The geometrical changes in the orientation of the thiol groups have a much stronger influence on the energies than the electronic contributions of the methyl and chloro groups. As described before, the electron hole localizes on one of the two thiolate ligands upon LLCT excitation. The most eye-catching geometry change along the reaction paths relates to the torsion angle of this donor thiolate. The other thiolate ligand does not significantly contribute to the charge transfer and therefore does not undergo substantial geometrical adjustments. While both thiolate ligands are nearly π-stacked in the T_{LC} states of the open forms (Figure 7 left; Figure S18 left), one of them is substantially displaced and the Zn–S bond of this ligand is markedly elongated upon transition from the ^{3}LC to the LLCT geometries (Figure 7 right; Figure S18 right). These geometry changes have only a marginal effect on the T_{LC} state, but they lead to a substantial stabilization of the LLCT states. At the intersection of the triplet potentials, the Zn–S bond is elongated by 0.19 Å in complex **1 A** and by 0.11 Å in complex **2 A** compared to the nuclear arrangements at their respective T_{LC} minima. To hamper the interconversion between the T_{LC} (phen) and LLCT states, it might therefore be advisable to involve a bidentate dithiolate ligand instead of two monodentate thiolate ligands.

Comparison of our experimental data with reported lifetimes shows a distinct difference at low temperatures: At 6.5 K we obtain a much shorter value of $\tau_{av} = 394$ μs (vs. $\tau = 8$ ms), while at 35 K our measured lifetime of 151 μs is similar to the previous one of 130 μs. It is possible that in our case the different sample preparation might lead to a less rigid environment with a lower energy barrier for the rate-determining $^3\text{LC} \rightsquigarrow \text{LLCT}$ transitions, consequently resulting in faster population of the LLCT states at lower temperatures.

LLCT Emission

The ^{3}LLCT lifetimes could be determined by averaging over a tri- or bi-exponential decay, of which the respective components vary between 6.5–297 K (see Table S2 of the Supporting Information). However, we note that we could not reproduce an additional fast lifetime of <15 ns that has previously been observed at all temperatures and rationalized as prompt fluorescence from the ^{1}LLCT state following direct population of this state by the laser pulse (*vide infra*). Our attention was caught by the fact that the average lifetime follows a sigmoidal trend upon raising the temperature, starting with small fluctuations between 6.5 K (394 µs) and 23 K (417 µs) followed by a distinct decline to a value of 4.42 µs at 77 K with an associated averaged radiative rate constant of $k_{r,77K} = \Phi_{em}/\tau_{av} = 7.7\times10^4\ s^{-1}$ ($\Phi_{em,77K} = 0.34$) (Figure 8). The lifetime then further decreases exponentially to a value of 80 ns at room temperature, while the experimentally determined quantum yield of the LLCT band shows a linear trend, suggesting that both the non-radiative (k_{nr}) and the radiative rate constants (k_r) change. Such a behavior is typical for multiple-state emission as found in TADF (TADF = thermally activated delayed fluorescence) emitters, which would be a very attractive mechanism for Zn(II) complexes to obtain high radiative rate constants as it bypasses the spin-forbidden phosphorescence.

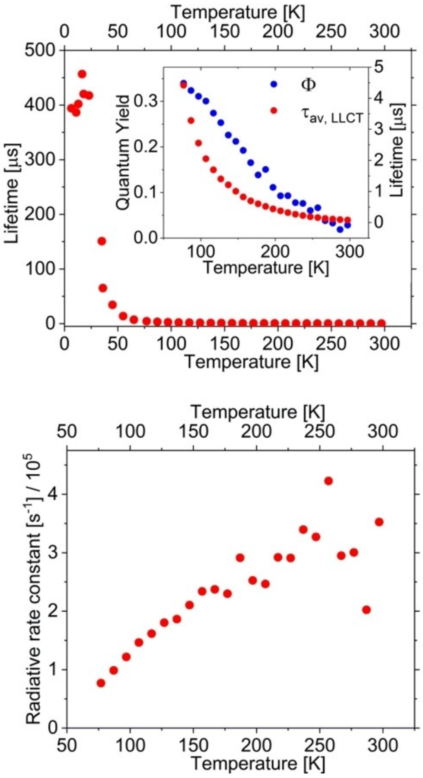

Figure 8. Temperature-dependent averaged observed emission lifetime (red) and quantum yield (blue) (top), and resulting averaged radiative rate constant $k_{r,av}$ (bottom) of the LLCT emission band of [Zn(SC$_6$H$_4$-4-Cl)$_2$(phen)] (**1**) in the solid state.

Evaluation of the temperature-dependence of k_r usually allows to determine the critical excited state parameters of the TADF process by using Eq. (1) for a three-state-model:[40]

$$\tau_{r,av} = \frac{3 + \exp\left(-\frac{\Delta E(S_1-T_1)}{k_B T}\right)}{\frac{3}{\tau(T_1)} + \frac{1}{\tau(T_1)}\exp\left(-\frac{\Delta E(S_1-T_1)}{k_B T}\right)} \quad (1)$$

where k_B is the Boltzmann constant, $\tau(S_1)$ and $\tau(T_1)$ are the radiative decay times of the singlet and triplet excited states, respectively. In this case, it is important to note that the multi-exponential lifetime decay is the result of the properties of the overall solid state sample and provides only an average single lifetime τ_{av}, from which only a $k_{r,av}$ can be determined by measuring the steady state quantum yield Φ of the overall sample. However, the TADF parameters such as $\Delta E(S_1–T_1)$, $\tau(S_1)$ and $\tau(T_1)$ are typically related to a single specific molecular structure. The origin of the multiple lifetime components and their absolute contributions to Φ are unknown, and could be the result of different conformers in the solid state, or of various specific environments and intermolecular interactions. Consequently, some assumptions are necessary in order to reasonably approximate $k_{r,av}$ from the observed τ and Φ. Firstly, the respective emitting states that generate the multiple lifetimes all participate in the same general mechanism. Secondly, their extinction coefficients are not temperature-dependent, which is justified as we have chosen an excitation wavelength in the UV, where $\pi\pi^*$ transitions occur and differences in conformation usually do not play a role. Thirdly, due to the CT character of the emission band and absence of any shoulders, the contributions of the lifetimes do not depend significantly on λ_{em}, which we have confirmed experimentally for a few temperatures. Thus, it is justified to relate the quantum yield from the steady state spectrum to τ_{av} observed at only one emission wavelength. Unfortunately, since the quantum yield is not temperature-independent and our equipment allows measurement of Φ only between 297–77 K, we cannot determine $k_{r,av}$ and $k_r(T_1)$ at lower temperatures. We have therefore simulated two scenarios for $T < 77$ K to estimate a range for the energy difference $\Delta E(S_1–T_1)$ and clarify the feasibility for TADF: a) Φ remains constant at 0.35 or b) linear increase of the quantum yield to reach $\Phi = 0.50$ at 25 K following the trend in Figure 8 (see also Table 3 and Figures S6–S7 of the Supporting Information).

Both scenarios yield rather low values for $\Delta E(S_1-T_1)$ of 242 and 247 cm^{-1} for PLQY of 35 % and 50 %, respectively, that are sensible considering the LLCT character of the involved states and absent temperature-dependent shift of the emission onset, which make a TADF process appear feasible. The radiative

Table 3. Calculated TADF parameters for **1** based on the fitting procedure [Eq. (1)].

	$\Delta E(S_1–T_1^{I,II,III})$ [cm^{-1}]	τ_r(S1) [ns]	$\tau_r(T_1^{I,II,III})$ [µs]
"35 %"-Scenario	247 ± 80	4 ± 14	1181 ± 16
"50 %"-Scenario	242 ± 48	20 ± 38	828 ± 12

lifetime of the emitting triplet state is very long with ca. 1 millisecond ($k_{\mathrm{ph}} = 8\times10^2/1.2\times10^3\ \mathrm{s}^{-1}$) and coincides with an expected weak SOC between the ^{3}LLCT state and S_n states that could provide oscillator strength (see below). Although the prompt fluorescence lifetimes $\tau(S_1)$ are in a range typical for TADF emitters to outcompete phosphorescence from the T_1 state after $T_1 \rightsquigarrow S_1$ rISC, they are certainly too short bearing in mind the enormous CT distance and resulting orbital overlap forbiddance of the transition $S_1 \rightarrow S_0$, which is also displayed in the very small extinction coefficient of the absorption. We explain this with the kinetic scheme underlying the typical TADF fit routine (Eq. (1)) requiring $k_{\mathrm{ISC}} \gg k_{\mathrm{rISC}}$ and both to be faster than either fluorescence k_{f} or phosphorescence k_{ph}, so that S_1 and T_1 can equilibrate before light emission. In addition, non-radiative decay to the electronic ground state is assumed to be markedly slower than radiative decay. The very low $\Delta E(S_1{-}T_1)$ and nearly non-existing transition orbital overlap can lead to $k_{ISC} \simeq k_{rISC}$ and a very small fluorescence rate constant k_f, which might then be on the timescale of k_{ISC}. Consequently, the observed rate constant k_{TADF} of $3.5\times10^5\ \mathrm{s}^{-1}$ at room temperature is then very similar to k_f, giving an estimated $\tau_r(S_1)$ of 2.9 μs (*vide infra*). Again, we emphasize that these calculated values have to be treated with care as this analysis is based on approximations, but nevertheless are quite helpful to evaluate the probability of TADF.

While information about the non-radiative vs. radiative deactivation pathways is available through the measured luminescence quantum yields, ISC and rISC rate constants are not directly accessible from experiment and are computed as follows. The zero-field splittings of the T_{LLCT} sublevels are minuscule (well below 1 cm^{-1}). In that case, the rate constant for singlet-triplet ISC or triplet-singlet rISC from a thermally equilibrated initial electronic state Ψ_a to a final state Ψ_b is given by Equation (2):

$$k^{\mathrm{FC}}_{(\mathrm{r})\mathrm{ISC},ab} = \frac{2\pi}{\hbar g_a Z_a} \underbrace{\sum_{\gamma_b}^{g_b}\sum_{\gamma_a}^{g_a} \left|\langle \Psi_{b,\gamma_b}|\hat{\mathcal{H}}_{\mathrm{SO}}|\Psi_{a,\gamma_a}\rangle\right|^2}_{\text{electronic SOCME}} \underbrace{\sum_{w}\sum_{v} e^{-\beta(E_{a,v}-E_{a,0})} \left|\langle\chi_w|\chi_v\rangle\right|^2 \delta(E_{a,v}-E_{b,w})}_{\text{FCWDOS}} \tag{2}$$

in FC approximation. Herein, g_a and g_b denominate the number of degenerate fine-structure components, v and w the vibrational wavefunctions χ associated to the electronic states Ψ_a and Ψ_b states, respectively, and Z_a is the canonical partition function of vibrational motion in the initial state, defined as [Eq. (3)]:

$$Z_a = \sum_v e^{-\beta(E_{a,v}-E_{a,0})} \tag{3}$$

with $E_{a,0}$ representing the zero vibrational energy of the intial state and $\beta = 1/k_B T$. The Fermi golden rule expression Eq. (2) is essentially determined by three factors:[39] The electronic SOCME, the FCWDOS and the temperature. The spin-component averaged electronic SOCME between the initial and final electronic states enters this equation quadratically. The vibrational density of final states at the energy of a particular vibrational level in the initial electronic state depends upon the geometric and energetic displacements of the respective minima and the vibrational frequencies. The temperature determines the probability of finding the molecule in a particular initial state (partition function Z_a) and broadens the energetic window in which a matching pair of initial and final states can be found in the FCWDOS (delta function).

Rate constants for fluorescence and spin component-averaged phosphorescence have been determined in FC approximation according to Equation (4):

$$k_r^a = \frac{\Delta E_a^3}{3\pi\varepsilon_0\hbar^4 c^3 g_a} \sum_{\gamma_a}^{g_a} \left|\langle \Psi_0|\hat{\mu}|\Psi_{a,\gamma_a}\rangle\right|^2, \tag{4}$$

where $\hat{\mu}$ is the electric dipole operator and $\Delta E_a$is the vertical energy of the electronic state a at its optimized geometry. Ψ_a and Ψ_0 are spin-orbit mixed DFT/MRSOCI wavefunctions of the inital and ground states, respectively. Therefore, Eq. (4) is equally applicable to fluorescence and phosphorescence. The separation of vibrational and electronic degrees of freedom, i.e. the FC approximation, is usually well justified in the case of strong fluorescence emission. In typical TADF emitters with (nearly) perpendicular donor and acceptor moieties and small transition dipole moments, however, vibronic interaction is known to accelerate the fluorescence substantially. Computationally, such interactions have been incorporated either by means of a Herzberg-Teller expansion of the transition dipole moment[41,42] or by addition of derivative coupling terms arising from the nuclear kinetic energy operator.[43] The good agreement between our experimental and computed fluorescence rate constants (*vide infra*) shows that vibronic coupling terms are of minor importance for the S_{LLCT} fluorescence of **1**. They are expected to enhance the weak ^{3}LC phosphorescence, however. We have nevertheless refrained here from evaluating these spin-vibronic interactions because they are computationally very expensive but not decisive for the TADF properties of the complexes.

All dithiolate complexes investigated in our computational study undergo large-amplitude displacements of the thiolate ligands upon geometry relaxation in the respective LLCT state, thereby releasing substantial excess energy with regard to the FC point. As the electronic and nuclear structures of the S_{LLCT} and T_{LLCT} states closely resemble one another, we only display difference densities of the T_{LLCT} states of **1 A** and **1 B** in Figure 9.

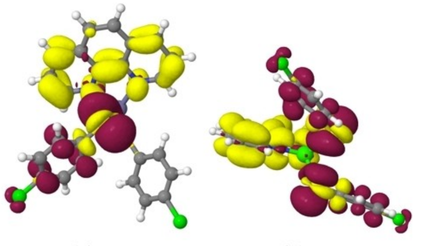

(a) **1A** (b) **1B**

Figure 9. DFT/MRCI difference densities of the T_{LLCT} states at the optimized T_{LLCT} geometries of **1** in implicit ethanol solution. For color codes and isovalues, see Figure 4.

Corresponding difference densities of compound **2** may be found in Figure S19 of the Supporting Information.

The most attractive nuclear arrangement appears to be a folded structure in which one thiolate ligand is placed at an angle with respect to the phen ligand and the other one points away from it. It represents the potential well into which the S_1 states of conformers **1 B** or **2 B** relax after electronic excitation. Here, electron density is transferred from both thiolate groups to the phen ligand. The corresponding T_{LLCT} minima can be found by starting from the optimized S_{LLCT} geometries and searching for the lowest triplet excited state (Figures 9(b) and S19(b) of the Supporting Information). A complication arises when the geometry optimization of the S_1 state is started from the FC point of the stretched-out conformers **1 A** or **2 A**. In this case, a minimum cannot be found for a face-to-face alignment of the thiolates. Due to electrostatic repulsion of the positively charged thiolate residues, one ligand starts rotating about the Zn–S bond and moves toward the negatively charged phen ligand (compare Figures 5 and 9). The excitation then localizes and only one thiolate ligand participates in the LLCT excitation. Moreover, the Zn–S bond of this ligand is elongated to an extent (2.83 Å for **1 A** and 2.69 Å for **2 A**, compared to 2.31 Å in the respective electronic ground state) that it can be considered effectively broken. In densely packed environments such as the crystalline state or rigid glasses, large-amplitude torsional and bending motions of the thiolate ligands are hindered by neighboring molecules.[44] Because the potential energy surfaces are very shallow with respect to torsion and bending angles involving the sulfur atoms of the donor moieties, these geometry restraints are not expected to cause significant energy penalties in the excited state. A comparison of the calculated adiabatic excitation energies with the experimental onsets of the LLCT emission may therefore be meaningful whereas vertical emission energies at the excited-state minimum geometries are not expected to match with the maxima of the broad LLCT emission bands. Furthermore, we expect the large-amplitude displacement of the thiolate ligand to substantially affect the dipole transition moment and the FC overlaps. We have therefore refrained from computing vibronic spectra of the **A** conformers.

Our experimentally measured broad LLCT band of **1** (Figure 8) has an onset between 20,000 cm^{-1} and 19,000 cm^{-1}, in agreement with previous estimates by Highland *et al.*[28] who assigned the positive phase of a TME spectrum to the ^{3}LLCT emission of **1**. For **2**, the onset of this band lies between 18,000 cm^{-1} and 17,000 cm^{-1} according to these authors. Hence, the calculated adiabatic LLCT excitation energies of the chlorinated conformer **1 A** (Table 1) and the methylated compound **2 A** (Supporting Information Table S4) fit reasonably well. Inspection of Table 2 (and Table S4 of the Supporting Information) reveals that the adiabatic T_{LLCT} and S_{LLCT} energies of their folded counterparts **1 B** and **2 B** are lower. This is true even on an absolute scale when the relative energies of the conformers in their electronic ground states are taken into consideration. In view of these results, we therefore suppose that the **A** conformers fold upon LLCT excitation in liquid solution whereas they are hindered to undergo this transformation and to lose a thiolate ligand in the crystalline state.

Our calculated rate constants for radiative and nonradiative transitions of the LLCT states of the **B** conformers are collected in Table 4. The computed 0-0 energy splitting of the S_{LLCT} and T_{LLCT} (423 cm^{-1}) matches well with the experimental estimates obtained according to Eq. (1) based on fits of the temperature dependence for quantum yields ranging between 0.35 and 0.5 (Table 3). We refrained from computing rate constants for the **A** forms because they are conformationally very flexible and do not provide reliable potential energy surfaces for such an endeavor.

In the cryogenic temperature regime close to 0 K, only fluorescence, ISC and phosphorescence need to be considered because rISC is too slow to repopulate the S_{LLCT} state and internal conversion to the S_0 state is not very probable at these temperatures. ISC outcompetes fluorescence by a factor of about 50–100 according to our calculations (see Table 4). We note that the mutual interactions of the LLCT and ^{3}LC states do not influence the TADF process at room temperature due to the high adiabatic energy differences of 0.67 and 0.86 eV for **1 B** and **2 B**, respectively.

The calculated radiative lifetimes of the LLCT fluorescence (3.4–4.3 μs), obtained from the probabilities of spontaneous $S_1 \rightarrow S_0$ emission at the S_{LLCT} geometry according to Eq. (4), are in the typical μs range observed in CT emissions of donor-acceptor compounds and agree very well with the 2.9 μs radiative lifetime derived from our experimental data (*vide supra*). The involvement of the sulfur atom in the LC and LLCT excitations does not only explain the branched triplet population kinetics observed in experiment, it also leads to sizable intensity borrowing from higher-lying bright states. The

Table 4. 0-0 energy splittings ΔE_{S-T} and spin component-averaged S_{LLCT}–T_{LLCT} SOC [cm^{-1}] and radiative as well as nonradiative rate constants k [s^{-1}] of the LLCT states of compounds **1 B** and **2 B** computed according to Equations (2)–(4).

	ΔE_{S-T}	S_{LLCT}		T_{LLCT}		Temperature T[K]	k_{ISC}	k_{rISC}
		k_F	SOC	k_P	SOC			
1 B	423	2.9×10^5	0.26	1.1×10^2	0.30	298	2.0×10^7	1.3×10^7
						77	2.8×10^7	1.6×10^4
						35	2.8×10^7	3.1×10^0
						10	1.1×10^7	–
2 B	472	2.3×10^5	0.38	1.5×10^2	0.64	298	7.1×10^5	2.8×10^5
						77	5.3×10^6	2.4×10^3
						35	2.9×10^5	0.1×10^0
						10	2.9×10^5	–

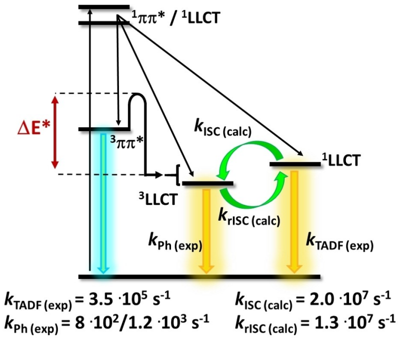

Scheme 2. Excited-state decay mechanism upon photoexcitation of [Zn(SC_6H_4-4-Cl)$_2$(phen)] as proposed in this work.

calculated T_{LLCT} phosphorescence lifetime of 9 ms (see Table 4) is, however, approximately an order of magnitude longer than the radiative T_{LLCT} lifetimes estimated from our temperature-dependent spectra on the basis on Eq. (1). Note that the theoretically and experimentally derived radiative lifetimes entail uncertainties associated with the large-amplitude motion of the thiolate ligand on the theoretical side and the limitation of the PLQY measurements to the temperature range between 297 and 77 K on the experimental side. The calculated phosphorescence lifetime fits well to the LLCT lifetime of complex **1** of 8 ms at 6.5 K, assigned to phosphorescence by Highland *et al.*,[28] which evolves to 0.66 ms when the temperature is raised to 23 K and which decreases to 0.13 ms at 35 K to 4.2 μs at 77 K. Phosphorescence is too slow, however, to explain the experimentally determined μs decay times at 77 K.

Due to the small singlet-triplet energy gaps ΔE_{S-T} and the internal heavy atom effect of the sulfur atoms, rISC appears to be sufficiently fast to repopulate the S_{LLCT} state even at liquid nitrogen temperature. At room temperature, the ISC and rISC rate constants of **1 B** have nearly equal magnitudes and are about 40–70 times larger than the pure radiative lifetimes. The excited singlet and triplet populations will therefore equilibrate, given that non-radiative deactivation by internal conversion to the electronic ground state does not dominate. Hence, we associate the averaged LLCT lifetime of 2.9 μs of our powdered sample of complex **1** (*vide supra*) with the lifetime of delayed fluorescence.

Summary and Conclusion

In this work, extensive quantum chemical and spectroscopical studies have been performed to elucidate the photophysical decay mechanisms of Zn(II) bis-thiolate diimine complexes and their potential suitability as triplet harvesters in electroluminescent devices. For [Zn($SC_6H_4$4-R)$_2$(phen)] (R=Me, Cl), temperature-dependent dual luminescence in organic glass and in the crystalline solid state had been reported by Crosby and coworkers.[24–28] The vibrationally structured high-energy band had been assigned to phosphorescence from a phenanthroline-centered locally excited $^3\pi\pi^*$ state and the broader lower-energy band to interligand thiolate→phen LLCT transitions. The results of our study in principle support the kinetic scheme proposed by Crosby *et al.*, but add an efficient reverse intersystem crossing (rISC) channel allowing the upconversion of ^{3}LLCT population to the ^{1}LLCT state at room temperature (Scheme 2). The heavy-atom effect caused by the participation of sulfur orbitals in the excitation of the ^{1}LLCT, ^{3}LLCT and ^{3}LC (phen) states in conjunction with their close energetic proximity opens the chance for substantial singlet-triplet mixing in the absorption region and rationalizes the branched triplet population kinetics observed in experiment. While weak phosphorescence from the ^{3}LC (phen) state dominates the short-wavelength emission, the red-shifted ^{3}LLCT emission is visible even at cryogenic temperatures. At room temperature, efficient ^{1}LLCT⇝^{3}LLCT ISC and rISC leads to quick equilibration of the singlet and triplet populations making thermally activated delayed fluorescence (TADF) the major emission channel.

Upon population of the LLCT states, one of the thiolate ligands starts to fold back toward the phen ligand due to the Coulomb attraction between electron hole and particle and the high conformational flexibility of the monodentate thiolate ligands. The large-amplitude motion in the LLCT states does not only have the consequence that the emission spectrum becomes very broad, it also makes the complex susceptible to photodissociation of the ligand because it is accompanied by substantial elongation of its Zn–S bond. To increase the color purity of the emission and the photostability of the complex, containment of the thiolate ligand flexibility therefore appears mandatory. Such a containment should be possible even in non-rigid environments if a bidentate dithiolate ligand is employed instead of two monodentate thiolates. Moreover, photolability issues could be mitigated by shifting the absorbance from the UV to the visible wavelength region. A study investigating the photophysical properties of fourfold-coordinated Zn(II) complexes involving bathochromically shifted phen derivatives as acceptors and bidentate dithiolates as donor ligand is currently under way. In a subsequent contribution, we will also report on the excited state behavior of the hemicage compound ZnL_3 where rigidification has been achieved by linking the three bipyridyl ligands via ethyl bridges to a mesityl core.

Experimental Methods

The zinc complex **1** has been synthesized according to an established procedure[25] and its identity and purity confirmed by elemental analysis, single-crystal X-ray diffraction, and multinuclear NMR spectroscopy (see the Supporting Information). Sample preparation was carried out under argon using glovebox techniques. Microcrystalline powder samples have been prepared by 10-fold grinding of the single-crystalline material with mortar and pestle. UV-Vis absorption spectra were measured on an Agilent Cary 5000 using standard 1 cm path length quartz cells, or a Praying Mantis set-up for solid state measurements. Emission and excitation spectra were recorded on an Edinburgh Instrument FLS1000 equipped with a 450 W Xenon arc lamp, a red sensitive photomultiplier (PMT-980) as the detector and double monochromators for the excitation and emission pathways. The emission was collected at right angles to the excitation source with the excitation wavelength selected by a double grated monochromator and detected by the respective PMT. The recorded emission and excitation spectra were corrected using the standard corrections supplied by the manufacturer for the sensitivity of the detector and the spectral power of the excitation source. Luminescence lifetimes were measured either using a μF2 60 W Xenon Flashlamp and multichannel scaling module (MCS) or with a variable pulsed LED (VPLED) and MCS. The quantum yields were measured using a Cryosphere and the mentioned FLS1000. Low temperature measurements were performed in an Advanced Research System closed cycle 4 K Cryostat equipped with a water-cooled helium compressor.

Computational Methods and Technical Details

The Gaussian 16 program package[45] was used for all geometry optimizations. The equilibrium geometries of the electronic ground states were determined with Kohn-Sham density functional theory (DFT).[46] Unless stated otherwise, the BH-LYP functional[47,48] functional[49,50] in conjunction with dispersion corrections[51] was used herein. For singlet excited-state geometries, time dependent DFT (TDDFT)[52] calculations were performed while the Tamm-Dancoff approximation (TDDFT-TDA)[53] was employed for the geometry optimization of the triplet states. With the exception of sulfur, all nonmetal atoms were represented by the def-SV(P) basis set[54] from the Turbomole basis set library. The def2-SVPD basis sets on sulfur and chlorine differ from the def-SV(P) basis by the addition of a diffuse *s*, *p*, and *d* function, respectively. For the Zn ion a relativistic small-core effective core potential[55] and the associated contracted 6s5p3d basis set were employed.

The Zn(II) diimine dithiolate complexes are very polar molecules in their electronic ground states, with static dipole moments of up to 25 D. The polarity of the matrix or solvent environment is thus expected to have large impact on their photophysical properties. Self-consistent reaction field calculations employing the polarizable continuum model PCM[56,57] were performed with the Gaussian 16 package[45] and point charges were exported for further use in subsequent multireference configuration interaction (MRCI) calculations of the spectral properties. The stationary points of the DFT and TDDFT potentials were verified as minima through a vibrational analysis using analytic second derivatives implemented in Gaussian 16.[45] The resulting normal mode frequencies and coordinates were further utilized to generate Franck-Condon (FC) factors and FC-weighted densities of states (FCWDOS) for determining spectral profiles and rate constants, respectively.

Kohn-Sham orbitals of the closed-shell ground-state determinant and three-index two-electron resolution-of-the-identity approximated integrals for subsequent DFT/MRCI calculations were generated with the Turbomole program package[58,59] simulating the solvent environment by importing the pre-computed field of point charges. Electronic excitation energies and oscillator strengths of the spin-allowed transitions were calculated with the DFT/MRCI method[60,61] employing the redesigned R2018 Hamiltonian parameterized for transition metal compounds.[62] Due to the size of the complexes, a tight configuration selection criterion (threshold 0.80 E_h) was used throughout. The DFT/MRCI secular equations were solved for 30 singlet and 30 triplet roots.

Electronic spin-orbit coupling matrix elements (SOCMEs) for the evaluation of intersystem crossing (ISC) rate constants were obtained with the SPOCK program.[63,64] The effective spin-orbit coupling (SOC) one-electron Hamiltonian comprised a relativistic ECP[55,65] on zinc and an atomic mean-field approximation of the Breit-Pauli spin-orbit operator[66,67] on all other centers. Phosphorescence lifetimes were computed using the variational multireference spin-orbit configuration interaction (MRSOCI) method.[68] The individual phosphorescence rate constants were averaged over the three triplet components as the zero-field splittings are small. Rate constants for ISC and reverse ISC (rISC) at a given temperature were obtained in FC approximation assuming a Boltzmann population of the vibrational levels in the initial state. The FCWDOS, needed – in addition to the electronic SOCMEs – for the computation of the ISC rate constants, was calculated via a fast Fourier transformation ansatz employing the Vibes program.[69,70] Before numerical integration using 65536 grid points in an interval between 0 and 300 fs, the time correlation function was damped by a Gaussian function of width 100 cm^{-1}.

Supporting Information Available

Details of the sample preparation, elemental analysis and crystal structure of complex 1; fit parameters of the measured lifetimes at various temperatures; computed absorption spectra and vertical as well as adiabatic excitation energies of compounds **2 A** and **2 B**; computed phosphorescence spectra and difference densities of selected electronic states of **1 B**, **2 A** and **2 B**; energy profiles of **2 A** along a linearly interpolated path connecting the ^{3}LC (phen) and LLCT minima; chemical structures of the zinc(II) thiolate complexes with atom numbers, selected geometry parameters of the complexes **1 A** and **2 A** along the linearly interpolated paths connecting the ^{3}LC (phen) and LLCT minima; Cartesian coordinates of all optimized stationary points of the complexes **1 A**, **1 B**, **2 A** and **2 B**.

Acknowledgements

This work was supported by Deutsche Forschungsgemeinschaft [DFG, Priority Program SPP 2102 "Light-controlled reactivity of metal complexes" (MA 1051/18-1 and STE 1834/7-1)]. Open Access funding enabled and organized by Projekt DEAL.

Conflict of Interest

The authors declare no conflict of interest.

Data Availability Statement

The data that support the findings of this study are available in the supplementary material of this article.

Keywords: density functional calculations · excited states · phosphorescence · thermally amplified delayed fluorescence · zinc

[1] E. Zysman-Colman (Ed.), *Iridium(III) in Optoelectronic and Photonics Applications*, John Wiley & Sons, Ltd. **2017**.

[2] H. Yersin (Ed.), *Highly Efficient OLEDs: Materials Based on Thermally Activated Delayed Fluorescence*, Wiley VCH **2018**.

[3] G. Hong, X. Gan, C. Leonhardt, Z. Zhang, J. Seibert, J. M. Busch, S. Bräse, *Adv. Mater.* **2021**, *33*, 2005630.

[4] D. Di, A. S. Romanov, L. Yang, J. M. Richter, J. P. H. Rivett, S. Jones, T. H. Thomas, M. Abdi Jalebi, R. H. Friend, M. Linnolahti, M. E. Bochmann, D. Credgington, *Science* **2017**, *356*, 159–163.

[5] R. Hamze, J. L. Peltier, D. Sylvinson, M. Jung, J. Cardenas, R. Haiges, M. Soleilhavoup, R. Jazzar, P. I. Djurovich, G. Bertrand, M. E. Thompson, *Science* **2019**, *363*, 601–606.

[6] R. Hamze, S. Shi, S. C. Kapper, D. S. Muthiah Ravinson, L. Estergreen, M. C. Jung, A. C. Tadle, R. Haiges, P. I. Djurovich, J. L. Peltier, R. Jazzar, G. Bertrand, S. E. Bradforth, M. E. Thompson, *J. Am. Chem. Soc.* **2019**, *141*, 8616–8626.

[7] M. Gernert, L. Balles-Wolf, F. Kerner, U. Müller, A. Schmiedel, M. Holzapfel, C. M. Marian, J. Pflaum, C. Lambert, A. Steffen, *J. Am. Chem. Soc.* **2020**, *142*, 8897–8909.

[8] J. Föller, C. M. Marian, *J. Phys. Chem. Lett.* **2017**, *8*, 5643–5647.

[9] N. Lüdtke, J. Föller, C. M. Marian, *Phys. Chem. Chem. Phys.* **2020**, *22*, 23530–23544.

[10] A. Steffen, B. Hupp, *Comprehensive Coordination Chemistry III*, Vol. 2 (Eds: E. C. Constable, G. Parkin, L. Que Jr), Elsevier: Oxford **2021**; pp 466–502.

[11] V. Wing-Wah Yam, K. Kam-Wing Lo, *Chem. Soc. Rev.* **1999**, *28*, 323–334.

[12] G. Cheng, G. K.-M. So, W.-P. To, Y. Chen, C.-C. Kwok, C. Ma, X. Guan, X. Chang, W.-M. Kwok, C.-M. Che, *Chem. Sci.* **2015**, *6*, 4623–4635.

[13] J. Tang, H.-Y. Yin, J.-L. Zhang, *Inorganic, Organometallic Transition Metal Complexes with Biological Molecules and Living Cells*, (Ed: K. K.-W. Lo) Academic Press **2017**; pp 1–53.

[14] A. Gusev, E. Braga, E. Zamnius, M. Kiskin, M. Kryukova, A. Baryshnikova, B. Minaev, G. Baryshnikov, H. Ågren, W. Linert, *RSC Adv.* **2019**, *9*, 22143–22152.

[15] A. N. Gusev, M. A. Kiskin, E. V. Braga, M. A. Kryukova, G. V. Baryshnikov, N. N. Karaush-Karmazin, V. A. Minaeva, B. F. Minaev, K. Ivaniuk, P. Stakhira, H. Ågren, W. Linert, *ACS Appl. Electron. Mater.* **2021**, *3*, 3436–3444.

[16] R. Diana, B. Panunzi, *Molecules* **2020**, *25*, 4984.

[17] R. Wang, L. Deng, M. Fu, J. Cheng, J. J. Li, *Mater. Chem.* **2012**, *22*, 23454–23460.

[18] Y. Sakai, Y. Sagara, H. Nomura, N. Nakamura, Y. Suzuki, H. Miyazaki, C. Adachi, *Chem. Commun.* **2015**, *51*, 3181–3184.

[19] T. Yu, V. K.-M. Au, D. P.-K. Tsang, M.-Y. Chan, V. W.-W. Yam, *Dalton Trans.* **2015**, *44*, 18983–18992.

[20] K. D. Oyler, F. J. Coughlin, S. Bernhard, *J. Am. Chem. Soc.* **2007**, *129*, 210–217.

[21] I. Y. Chan, W. G. van Dorp, T. J. Schaafsma, J. H. van der Waals, *Mol. Phys.* **1971**, *22*, 753–760.

[22] A. Harriman, *J. Chem. Soc. Faraday Trans. 1* **1980**, *76*, 1978–1985.

[23] M. Pineiro, A. L. Carvalho, M. M. Pereira, A. M. d R Gonsalves, L. G. Arnaut, S. J. Formosinho, *Chem. Eur. J.* **1998**, *4*, 2299–2307.

[24] K. A. Truesdell, G. A. Crosby, *J. Am. Chem. Soc.* **1985**, *107*, 1787–1788.

[25] G. A. Crosby, R. G. Highland, K. A. Truesdell, *Coord. Chem. Rev.* **1985**, *64*, 41–52.

[26] K. J. Jordan, W. F. Wacholtz, G. A. Crosby, *Inorg. Chem.* **1991**, *30*, 4588–4593.

[27] R. G. Highland, G. A. Crosby, *Chem. Phys. Lett.* **1985**, *119*, 454–458.

[28] R. G. Highland, J. G. Brummer, G. A. Crosby, *J. Phys. Chem.* **1986**, *90*, 1593–1598.

[29] A. M. Galin, Y. V. Razskazovsky, M. Y. Mel'nikov, *J. Photochem. Photobiol. A* **1993**, *72*, 35–40.

[30] P. J. Gronlund, J. A. Burt, W. F. Wacholtz, *Inorg. Chim. Acta* **1995**, *234*, 13–18.

[31] O. Mrózek, M. Gernert, A. Belyaev, M. Mitra, L. Janiak, C. M. Marian, A. Steffen, *Chem. Eur. J.* **2022**, *28*, e202201114.

[32] B. Minaev, H. Ågren, *Chem. Phys.* **2005**, *315*, 215–239.

[33] J. A. Burt, G. A. Crosby, *Chem. Phys. Lett.* **1994**, *220*, 493–496.

[34] T. L. Cremers, D. R. Bloomquist, R. D. Willett, G. A. Crosby, *Acta Crystallogr.* **1980**, *B36*, 3097–3099.

[35] S. Scheins, S.-L. Zheng, J. B. Benedict, P. Coppens, *Acta Crystallogr. Sect. B* **2010**, *66*, 366–372.

[36] G. Baryshnikov, B. Minaev, H. Ågren, *Chem. Rev.* **2017**, *117*, 6500–6537.

[37] B. de Souza, G. Farias, F. Neese, R. Izsák, *J. Chem. Theory Comput.* **2019**, *15*, 1896–1904.

[38] T. J. Penfold, E. Gindensperger, C. Daniel, C. M. Marian, *Chem. Rev.* **2018**, *118*, 6975–7025.

[39] C. M. Marian, *Annu. Rev. Phys. Chem.* **2021**, *72*, 617.

[40] Y. Tsuchiya, S. Diesing, F. Bencheikh, Y. Wada, P. L. dos Santos, H. Kaji, E. Zysman-Colman, I. D. W. Samuel, C. Adachi, *J. Phys. Chem. A* **2021**, *125*, 8074–8089.

[41] Y. Wada, K. Shizu, H. Kaji, *J. Phys. Chem. A* **2021**, *125*, 4534–4539.

[42] A. Rodríguez-Serrano, F. Dinkelbach, C. M. Marian, *Phys. Chem. Chem. Phys.* **2021**, *23*, 3668–3678.

[43] S. W. Park, J. H. Yang, H. Choi, Y. M. Rhee, D. Kim, *J. Phys. Chem. A* **2020**, *124*, 10384–10392.

[44] R. Kamiński, M. S. Schmøkel, P. Coppens, *J. Phys. Chem. Lett.* **2010**, *1*, 2349–2353.

[45] M. J. Frisch, G. W. Trucks, H. B. Schlegel, G. E. Scuseria, M. A. Robb, J. R. Cheeseman, G. Scalmani, V. Barone, G. A. Petersson, H. Nakatsuji, et al., *Gaussian 16, Revision A.03.*, Gaussian Inc. Wallingford CT **2016**.

[46] M. Von Arnim, R. Ahlrichs, R. J. Comput, *Chem.* **1998**, *19*, 1746–1757.

[47] C. Lee, W. Yang, R. G. Parr, *Phys. Rev. B* **1988**, *37*, 785–789.

[48] A. D. Becke, *J. Chem. Phys.* **1993**, *98*, 1372–1377.

[49] J. P. Perdew, K. Burke, M. Ernzerhof, *Phys. Rev. Lett.* **1996**, *77*, 3865–3868.

[50] C. Adamo, V. Barone, *J. Chem. Phys.* **1999**, *110*, 6158–6170.

[51] S. Grimme, J. Antony, S. Ehrlich, H. Krieg, *J. Chem. Phys.* **2010**, *132*, 154104.

[52] F. Furche, R. Ahlrichs, *J. Chem. Phys.* **2002**, *117*, 7433–7447.

[53] S. Hirata, M. Head-Gordon, *Chem. Phys. Lett.* **1999**, *314*, 291–299.

[54] A. Schäfer, H. Horn, R. Ahlrichs, *J. Chem. Phys.* **1992**, *97*, 2571–2577.

[55] D. Figgen, G. Rauhut, M. Dolg, H. Stoll, *Chem. Phys.* **2005**, *311*, 227–244.

[56] E. Cancès, B. Mennucci, J. Tomasi, *J. Chem. Phys.* **1997**, *107*, 3032.

[57] B. Mennucci, E. Cancès, J. Tomasi, *J. Phys. Chem. B* **1997**, *101*, 10506.

[58] R. Ahlrichs, M. Bär, M. Häser, H. Horn, C. Kölmel, *Chem. Phys. Lett.* **1989**, *162*, 165–169.

[59] .TURBOMOLE V6.6 2014, a development of University of Karlsruhe and Forschungszentrum Karlsruhe GmbH, 1989–2007, TURBOMOLE GmbH, since 2007; available from http://www.turbomole.com.

[60] S. Grimme, M. Waletzke, *J. Chem. Phys.* **1999**, *111*, 5645–5655.

[61] C. M. Marian, A. Heil, M. Kleinschmidt, *Mol. Sci.* **2019**, *9*, e1394.

[62] A. Heil, M. Kleinschmidt, C. M. Marian, *J. Chem. Phys.* **2018**, *149*, 164106.

[63] M. Kleinschmidt, J. Tatchen, C. M. Marian, *J. Comput. Chem.* **2002**, *23*, 824–833.

[64] M. Kleinschmidt, C. M. Marian, *Chem. Phys.* **2005**, *311*, 71–79.

[65] M. Kleinschmidt, C. van Wüllen, C. M. Marian, *J. Chem. Phys.* **2015**, *142*, 094301.

[66] B. A. Heß, C. M. Marian, U. Wahlgren, O. Gropen, *Chem. Phys. Lett.* **1996**, *251*, 365–371.

[67] AMFI is an atomic spin-orbit integral program written by B. Schimmelpfennig, University of Stockholm, **1996**.

[68] M. Kleinschmidt, J. Tatchen, C. M. Marian, *J. Chem. Phys.* **2006**, *124*, 124101.

[69] M. Etinski, J. Tatchen, C. M. Marian, *J. Chem. Phys.* **2011**, *134*, 154105.

[70] M. Etinski, J. Tatchen, C. M. Marian, *Phys. Chem. Chem. Phys.* **2014**, *16*, 4740–4751.

[71] Deposition Number(s) 2173213 (for **1**) contain(s) the supplementary crystallographic data for this paper. These data are provided free of charge by the joint Cambridge Crystallographic Data Centre and Fachinformationszentrum Karlsruhe Access Structures service.

Manuscript received: May 24, 2022
Revised manuscript received: August 24, 2022
Accepted manuscript online: September 4, 2022
Version of record online: October 5, 2022

Electronic Supplementary Information for Revisiting LLCT Phosphorescence Emission from Zinc(II) Diimine Bis-Thiolate Complexes: It's Actually TADF

Nora Lüdtke,[†] Julia Kuhnt,[‡] Tabea Heil,[‡] Andreas Steffen,[*,‡] and Christel M. Marian[*,†]

[†]Institute of Theoretical and Computational Chemistry, Heinrich-Heine-University Düsseldorf, Universitätsstr. 1, 40225 Düsseldorf, Germany

[‡]Faculty of Chemistry and Chemical Biology, TU Dortmund University, Otto-Hahn-Str. 6, 44227 Dortmund, Germany

E-mail: Andreas.Steffen@tu-dortmund.de; Christel.Marian@hhu.de

Experimental

General considerations

For photophysical measurements, dry and degassed solvents of HPLC grade were used. Traces of water in the organic solvents were removed using an Inert Systems PureSolv MD 7 solvent purification system. The solvents were then deoxygenated by purging with argon. All starting materials were purchased from commercial sources and used for synthesis without further purification. The ^{1}H and $^{13}C\{^{1}H\}$ NMR spectra were obtained from a Bruker Avance 400 (^{1}H, 400 MHz; $^{13}C\{^{1}H\}$ 100 MHz) NMR spectrometer and the chemical shifts are given in parts per million (ppm, δ scale) relative to the solvent signal. An Elementar vario MICRO cube was used to perform the elemental analyses.

Synthesis

[Zn(4-ClPhS)$_2$(phen)] (**1**) was prepared via the procedure published previously.[1] Zn(OAc)$_2\cdot$2H$_2$O was dissolved (0.220 g, 1.000 mmol) in 20 mL ethanol under reflux and combined with a solution of 4-chlorothiophenolate (0.289 g, 2.000 mmol) in 10 mL hot ethanol. A second solution of phenanthroline (0.180 g, 1.000 mmol) in 10 mL ethanol was added dropwise to the first light yellow mixture resulting in an increase in color intensity. After stirring for two minutes and cooling down to room temperature, yellow crystals were obtained which were filtered, washed with ethanol (3x 20 mL) and recrystallized via vapor diffusion of dichloromethane/pentane to give 0.294 g (55 %) of the product.

^{1}H NMR (400 MHz, $CDCl_3$): δ 6.62 – 6.66 (m, 4 H), 7.02 – 7.05 (m, 4 H), 7.90 (dd, J_1 = 4.74 Hz, J_2 = 8.20 Hz, 2 H), 7.95 (s, 2 H), 8.52 (dd, J_1 = 1.46 Hz, J_2 = 8.18 Hz, 2 H), 8.95 (dd, J_1 = 1.49 Hz, J_2 = 4.78 Hz, 2 H) ppm. $^{13}C\{^{1}H\}$ NMR (100 MHz, $CDCl_3$): δ 125.48, 127.08, 127.56, 128.88, 129.02, 134.55, 139.19, 139.24, 141.08, 149.38 ppm. Elem. Anal. Calcd. (%) for $C_{24}H_{16}Cl_2N_2S_2Zn$: C, 54.10; H, 3.03; N, 5.26. Found: C, 54.10; H, 3.00; N, 5.30.

NMR spectra

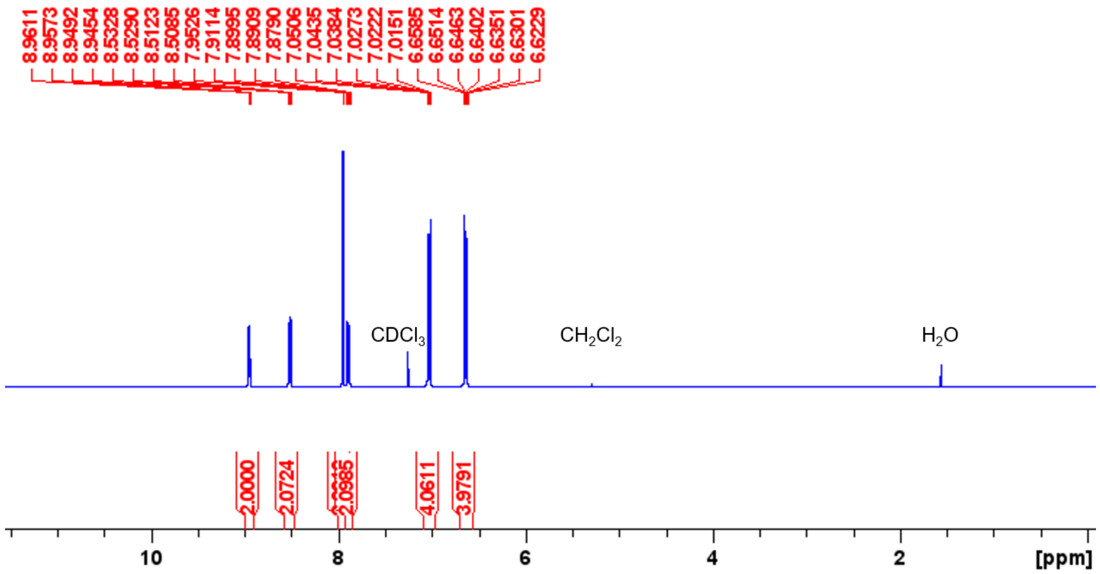

Figure S1. ^{1}H NMR spectrum of **1** in CDCl$_3$.

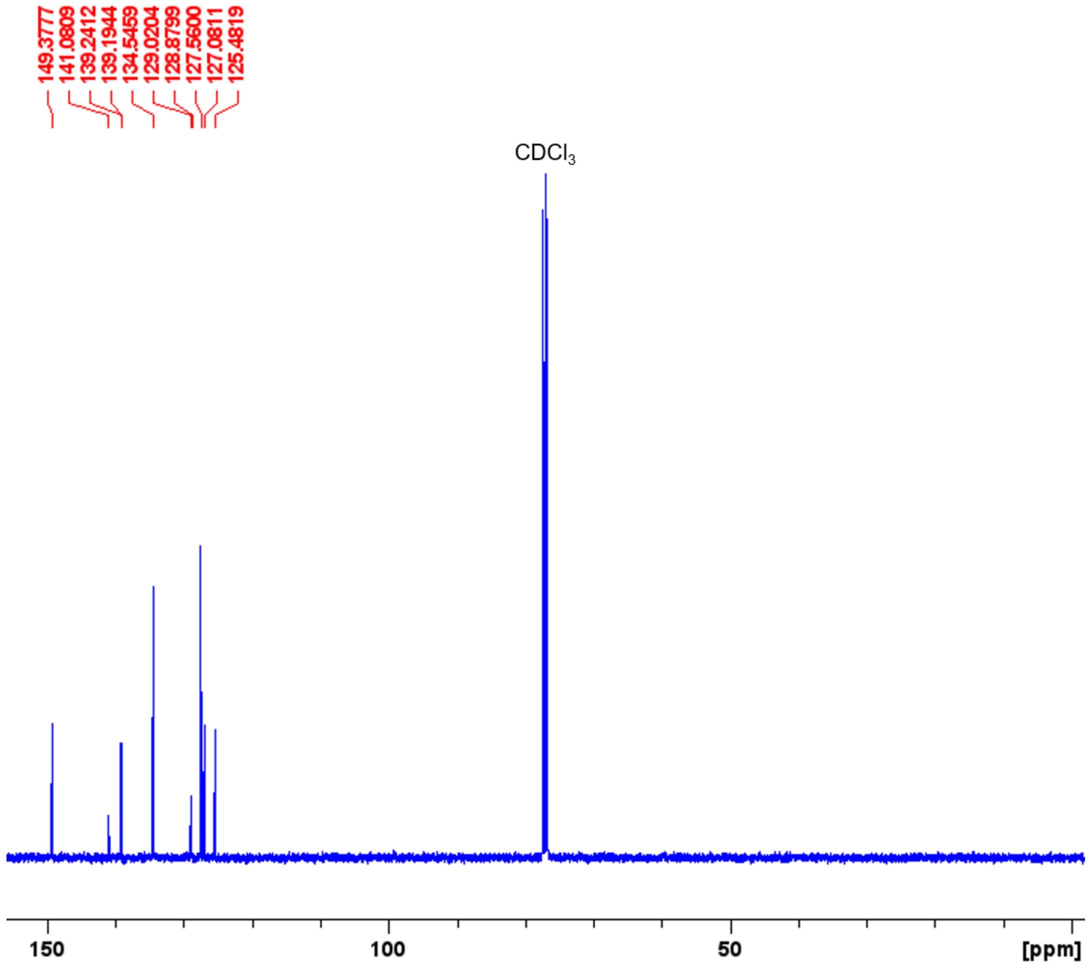

Figure S2. ^{13}C{^{1}H} NMR spectrum of **1** in CDCl$_3$.

Crystallographic Details

The crystal of **1** was immersed in a film of NVH or perfluoropolyether oil, mounted on a polyimide microloop (MicroMounts of MiTeGen) and transferred to stream of cold nitrogen (Bruker Kryoflex2), and measured at a temperature of 100 K. The X-ray diffraction data were collected on a Bruker D8 diffractometer with a CMOS Photon 100 and multilayer optics monochromated MoKα (0.71073Å) radiation (INCOATEC microfocus sealed tube). The frames were integrated with the Bruker SAINT software package using a narrow-frame algorithm. The APEX3 v2018.7-0 program package was used for cell refinements and data reductions. The structure was solved using intrinsic phasing method[2,3], refined and visualized with the OLEX2-1.5 program[4]. A semiempirical absorption correction (SADABS) was applied to all data. All non-hydrogen atoms were refined anisotropically. Hydrogen atoms were included in structure factor calculations. All Hydrogen atoms were assigned to idealised geometric positions. The crystallographic details are summarized in Table S1.

Table S1. Crystal data and structure refinement for **1**.

Identification code	**1**
CCDC number	**2173213**
Empirical formula	$C_{24}H_{16}Cl_2N_2S_2Zn$
Formula weight	532.78
Temperature/K	100.0
Crystal system	monoclinic
Space group	$P2_1/n$
a/Å	10.9672(3)
b/Å	11.7203(3)
c/Å	17.2366(4)
α/°	90
β/°	91.7070(10)
γ/°	90
Volume/Å^3	2214.59(10)
Z	4
ρ_{calc}g/cm^3	1.598
μ/mm^{-1}	1.554
F(000)	1080.0
Crystal size/mm^3	0.204 × 0.096 × 0.093
Radiation	MoKα (λ = 0.71073)
2Θ range for data collection/°	5.564 to 51.986

Index ranges	$-13 \leq h \leq 13$, $-13 \leq k \leq 14$, $-21 \leq l \leq 21$
Reflections collected	14548
Independent reflections	4349 [R_{int} = 0.0835, R_{sigma} = 0.0790]
Data/restraints/parameters	4349/0/280
Goodness-of-fit on F^2	0.983
Final R indexes [$I>=2\sigma$ (I)]	R_1 = 0.0401, wR_2 = 0.0750
Final R indexes [all data]	R_1 = 0.0722, wR_2 = 0.0844
Largest diff. peak/hole / e Å^{-3}	0.37/-0.42

[a] $R_1 = \sum||F_o|-|F_c||/\sum|F_o|$; $wR_2 = [\sum[w(F_o^2-F_c^2)^2/\sum[(wF_o^2)^2]]^{1/2}$; $w = 1/[\sigma^2(F_o^2)+(aP)^2+bP]$, where $P = (F_o^2+2F_c^2)/3$ [b] GooF = $S = [[\sum w(F_o^2-F_c^2)^2]/(m-n)]^{1/2}$, where m = number of reflexes and n = number of parameters

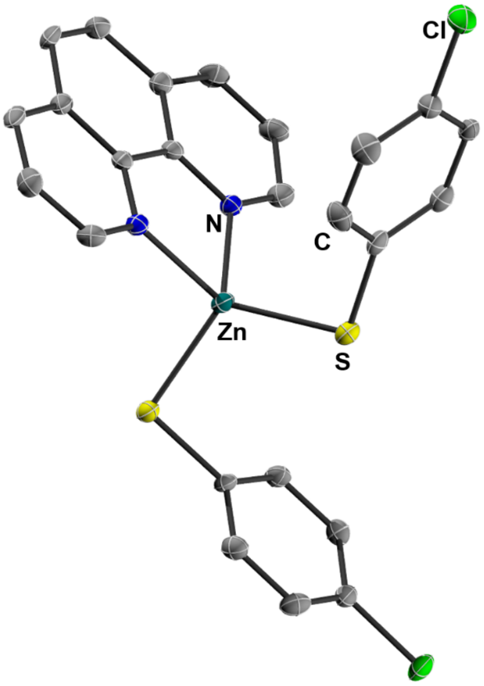

Figure S3. Molecular structure of **1** in the single crystalline solid state.

Luminescence measurements

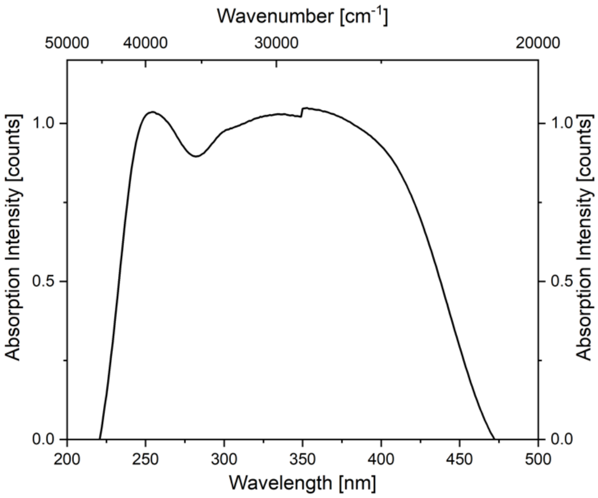

Figure S4. Normalized absorption spectrum of [Zn(4-ClPhS)$_2$(phen)] (**1**) in the solid state at 297 K.

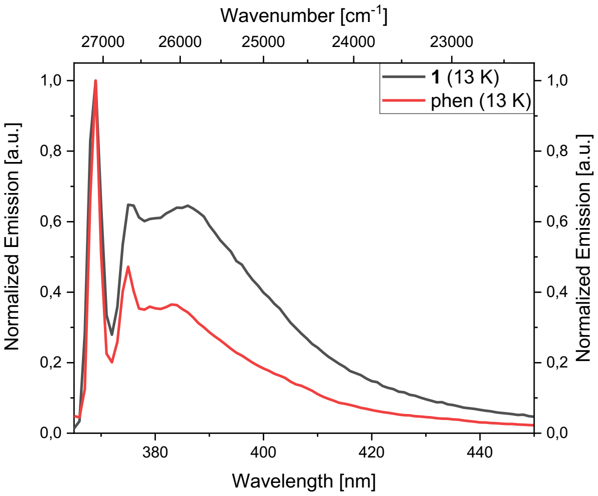

Figure S5. Normalized emission spectrum (λ_{ex} = 320 nm) of ground [Zn(4-ClPhS)$_2$(phen)] (**1**) and ground neat phenanthroline (phen) in the solid state at 13 K.

Table S2. Fit parameters of the measured lifetime of the LLCT band at 587 nm.

T [K]	τ_1 [µs]	B_1	τ_2 [µs]	B_2	τ_3 [µs]	B_3	τ_{amp} [µs][a]	χ^2
6.5	235.885	0.923	1275.372	0.048	3987.183	0.029	394.118	1.132
18.0	73.939	0.531	558.691	0.204	1009.178	0.264	420.147	1.129
23.0	37.833	0.297	465.743	0.464	795.294	0.239	417.421	1.114
35.0	108.020	0.836	174.843	0.163	22515.070	0.001	150.914	1.104
45.0	12.179	0.072	35.466	0.920	111.436	0.008	34.381	1.121
65.0	0.324	0.089	6.551	0.644	10.548	0.267	7.060	1.003
77.0	1.516	0.165	4.880	0.822	11.584	0.013	4.417	1.067
87.0	0.382	0.065	3.384	0.905	6.426	0.030	3.282	1.113
97.0	0.025	0.031	2.586	0.952	5.374	0.018	2.557	1.098
107.0	0.023	0.019	2.069	0.979	11.511	0.002	2.053	1.187
117.0	1.684	0.998	8.229	0.002	-	-	1.697	1.121
127.0	1.394	0.996	3.941	0.004	-	-	1.403	1.155
137.0	1.176	0.999	25.733	0.002	-	-	1.213	1.136
147.0	0.997	0.999	12.593	0.001	-	-	1.008	1.042
157.0	0.128	0.032	0.845	0.968	-	-	0.822	1.100
167.0	0.156	0.065	0.734	0.935			0.697	1.088
177.0	0.200	0.091	0.642	0.909	-	-	0.602	1.112
187.0	0.283	0.186	0.570	0.814	-	-	0.517	1.034
197.0	0.283	0.325	0.516	0.675	-	-	0.440	1.029
207.0	0.303	0.667	0.521	0.333	-	-	0.376	1.064
217.0	0.264	0.769	0.496	0.231	-	-	0.318	1.148
227.0	0.232	0.879	0.524	0.121	-	-	0.267	1.086
237.0	0.198	0.926	0.546	0.074	-	-	0.224	1.244
247.0	0.166	0.955	0.585	0.045	-	-	0.185	1.063
257.0	0.140	0.965	0.619	0.035	-	-	0.157	1.115
267.0	0.111	0.969	0.688	0.032	-	-	0.129	1.144
277.0	0.094	0.974	0.725	0.026	-	-	0.110	1.184
287.0	0.078	0.978	0.721	0.023	-	-	0.092	1.115
297.0	0.060	0.983	1.236	0.017	-	-	0.080	1.181

[a] amplitude average lifetime was calculated via $\Sigma B_i\tau_i/\Sigma B_i$[5]

Table S3. Fit parameters of the measured lifetime of the $^3\pi\pi^*$ band at 458 nm.

T [K]	τ_1 [ms]	B_1	τ_2 [ms]	B_2	τ_3 [ms]	B_3	τ_{amp} [ms][a]	χ^2
6.5	69.007	0.434	326.404	0.474	973.459	0.092	274.191	1.276

[a] amplitude average lifetime was calculated via $\Sigma B_i\tau_i/\Sigma B_i$[5]

References

[1] G. A. Crosby, R. G. Highland, K. A. Truesdell, *Coord. Chem. Rev.* **1985**, *64*, 41 – 52.

[2] G. M. Sheldrick, *Acta Crystallogr. A* **2015**, *71*, 3–8.

[3] G. M. Sheldrick, *Acta Crystallogr. C* **2015**, *71*, 3–8.

[4] O. V. Dolomanov, L. J. Bourhis, R. J. Gildea, J. A. K. Howard, H. Puschmann, *J. Appl. Crystallogr.* **2009**, *42*, 339–341.

[5] J. R. Lakowicz, *Principles of Fluorescence Spectroscopy*, Springer Science+Business Media, New York, **2006**.

Computational

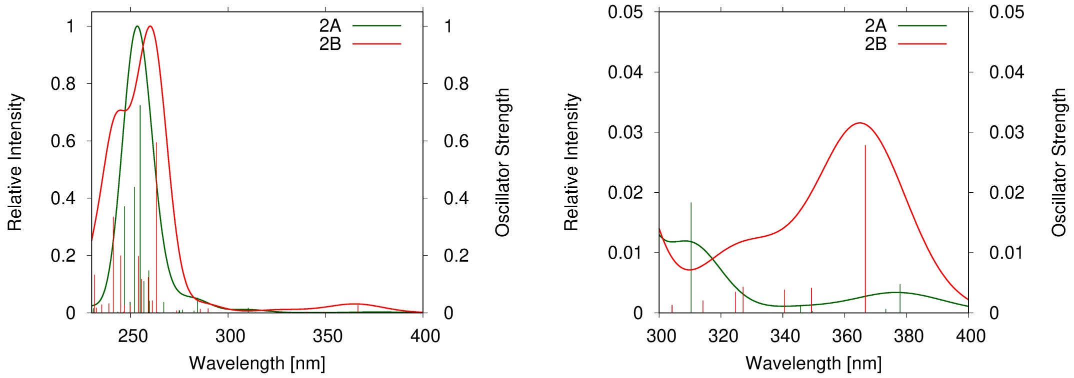

(a) Overview spectra of **2** (b) Zoom on the low energy regime of **2**

Figure S8: Calculated absorption spectra in implicit ethanol environment of conformers **A** (green), **B** (red) of Zn(4-Me-Ph-S)$_2$(phen) (**2**).

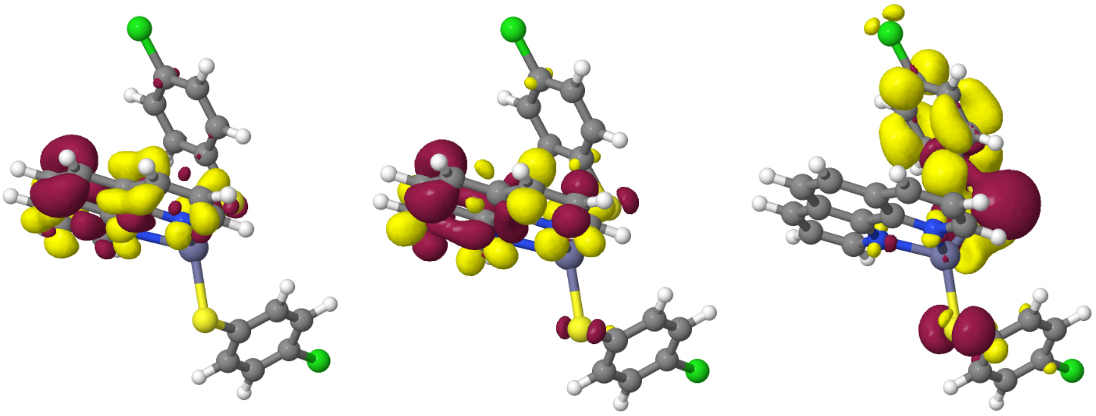

(a) S$_5$ (b) S$_{13}$ (c) S$_{17}$

Figure S9: DFT/MRCI difference densities of the most prominent singlet LC excitations of compound **1B** at the S$_0$ geometry in ethanol. Areas losing electron density in comparison to the electronic ground state are shown in red (isovalue -0.001), areas gaining electron density in yellow (isovalue +0.001).

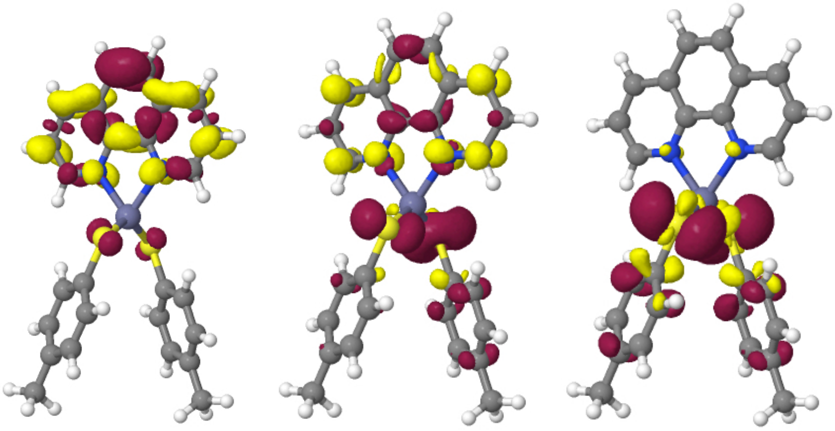

(a) S_5 (b) S_{13} (c) S_{17}

Figure S10: DFT/MRCI difference densities of the most prominent singlet LC excitations of compound **2A** at the S_0 geometry in ethanol. Areas losing electron density in comparison to the electronic ground state are shown in red (isovalue -0.001), areas gaining electron density in yellow (isovalue +0.001).

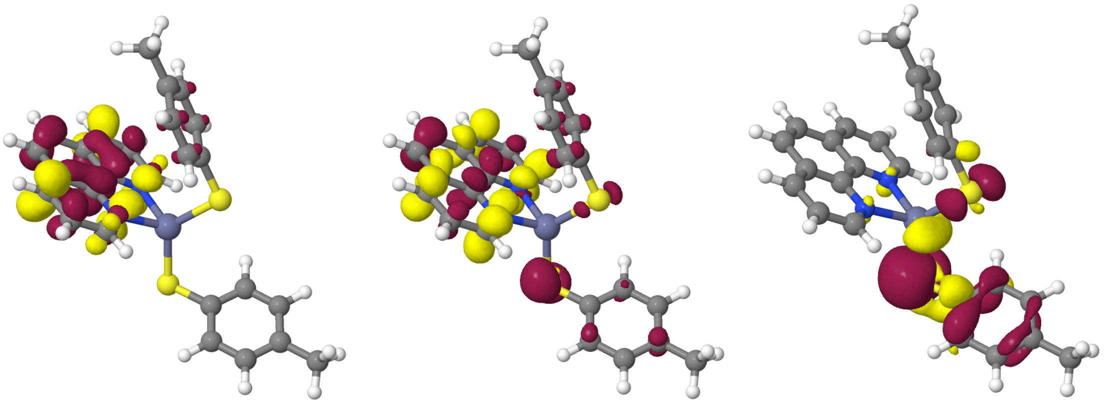

(a) S_5 (b) S_{13} (c) S_{17}

Figure S11: DFT/MRCI difference densities of the most prominent singlet LC excitations of compound **2B** at the S_0 geometry in ethanol. Areas losing electron density in comparison to the electronic ground state are shown in red (isovalue -0.001), areas gaining electron density in yellow (isovalue +0.001).

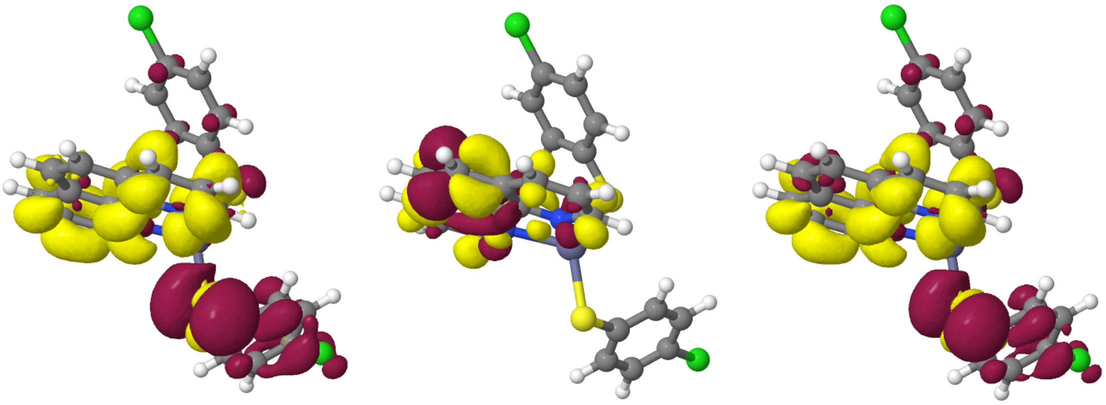
(a) S_1 (b) T_1 (c) T_2

Figure S12: DFT/MRCI difference densities of the low-lying singlet and triplet excitations of compound **1B** in ethanol at the S_0 geometry. Areas losing electron density in comparison to the electronic ground state are shown in red (isovalue -0.001), areas gaining electron density in yellow (isovalue +0.001).

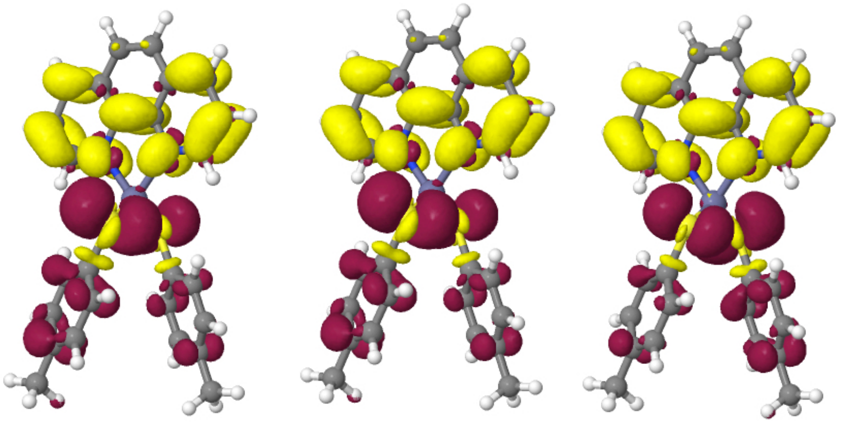
(a) S_1 (b) T_1 (c) T_2

Figure S13: DFT/MRCI difference densities of the low-lying singlet and triplet excitations of compound **2A** in ethanol at the S_0 geometry. Areas losing electron density in comparison to the electronic ground state are shown in red (isovalue -0.001), areas gaining electron density in yellow (isovalue +0.001).

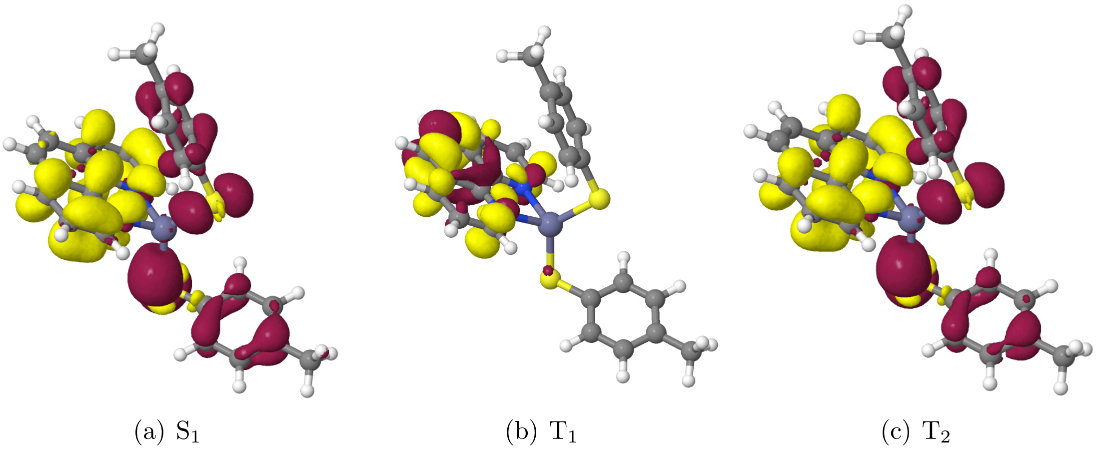

(a) S_1 (b) T_1 (c) T_2

Figure S14: DFT/MRCI difference densities of the low-lying singlet and triplet excitations of compound **2B** in ethanol at the S_0 geometry. Areas losing electron density in comparison to the electronic ground state are shown in red (isovalue -0.001), areas gaining electron density in yellow (isovalue +0.001).

Table S4: DFT/MRCI excitation energies (ΔE/eV) of **2A** in ethanol at various molecular geometries. The DFT/MRCI energy of the S_0 state at the DFT-optimized S_0 minimum geometry in a polarizable ethanol environment serves as common origin. 0–0 energies including zero-point vibrational energy corrections are given in parentheses.

state	optimized geometry			
	S_0	S^a_{LLCT}	T^a_{LLCT}	$T_{LC(phen)}$
S_0	0.00	0.39	0.45	0.37
S_{LLCT}	3.28	2.21 (**2.15**)	2.27	3.51
S'_{LLCT}	3.32	2.89	2.94	3.54
T_{LLCT}	3.23	2.15	2.20 (**2.13**)	3.47
T'_{LLCT}	3.27	2.85	2.90	3.50
$T_{LC(phen)}$	3.38	3.58	3.61	2.87 (**2.71**)
$T'_{LC(phen)}$	3.63	3.69	3.73	3.59

^{a}Structure with one strongly elongated Zn-thiolate bond.

Table S5: DFT/MRCI excitation energies (ΔE/eV) of **2B** in ethanol at various molecular geometries. The DFT/MRCI energy of the S_0 state at the DFT-optimized S_0 minimum geometry in a polarizable ethanol environment serves as common origin. 0–0 energies including zero-point vibrational energy corrections are given in parentheses. The ground state of conformer **2B** lies 0.10 eV above conformer **2A** in implicit ethanol solution.

state	optimized geometry			
	S_0	S_{LLCT}	T_{LLCT}	$T_{LC(phen)}$
S_0	0.00	0.29	0.27	0.36
S_{LLCT}	3.38	1.93 (**1.87**)	1.92	3.59
S'_{LLCT}	3.55	2.64	2.63	3.76
T_{LLCT}	3.31	1.88	1.87 (**1.81**)	3.57
T'_{LLCT}	3.48	2.60	2.59	3.72
$T_{LC(phen)}$	3.27	3.53	3.50	2.84 (**2.67**)
$T'_{LC(phen)}$	3.56	3.63	3.58	3.55

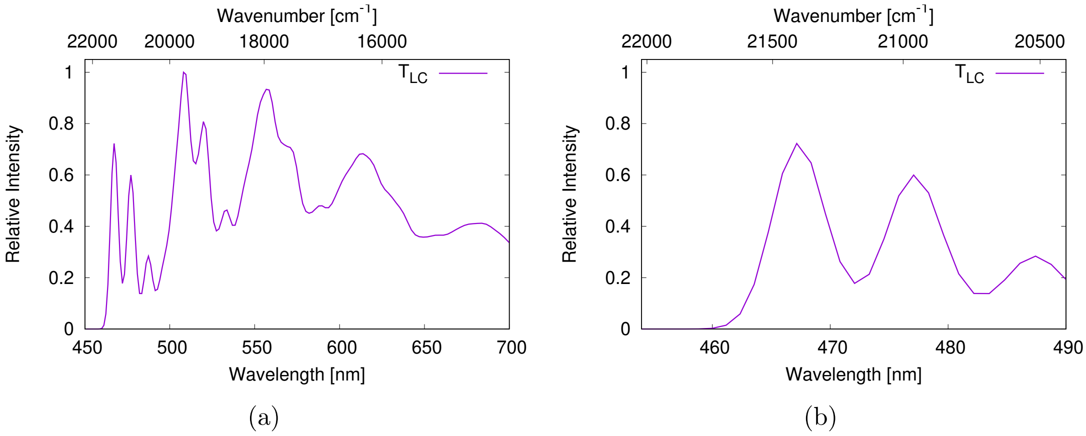

(a) (b)

Figure S15: Computed $^3\pi\pi^*$ phosphorescence emission spectrum of conformer **1B** at 10 K (left) with zoom on the $^3\pi\pi^*$ band (right).

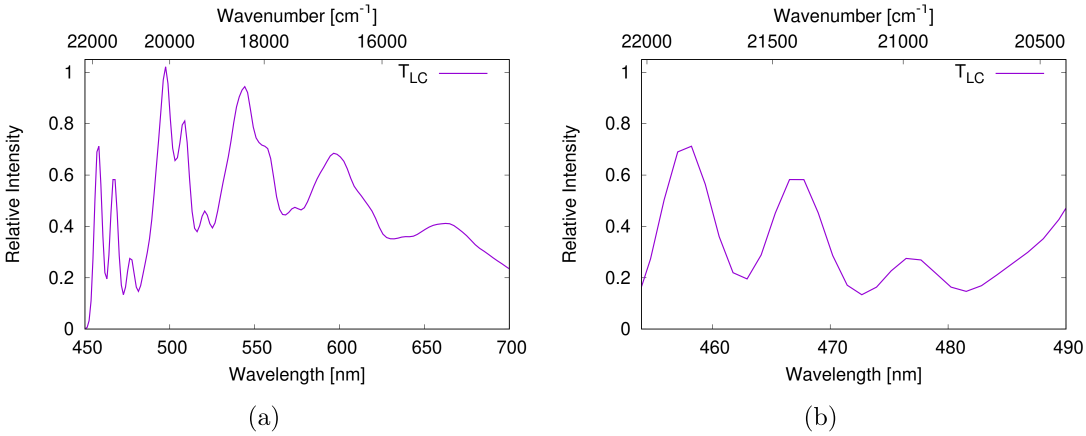

(a) (b)

Figure S16: Computed $^3\pi\pi^*$ phosphorescence emission spectrum of conformer **2A** at 10 K (left) with zoom on the $^3\pi\pi^*$ band (right).

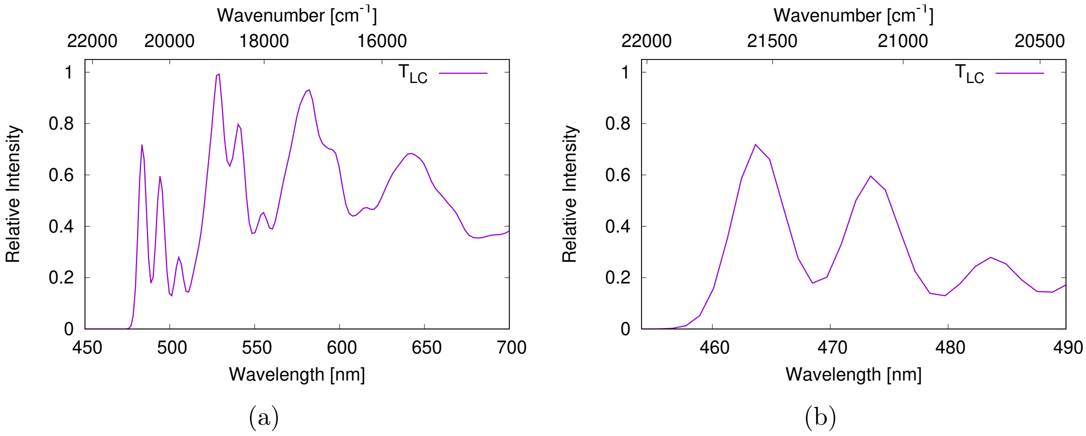

(a) (b)

Figure S17: Computed $^3\pi\pi^*$ phosphorescence emission spectrum of conformer **2B** at 10 K (left) with zoom on the $^3\pi\pi^*$ band (right).

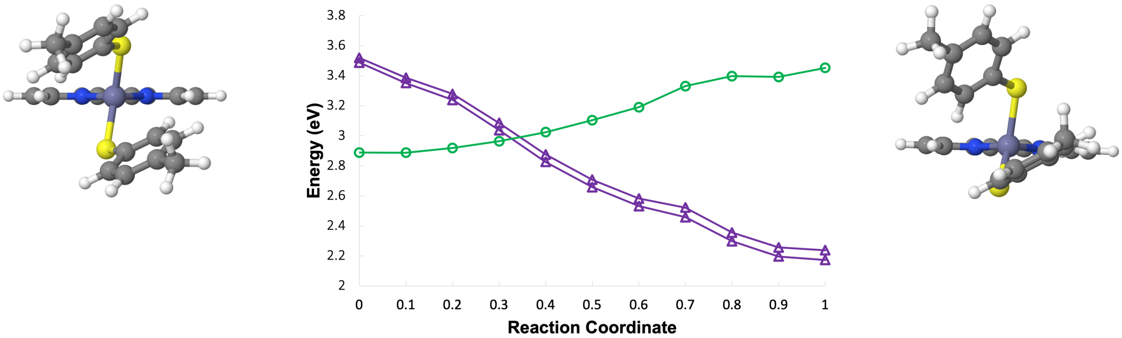

Figure S18: DFT/MRCI energy profiles of complex **2A** (middle) in implicit ethanol environment along linearly interpolated paths connecting the connecting the $\mathrm{T_{LC}}$ minimum (reaction coordinate 0) with the $\mathrm{T_{LLCT}}$ minimum (reaction coordinate 1). Filled symbols: singlets, unfilled symbols triplets, violet: LLCT, green: LC $\pi\pi^*$ (phen). Orientation of the thiolate ligands at the $\mathrm{T_{LC}}$ minimum geometries (left) and at the intersection between the $\mathrm{T_{LC}}$ and $\mathrm{T_{LLCT}}$ potentials (right).

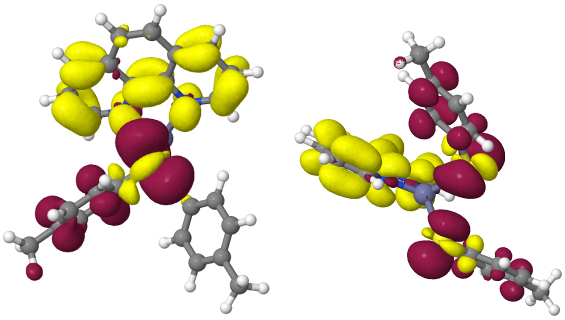

(a) **2A** (b) **2B**

Figure S19: DFT/MRCI difference densities of the $\mathrm{T_{LLCT}}$ states at the optimized $\mathrm{T_{LLCT}}$ geometries of **2** in implicit ethanol solution. Areas losing electron density in comparison to the electronic ground state are shown in red (isovalue -0.001), areas gaining electron density in yellow (isovalue +0.001).

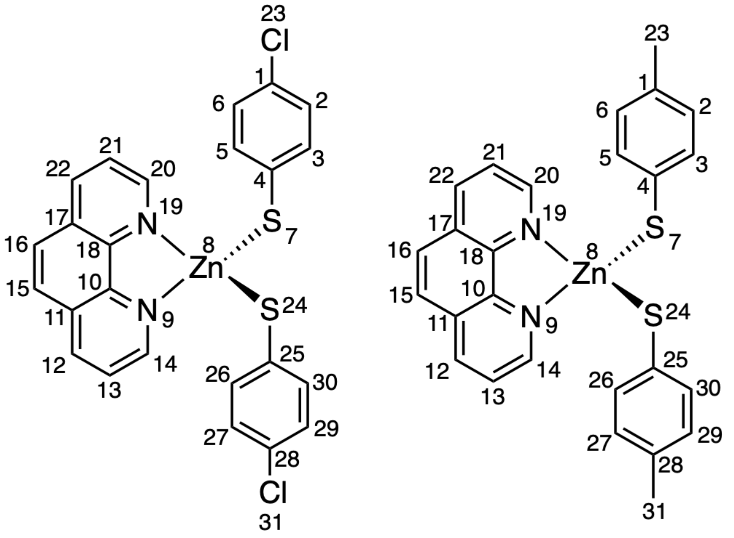

1

2

Chart 1: Chemical structures of the zinc(II) thiolate complexes **1** and **2** with atom numbers.

[H]

Table S6: Calculated bond lengths (in Å) of complex **1A** in ethanol with strong changes along the calculated path from the lowest T_{LC} to the lowest T_{LLCT} state geometry.

bond	p0.0	p0.1	p0.2	p0.3	p0.4	p0.5	p0.6	p0.7	p0.8	p0.9	p1.0
Zn-S7	2.31	2.36	2.41	2.46	2.50	2.55	2.60	2.65	2.69	2.74	2.79
Zn-S24	2.31	2.31	2.31	2.30	2.30	2.30	2.29	2.29	2.29	2.28	2.28
Zn-N9	2.15	2.14	2.13	2.12	2.11	2.10	2.09	2.08	2.06	2.05	2.04
Zn-N19	2.15	2.14	2.12	2.11	2.09	2.08	2.06	2.05	2.03	2.02	2.01
S7-C4	1.77	1.77	1.76	1.76	1.75	1.75	1.74	1.74	1.73	1.73	1.72
S24-C25	1.77	1.78	1.78	1.78	1.78	1.78	1.78	1.78	1.78	1.78	1.78
N9-C10	1.31	1.32	1.32	1.33	1.34	1.34	1.35	1.35	1.36	1.36	1.37
N9-C14	1.35	1.34	1.34	1.34	1.34	1.34	1.33	1.33	1.33	1.33	1.33
N19-C18	1.31	1.32	1.33	1.33	1.34	1.35	1.36	1.36	1.37	1.38	1.38
N19-C20	1.35	1.35	1.35	1.35	1.35	1.35	1.35	1.35	1.35	1.35	1.35
C10-C18	1.48	1.47	1.46	1.45	1.45	1.44	1.43	1.42	1.42	1.41	1.40
C15-C16	1.46	1.45	1.44	1.43	1.42	1.41	1.40	1.39	1.38	1.37	1.35

Table S7: Calculated bond lengths (in Å) of complex **2A** in ethanol with strong changes along the calculated path from the lowest T_{LC} to the lowest T_{LLCT} state geometry.

bond	p0.0	p0.1	p0.2	p0.3	p0.4	p0.5	p0.6	p0.7	p0.8	p0.9	p1.0
Zn-S7	2.31	2.35	2.38	2.42	2.46	2.50	2.54	2.57	2.61	2.65	2.69
Zn-S24	2.31	2.31	2.31	2.30	2.30	2.29	2.29	2.29	2.28	2.28	2.28
Zn-N9	2.15	2.14	2.13	2.11	2.10	2.09	2.08	2.06	2.05	2.04	2.03
Zn-N19	2.16	2.14	2.13	2.11	2.10	2.09	2.07	2.06	2.05	2.04	2.03
S7-C4	1.78	1.77	1.77	1.76	1.75	1.74	1.74	1.73	1.72	1.72	1.71
S24-C25	1.78	1.78	1.78	1.78	1.78	1.78	1.78	1.78	1.78	1.78	1.78
N9-C10	1.31	1.32	1.33	1.33	1.34	1.34	1.35	1.36	1.36	1.37	1.37
N9-C14	1.35	1.34	1.34	1.34	1.34	1.34	1.34	1.34	1.34	1.33	1.33
N19-C18	1.31	1.32	1.33	1.33	1.34	1.34	1.35	1.36	1.36	1.37	1.38
N19-C20	1.35	1.34	1.34	1.34	1.34	1.34	1.34	1.34	1.34	1.34	1.34
C10-C18	1.48	1.47	1.46	1.45	1.45	1.44	1.43	1.42	1.42	1.41	1.40
C15-C16	1.46	1.45	1.44	1.43	1.42	1.41	1.40	1.39	1.37	1.36	1.35

.

Table S8: Calculated bond angles (in °) of complex **1A** in ethanol with strong changes along the calculated path from the lowest T_{LC} to the lowest T_{LLCT} state geometry.

angle	p0.0	p0.1	p0.2	p0.3	p0.4	p0.5	p0.6	p0.7	p0.8	p0.9	p1.0
Zn-S7-C4	106.3	106.5	106.6	106.7	106.9	107.0	107.2	107.3	107.4	107.6	107.7
Zn-S24-C25	106.3	106.1	105.9	105.8	105.6	105.4	105.2	105.0	104.8	104.6	104.4
Zn-N9-C10	114.0	113.6	113.2	112.8	112.4	112.0	111.6	111.2	110.8	110.4	110.0
Zn-N9-C14	125.7	126.2	126.7	127.2	127.8	128.3	128.8	129.3	129.8	130.3	130.9
Zn-N19-C18	114.0	113.7	113.4	113.1	112.8	112.5	112.1	111.8	111.4	111.1	110.7
Zn-N19-C20	125.7	126.2	126.7	127.1	127.6	128.1	128.6	129.2	129.7	130.2	130.7
S7-Zn-N9	102.1	100.6	99.1	97.6	96.1	94.7	93.2	91.7	90.2	88.7	87.2
S7-Zn-N19	115.3	111.0	106.7	102.4	98.1	93.8	89.5	85.2	81.0	76.8	72.6
S24-Zn-N9	115.3	119.6	123.7	127.4	130.8	133.6	135.8	137.3	138.0	137.8	136.9
S24-Zn-N19	102.1	105.3	108.6	111.8	115.0	118.2	121.4	124.6	127.8	131.0	134.2

Continued on next page

Table S8: Calculated bond angles (in °) of complex **1A** in ethanol with strong changes along the calculated path from the lowest T_{LC} to the lowest T_{LLCT} state geometry.

angle	p0.0	p0.1	p0.2	p0.3	p0.4	p0.5	p0.6	p0.7	p0.8	p0.9	p1.0
S7-Zn-S24	131.9	130.3	128.6	126.8	125.0	123.4	122.0	120.9	120.1	119.8	119.9
N9-Zn-N19	77.2	77.8	78.4	79.0	79.6	80.2	80.8	81.4	82.0	82.7	83.3
S7-C4-C3	122.7	122.6	122.4	122.3	122.1	122.0	121.8	121.7	121.5	121.3	121.2
S7-C4-C5	119.3	119.4	119.5	119.6	119.7	119.8	119.9	120.0	120.1	120.2	120.3
S24-C25-C26	122.7	122.7	122.7	122.7	122.7	122.7	122.7	122.7	122.7	122.7	122.7
S24-C25-C30	119.3	119.3	119.3	119.3	119.3	119.3	119.3	119.3	119.2	119.2	119.2
N9-C10-C11	122.8	122.6	122.5	122.3	122.2	122.0	121.8	121.7	121.5	121.3	121.2
N9-C10-C18	117.4	117.4	117.5	117.6	117.6	117.7	117.8	117.9	117.9	118.0	118.1
N9-C14-C13	121.6	121.7	121.9	122.1	122.2	122.4	122.5	122.7	122.9	123.0	123.2
N19-C18-C10	117.4	117.4	117.5	117.5	117.5	117.6	117.6	117.7	117.7	117.8	117.8
N19-C18-C!7	122.8	122.7	122.6	122.4	122.3	122.2	122.1	121.9	121.8	121.7	121.6
N19-C20-C21	121.6	121.7	121.8	122.0	122.1	122.2	122.4	122.5	122.6	122.7	122.9

Table S9: Calculated bond angles (in °) of complex **2A** in ethanol with strong changes along the calculated path from the lowest T_{LC} to the lowest T_{LLCT} state geometry.

angle	p0.0	p0.1	p0.2	p0.3	p0.4	p0.5	p0.6	p0.7	p0.8	p0.9	p1.0
Zn-S7-C4	106.9	107.4	107.9	108.5	109.0	109.5	110.0	110.5	111.0	111.6	112.1
Zn-S24-C25	107.2	106.9	106.6	106.3	106.0	105.7	105.4	105.1	104.8	104.5	104.2
Zn-N9-C10	114.2	113.7	113.2	112.7	112.2	111.7	111.2	110.8	110.3	109.8	109.3
Zn-N9-C14	125.5	126.1	126.7	127.3	127.9	128.5	129.1	129.7	130.2	130.8	131.3
Zn-N19-C18	113.9	113.6	113.2	112.8	112.3	111.9	111.4	110.9	110.4	109.8	109.3
Zn-N19-C20	125.8	126.3	126.8	127.3	127.9	128.5	128.9	129.5	130.0	130.6	131.1
S7-Zn-N9	101.9	100.4	98.9	97.4	95.9	111.9	93.0	91.5	90.0	88.5	87.0
S7-Zn-N19	112.4	109.9	107.5	105.1	102.6	128.4	97.9	95.5	93.2	90.9	88.7
S24-Zn-N9	113.1	117.8	122.2	126.3	130.0	94.5	135.6	137.4	138.3	138.3	137.5
S24-Zn-N19	104.0	107.1	110.1	113.1	116.1	100.2	122.2	125.2	128.2	131.2	134.2
S7-Zn-S24	134.0	131.2	128.4	125.5	122.6	133.1	117.2	114.7	112.4	110.3	108.5

Continued on next page

Table S9: Calculated bond angles (in °) of complex **2A** in ethanol with strong changes along the calculated path from the lowest T_{LC} to the lowest T_{LLCT} state geometry.

angle	p0.0	p0.1	p0.2	p0.3	p0.4	p0.5	p0.6	p0.7	p0.8	p0.9	p1.0
N9-Zn-N19	77.1	77.7	78.4	79.1	79.7	119.1	81.1	81.7	82.4	83.0	83.7
S7-C4-C3	122.8	122.2	122.7	122.6	122.5	119.8	122.4	122.4	122.3	122.2	122.2
S7-C4-C5	119.5	119.6	119.6	119.6	119.6	80.4	119.7	119.7	119.7	119.7	119.7
S24-C25-C26	122.9	122.9	122.9	122.9	122.9	122.5	122.9	122.9	122.9	122.9	122.9
S24-C25-C30	119.3	119.3	119.3	119.3	119.3	119.6	119.3	119.3	119.3	119.3	119.3
N9-C10-C11	122.8	122.6	122.4	122.3	122.1	122.9	121.7	121.6	121.4	121.2	121.0
N9-C10-C18	117.4	117.5	117.6	117.6	117.7	119.3	117.9	118.0	118.1	118.2	118.3
N9-C14-C13	121.6	121.8	121.9	122.1	122.3	121.9	122.6	122.8	123.0	123.2	123.3
N19-C18-C10	117.4	117.5	117.6	117.7	117.7	117.8	117.9	118.0	118.0	118.1	118.2
N19-C18-C!7	122.8	122.6	122.5	122.3	122.1	122.0	121.8	121.6	121.4	121.3	121.1
N19-C20-C21	121.6	121.8	121.9	122.1	122.3	122.5	122.6	122.8	123.0	123.1	123.3

Table S10: Calculated dihedral angles (in °) of complex **1A** in ethanol with strong changes along the calculated path from the lowest T_{LC} to the lowest T_{LLCT} state geometry.

angle	p0.0	p0.1	p0.2	p0.3	p0.4	p0.5	p0.6	p0.7	p0.8	p0.9	p1.0
Zn-S7-C4-C3	-41.1	-32.5	-24.0	-15.4	-6.9	1.7	10.2	18.8	27.3	35.9	44.4
Zn-S7-C4-C5	140.7	149.0	157.4	165.7	174.1	-177.5	-169.2	-160.8	-152.5	-144.1	-135.8
Zn-S24-C25-C26	-41.1	-41.5	-41.9	-42.2	-42.8	-43.2	-43.6	-44.1	-44.5	-44.9	-45.3
Zn-S24-C25-C30	140.7	140.2	139.8	139.4	138.9	138.5	138.1	137.7	137.2	136.8	136.4
Zn-N9-C10-C11	179.6	179.5	179.3	179.1	178.9	178.7	178.5	178.4	178.2	178.0	177.8
Zn-N9-C10-C18	-0.4	-0.5	-0.7	-0.9	-1.0	-1.2	-1.4	-1.5	-1.7	-1.9	-2.0
Zn-N9-C10-C13	179.4	-179.2	-179.1	-178.9	-178.7	-178.5	-178.3	-178.1	-177.9	-177.7	-177.4
Zn-N19-C18-C10	-0.4	-0.1	0.2	0.6	0.9	1.2	1.5	1.9	2.2	2.5	2.8
Zn-N19-C18-C17	179.6	180.0	-179.7	-179.4	-179.1	-178.8	-178.4	-178.1	-177.8	-177.5	-177.1
Zn-N19-C20-C21	-179.4	-179.8	179.8	179.4	178.9	178.5	178.1	177.6	177.1	176.6	176.1
S7-Zn-N9-C10	-113.4	-109.0	-104.7	-100.4	-96.0	-91.7	-87.3	-83.0	-78.7	-74.3	-70.0
S7-Zn-N9-C14	65.9	70.1	74.3	78.5	82.7	86.9	91.1	95.3	99.5	103.7	107.9

Continued on next page

Table S10: Calculated dihedral angles (in °) of complex **1A** in ethanol with strong changes along the calculated path from the lowest T_{LC} to the lowest T_{LLCT} state geometry.

angle	p0.0	p0.1	p0.2	p0.3	p0.4	p0.5	p0.6	p0.7	p0.8	p0.9	p1.0
S7-Zn-N19-C18	97.7	96.7	95.7	94.7	93.7	92.7	91.6	90.4	89.1	87.7	86.1
S7-Zn-N19-C20	-83.1	-83.6	-84.1	-84.6	-85.1	-85.7	-86.3	-87.0	-87.7	-88.6	-89.6
S24-Zn-N9-C10	97.7	101.2	105.3	109.9	115.2	121.2	127.8	135.0	142.5	150.0	157.3
S24-Zn-N9-C14	-83.1	-79.6	-75.7	-71.2	-66.0	-60.2	-53.7	-46.7	-39.3	-31.9	-24.9
S24-Zn-N19-C18	-113.4	-117.9	-122.4	-126.9	-131.4	-135.9	-140.5	-145.0	-149.6	-154.2	-158.8
S24-Zn-N19-C20	65.9	61.9	57.8	53.8	49.8	45.7	41.7	37.6	33.6	29.6	25.5
S7-Zn-S24-C25	-25.8	-27.8	-29.8	-31.6	-33.4	-35.0	-36.5	-37.9	-39.2	-40.3	-41.2
S24-Zn-S7-C4	-25.8	-24.7	-24.3	-24.8	-26.1	-28.1	-30.9	-34.4	-38.5	-43.2	-48.5
N9-Zn-N19-C18	0.1	-0.2	-0.5	-0.8	-1.1	-1.4	-1.7	-2.0	-2.4	-2.7	-3.0
N9-Zn-N19-C20	179.4	179.6	179.7	179.9	-179.9	-179.7	-179.6	-179.4	-179.1	-178.9	-178.7
N19-Zn-N9-C10	0.1	0.4	0.6	0.9	1.1	1.4	1.7	1.9	2.2	2.5	2.8
N19-Zn-N9-C10	179.4	179.5	179.6	179.8	179.9	-180.0	-179.9	-179.7	-179.6	-179.5	-179.4

Table S11: Calculated dihedral angles (in °) of complex **2A** in ethanol with strong changes along the calculated path from the lowest T_{LC} to the lowest T_{LLCT} state geometry.

angle	p0.0	p0.1	p0.2	p0.3	p0.4	p0.5	p0.6	p0.7	p0.8	p0.9	p1.0
Zn-S7-C4-C3	-40.9	-35.2	-29.5	-23.8	-18.1	-12.5	-6.8	-1.1	4.6	10.3	16.0
Zn-S7-C4-C5	141.4	146.8	152.3	157.8	163.3	168.7	174.2	179.7	-174.8	-169.4	-163.9
Zn-S24-C25-C26	-39.4	-40.1	-40.9	-41.6	-42.3	-43.0	-43.7	-44.4	-45.1	-45.8	-46.5
Zn-S24-C25-C30	142.9	142.1	141.4	140.6	139.8	139.1	138.3	137.5	136.8	136.0	135.2
Zn-N9-C10-C11	179.5	178.8	178.1	177.4	176.7	176.0	175.3	174.6	173.9	173.2	172.5
Zn-N9-C10-C18	-0.6	-1.3	-2.0	-2.7	-3.5	-4.2	-4.9	-5.6	-6.4	-7.1	-7.8
Zn-N9-C10-C13	-179.4	-178.7	-177.8	-177.0	-176.2	-175.3	-174.4	-173.5	-172.6	-171.7	-170.7
Zn-N19-C18-C10	0.7	1.4	2.2	3.0	3.8	4.6	5.3	6.1	6.9	7.7	8.4
Zn-N19-C18-C17	-179.3	-178.6	-177.8	-177.1	-176.3	-175.6	-174.8	-174.1	-173.3	-172.6	-171.8
Zn-N19-C20-C21	179.2	178.3	177.3	176.4	175.4	174.5	173.5	172.4	171.4	170.3	169.2
S7-Zn-N9-C10	-109.8	-106.8	-103.8	-100.7	-97.7	-94.7	-91.6	-88.6	-85.6	-82.5	-79.5

Continued on next page

Table S11: Calculated dihedral angles (in °) of complex **2A** in ethanol with strong changes along the calculated path from the lowest T_{LC} to the lowest T_{LLCT} state geometry.

angle	p0.0	p0.1	p0.2	p0.3	p0.4	p0.5	p0.6	p0.7	p0.8	p0.9	p1.0
S7-Zn-N9-C14	69.6	71.9	74.2	76.5	78.8	81.0	83.3	85.5	87.7	89.9	92.1
S7-Zn-N19-C18	97.0	95.2	93.3	91.5	89.6	87.7	85.8	83.8	81.7	79.6	77.5
S7-Zn-N19-C20	-82.4	-83.3	-84.2	-85.2	-86.1	-87.1	-88.0	-89.1	-90.1	-91.2	-92.3
S24-Zn-N9-C10	100.6	104.5	108.9	114.0	119.7	126.2	133.4	141.3	149.6	158.0	166.1
S24-Zn-N9-C14	-80.0	-76.8	-73.1	-68.8	-63.8	-58.1	-51.7	-44.6	-37.1	-29.6	-22.3
S24-Zn-N19-C18	-111.7	-117.2	-122.8	-128.3	-133.9	-139.5	-145.1	-150.7	-156.4	-162.0	-167.7
S24-Zn-N19-C20	69.0	64.3	59.7	55.0	50.4	45.7	41.1	36.5	31.8	27.2	22.5
S7-Zn-S24-C25	-23.0	-24.1	-25.0	-25.7	-26.3	-26.9	-27.4	-27.9	-28.3	-28.8	-29.2
S24-Zn-S7-C4	-28.0	-28.8	-30.2	-32.3	-35.0	-38.3	-42.2	-46.5	-51.4	-56.8	-62.6
N9-Zn-N19-C18	-0.7	-1.6	-2.5	-3.3	-4.2	-5.1	-6.0	-6.9	-7.9	-8.8	-9.7
N9-Zn-N19-C20	-179.9	179.9	180.0	180.0	-180.0	-179.9	-179.8	-179.8	-179.7	-179.6	179.5
N19-Zn-N9-C10	0.7	1.5	2.4	3.3	4.1	5.0	5.9	6.8	7.7	8.6	9.5
N19-Zn-N9-C10	-179.9	-179.8	-179.6	-179.5	-179.4	-179.3	-179.2	-179.1	-179.0	-179.0	-178.9

Table S12: Cartesian coordinates of the optimized S_0 geometry of conformer **1A**.

atom	x	y	z
Zn	3.3300570	6.4388910	4.4361070
S	4.6635620	7.3577320	6.0934680
S	1.9749770	7.3199010	2.7794270
N	4.2823060	4.7858300	3.4327490
N	2.4528430	4.7428730	5.4199410
C	5.0666470	9.0129010	5.6012060
C	5.3091490	9.3726590	4.2726580
C	5.6467830	10.6740340	3.9295280
C	5.7554940	11.6345650	4.9231920

Continued on next page

Table S12: Cartesian coordinates of the optimized S_0 geometry of conformer **1A**.

atom	x	y	z
C	5.5291340	11.3074390	6.2509860
C	5.1849790	10.0041020	6.5804460
C	1.6368520	9.0039590	3.2208220
C	1.5717450	9.9738810	2.2160200
C	1.2829230	11.2990830	2.5100020
C	1.0591310	11.6687280	3.8270150
C	1.1147900	10.7294730	4.8452740
C	1.3970900	9.4063650	4.5373840
C	5.1692810	4.8434150	2.4658360
C	5.7197630	3.6938990	1.8833670
C	5.3173050	2.4625570	2.3384700
C	4.3663980	2.3796600	3.3732310
C	3.8887540	1.1390830	3.9085320
C	2.9732250	1.1177290	4.9051160
C	2.4534020	2.3351190	5.4539780
C	1.5008490	2.3734460	6.4897990
C	1.0556920	3.5848290	6.9584190
C	1.5647260	4.7588380	6.3878010
C	2.9013250	3.5659710	4.9496950
C	3.8759900	3.5888440	3.8902650
H	5.2318070	8.6289060	3.4875070
H	5.8266720	10.9358640	2.8930440
Cl	6.1819020	13.2753100	4.4965640

Continued on next page

Table S12: Cartesian coordinates of the optimized S_0 geometry of conformer **1A**.

atom	x	y	z
H	5.6150720	12.0627270	7.0238880
H	5.0003620	9.7536530	7.6198400
H	1.7556880	9.6895390	1.1852840
H	1.2386400	12.0382300	1.7182080
Cl	0.7041810	13.3373080	4.2087620
H	0.9372840	11.0252300	5.8730030
H	1.4358820	8.6775480	5.3392320
H	6.4492750	3.7921190	1.0884270
H	5.7232520	1.5521000	1.9096840
H	4.2782050	0.2144290	3.4968150
H	2.6157550	0.1758360	5.3067200
H	1.1271260	1.4447410	6.9085250
H	0.3236410	3.6490680	7.7545070
H	5.4651050	5.8318890	2.1281900
H	1.2339500	5.7327220	6.7354340

Table S13: Cartesian coordinates of the optimized S_{LLCT} geometry of conformer **1A**.

atom	x	y	z
Zn	0.5155480	3.6130850	2.4385990
S	1.9593390	2.1010590	1.5128350
N	-0.6523650	4.9400480	1.4470860
C	1.7941710	0.7122740	2.6017770
C	1.8388720	0.8399850	4.0009050

Continued on next page

Table S13: Cartesian coordinates of the optimized S_{LLCT} geometry of conformer **1A**.

atom	x	y	z
C	1.6946460	-0.2686330	4.8340310
C	1.5158670	-1.5282820	4.2674030
C	1.4872510	-1.6895060	2.8829870
C	1.6237600	-0.5725750	2.0613050
C	-1.7916400	8.2976660	2.6156520
C	-1.6611800	7.1463890	1.7613100
C	-2.2900300	7.0204410	0.5245610
C	-2.0910740	5.8520100	-0.2409660
C	-1.2701500	4.8542920	0.2618570
C	-0.8336430	6.0723640	2.2136050
H	2.0049080	1.8229070	4.4510760
H	1.7274360	-0.1509790	5.9198900
Cl	1.3283490	-2.9201320	5.3007670
H	1.3494120	-2.6820720	2.4470520
H	1.5865960	-0.7002510	0.9757540
H	-2.4259180	9.1229660	2.2778350
H	-2.5683010	5.7231610	-1.2143470
H	-2.9297690	7.8274180	0.1560070
S	-1.1695090	2.2725590	3.7924570
N	0.6310760	5.0873830	3.8279090
C	-1.1455740	8.3731600	3.8119450
C	-0.1661390	6.1495070	3.4508530
C	-1.9864800	1.0867980	2.8603340

Continued on next page

Table S13: Cartesian coordinates of the optimized S$_{LLCT}$ geometry of conformer **1A**.

atom	x	y	z
C	1.2872370	5.1564080	4.9942340
C	-0.3008630	7.3056640	4.2806660
H	-1.2560460	9.2598570	4.4437120
C	-1.6569580	0.8220310	1.5078260
C	-3.0407340	0.3527040	3.4626040
C	1.2035670	6.2417180	5.8523930
C	0.3921940	7.3372340	5.4884970
C	-2.3564540	-0.1294260	0.7856740
H	-0.8314490	1.3641910	1.0386900
C	-3.7463640	-0.5938230	2.7422570
H	-3.2951310	0.5465090	4.5075810
H	1.7624200	6.2360500	6.7901640
H	0.3054210	8.2098190	6.1421460
C	-3.3991910	-0.8286130	1.4053250
H	-2.1020530	-0.3363680	-0.2558090
H	-4.5615320	-1.1546190	3.2037610
Cl	-4.2740520	-2.0102370	0.5037700
H	1.9097970	4.2924030	5.2498060
H	-1.0931220	3.9360040	-0.3078780

Table S14: Cartesian coordinates of the optimized T_{LLCT} geometry of conformer **1A**.

atom	x	y	z
C	0.000000	0.000000	0.000000
C	0.000000	0.000000	1.391469
C	1.205737	0.000000	2.065246
C	2.425662	0.006039	1.361708
C	2.390270	0.007799	-0.046084
C	1.187171	0.005326	-0.725440
S	3.935370	0.015686	2.192781
Zn	3.774929	-1.842139	4.266695
N	5.803262	-1.669565	4.442283
C	6.416966	-2.238356	3.357691
C	7.833616	-2.210061	3.213850
C	8.577297	-1.591487	4.210347
C	7.930885	-1.023248	5.307965
C	6.546638	-1.090663	5.374191
C	8.403509	-2.821726	2.049548
C	7.620792	-3.406548	1.111704
C	6.187427	-3.443612	1.237906
C	5.609883	-2.848786	2.387583
N	4.241522	-2.847655	2.592412
C	3.448657	-3.417769	1.654472
C	3.942427	-4.005469	0.523502
C	5.344417	-4.024737	0.298208
Cl	-1.513058	-0.004763	-0.848214

Continued on next page

Table S14: Cartesian coordinates of the optimized T_{LLCT} geometry of conformer **1A**.

atom	x	y	z
S	1.974489	-1.832102	5.668192
C	1.661738	-0.109156	5.975619
C	2.678968	0.799514	6.278117
C	2.398860	2.134239	6.532774
C	1.083485	2.571781	6.498543
C	0.051788	1.691665	6.213450
C	0.345935	0.360444	5.950549
Cl	0.724359	4.251082	6.818246
H	3.708756	0.463719	6.322435
H	3.200966	2.826762	6.761037
H	-0.974372	2.040074	6.189459
H	-0.463385	-0.323729	5.718706
H	8.067619	-3.866142	0.235764
H	3.260730	-4.460010	-0.185813
H	5.755927	-4.486216	-0.592284
H	9.482506	-2.806722	1.933393
H	1.216849	-0.002455	3.149061
H	3.322023	0.011169	-0.599754
H	8.485490	-0.536889	6.100874
H	9.659059	-1.554910	4.128419
H	-0.936136	-0.000981	1.936683
H	1.164223	0.006026	-1.808482
H	6.015652	-0.657709	6.216859

Continued on next page

Table S14: Cartesian coordinates of the optimized T_{LLCT} geometry of conformer **1A**.

atom	x	y	z
H	2.382195	-3.389292	1.852788

Table S15: Cartesian coordinates of the optimized T_{LC}(phen) geometry of conformer **1A**.

atom	x	y	z
C	0.000000	0.000000	0.000000
C	0.000000	0.000000	1.386256
C	1.208634	0.000000	2.067818
C	2.427471	0.011478	1.383256
C	2.393992	0.009051	-0.014426
C	1.191737	0.000452	-0.707788
S	3.995056	-0.015866	2.215054
Zn	3.791126	1.399885	4.033591
N	5.837513	1.639542	4.651891
C	6.106671	1.114704	5.825731
C	7.405571	1.159280	6.412739
C	8.417735	1.805185	5.653070
C	8.106584	2.343818	4.420571
C	6.805874	2.247172	3.942286
C	7.607452	0.584196	7.665183
C	6.505422	-0.060318	8.383141
C	5.228986	-0.120266	7.828879
C	4.997676	0.457556	6.545786
N	3.823917	0.435539	5.956203

Continued on next page

Table S15: Cartesian coordinates of the optimized T_{LC}(phen) geometry of conformer **1A**.

atom	x	y	z
C	2.770967	-0.142634	6.562413
C	2.886349	-0.732757	7.814765
C	4.108732	-0.728504	8.456448
Cl	-1.519494	0.000789	-0.864037
S	2.420870	3.222182	4.426865
C	2.004783	3.886447	2.834516
C	2.934290	3.998785	1.796384
C	2.581475	4.543185	0.569815
C	1.285801	4.994944	0.372717
C	0.343899	4.907403	1.385811
C	0.706949	4.353059	2.605294
Cl	0.835330	5.680988	-1.170605
H	3.952408	3.655035	1.942493
H	3.314095	4.617315	-0.225795
H	-0.667656	5.262711	1.225550
H	-0.035327	4.277445	3.392846
H	6.693587	-0.494922	9.357354
H	2.017298	-1.189322	8.273971
H	4.227019	-1.182852	9.433989
H	8.589616	0.610980	8.121267
H	1.197454	-0.007325	3.152205
H	3.324802	0.018950	-0.571583
H	8.861875	2.840018	3.822330

Continued on next page

Table S15: Cartesian coordinates of the optimized T_{LC}(phen) geometry of conformer **1A**.

atom	x	y	z
H	9.424705	1.867422	6.050746
H	-0.935674	-0.003345	1.933729
H	1.185069	0.000164	-1.791820
H	6.518496	2.654770	2.980124
H	1.830598	-0.122402	6.024108

Table S16: Cartesian coordinates of the optimized S_0 geometry of conformer **1B**.

atom	x	y	z
Zn	3.3298480	6.4389530	4.4363000
S	4.6638610	7.3581540	6.0930130
S	1.9740350	7.3198140	2.7801260
N	4.2811400	4.7860040	3.4318050
N	2.4539950	4.7427460	5.4210920
C	5.0669960	9.0131440	5.6002000
C	5.3092210	9.3725610	4.2715010
C	5.6469460	10.6738240	3.9279900
C	5.7560210	11.6345690	4.9213880
C	5.5299800	11.3077780	6.2493340
C	5.1857050	10.0045800	6.5791740
C	1.6357590	9.0038020	3.2216860
C	1.5700680	9.9737260	2.2169140
C	1.2811140	11.2988690	2.5110150
C	1.0577490	11.6684610	3.8281180

Continued on next page

Table S16: Cartesian coordinates of the optimized S_0 geometry of conformer **1B**.

atom	x	y	z
C	1.1139960	10.7292140	4.8463440
C	1.3964360	9.4061560	4.5383390
C	5.1668990	4.8437460	2.4637830
C	5.7168820	3.6943360	1.8806560
C	5.3152430	2.4629170	2.3362880
C	4.3656400	2.3798440	3.3722220
C	3.8889420	1.1391900	3.9081960
C	2.9747330	1.1176940	4.9059890
C	2.4553250	2.3349980	5.4554540
C	1.5041740	2.3731790	6.4925500
C	1.0592820	3.5844980	6.9616370
C	1.5671540	4.7585790	6.3901260
C	2.9022620	3.5659290	4.9504520
C	3.8756260	3.5889430	3.8898200
H	5.2315680	8.6286670	3.4865060
H	5.8265860	10.9353940	2.8913950
Cl	6.1825740	13.2751570	4.4942590
H	5.6162030	12.0632410	7.0220340
H	5.0012940	9.7543960	7.6186690
H	1.7536570	9.6894210	1.1861040
H	1.2363760	12.0380150	1.7192460
Cl	0.7026560	13.3369720	4.2100310
H	0.9368300	11.0249230	5.8741450

Continued on next page

Table S16: Cartesian coordinates of the optimized S_0 geometry of conformer **1B**.

atom	x	y	z
H	1.4357180	8.6773610	5.3401930
H	6.4453890	3.7926720	1.0848100
H	5.7208500	1.5525400	1.9070120
H	4.2780490	0.2146020	3.4960060
H	2.6180110	0.1757430	5.3081190
H	1.1312880	1.4444140	6.9118930
H	0.3283160	3.6486110	7.7587280
H	5.4620910	5.8322740	2.1257470
H	1.2364790	5.7324220	6.7379630

Table S17: Cartesian coordinates of the optimized S_{LLCT} geometry of conformer **1B**.

atom	x	y	z
Zn	1.0311050	3.6213920	2.1249030
S	2.2687190	1.8485670	1.3979990
N	-0.4303530	4.7441570	1.3140110
C	2.1294190	0.6269990	2.6811480
C	2.2153480	0.9349880	4.0414930
C	2.1341090	-0.0558620	5.0095880
C	1.9742520	-1.3766340	4.6196730
C	1.8937340	-1.7140990	3.2778520
C	1.9675630	-0.7129510	2.3192430
C	-2.3021620	7.5037960	2.9769020
C	-1.9613380	6.5209500	1.9799570

Continued on next page

Table S17: Cartesian coordinates of the optimized S_{LLCT} geometry of conformer **1B**.

atom	x	y	z
C	-2.6794660	6.3230890	0.8134760
C	-2.2626340	5.3324450	-0.0986760
C	-1.1464990	4.5826470	0.1968300
C	-0.8205770	5.7031040	2.2188640
H	2.3559020	1.9625840	4.3564400
H	2.2009550	0.2011720	6.0605490
Cl	1.8741890	-2.6289380	5.8336370
H	1.7692990	-2.7487100	2.9794060
H	1.8964330	-0.9798880	1.2702160
H	-3.1714510	8.1298680	2.8014330
H	-2.8004520	5.1581700	-1.0226210
H	-3.5539850	6.9310200	0.6069080
S	-1.1633880	2.5668480	3.6809660
N	1.0216120	5.0295410	3.5723280
C	-1.5698560	7.6530380	4.1026860
C	-0.0629730	5.8537540	3.3898030
C	-2.1789070	1.6305010	2.6692380
C	1.7536210	5.1640840	4.6795410
C	-0.4142480	6.8345170	4.3619720
H	-1.8445980	8.4003410	4.8405490
C	-1.6917820	1.0453230	1.4796480
C	-3.5346450	1.4292260	3.0113500
C	1.4769730	6.0919170	5.6614920

Continued on next page

Table S17: Cartesian coordinates of the optimized S_{LLCT} geometry of conformer **1B**.

atom	x	y	z
C	0.3682490	6.9408440	5.4980910
C	-2.5196710	0.2942830	0.6710040
H	-0.6514760	1.1817560	1.2060520
C	-4.3669560	0.6859950	2.2019640
H	-3.9190420	1.8697990	3.9237450
H	2.1100380	6.1560820	6.5378810
H	0.1227350	7.6787690	6.2549020
C	-3.8526470	0.1238480	1.0349840
H	-2.1417980	-0.1571810	-0.2381860
H	-5.4068350	0.5364030	2.4652510
Cl	-4.8940760	-0.8105840	0.0174190
H	2.6010750	4.4920900	4.7793360
H	-0.8013680	3.8114870	-0.4853450

Table S18: Cartesian coordinates of the optimized T_{LLCT} geometry of conformer **1B**.

atom	x	y	z
Zn	0.7576150	3.5145640	2.3686420
S	2.1797640	1.9393030	1.5308330
N	-0.7065230	4.6407850	1.5812920
C	2.1617730	0.6372970	2.7413390
C	2.2580240	0.8821420	4.1134650
C	2.2613030	-0.1582550	5.0312690
C	2.1799890	-1.4660010	4.5773810

Continued on next page

Table S18: Cartesian coordinates of the optimized T_{LLCT} geometry of conformer **1B**.

atom	x	y	z
C	2.0957710	-1.7409900	3.2218110
C	2.0833540	-0.6906880	2.3137910
C	-2.1446120	7.8110020	2.9251490
C	-1.9749060	6.6759370	2.0564350
C	-2.7635540	6.4351510	0.9377490
C	-2.5081840	5.2824550	0.1485830
C	-1.4969010	4.4333620	0.5016280
C	-0.9443540	5.7539290	2.3678770
H	2.3375900	1.9003150	4.4770300
H	2.3316950	0.0500120	6.0927480
Cl	2.1836120	-2.7802810	5.7279840
H	2.0336520	-2.7656510	2.8737040
H	2.0080540	-0.9093440	1.2539030
H	-2.9287570	8.5227090	2.6869440
H	-3.0992280	5.0738900	-0.7355070
H	-3.5606630	7.1211160	0.6744090
S	-1.6357380	2.7325780	3.5681150
N	0.8421470	5.0163970	3.7514270
C	-1.3568560	8.0015880	4.0101970
C	-0.1304720	5.9457650	3.4930050
C	-2.4085820	1.6094840	2.5139010
C	1.6262720	5.1796190	4.8072190
C	-0.3153660	7.0743270	4.3418570

Continued on next page

Table S18: Cartesian coordinates of the optimized T_{LLCT} geometry of conformer **1B**.

atom	x	y	z
H	-1.5029080	8.8656670	4.6505010
C	-1.6840100	0.5727050	1.8947860
C	-3.7894580	1.7114240	2.2571420
C	1.5109700	6.2518160	5.6802420
C	0.5245770	7.2082050	5.4397070
C	-2.3125620	-0.3279010	1.0571660
H	-0.6202710	0.4819850	2.0819050
C	-4.4230860	0.8149150	1.4182350
H	-4.3586530	2.5055540	2.7262920
H	2.1814260	6.3321340	6.5269260
H	0.4079290	8.0584870	6.1042920
C	-3.6780420	-0.1981580	0.8230370
H	-1.7520020	-1.1261640	0.5858280
H	-5.4854120	0.8971480	1.2227650
Cl	-4.4685470	-1.3252320	-0.2322550
H	2.3851170	4.4195920	4.9684520
H	-1.2788420	3.5458110	-0.0833380

Table S19: Cartesian coordinates of the optimized T_{LC}(phen) geometry of conformer **1B** (p0.0).

atom	x	y	z
Zn	-0.5741330	3.4672850	2.8314240
S	1.2836090	2.5242810	1.8251580

Continued on next page

Table S19: Cartesian coordinates of the optimized T_{LC}(phen) geometry of conformer **1B** (p0.0).

atom	x	y	z
N	-0.9773070	5.1484100	1.5512890
C	1.4874280	0.9204050	2.5572710
C	1.3141250	0.6864540	3.9245870
C	1.5025430	-0.5760280	4.4686080
C	1.8808240	-1.6236090	3.6432690
C	2.0711280	-1.4215910	2.2852650
C	1.8712300	-0.1559910	1.7518430
C	-0.7869250	8.7476230	2.1307630
C	-0.9983410	7.5523360	1.4476210
C	-1.4145130	7.4649650	0.0919180
C	-1.5960900	6.2250320	-0.4873850
C	-1.3702470	5.0800350	0.2662210
C	-0.7929500	6.3150710	2.1263690
H	1.0252950	1.5005770	4.5802220
H	1.3582560	-0.7402170	5.5304210
Cl	2.1189030	-3.2163930	4.3228140
H	2.3672300	-2.2448420	1.6451460
H	2.0118730	-0.0035420	0.6869910
H	-0.9388860	9.6939070	1.6259530
H	-1.9117770	6.1330700	-1.5200780
H	-1.5846990	8.3748070	-0.4730900
S	-2.4319010	2.5242960	3.8376460
N	-0.1708290	5.1483600	4.1115650

Continued on next page

Table S19: Cartesian coordinates of the optimized T_{LC}(phen) geometry of conformer **1B** (p0.0).

atom	x	y	z
C	-0.3605500	8.7475970	3.5320250
C	-0.3549780	6.3150440	3.5364650
C	-2.6356310	0.9204060	3.1055320
C	0.2220760	5.0799370	5.3966410
C	-0.1493720	7.5522830	4.2151940
H	-0.2084070	9.6938610	4.0368150
C	-2.4623280	0.6864930	1.7382090
C	-3.0193450	-0.1560300	3.9109460
C	0.4481190	6.2249060	6.1502290
C	0.2667840	7.4648620	5.5709000
C	-2.6506660	-0.5759920	1.1941650
H	-2.1735570	1.5006510	1.0825940
C	-3.2191630	-1.4216330	3.3775020
H	-3.1599800	-0.0036090	4.9758030
H	0.7637800	6.1329030	7.1829260
H	0.4371490	8.3746830	6.1358860
C	-3.0288620	-1.6236130	2.0194920
H	-2.5063780	-0.7401520	0.1323480
H	-3.5151970	-2.2449190	4.0176080
Cl	-3.2668400	-3.2164030	1.3399250
H	0.3511460	4.0872300	5.8117930
H	-1.4995060	4.0873450	-0.1489110

Table S20: Cartesian coordinates of the optimized S_0 geometry of conformer **2A**.

atom	x	y	z
Zn	-0.690380	3.429869	2.920875
S	1.241306	2.379912	2.198400
N	-0.900022	5.082612	1.552235
C	1.266958	0.748939	2.908156
C	0.857900	0.482708	4.216833
C	0.931020	-0.801232	4.739916
C	1.420070	-1.869201	3.988230
C	1.836761	-1.597365	2.686236
C	1.759103	-0.317616	2.152577
C	-0.628601	8.728595	2.114030
C	-0.829566	7.487006	1.427220
C	-1.132345	7.401242	0.055282
C	-1.307345	6.169371	-0.525224
C	-1.180071	5.022823	0.270314
C	-0.723971	6.280432	2.136503
H	0.479738	1.289226	4.836436
H	0.603712	-0.972387	5.762156
C	1.469617	-3.262328	4.551183
H	2.229127	-2.402530	2.070537
H	2.086594	-0.142484	1.132493
H	-0.713797	9.650787	1.549564
H	-1.540420	6.068494	-1.578428
H	-1.224328	8.309911	-0.530612

Continued on next page

Table S20: Cartesian coordinates of the optimized S_0 geometry of conformer **2A**.

atom	x	y	z
S	-2.717932	2.670262	3.721769
N	-0.323194	5.132683	4.189176
C	-0.338957	8.753462	3.435888
C	-0.416119	6.307131	3.542395
C	-2.998886	1.069355	2.998157
C	-0.043943	5.120234	5.472577
C	-0.224511	7.538861	4.187588
H	-0.188094	9.695937	3.950933
C	-2.699057	0.778967	1.664955
C	-3.584439	0.059870	3.765067
C	0.165027	6.295176	6.207052
C	0.074388	7.504176	5.562687
C	-2.964736	-0.473618	1.129164
H	-2.254235	1.543149	1.036079
C	-3.854855	-1.188468	3.219118
H	-3.831812	0.254211	4.804053
H	0.393168	6.233408	7.264364
H	0.230274	8.433532	6.100736
C	-3.546584	-1.485270	1.892745
H	-2.717405	-0.664120	0.088036
H	-4.314498	-1.949154	3.844720
C	-3.804459	-2.848547	1.313761
H	0.020062	4.148812	5.952773

Continued on next page

Table S20: Cartesian coordinates of the optimized S_0 geometry of conformer **2A**.

atom	x	y	z
H	-1.311896	4.034283	-0.158651
H	2.258887	-3.855977	4.078343
H	0.521176	-3.791087	4.387166
H	1.651453	-3.250772	5.631089
H	-4.063506	-2.788964	0.251246
H	-4.621690	-3.356220	1.836431
H	-2.916341	-3.489333	1.395650

Table S21: Cartesian coordinates of the optimized S_{LLCT} geometry of conformer **2A**.

atom	x	y	z
Zn	0.749023	3.435807	2.308758
S	2.127032	1.765824	1.605291
N	-0.577464	4.657032	1.384313
C	1.925407	0.489073	2.831090
C	1.949513	0.744631	4.204471
C	1.819271	-0.287026	5.124192
C	1.670753	-1.612607	4.716519
C	1.649325	-1.862878	3.345740
C	1.770604	-0.835092	2.418631
C	-2.297966	7.613808	2.862460
C	-1.986905	6.574513	1.914181
C	-2.650264	6.404236	0.711844
C	-2.269861	5.354836	-0.148688

Continued on next page

Table S21: Cartesian coordinates of the optimized S_{LLCT} geometry of conformer **2A**.

atom	x	y	z
C	-1.239919	4.523416	0.232350
C	-0.936802	5.669499	2.242619
H	2.076592	1.760697	4.563016
H	1.837828	-0.051835	6.185082
C	1.567924	-2.728237	5.718750
H	1.528709	-2.882455	2.989603
H	1.740027	-1.064689	1.358290
H	-3.098330	8.305567	2.618709
H	-2.767309	5.198290	-1.098054
H	-3.455221	7.078433	0.438474
S	-1.298165	2.339255	3.660222
N	0.764462	4.890390	3.719974
C	-1.620357	7.736783	4.024881
C	-0.237020	5.793017	3.452081
C	-2.242792	1.310799	2.673026
C	1.445645	5.003827	4.860842
C	-0.555339	6.832836	4.373891
H	-1.870118	8.528603	4.724281
C	-1.779420	0.828744	1.427928
C	-3.534131	0.921175	3.099902
C	1.196153	5.983743	5.798551
C	0.171802	6.914425	5.547980
C	-2.572118	0.003503	0.658817

Continued on next page

Table S21: Cartesian coordinates of the optimized S_{LLCT} geometry of conformer **2A**.

atom	x	y	z
H	-0.788515	1.102862	1.084089
C	-4.315376	0.101815	2.317585
H	-3.901982	1.281861	4.053673
H	1.785659	6.026252	6.706115
H	-0.050657	7.696457	6.266700
C	-3.851743	-0.376264	1.082524
H	-2.198113	-0.357503	-0.293690
H	-5.305750	-0.180218	2.660020
C	-4.694483	-1.296003	0.256264
H	2.228631	4.269393	5.026657
H	-0.923515	3.706444	-0.409519
H	1.050127	-3.596096	5.297869
H	1.027960	-2.409979	6.616809
H	2.562590	-3.064765	6.040132
H	-4.409746	-1.261166	-0.799060
H	-5.757121	-1.050095	0.345107
H	-4.570185	-2.332178	0.598690

Table S22: Cartesian coordinates of the optimized T_{LLCT} geometry of conformer **2A**.

atom	x	y	z
C	0.000000	0.000000	0.000000
C	0.000000	0.000000	1.400425
C	1.178606	0.000000	2.115835

Continued on next page

Table S22: Cartesian coordinates of the optimized T_{LLCT} geometry of conformer **2A**.

atom	x	y	z
C	2.423299	0.003815	1.446445
C	2.419289	0.008593	0.031685
C	1.234139	0.002303	-0.667670
S	3.911026	0.000114	2.289803
Zn	3.609644	-0.699063	4.866657
N	5.570580	-1.210891	4.848246
C	5.711883	-2.444692	4.258978
C	7.002074	-2.978428	3.971196
C	8.113311	-2.223937	4.302512
C	7.945195	-0.966730	4.910308
C	6.665675	-0.514935	5.156255
C	7.068759	-4.275091	3.348774
C	5.950955	-4.971887	3.047964
C	4.638057	-4.453499	3.337265
C	4.551838	-3.171192	3.951994
N	3.334238	-2.614336	4.265460
C	2.221266	-3.291947	3.972447
C	2.226463	-4.531617	3.372098
C	3.463222	-5.125183	3.048725
C	-1.282908	0.029979	-0.769470
S	2.289505	0.850536	5.885771
C	2.606951	2.353916	4.984437
C	3.895099	2.787086	4.660241

Continued on next page

Table S22: Cartesian coordinates of the optimized T_{LLCT} geometry of conformer **2A**.

atom	x	y	z
C	4.096284	3.982205	3.983202
C	3.027915	4.798138	3.611368
C	1.745090	4.362971	3.938657
C	1.534596	3.164085	4.608692
C	3.256355	6.108813	2.911642
H	4.754088	2.187884	4.943415
H	5.111562	4.286573	3.742959
H	0.886996	4.968596	3.659708
H	0.521356	2.850820	4.839302
H	6.023228	-5.947806	2.577979
H	1.290085	-5.034066	3.162344
H	3.500780	-6.102390	2.578742
H	8.048230	-4.685561	3.123675
H	1.154759	0.008769	3.199630
H	3.366634	0.013361	-0.495194
H	8.796398	-0.356406	5.185902
H	9.106915	-2.607127	4.093860
H	-0.945734	-0.001541	1.932458
H	1.252636	-0.000572	-1.752701
H	6.503326	0.452709	5.622369
H	1.284292	-2.809135	4.234214
H	2.378537	6.409059	2.330504
H	4.114092	6.055113	2.232848

Continued on next page

Table S22: Cartesian coordinates of the optimized T_{LLCT} geometry of conformer **2A**.

atom	x	y	z
H	3.462166	6.911686	3.632013
H	-2.113141	-0.369878	-0.180553
H	-1.202236	-0.539211	-1.700640
H	-1.536862	1.063624	-1.040487

Table S23: Cartesian coordinates of the optimized T_{LC}(phen) geometry of conformer **2A**.

atom	x	y	z
C	0.000000	0.000000	0.000000
C	0.000000	0.000000	1.394649
C	1.182974	0.000000	2.120755
C	2.422239	0.008855	1.476097
C	2.426487	0.006027	0.079694
C	1.238236	-0.002559	-0.639666
S	3.966873	-0.034495	2.358109
Zn	3.735433	1.355115	4.185692
N	5.770436	1.540628	4.861909
C	6.017995	0.931237	5.998602
C	7.307798	0.927025	6.607611
C	8.333001	1.626343	5.915491
C	8.042854	2.257525	4.722374
C	6.750433	2.198425	4.216269
C	7.489250	0.256780	7.814838
C	6.375838	-0.440570	8.462078

Continued on next page

Table S23: Cartesian coordinates of the optimized T_{LC}(phen) geometry of conformer **2A**.

atom	x	y	z
C	5.107008	-0.450367	7.887528
C	4.894434	0.229696	6.651960
N	3.726915	0.265634	6.050554
C	2.664238	-0.353359	6.595847
C	2.761987	-1.046211	7.796147
C	3.976622	-1.101977	8.449896
C	-1.285204	0.029486	-0.779450
S	2.457391	3.231170	4.625913
C	2.037576	3.960799	3.058563
C	2.934001	4.032912	1.989823
C	2.574173	4.645274	0.797046
C	1.314364	5.216985	0.620958
C	0.426590	5.151991	1.693421
C	0.775569	4.533668	2.887013
C	0.921284	5.852861	-0.683375
H	3.926783	3.606605	2.091466
H	3.296629	4.682826	-0.014145
H	-0.562959	5.590979	1.596653
H	0.056996	4.495295	3.699819
H	6.549163	-0.953496	9.400305
H	1.885494	-1.534493	8.205948
H	4.081346	-1.636184	9.387802
H	8.463898	0.246605	8.287424

Continued on next page

Table S23: Cartesian coordinates of the optimized T_{LC}(phen) geometry of conformer **2A**.

atom	x	y	z
H	1.141663	-0.009737	3.205002
H	3.373300	0.010625	-0.451312
H	8.808171	2.796929	4.176514
H	9.333385	1.656156	6.333131
H	-0.946096	-0.006336	1.929679
H	1.279437	-0.008292	-1.725735
H	6.478338	2.678598	3.283421
H	1.729892	-0.283470	6.051152
H	0.153280	6.619632	-0.538071
H	0.512264	5.109282	-1.380378
H	1.781104	6.319561	-1.175644
H	-2.079359	-0.518727	-0.261432
H	-1.159151	-0.410727	-1.773986
H	-1.640519	1.059007	-0.920536

Table S24: Cartesian coordinates of the optimized S_0 geometry of conformer **2B**.

atom	x	y	z
Zn	2.1380450	10.1854660	2.5471940
S	1.8306540	12.4769100	2.4932420
S	0.8686360	8.7209370	3.8055050
N	4.1956350	9.5816600	2.5988020
N	2.4499230	9.4680580	0.5498420
C	5.0176030	9.6523340	3.6205240

Continued on next page

Table S24: Cartesian coordinates of the optimized S_0 geometry of conformer **2B**.

atom	x	y	z
C	6.3406150	9.1958160	3.5508500
C	6.7943350	8.6544580	2.3732190
C	5.9278430	8.5695210	1.2671250
C	6.3134940	8.0217710	0.0001080
C	5.4373150	7.9666510	-1.0302710
C	4.0972630	8.4541290	-0.8851230
C	3.1430900	8.4257450	-1.9197520
C	1.8805130	8.9158820	-1.6924170
C	1.5728570	9.4336420	-0.4271600
C	3.6904080	8.9944760	0.3444340
C	4.6223040	9.0542180	1.4392570
C	0.7047140	12.7988190	3.8376250
C	-0.5666680	12.2222770	3.8926670
C	-1.4386800	12.5165220	4.9317960
C	-1.0848700	13.3995840	5.9523150
C	0.1798310	13.9808200	5.8874270
C	1.0611250	13.6860730	4.8541500
C	1.7156280	7.1803150	3.5008620
C	1.4350970	6.4109860	2.3696490
C	2.0793940	5.2002000	2.1514390
C	3.0252590	4.7076600	3.0498120
C	3.2963630	5.4742820	4.1823600
C	2.6572380	6.6869980	4.4060820

Continued on next page

Table S24: Cartesian coordinates of the optimized S_0 geometry of conformer **2B**.

atom	x	y	z
C	-2.0243450	13.6914490	7.0891300
C	3.7431810	3.4117800	2.7939320
H	4.6273090	10.0848790	4.5365030
H	6.9822820	9.2757040	4.4201420
H	7.8130460	8.2913690	2.2850130
H	7.3263980	7.6516610	-0.1159950
H	5.7356880	7.5510030	-1.9865790
H	3.4136030	8.0174100	-2.8880320
H	1.1237240	8.9092710	-2.4677100
H	0.5840610	9.8280020	-0.2142640
H	-0.8791030	11.5384120	3.1102560
H	-2.4208710	12.0511080	4.9436470
H	0.4881370	14.6793570	6.6608600
H	2.0408140	14.1529460	4.8364840
H	0.6997600	6.7634160	1.6536650
H	1.8355150	4.6245050	1.2623790
H	4.0214610	5.1171650	4.9089790
H	2.8903640	7.2593930	5.2981730
H	4.0425370	2.9294890	3.7302230
H	-1.8058510	14.6609200	7.5484210
H	-3.0669960	13.6993560	6.7538380
H	3.1151610	2.7110630	2.2338690
H	4.6555230	3.5737320	2.2044450

Continued on next page

Table S24: Cartesian coordinates of the optimized S_0 geometry of conformer **2B**.

atom	x	y	z
H	-1.9428640	12.9303980	7.8765550

Table S25: Cartesian coordinates of the optimized S_{LLCT} geometry of conformer **2B**.

atom	x	y	z
Zn	2.6452920	9.6612160	2.8662380
S	2.5997850	10.8607160	4.9027480
S	1.1815650	8.1028970	3.9958140
N	4.4785860	9.1357970	2.2268770
N	2.2924520	10.0148270	0.9131950
C	5.5562500	8.7051340	2.8909090
C	6.7388750	8.3667910	2.2721340
C	6.8310000	8.4751270	0.8706050
C	5.7365230	8.9197130	0.1485820
C	5.7259190	9.0678710	-1.2842520
C	4.6296180	9.5061030	-1.9418290
C	3.4185400	9.8457100	-1.2414040
C	2.2659340	10.2926810	-1.8644310
C	1.1305960	10.5938270	-1.0906720
C	1.1979500	10.4391650	0.2773010
C	3.4117750	9.7083410	0.1760750
C	4.5478580	9.2518570	0.8577380
C	1.1165260	11.7978880	4.9074500
C	0.6582690	12.4821350	3.7748870

Continued on next page

Table S25: Cartesian coordinates of the optimized S_{LLCT} geometry of conformer **2B**.

atom	x	y	z
C	-0.4991730	13.2429920	3.8288760
C	-1.2423820	13.3531440	5.0048790
C	-0.7766640	12.6757600	6.1350850
C	0.3767220	11.9119400	6.0925130
C	2.0697970	6.6113870	4.1223390
C	2.8829970	6.1312470	3.0827890
C	3.5457620	4.9221830	3.2060160
C	3.4340260	4.1472100	4.3616170
C	2.6198980	4.6255930	5.3964560
C	1.9525680	5.8288310	5.2858050
C	-2.5125950	14.1515370	5.0520880
C	4.1759100	2.8522540	4.5062900
H	5.4551710	8.6289560	3.9694530
H	7.5786840	8.0252450	2.8648500
H	7.7494840	8.2148790	0.3553200
H	6.6292050	8.8164880	-1.8313320
H	4.6427240	9.6099850	-3.0223000
H	2.2446120	10.4064510	-2.9432450
H	0.2135600	10.9425300	-1.5495240
H	0.3381750	10.6642840	0.9012500
H	1.2237960	12.4302560	2.8509330
H	-0.8285530	13.7679670	2.9369270
H	-1.3295050	12.7485160	7.0672720

Continued on next page

Table S25: Cartesian coordinates of the optimized S_{LLCT} geometry of conformer **2B**.

atom	x	y	z
H	0.7151510	11.3931990	6.9832480
H	2.9869310	6.7096830	2.1726880
H	4.1629520	4.5708870	2.3847630
H	2.5108020	4.0387350	6.3037340
H	1.3288930	6.1811640	6.1002940
H	3.5536700	2.0890350	4.9856840
H	-2.6472730	14.6288120	6.0282280
H	-2.5245730	14.9291620	4.2821800
H	4.5076660	2.4709710	3.5361510
H	5.0671700	2.9837710	5.1340650
H	-3.3854210	13.5071500	4.8821420

Table S26: Cartesian coordinates of the optimized T_{LLCT} geometry of conformer **2B**.

atom	x	y	z
Zn	2.7001710	9.7952200	2.9736520
S	2.6306160	10.9972990	4.9963280
S	1.2163060	8.2242160	4.1197630
N	4.4916230	9.1389800	2.3387780
N	2.3519650	10.1115770	1.0162760
C	5.5457420	8.6602050	3.0079430
C	6.6860050	8.1990520	2.3892340
C	6.7581250	8.2257650	0.9825990
C	5.6862230	8.7148260	0.2553100

Continued on next page

Table S26: Cartesian coordinates of the optimized T_{LLCT} geometry of conformer **2B**.

atom	x	y	z
C	5.6558880	8.7834020	-1.1832480
C	4.5809570	9.2652080	-1.8456470
C	3.4142090	9.7345030	-1.1449030
C	2.2832620	10.2278160	-1.7725380
C	1.1903440	10.6556290	-0.9975990
C	1.2761820	10.5759040	0.3756130
C	3.4289250	9.6805190	0.2781190
C	4.5420750	9.1767580	0.9647040
C	1.1109560	11.8807940	4.9505530
C	0.6935400	12.5903270	3.8181060
C	-0.4963510	13.3016620	3.8279820
C	-1.3134350	13.3359560	4.9587800
C	-0.8872940	12.6359670	6.0901270
C	0.2985540	11.9206090	6.0909500
C	2.1022380	6.7288650	4.1258470
C	2.7288180	6.2299310	2.9704950
C	3.4094080	5.0257080	3.0014650
C	3.5044730	4.2758340	4.1758650
C	2.8722980	4.7695270	5.3245990
C	2.1854280	5.9665400	5.3058410
C	-2.6184840	14.0779810	4.9542020
C	4.2793160	2.9932150	4.2184290
H	5.4604140	8.6490010	4.0904480

Continued on next page

Table S26: Cartesian coordinates of the optimized T_{LLCT} geometry of conformer **2B**.

atom	x	y	z
H	7.5092380	7.8256470	2.9860070
H	7.6432510	7.8678770	0.4675350
H	6.5255420	8.4335310	-1.7307060
H	4.5776480	9.3058320	-2.9304150
H	2.2457290	10.2791860	-2.8556710
H	0.2908320	11.0432810	-1.4598940
H	0.4481920	10.8977150	1.0000530
H	1.3149090	12.5981580	2.9290690
H	-0.7933240	13.8469920	2.9367910
H	-1.4973060	12.6504180	6.9888120
H	0.6041670	11.3821010	6.9818290
H	2.6662200	6.7890420	2.0441750
H	3.8787150	4.6586330	2.0938800
H	2.9238340	4.2001180	6.2477990
H	1.7053450	6.3324070	6.2069480
H	3.7989260	2.2588780	4.8732280
H	-2.8395870	14.5023850	5.9389250
H	-2.6135630	14.8902140	4.2207180
H	4.3845320	2.5557190	3.2212680
H	5.2901170	3.1660690	4.6116660
H	-3.4484120	13.4070040	4.6954110

Table S27: Cartesian coordinates of the optimized T$_{LC}$(phen) geometry of conformer **2B**.

atom	x	y	z
Zn	2.1325950	10.1830380	2.5451950
S	1.8406070	12.4738670	2.4886470
S	0.8694750	8.7066860	3.7925960
N	4.1881580	9.5646930	2.5901850
N	2.4527380	9.4631110	0.5484050
C	5.0072120	9.6448790	3.6537710
C	6.3176720	9.1866270	3.5975570
C	6.7937720	8.6347030	2.4250340
C	5.9388000	8.5437040	1.2938010
C	6.3132080	8.0094010	0.0631690
C	5.3660140	7.9558420	-1.0529370
C	4.0667150	8.4379580	-0.9125210
C	3.0877430	8.4252630	-1.9424050
C	1.8276320	8.9316610	-1.6922890
C	1.5351530	9.4457640	-0.4352760
C	3.6591300	8.9891090	0.3379970
C	4.6141540	9.0438810	1.4625800
C	0.7143690	12.8004410	3.8318060
C	-0.5571890	12.2245130	3.8887000
C	-1.4290220	12.5226650	4.9268320
C	-1.0748210	13.4092100	5.9442000
C	0.1900660	13.9898070	5.8772720
C	1.0713130	13.6910760	4.8451020

Continued on next page

Table S27: Cartesian coordinates of the optimized T_{LC}(phen) geometry of conformer **2B**.

atom	x	y	z
C	1.7299660	7.1735160	3.4874330
C	1.4813960	6.4188160	2.3391010
C	2.1361420	5.2135290	2.1210220
C	3.0608640	4.7124760	3.0364980
C	3.3000090	5.4647260	4.1858080
C	2.6505310	6.6718920	4.4095180
C	-2.0141180	13.7052810	7.0800580
C	3.7903920	3.4229010	2.7816500
H	4.5921160	10.0837800	4.5534940
H	6.9515640	9.2668310	4.4729930
H	7.8122690	8.2691570	2.3541200
H	7.3169700	7.6274300	-0.0784730
H	5.6878930	7.5338390	-1.9972380
H	3.3417360	8.0180860	-2.9149050
H	1.0650740	8.9333810	-2.4624950
H	0.5598540	9.8531220	-0.1956650
H	-0.8699400	11.5380810	3.1086400
H	-2.4113440	12.0576010	4.9403770
H	0.4986240	14.6909030	6.6482700
H	2.0512600	14.1573360	4.8258590
H	0.7628770	6.7779840	1.6094720
H	1.9171570	4.6489970	1.2184440
H	4.0080490	5.1006480	4.9256570

Continued on next page

Table S27: Cartesian coordinates of the optimized T_{LC}(phen) geometry of conformer **2B**.

atom	x	y	z
H	2.8590990	7.2333450	5.3145070
H	4.0660200	2.9281630	3.7187220
H	-1.7954570	14.6763640	7.5358300
H	-3.0567980	13.7120410	6.7448550
H	3.1805120	2.7282790	2.1946280
H	4.7178470	3.5965700	2.2197320
H	-1.9325590	12.9470240	7.8701640

Paper III

Inorganic Chemistry

pubs.acs.org/IC Article

Finding Design Principles of OLED Emitters through Theoretical Investigations of Zn(II) Carbene Complexes

Nora Lüdtke, Andreas Steffen,* and Christel M. Marian*

Cite This: https://doi.org/10.1021/acs.inorgchem.2c03301

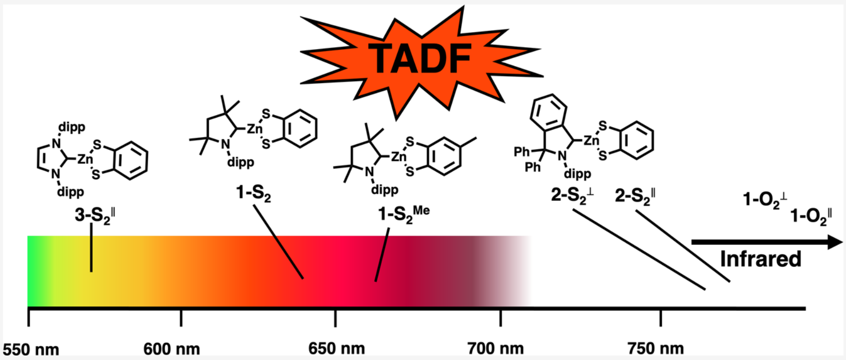

ABSTRACT: In this work, Zn(II) carbene complexes carrying a dianionic 1,2-dithiolbenzene (dtb) or 1,2-diolbenzene (dob) ligand were investigated regarding their suitability as organic light-emitting diode (OLED) emitter. For the optimization of the complexes, density functional-based methods were used and frequency analyses verified the obtained structures as minima. All calculations were carried out including a polarizable continuum model to mimic solvent—solute interactions. Multireference configuration interaction methods were used to determine excitation energies, spin-orbit couplings, and luminescence properties. Rate constants of spin-allowed and spin-forbidden transitions were calculated according to a Fermi golden rule expression. Using carbene ligands with varying σ-donor and π-acceptor strengths, the luminescence is found to be tunable from yellow to orange/red to deep red/near-infrared. The calculated intersystem crossing (ISC) time constants indicate thermally activated delayed fluorescence (TADF) to be the main decay channel. In contrast to many d^{10} coinage metal complexes, a parallel orientation of dtb or dob and the carbene ligand is found to be highly favorable. For the complexes with a cyclic (alkyl)(amino) carbene (CAAC) or cyclic (amino)(aryl) carbene (CAArC) ligand, the S_1 and T_1 states have ligand-to-ligand charge-transfer (LLCT) character and are energetically close. The complex with a classical N-heterocyclic carbene (NHC) ligand has S_1 and T_1 states with mixed ligand-to-metal charge-transfer (LMCT)/LLCT character and is a very rare example in which the zinc ion contributes to the excitation.

INTRODUCTION

The demand for highly performing organic light-emitting diodes (OLEDs) for displays and lighting systems recently bolstered the development of new emitter materials.[1−5] Thermally activated delayed fluorescence (TADF) is looked upon as a significant emerging technology in this field.[6−10] The TADF process rests upon reverse intersystem crossing (rISC) of the triplet-excited dopant to the first excited singlet state, which then emits delayed fluorescence. With high rISC rate constants, an internal quantum efficiency of up to 100% can be achieved in electroluminescent devices. One prerequisite for TADF is a thermally surmountable singlet—triplet gap ΔE_{S-T}. In addition, the spin—orbit coupling (SOC) between the first excited singlet and triplet states and the overlaps of their vibrational wavefunctions are crucial for efficient ISC and rISC.[11−13]

Most of the TADF emitters used today are based either on purely organic donor—acceptor molecules or on metal—organic complexes.[9] In the former, the small SOC of their charge-transfer (CT) states often leads to slow forward and backward ISC processes. Long residence times in the excited triplet state make TADF emitters particularly vulnerable to photochemical degradation or triplet—triplet annihilation.[14] One strategy to accelerate the rISC process is to devise donor—acceptor compounds with an energetically proximate locally excited (LE) state that mediates the interconversion of ^{1}CT and ^{3}CT states by spin—vibronic coupling.[11,15−17] Another strategy involves the implementation of transition metals with d^{10}

Received: September 16, 2022

configuration in the electronic ground state to increase SOC. In these complexes, low-lying metal-centered (MC) d−d* excitations that cause metal−ligand bond dissociation in d^6 and d^8 systems and eventually lead to the degradation of the OLED dye are absent. In particular, many recent investigations on metal−organic TADF emitters address copper(I) complexes.[18−26] Some design criteria for two-coordinated Cu(I) complexes with efficient TADF have already been established.[4,12,24,27] Linear Cu(I) complexes with S$_1$ and T$_1$ states of predominant ligand-to-ligand CT (LLCT) character appear to favor a TADF mechanism. Pure LLCT states have smaller singlet−triplet energy gaps than metal-to-ligand charge-transfer (MLCT) states but also much lower SOC and therefore lower ISC and rISC rate constants. Admixture of a small percentage of MLCT character to the LLCT wavefunction smoothes out this problem. In complexes with a dominating MLCT character of the lowest excited singlet and triplet states, ΔE_{S-T} can be substantial and hence the rISC rate constants are typically much smaller than the phosphorescence rate constants. In contrast to metal-free TADF complexes, low-lying ligand-centered (LC) triplet states lead to reduced ISC and rISC rate constants and often exhibit nonradiative deactivations.[27]

Like Cu(I) compounds, Zn(II) complexes exhibit a d^{10} electron configuration and are therefore not prone to degradation by MC states. Moreover, zinc is more earth abundant than copper and hence less expensive. A downside of Zn(II) is the higher oxidation state compared to Cu(I). Therefore, the propensity of MLCT states is low in Zn(II). Formerly investigated zinc complexes mainly showed prompt fluorescence and only a few were reported to be phosphorescent.[28−38] A recent re-investigation of the photophysical behavior of zinc(II) diimine bis-thiolate complexes revealed that their room-temperature LLCT emission actually shows TADF characteristics.[39] With regard to lighting applications, Zn(II) complexes were mostly employed as fluorescent emitters or hosts for fluorescent and phosphorescent dopants.[40−43] The growing interest in new TADF-based OLED emitters strongly promoted research on Zn(II) emitters. In 2015, Sakai et al. reported monomeric Zn(II) complexes with intraligand charge-transfer characteristics emitting TADF.[44] Berezin et al. observed TADF in a proton-transfer system coordinated to Zn(II).[45] Dinuclear zinc complexes with donor−acceptor-type ligands exhibiting strong TADF in the solid state were presented by Xiong et al.[46] Goswami et al.[47] investigated three Zn(II) complexes with iminophosphonamide ligands, of which one showed TADF and two prompt fluorescence. All of the TADF-emitting Zn(II) complexes mentioned above have in common that zinc has mainly a stabilizing role and is not electronically involved in the electric dipole transition. Moreover, none of the Zn(II) complexes, which have so far been reported to show TADF characteristics, bears a carbene ligand although many efficient Cu(I)-based TADF emitters do so.

In search of guidelines for the design of new zinc-based TADF emitters, we constructed a series of trigonally coordinated Zn(II) carbene complexes in this work that carry a dianionic 1,2-dithiolbenzene (dtb) or 1,2-diolbenzene (dob) ligand. We chose carbene ligands with different σ-donor and π-acceptor strengths and examined their influence on the photophysical properties: a classical N-heterocyclic carbene (NHC), a cyclic (alkyl)(amino) carbene (CAAC), and a cyclic (amino)(aryl) carbene (CAArC). NHC ligands are known for their σ-donor strengths but rather low π-accepting character.[48] CAAC ligands are stronger σ-donors and π-acceptors than classical NHC ligands.[49] CAArCs have even higher π-acceptors than CAACs but similar σ-donor strengths.[25] The chemical structures of the quantum chemically investigated complexes are shown in Chart 1.

Chart 1. Structures of the Investigated Zn(II) Complexes with a Dithiol or Diol Ligand[a]

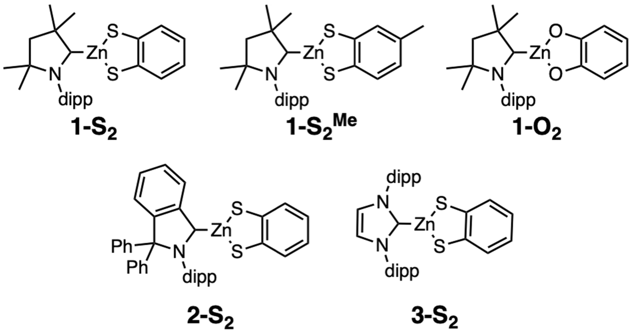

[a]The acronym dipp designates a 2,6-diisopropylphenyl residue.

METHODS AND COMPUTATIONAL DETAILS

For the optimization of the complexes and the vibrational frequency analyses of the states, the Gaussian 16 program was used.[52] The ground-state geometries were obtained with Kohn−Sham density functional theory (DFT).[53] The geometries of the excited singlet states were optimized with time-dependent DFT (TDDFT)[54] and the optimization of the excited triplet states was carried out with the Tamm−Dancoff approximation (TDA)[55] to TDDFT. For zinc, the 10-mdf 6s5p3d basis set with defpp-ecp was used.[56] Sulfur is represented by the def2-SVPD basis and all other atoms by the def-SV(P) basis set.[57] The BH-LYP functional was used for all calculations.[58,59] Test calculations in our group had shown that hybrid functionals with a high percentage of nonlocal exchange contributions yield better geometry parameters for Zn complexes than functionals including merely 20 or 25% nonlocal exchange.[60] As the DFT/MRCI method is parameterized for a Kohn−Sham reference employing the BH-LYP functional (see below), it appeared natural to use the BH-LYP functional with 50% nonlocal exchange even for geometry optimizations. The implicit tetrahydrofuran (THF) solvent environment was incorporated via the polarizable continuum model (PCM)[61,62] of the Gaussian 16 package.[52] The PCM point charges of the Gaussian 16 calculations were extracted and transferred to the Turbomole package[63,64] that was used to generate closed-shell Kohn−Sham molecular orbitals and two-electron integrals for subsequent multireference configuration interaction (MRCI) calculations. To construct the two-electron integrals in the resolution-of-the-identity approximation, the auxiliary basis sets[65,66] from the Turbomole library were employed. For the DFT/MRCI[67,68] calculations, the R2018 Hamiltonian[69] with tight parameters (threshold of 0.80 E_h) was chosen and the secular equations were solved for 30 singlet and triplet roots. The outcome of the DFT/MRCI runs formed the basis for the computation of excitation energies and oscillator strengths of the spin-allowed transitions and for subsequent SOC calculations.

Spin−orbit coupling matrix elements (SOCMEs) were obtained with the SPOCK program.[70,71] ISC and rISC rate constants were computed according to Fermi's golden rule and in Franck−Condon (FC) approximation for temperatures of 77 and 298 K. Herein, a Boltzmann distribution is assumed for the population of the vibrational levels of the initial state. Further, it is assumed that the rate constants are additive in the S$_1$ $\rightsquigarrow$ T$_1$ case (ISC) and that they can be averaged over all triplet sublevels in the T$_1$ $\rightsquigarrow$ S$_1$ case (rISC).

https://doi.org/10.1021/acs.inorgchem.2c03301

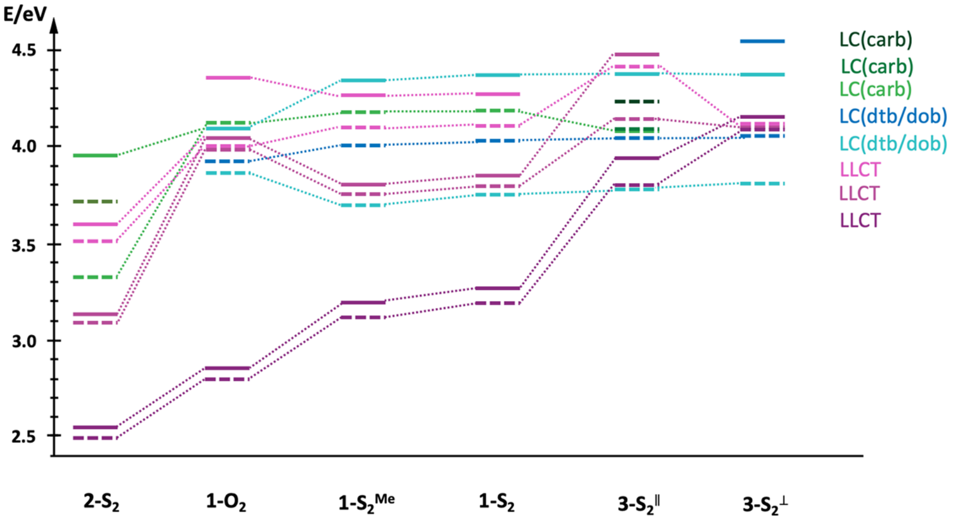

Figure 1. Vertical excitation energies of the screened Zn(II) complexes in THF calculated with DFT/MRCI at the respective ground-state geometries. The compounds have been sorted according to the excitation energy of the first excited state. Dashed lines represent triplet states, and solid lines represent singlet states. The following color codes have been used: violet and pink LLCT ($\pi_{\mathrm{dtb/dob}} \rightarrow \pi^*_{\mathrm{carb}}$), green LC ($\pi_{\mathrm{carb}} \rightarrow \pi^*_{\mathrm{carb}}$), and blue LC ($\pi_{\mathrm{dtb/dob}} \rightarrow \pi^*_{\mathrm{dtb/\ dob}}$).

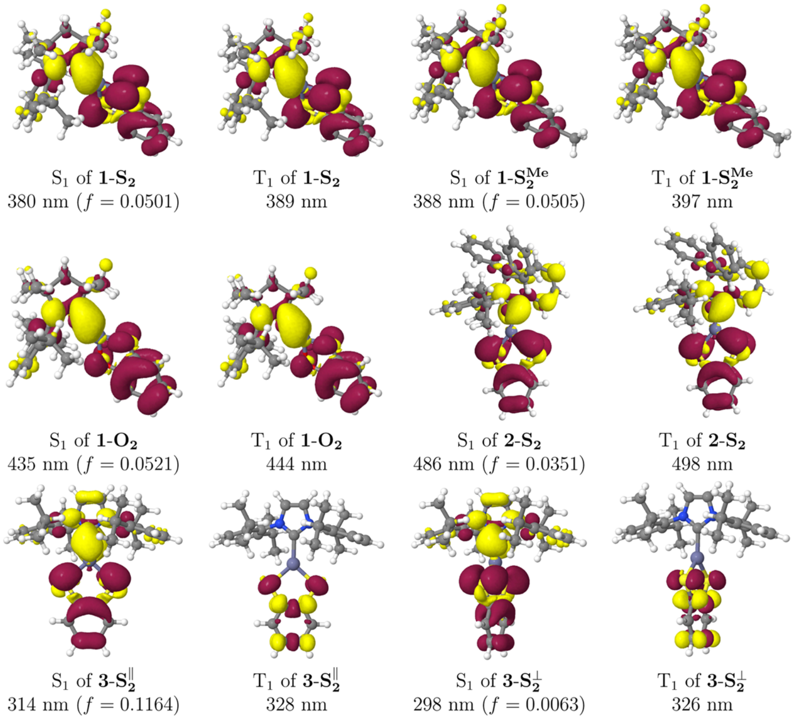
S$_1$ of **1-S$_2$** 380 nm (f = 0.0501)
T$_1$ of **1-S$_2$** 389 nm
S$_1$ of **1-S$_2^{Me}$** 388 nm (f = 0.0505)
T$_1$ of **1-S$_2^{Me}$** 397 nm

S$_1$ of **1-O$_2$** 435 nm (f = 0.0521)
T$_1$ of **1-O$_2$** 444 nm
S$_1$ of **2-S$_2$** 486 nm (f = 0.0351)
T$_1$ of **2-S$_2$** 498 nm

S$_1$ of **3-S$_2^{\parallel}$** 314 nm (f = 0.1164)
T$_1$ of **3-S$_2^{\parallel}$** 328 nm
S$_1$ of **3-S$_2^{\perp}$** 298 nm (f = 0.0063)
T$_1$ of **3-S$_2^{\perp}$** 326 nm

Figure 2. DFT/MRCI difference densities of the S$_1$ and T$_1$ excited states of complexes **1-S$_2$**–**3-S$_2$** in THF at the ground-state geometry. Areas losing electron density upon electronic excitation from the ground state are shown in red, and areas gaining electron density are shown in yellow.

$$k_{\mathrm{ISC}} = \frac{2\pi}{\hbar \sum_j \mathrm{e}^{-(E_{bj}-E_{b0})/k_{\mathrm{B}}T}} |\langle {}^3\phi_a^{(0)}|\hat{H}_{\mathrm{SO}}|{}^1\phi_b^{(0)}\rangle|^2 \times \sum_{j,k} \mathrm{e}^{-(E_{bj}-E_{b0})/k_{\mathrm{B}}T} |\langle \nu_{ak}|\nu_{bj}\rangle|^2 \delta(E_{bj} - E_{ak}) \quad (1)$$

$$k_{\mathrm{rISC}} = \frac{2\pi}{3\hbar \sum_k \mathrm{e}^{-(E_{ak}-E_{a0})/k_{\mathrm{B}}T}} |\langle {}^3\phi_a^{(0)}|\hat{H}_{\mathrm{SO}}|{}^1\phi_b^{(0)}\rangle|^2 \times \sum_{k,j} \mathrm{e}^{-(E_{ak}-E_{a0})/k_{\mathrm{B}}T} |\langle \nu_{ak}|\nu_{bj}\rangle|^2 \delta(E_{bj} - E_{ak}) \quad (2)$$

The FC-weighted density of states was obtained with the fast Fourier transformation ansatz of the VIBES program in harmonic oscillator approximation.[72,73] Phosphorescence rate constants were computed with the variational multireference spin−orbit configuration interaction (MRSOCI) method.[74] As the zero-field splitting is small in comparison to room temperature, the three individual triplet components of the rate constant were averaged.

■ RESULTS AND DISCUSSION

Following the protocol of previous theoretical studies on linear carbene Cu(I) complexes,[27] we started the search for design principles of TADF-emitting Zn(II) complexes by scanning their excited-state energies and electronic structures in the FC region. The photophysical decay pathways of the most promising compounds were subsequently investigated in more detail.

Franck–Condon Region. In Figure 1, the vertical excitation energies at the respective ground-state geometries of the complexes are displayed. Computed absorption spectra of all compounds may be found in Figure S1 in the Supporting Information (SI).

The lowest singlet and triplet excited states of the complexes **1-S$_2$**–**2-S$_2$** have LLCT character, where the electron density is transferred from the π orbitals of the dtb or dob ligand to the lowest π^* orbital of the carbene (see Figure 2 for difference densities). The zinc atom does not contribute to these electronic excitations. The energy gap between the T_1 and S_1 states is very low and in a thermally surmountable range. Small contributions from LC excitations lead to a reasonable dipole oscillator strength of $f = 0.0501$ for the $S_1 \leftarrow S_0$ absorption of complex **1-S$_2$** in the violet spectral region. Complex **1-S$_2^{Me}$** differs from complex **1-S$_2$** by the methyl group on the dtb ligand. The substitution leads to a small reduction in the vertical excitation energies, but the order and electronic structure of the excited states are preserved. Complex **1-O$_2$** features a dob instead of a dtb ligand. Surprisingly, the substitution of sulfur by oxygen results in a significant reduction of the vertical excitation energies of the lowest S_{LLCT} and T_{LLCT} state of complex **1-O$_2$** by about 0.4 eV in comparison to complexes **1-S$_2$** and **1-S$_2^{Me}$**. This is a consequence of the significantly closer O–C distance in **1-O$_2$** (133 pm) compared to the S–C distance (177 pm) in **1-S$_2$** and the antibonding π interactions of these centers in the highest occupied molecular orbital (HOMO) orbital. The concomitant rise of the HOMO energy overcompensates the higher electronegativity of the oxygen centers. Counter-intuitively, therefore the deprotonated dob ligand is a stronger electron donor than the corresponding dithiolate. The pattern is irregular, however, because the second pair of S_{LLCT} and T_{LLCT} states, resulting from a HOMO − 1 to lowest unoccupied molecular orbital (LUMO) excitation, is found at higher energies than in complex **1-S$_2$**. An even stronger redshift of the vertical LLCT excitation energies of about 0.7 eV compared to complex **1-S$_2$** can be found for complex **2-S$_2$**. The NHC ligand is a weaker π-acceptor than the CAAC or CAArC ligand. Accordingly, the LLCT excitations are higher in energy for complex **3-S$_2$** than for complexes **1-S$_2$**–**2-S$_2$**. These trends are clearly visible in Figure 1. However, while the S_1 state still has LLCT character in **3-S$_2$**, the T_1 is an LC state localized on the dtb ligand. Due to the exchange interactions between the open shells, the singlet–triplet energy splitting of locally excited $\pi\pi^*$ states is much larger than for CT states. As a consequence, the ^{1}LC states localized on the dithiobenzene moiety of **1-S$_2$**, **1-S$_2^{Me}$**, **2-S$_2$**, and **3-S$_2$** show up at about 4.3 eV, whereas their triplet counterparts are found at about 0.6 eV lower in energy. In the CAArC complex **2-S$_2$**, the carbene localized LC states are the lowest LC excited states due to the delocalization of the π^*_{carb} orbital over the fused arene system.

A particular feature of complex **3-S$_2$** is that two stable nearly isoenergetic conformers exist in the electronic ground state. In the first, the dtb ligand and the five-membered ring of the NHC ligand are approximately coplanar. This geometry is referred to as complex **3-S$_2^{\parallel}$** in the following. In the second conformer, labeled **3-S$_2^{\perp}$**, the dtb plane is almost orthogonal to the imidazolylidene plane. The ground-state energy of complex **3-S$_2^{\parallel}$** is 0.02 eV lower than of conformer **3-S$_2^{\perp}$**, so both conformers should coexist in solution. Earlier theoretical studies on NHC-ZnX$_2$ (X = H, Me, Et) complexes by Jabłoński predicted a correlation between the torsional angle θ of the ZnX$_2$ plane with respect to the ring plane of the imidazole-2-ylidene unit and the size of the R substituents at the NHC nitrogen atoms.[75] For R = dipp, θ values close to 55° had been found. Our present results indicate, however, that dithiolate ligands (X = S$^-$) behave differently in this respect. The vertical excitation energies of the T_1 and T_2 states of **3-S$_2^{\parallel}$** are nearly identical and close to the S_1 excitation energy in the FC region. Therefore, the emission properties of this conformer will be investigated in more detail despite the fact that the lowest absorption band lies in the UV spectral region. For the perpendicular form, the S_1–T_1 energy gap is substantial. Hence, no TADF is expected to occur for conformer **3-S$_2^{\perp}$**. Moreover, we note the markedly reduced oscillator strength of the $S_1 \leftarrow S_0$ absorption for the perpendicular arrangement of the ligands in complex **3-S$_2$** (Figure 2).

Photophysical Properties. The adiabatic S_1 and T_1 energies of the complexes do not strictly follow the trends observed for the vertical excitation energies in the FC region (Table 1). As expected, the N–C$_{carb}$ and Zn–S or Zn–O bonds are elongated. Less obvious are the strong bond length alterations in the benzene ring and the neighboring C–S or C–O bonds. Altogether, the reorganization of the molecular frame in the LLCT states results in substantial Stokes shifts.

Table 1. DFT/MRCI Excitation Energies (ΔE/eV) of Complexes 1-S$_2$–3-S$_2$ in THF at Various Molecular Geometries[a]

		optimized geometry				
complex	state	S_0	S_{LLCT}	T_{LLCT}	$S^{\perp}_{LLCT}$	$T^{\perp}_{LLCT}$
1-S$_2$	S_0	0.00	0.49	0.53		
	S_1	3.27	2.46 (2.38)	2.51		
	T_1	3.19	2.39	2.43 (2.34)		
1-S$_2^{Me}$	S_0	0.00	0.47	0.50		
	S_1	3.19	2.39 (2.32)	2.42		
	T_1	3.12	2.32	2.34 (2.27)		
1-O$_2$	S_0	0.00	0.64	0.67	0.49	
	S_1	2.85	1.81 (1.72)	1.83	1.81 (1.74)	
	T_1	2.79	1.74	1.76 (1.70)	1.77	
2-S$_2$	S_0	0.00	0.32	0.36	0.32	0.33
	S_1	2.55	1.90 (1.84)	1.93	1.92 (1.88)	1.94
	T_1	2.49	1.84	1.86 (1.80)	1.87	1.88 (1.84)

		optimized geometry		
complex	state	S_0	S_{LMCT}	T_{LMCT}
3-S$_2^{\parallel}$	S_0	0.00	0.56	0.56
	S_1	3.94	2.75 (2.68)	2.75
	T_1	3.79	2.64	2.64 (2.57)

[a] The DFT/MRCI energy of the S_0 state at the DFT-optimized S_0 minimum geometry in a polarizable THF environment serves as common origin. 0–0 Energies including zero-point vibrational energy (ZPVE) corrections are given in parentheses.

Table 2. Vertical Emission Wavelength λ [nm], Spin Component-Averaged S_{LLCT}−T_{LLCT} SOC [cm^{-1}], and Radiative as well as Nonradiative Rate Constants k [s^{-1}] of the LLCT States of Compounds 1-S$_2$−2-S$_2$[a]

	S_{LLCT}			T_{LLCT}					
	λ_F	k_F	SOC	λ_P	k_P	SOC	T [K]	k_{ISC}	k_{rISC}
1-S$_2$	629	1×10^7	2.66	654	1×10^1	2.37	298	7×10^9	5×10^8
							77	6×10^9	5×10^6
1-S$_2^{Me}$	645	1×10^7	3.21	673	7×10^0	3.21	298	4×10^9	1×10^8
							77	2×10^9	1×10^5
1-O$_2^{\parallel}$	1063	9×10^6	0.42	1134	3×10^{-1}	0.43	298	9×10^7	4×10^7
							77	2×10^8	2×10^6
1-O$_2^{\perp}$	970	5×10^6	2.54						
2-S$_2^{\parallel}$	783	8×10^6	1.65	828	9×10^0	1.55	298	1×10^9	7×10^7
							77	5×10^8	2×10^5
2-S$_2^{\perp}$	771	4×10^6	3.31	799	2×10^2	3.60	298	1×10^9	8×10^6
							77	4×10^8	2×10^3
3-S$_2^{\parallel}$	566	3×10^6	3.56	597	4×10^2	3.56	298	2×10^7	1×10^6
							77	2×10^5	6×10^4

[a] For complex **3-S$_2$**, the S_{LMCT} and T_{LMCT} geometries were selected.

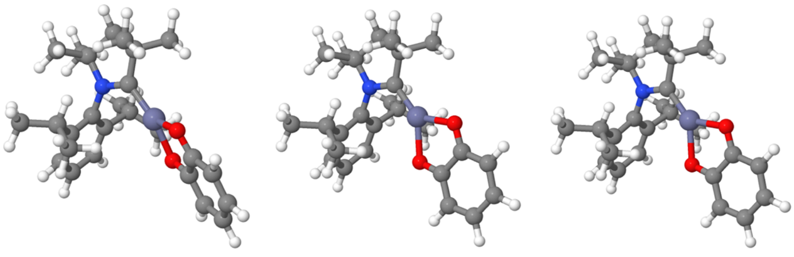

$S^{\perp}_{LLCT}$ $S^{\parallel}_{LLCT}$ T_{LLCT}

Figure 3. Optimized $S^{\perp}_{LLCT}$, $S^{\parallel}_{LLCT}$, and T_{LLCT} geometries of complex **1-O$_2$** in THF.

While the S_{LLCT} and T_{LLCT} states of **1-S$_2$** and **1-S$_2^{Me}$** exhibit nearly identical relaxation energies of about 0.80 eV, the relaxation energies of the corresponding states of the dob complex **1-O$_2$** are somewhat larger than 1 eV. Simultaneously, the S_0 potential energy rises by 0.64 eV. Both effects add up to a huge Stokes shift of about 1.7 eV for **1-O$_2$**, thus moving the emission wavelength to the near-infrared spectral region. For this compound, we found a secondary S_1 minimum with nearly identical energy but with a perpendicular orientation of the CAAC and diolate ligands, denoted by $S^{\perp}_{LLCT}$ in the following. The corresponding triplet conformation is not stable and reverts to the parallel orientation of the ligands. The smallest, but still substantial Stokes shift of about 1 eV is found for the CAArC-Zn-dithiolate complex **2-S$_2$**. Even this compound exhibits a secondary S_1 minimum with perpendicular configuration of the ligands. In this case, a corresponding T_1 equilibrium geometry could be optimized. The electronic structures of the S_1 and T_1 states of complex **3-S$_2^{\parallel}$** change upon geometry relaxation from predominantly LLCT to LMCT character. This is remarkable as **3-S$_2^{\parallel}$** is the only complex in this series involving the zinc atom in low-lying electronic excitations. The implications of these findings for the photophysical properties of the complexes will be discussed in more detail below.

The adiabatic S_1−T_1 energy gaps of all complexes remain in a thermally surmountable range, thus fulfilling at least one prerequisite for TADF. Whether TADF is expected to be efficient depends, of course, on further parameters. Besides the singlet−triplet energy gap and the temperature, the overlap of the vibrational wavefunctions and the mutual SOC of the initial and final electronic states are key factors determining the ISC and rISC rate constants in FC approximation (eqs 1 and 2).

The FC overlaps of the S_{LLCT} and T_{LLCT} states of complex **1-S$_2$** are large because their relaxed geometries are very similar and the energy difference is minuscule. The bond angles of their minimum nuclear arrangements differ by less than 0.4°, the dihedral angles by less than 1.0°, and the bond lengths by less than 0.02 Å. Therefore, the potential energy surfaces can be considered nested and the weak coupling case applies, suggesting an exponential decrease of the ISC and rISC rate constants with growing ΔE_{S-T}.[76] Previous investigations of Cu(I) complexes showed, that an MLCT contribution to the lowest singlet and triplet excitations increases their mutual SOC substantially.[27,77] As mentioned before, the zinc orbitals do not participate in the S_1 and T_1 excitations of the complexes **1-S$_2$−2-S$_2$** at any optimized geometry and hence do not promote SOC. Instead, the involvement of the sulfur atoms in the LLCT excitations leads to an increase in the SOC. Together with the calculated ΔE_{S-T} of only 300 cm^{-1}, these factors lead to very high ISC and rISC rate constants of 7×10^9 and 5×10^8 s^{-1} at 298 K, respectively (Table 2). Even at 77 K, the rISC ($k_{rISC} = 5 \times 10^6$ s^{-1}) and fluorescence rate constants ($k_F = 1 \times 10^7$ s^{-1}) are of comparable magnitude. Since the rISC is much faster than the phosphorescence ($k_{P,ave} = 10.0$ s^{-1}), TADF is expected to be the main decay channel. The ISC and rISC rate constants of complex **1-S$_2^{Me}$** at 298 K are of the same order of magnitude as the ones of complex **1-S$_2$**. Also, the fluorescence constants are nearly unchanged, in agreement with the small impact of the methyl group on the

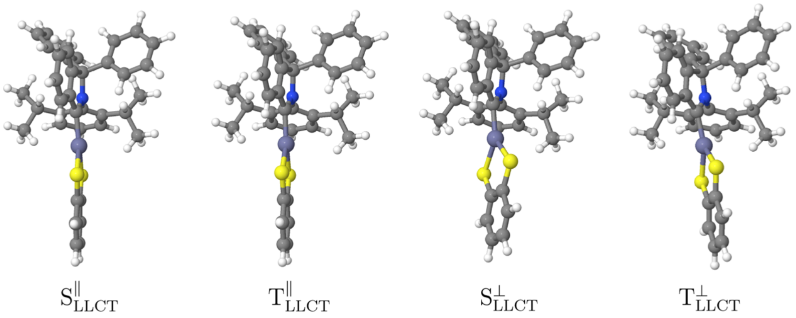

Figure 4. Optimized S_{LLCT} and T_{LLCT} geometries of complex **2-S$_2$** in THF.

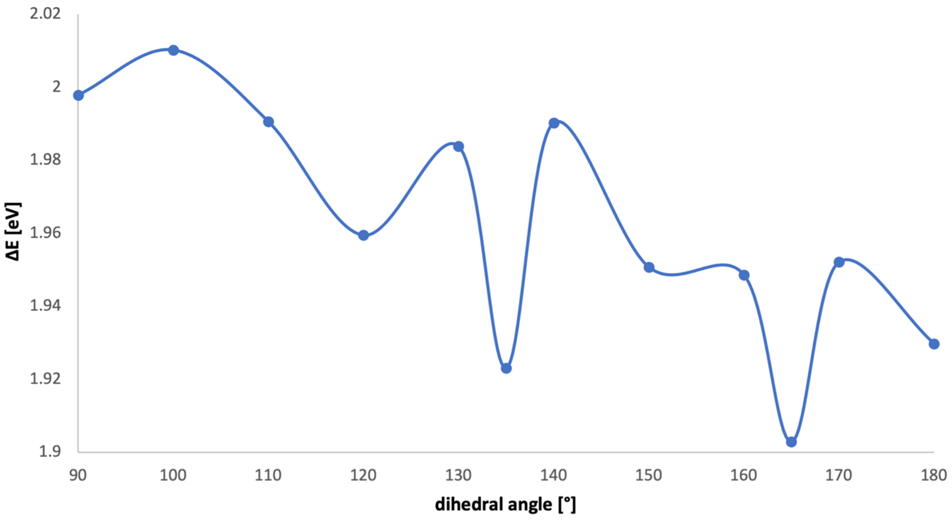

Figure 5. Relaxed scan of the C18−C_{carb}−Zn−S66 dihedral angle of complex **2-S$_2$**. The DFT/MRCI energy of the S_0 state at the DFT-optimized S_0 minimum geometry in a polarizable THF environment serves as the common origin.

excitation energies. The lower rISC rate constant of complex **1-S_2^{Me}** at 77 K is attributed to the somewhat larger adiabatic S_1−T_1 energy gap of 0.05 eV compared to 0.03 eV in **1-S$_2$**. This variation should not be overinterpreted, however, in view of the uncertainties inherent to the computational protocol.

Due to the pronounced changes in the geometry parameters in the S_1 and S_0 minimum nuclear arrangements, their emission is predicted to be spectrally broad, however. The largest variations are observed for the dihedral angles with sulfur contribution. Pursuing the aim to narrow the spectral width of the emission band, the large-amplitude motions of the dtb ligand have to be confined by introducing sterically demanding substituents, for example, either at the CAAC or at the benzene ring of the dtb ligand.

Two different S_{LLCT} minimum geometries of complex **1-O$_2$** were found. They are sketched in Figure 3. The orientation of the dob ligand is well represented by the N−C_{carb}−Zn−O dihedral angle. With the ground-state minimum nuclear arrangement as the starting point, the dob ligand is rotated out of the carbene plane through an N−C_{carb}−Zn−O dihedral angle of 40°. This geometry is referred to as $S_{LLCT}^{\perp}$. For the other S_{LLCT} geometry, labeled $S_{LLCT}^{\parallel}$, the N−C_{carb}−Zn−O dihedral angle of 4° shows that the dob and the carbene are nearly coplanar. This geometry is very close to the optimized T_{LLCT} geometry, which served as the starting point. The adiabatic excitation energies at the $S_{LLCT}^{\perp}$ and $S_{LLCT}^{\parallel}$ are nearly identical, but we note a shift of the ground-state energy of 0.15 eV between these geometries (Table 1). Fluorescence lifetimes of both S_1 conformers are remarkably short (submicrosecond region) taking into consideration that complex **1-O$_2$** emits in the near-infrared region. In contrast to the radiative rates, the ISC and rISC rates of the two S_1 conformers are vastly different. While the FC factors for the nonradiative transitions between the $S_{LLCT}^{\parallel}$ conformation and the T_{LLCT} minimum of complex **1-O$_2$** are of similar magnitude as for complex **1-S$_2$**, the substitution of the sulfur atoms by the oxygen atoms leads to a decrease of the SOCME by a factor of about 5−6 (see Table 2). As the SOCME enters the rate eqs 1 and 2 quadratically, this decrease leads to a substantial reduction of the (r)ISC rate constants. The rISC process still has a higher probability than fluorescence at room temperature, though. This is not the case when the dob ligand is markedly rotated out of the plane in the S_1 state. The T_{LLCT} potential does not exhibit a minimum structure for a perpendicular arrangement of the ligands according to our calculations but rather forms a saddle point here. The evaluation of nonradiative transition probabilities in the VIBES program according to eqs 1 or 2 rests on an adiabatic picture. Because the FC and harmonic oscillator approximations are not well justified in case of large displacements in a torsional coordinate, we refrained from computing ISC and rISC rate constants for transitions between the $S_{LLCT}^{\perp}$ and $T_{LLCT}^{\parallel}$ minimum potential energy wells.

In the case of complex **2-S$_2$**, at least two S_{LLCT} minima exist, an $S_{LLCT}^{\parallel}$ structure (C18−C_{carb}−Zn−S66 dihedral angle of 165°) and an $S_{LLCT}^{\perp}$ structure (C18−C_{carb}−Zn−S66 dihedral angle of 135°). The nuclear arrangements of the complex in these minima are displayed in Figure 4 together with the corresponding $\mathrm{T}^{\parallel}_{\mathrm{LLCT}}$ and $\mathrm{T}^{\perp}_{\mathrm{LLCT}}$ structures which exhibit very similar C18−$\mathrm{C_{carb}}$−Zn−S66 dihedral angles as their singlet counterparts, namely, 166 and 136°, respectively. Hence, radiative and nonradiative rate constants could be determined for both conformers.

The fluorescence rate constant of the $\mathrm{S}^{\parallel}_{\mathrm{LLCT}}$ conformer $k_{\mathrm{F}} = 8.05 \times 10^{6}\ \mathrm{s}^{-1}$ is more than twice as high as the one of the $\mathrm{S}^{\perp}_{\mathrm{LLCT}}$ conformer ($k_{\mathrm{F}} = 3.88 \times 10^{6}\ \mathrm{s}^{-1}$), but still in the same ballpark. As for **1-O$_2$**, the twist of the dtb ligand leads to an increase in the electronic SOC (Table 2). The sum over squared SOCMEs at the $\mathrm{S}^{\parallel}_{\mathrm{LLCT}}$ geometry of 2.4 cm^{-2} is similar to the one at the $\mathrm{T}^{\parallel}_{\mathrm{LLCT}}$ geometry (2.7 cm^{-2}), but it is much smaller than the values at the $\mathrm{S}^{\perp}_{\mathrm{LLCT}}$ (11.0 cm^{-2}) and $\mathrm{T}^{\perp}_{\mathrm{LLCT}}$ (13.0 cm^{-2}) geometries. Due to a slightly reduced FC-weighted density of states in the perpendicular arrangement, the forward ISC rate constants of both conformers are almost identical, whereas rISC appears to be more favorable for a nearly coplanar orientation of the ligands. Note, however, that rISC is predicted to be much faster than phosphorescence, even at 77 K. Furthermore, the adiabatic energy difference of 0.02 eV between the $\mathrm{S_1}$ minima (0.04 eV if ZPVE corrections are applied) is very small. These findings suggest that the potential energy surface of the $\mathrm{S_{LLCT}}$ state is very flat. To verify this assumption, a relaxed scan of the C18−$\mathrm{C_{carb}}$−Zn−S66 dihedral angle between 90 and 180° was carried out. The adiabatic $\mathrm{S_0}$−$\mathrm{S_1}$ energies of the DFT/MRCI calculations are plotted in Figure 5. The highest $\mathrm{S_1}$ energy was found for a geometry with a dihedral angle of 100° and the lowest for a geometry with a dihedral angle of 165°. With a barrier height of 0.11 eV, the transition state can be easily surmounted, given an excess energy of 0.65 eV after electronic excitation (Table 1).

Due to the high density of low-lying triplet states in the FC region, one $\mathrm{S_1}$ and three $\mathrm{T_1}$ minimum geometries were optimized for complex **3-S$_2$**. Two of them are ^{3}LC states, one featuring local excitations on the dtb ligand, the other on the NHC ligand. The third $\mathrm{T_1}$ minimum and the $\mathrm{S_1}$ minimum are associated with a mixed LMCT/LLCT excitation (Figure 6).

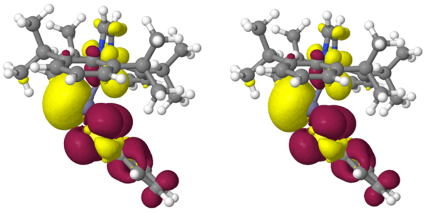
$\mathrm{S_1}$ @ $\mathrm{S_{LMCT}}$ $\mathrm{T_1}$ @ $\mathrm{T_{LMCT}}$

Figure 6. DFT/MRCI difference densities of the lowest-lying excited states of complex **3-S$_2$** in THF at the different excited-state geometries. For color codes, see Figure 2.

The $\mathrm{T_1}$ energy at the LMCT/LLCT minimum is 0.51 eV lower than at the LC(dtb) minimum and 0.98 eV lower than at the LC(NHC) minimum (Table S1 in the SI). Therefore, we focus on the photophysical properties of the LMCT/LLCT states. Here, the dtb ligand is not rotated, but instead it is bent. Upon geometry relaxation in the excited state, the leading configuration continues to be a HOMO−LUMO excitation. However, while the HOMO essentially retains its character, the LUMO transforms from a pure NHC π^* orbital at the ground-state geometry to an orbital with large amplitudes at the zinc atom and smaller ones at the carbene carbon and the nitrogen atoms at the $\mathrm{S_{LMCT/LLCT}}$ or $\mathrm{T_{LMCT/LLCT}}$ minimum geometry (Figure 7).

The calculated fluorescence rate constant of $3.0 \times 10^{6}\ \mathrm{s}^{-1}$ is nearly one order of magnitude smaller than for the CAAC complex **1-S$_2$**, but still in an acceptable range. Due to the participation of the zinc atom in the electronic excitation, the mutual electronic $\mathrm{S_1}$−$\mathrm{T_1}$ SOCME is the largest among all complexes investigated in this work. Fluorescence, ISC, and rISC are predicted to proceed at the submicrosecond time scale at room temperature, much faster than phosphorescence for which we compute a radiative lifetime of 2.5 ms. Hence, we expect prompt and delayed fluorescence to be measurable for complex **3-S$_2$** in the bent conformation where the vertical $\mathrm{S_1}$ excitation energy of 2.19 eV (566 nm) suggests a yellow emission. If the bending of the dtb ligand is prevented by steric hindrance in the solid state, for example, complex **3-S$_2$** is expected to be nonemissive at room temperature because then the ^{3}LC(dtb) state forms the lowest $\mathrm{T_1}$ minimum as the $\mathrm{S_{LMCT/LLCT}}$ and $\mathrm{T_{LMCT/LLCT}}$ states cannot be reached under these constraints.

■ CONCLUSIONS AND OUTLOOK

Based on extensive quantum chemical calculations, four three-coordinate Zn(II) carbene complexes (**1-S$_2$**, **1-S$_2^{\mathrm{Me}}$**, **1-O$_2$**, and **2-S$_2$**) with $\mathrm{S_1}$ and $\mathrm{T_1}$ states of LLCT type and very small $\Delta E_{\mathrm{S-T}}$ have been designed in this work. They are predicted to show submicrosecond emission with TADF characteristics in mildly polar environments provided that they are chemically stable. Complex **3-S$_2$**, which involves a classical NHC and a dtb ligand, is special in the sense that it exhibits $\mathrm{S_1}$ and $\mathrm{T_1}$ states of LMCT/LLCT type involving the 4s/4p shell of the zinc ion as acceptor in addition to the π^* orbital of the NHC. Due to the lower π-acceptor strength of the IPr ligand, its LLCT states lie higher in energy than those of the CAAC and CAArC complexes and can therefore more easily mix in LMCT character. This admixture enlarges the $\mathrm{S_1}$−$\mathrm{T_1}$ energy gap which is only partially compensated by an increased mutual SOC. In total, these effects lead to a substantial reduction of the rISC rate constant and hence the TADF probability in comparison to the other complexes with coplanar orientation of the carbene and dtb or dob ligands.

Using carbenes with different π-acceptor strengths, the luminescence can be tuned from yellow (**3-S$_2$** comprising the classical NHC IPr) over orange/red (**1-S$_2$** and **1-S$_2^{\mathrm{Me}}$** featuring $^{\mathrm{Me}}$CAAC) to deep red/near-infrared (**2-S$_2$** employing a CAArC). **1-O$_2$** differs from **1-S$_2$** in that the dithiolate ligand has been replaced by the corresponding oxygen-containing compound. Surprisingly, the absorption is substantially red-shifted by this replacement and the emission is shifted to the infrared region. With a radiative lifetime of about 100 ns, there are good chances to compete against nonradiative deactivation and to observe NIR-TADF for this compound.

The rotation of the ligands in complexes **1-O$_2$** and **2-S$_2$** away from a coplanar orientation leads to a decrease of the fluorescence and rISC rate constants. Accordingly, the rotation of the dtb or dob ligands ought to be restricted to accomplish efficient TADF. One way to reach this goal is ridification by dimerization of the complexes as observed earlier for CAAC-Zn-dihalides,[38] for example. Indeed, recent experiments show that complex **1-S$_2$** dimerizes in the solid state.[50] Two monomers form a μ-bridged complex in which each Zn atom is surrounded by three S atoms and one carbene leading to a

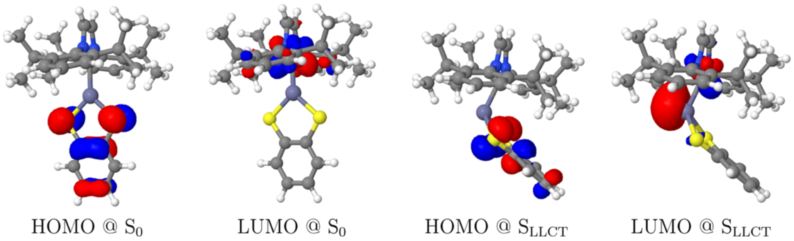

Figure 7. HOMO and LUMO orbitals of complex **3-S_2** in THF at the optimized ground state and S_1 geometries.

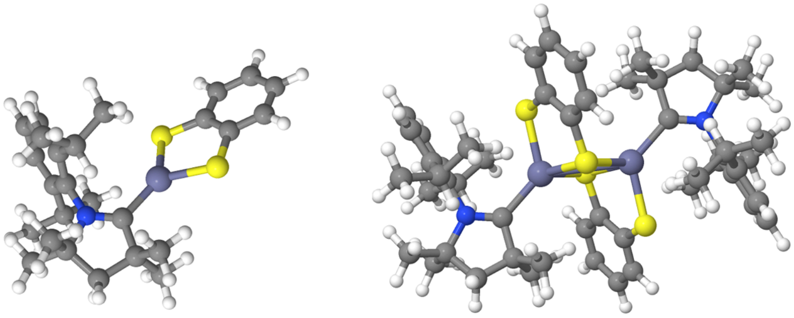

Figure 8. Optimized ground-state geometries of monomeric complex **1-S_2** (left) and its μ-bridged dimeric form (right) complex in THF.

structure similar to the one in Figure 8 with strongly deflected dtb ligands. While the dtb ligand is not sterically restrained and can easily rotate in the monomer, this rotation is hindered in the dimer. Accompanying calculations show that the S_1-T_1 energy gap at the ^{1}LLCT geometry is very small and ISC and rISC are fast in the dimer as well. So, in principle, TADF should be observable. However, due to the bent arrangement of the dtb and CAAC π-systems, the calculated fluorescence rate constant of the dimer is about a 100 times lower than for the monomeric complex **1-S_2** so that the probability of side reactions increases. A second way to prevent the rotation of the ligands is an increase of their steric demand. The ^{Me}CAAC ligand of complex **1-S_2** has two methyl groups on one side of the five-membered ring. Substitution of these methyl groups by bulkier residues might lower the probability of a deflection of dtb ligand and the formation of a μ-bridged dimer. Synthesis and spectroscopical characterization of a ^{Menth}CAAC-Zn(II)-dtb complex, where the ^{Me}CAAC of compound **1-S_2** has been replaced by a CAAC involving a menthene ring, and of a ^{Me}CAAC-Zn(II)-dtb-tbu complex that features a *tert*-butyl residue instead of a methyl group on the dtb ring, are underway and will be presented in a separate paper.[51]

■ ASSOCIATED CONTENT

Supporting Information

The Supporting Information is available free of charge at https://pubs.acs.org/doi/10.1021/acs.inorgchem.2c03301.

> Computed absorption spectra of compounds **1-S_2**, **1-S_2^{Me}**, **1-O_2**, **2-S_2**, **3-$S_2^{\parallel}$**, and **3-$S_2^{\perp}$** in THF solution; DFT/MRCI excitation energies of low-lying singlet and triplet states of complex 3-S_2 at selected minimum geometries (PDF)

■ AUTHOR INFORMATION

Corresponding Authors

Andreas Steffen − *Faculty of Chemistry and Chemical Biology, TU Dortmund University, D-44227 Dortmund, Germany;* orcid.org/0000-0002-6952-7391; Email: Andreas.Steffen@tu-dortmund.de

Christel M. Marian − *Institute of Theoretical and Computational Chemistry, Heinrich-Heine-University Düsseldorf, D-40225 Düsseldorf, Germany;* orcid.org/0000-0001-7148-0900; Email: Christel.Marian@hhu.de

Author

Nora Lüdtke − *Institute of Theoretical and Computational Chemistry, Heinrich-Heine-University Düsseldorf, D-40225 Düsseldorf, Germany*

Complete contact information is available at: https://pubs.acs.org/10.1021/acs.inorgchem.2c03301

Notes

The authors declare no competing financial interest.

■ ACKNOWLEDGMENTS

The authors gratefully acknowledge financial support by the Deutsche Forschungsgemeinschaft (DFG) through SPP 2102, projects MA 1051/18-1 and STE 1834/7-1.

■ REFERENCES

(1) Adachi, C. Third-generation organic electroluminescence materials. *Jpn. J. Appl. Phys.* **2014**, *53*, No. 060101.

(2) Jou, J.-H.; Kumar, S.; Agrawal, A.; Li, T.-H.; Sahoo, S. Approaches for fabricating high efficiency organic light emitting diodes. *J. Mater. Chem. C* **2015**, *3*, 2974−3002.

(3) Ravaro, L. P.; Zanoni, K. P.; de Camargo, A. S. Luminescent Copper(I) complexes as promising materials for the next generation of energy-saving OLED devices. *Energy Rep.* **2020**, *6*, 37−45.

(4) Steffen, A.; Hupp, B. In *Comprehensive Coordination Chemistry III*; Constable, E. C.; Parkin, G.; Que, L., Eds.; Elsevier: Oxford, 2021; pp 466−502.

(5) Hong, G.; Gan, X.; Leonhardt, C.; Zhang, Z.; Seibert, J.; Busch, J. M.; Bräse, S. A Brief History of OLEDs-Emitter Development and Industry Milestones. *Adv. Mater.* **2021**, *33*, No. 2005630.

(6) Uoyama, H.; Goushi, K.; Shizu, K.; Nomura, H.; Adachi, C. Highly efficient organic light-emitting diodes from delayed fluorescence. *Nature* **2012**, *492*, 234−238.

(7) Yang, Z.; Mao, Z.; Xie, Z.; Zhang, Y.; Liu, S.; Zhao, J.; Xu, J.; Chi, Z.; Aldred, M. P. Recent advances in organic thermally activated delayed fluorescence materials. *Chem. Soc. Rev.* **2017**, *46*, 915−1016.

(8) Dias, F. B.; Penfold, T. J.; Monkman, A. P. Photophysics of thermally activated delayed fluorescence molecules. *Methods Appl. Fluoresc.* **2017**, *5*, No. 012001.

(9) Yersin, H., Ed. *Highly Efficient OLEDs: Materials Based on Thermally Activated Delayed Fluorescence*; Wiley VCH, 2018.

(10) Adachi, C.; Xie, G.; Reineke, S.; Zysman-Colman, E. Editorial: Recent Advances in Thermally Activated Delayed Fluorescence Materials. *Front. Chem.* **2020**, *8*, No. 625910.

(11) Penfold, T. J.; Gindensperger, E.; Daniel, C.; Marian, C. M. Spin-Vibronic Mechanism for Intersystem Crossing. *Chem. Rev.* **2018**, *118*, 6975−7025.

(12) Eng, J.; Penfold, T. J. Understanding and Designing Thermally Activated Delayed Fluorescence Emitters: Beyond the Energy Gap Approximation. *Chem. Rec.* **2020**, *20*, 831−856.

(13) Marian, C. M. Understanding and Controlling Intersystem Crossing in Molecules. *Annu. Rev. Phys. Chem.* **2021**, *72*, 617−640.

(14) Leitl, M. J.; Zink, D. M.; Schinabeck, A.; Baumann, T.; Volz, D.; Yersin, H. Copper(I) Complexes for Thermally Activated Delayed Fluorescence: From Photophysical to Device Properties. *Top. Curr. Chem.* **2016**, *374*, No. 25.

(15) Etherington, M. K.; Gibson, J.; Higginbotham, H. F.; Penfold, T. J.; Monkman, A. P. Revealing the spin-vibronic coupling mechanism of thermally activated delayed fluorescence. *Nat. Commun.* **2016**, *7*, No. 13680.

(16) Gibson, J.; Monkman, A. P.; Penfold, T. J. The Importance of Vibronic Coupling for Efficient Reverse Intersystem Crossing in Thermally Activated Delayed Fluorescence Molecules. *ChemPhysChem* **2016**, *17*, 2956−2961.

(17) Kaminski, J. M.; Rodrıguez-Serrano, A.; Dinkelbach, F.; Miranda-Salinas, H.; Monkman, A. P.; Marian, C. M. Vibronic effects accelerate the intersystem crossing processes of the through-space charge transfer states in the triptycene bridged acridine-triazine donor-acceptor molecule TpAT-tFFO. *Chem. Sci.* **2022**, *13*, 7057−7066.

(18) Bergmann, L.; Friedrichs, J.; Mydlak, M.; Baumann, T.; Nieger, M.; Bräse, S. Outstanding luminescence from neutral copper(I) complexes with pyridyl-tetrazolate and phosphine ligands. *Chem. Commun.* **2013**, *49*, 6501−6503.

(19) Czerwieniec, R.; Yersin, H. Diversity of Copper(I) Complexes Showing Thermally Activated Delayed Fluorescence: Basic Photophysical Analysis. *Inorg. Chem.* **2015**, *54*, 4322−4327.

(20) Czerwieniec, R.; Leitl, M. J.; Homeier, H. H.; Yersin, H. Cu(I) complexes - Thermally activated delayed fluorescence. Photophysical approach and material design. *Coord. Chem. Rev.* **2016**, *325*, 2−28.

(21) Di, D.; Romanov, A. S.; Yang, L.; Richter, J. M.; Rivett, J. P. H.; Jones, S.; Thomas, T. H.; Abdi Jalebi, M.; Friend, R. H.; Linnolahti, M.; Bochmann, M.; Credgington, D. High-performance light-emitting diodes based on carbene-metal-amides. *Science* **2017**, *356*, 159−163.

(22) Shi, S.; Jung, M. C.; Coburn, C.; Tadle, A.; Sylvinson, M. R. D.; Djurovich, P. I.; Forrest, S. R.; Thompson, M. E. Highly Efficient Photo- and Electroluminescence from Two-Coordinate Cu(I) Complexes Featuring Nonconventional N-Heterocyclic Carbenes. *J. Am. Chem. Soc.* **2019**, *141*, 3576−3588.

(23) Hamze, R.; Shi, S.; Kapper, S. C.; Muthiah Ravinson, D. S.; Estergreen, L.; Jung, M.-C.; Tadle, A. C.; Haiges, R.; Djurovich, P. I.; Peltier, J. L.; Jazzar, R.; Bertrand, G.; Bradforth, S. E.; Thompson, M. E. "Quick-Silver" from a Systematic Study of Highly Luminescent, Two-Coordinate, d10 Coinage Metal Complexes. *J. Am. Chem. Soc.* **2019**, *141*, 8616−8626.

(24) Hamze, R.; Peltier, J. L.; Sylvinson, D.; Jung, M.; Cardenas, J.; Haiges, R.; Soleilhavoup, M.; Jazzar, R.; Djurovich, P. I.; Bertrand, G.; Thompson, M. E. Eliminating nonradiative decay in Cu(I) emitters: >99% quantum efficiency and microsecond lifetime. *Science* **2019**, *363*, 601−606.

(25) Gernert, M.; Balles-Wolf, L.; Kerner, F.; Müller, U.; Schmiedel, A.; Holzapfel, M.; Marian, C. M.; Pflaum, J.; Lambert, C.; Steffen, A. Cyclic (Amino)(aryl)carbenes Enter the Field of Chromophore Ligands: Expanded π System Leads to Unusually Deep Red Emitting CuI Compounds. *J. Am. Chem. Soc.* **2020**, *142*, 8897−8909.

(26) Hölzel, T.; Belyaev, A.; Terzi, M.; Stenzel, L.; Gernert, M.; Marian, C. M.; Steffen, A.; Ganter, C. Linear Carbene Pyridine Copper Complexes with Sterically Demanding N,N′-Bis(trityl)-imidazolylidene: Syntheses, Molecular Structures, and Photophysical Properties. *Inorg. Chem.* **2021**, *60*, 18529−18543.

(27) Lüdtke, N.; Föller, J.; Marian, C. M. Understanding the Luminescence Properties of Cu(I) Complexes: A Quantum Chemical Perusal. *Phys. Chem. Chem. Phys.* **2020**, *22*, 23530−23544.

(28) Chan, I.; van Dorp, W.; Schaafsma, T.; van der Waals, J. The lowest triplet state of Zn porphin. *Mol. Phys.* **1971**, *22*, 753−760.

(29) Harriman, A. Luminescence of porphyrins and metalloporphyrins. Part 1. - Zinc(II), nickel(II) and manganese(II) porphyrins. *J. Chem. Soc., Faraday Trans. 1* **1980**, *76*, 1978−1985.

(30) Pineiro, M.; Carvalho, A. L.; Pereira, M. M.; Gonsalves, A. M. d. R.; Arnaut, L. G.; Formosinho, S. J. Photoacoustic Measurements of Porphyrin Triplet-State Quantum Yields and Singlet-Oxygen Efficiencies. *Chem.—Eur. J.* **1998**, 2299−2307.

(31) Oyler, K. D.; Coughlin, F. J.; Bernhard, S. Controlling the Helicity of 2,2′-Bipyridyl Ruthenium(II) and Zinc(II) Hemicage Complexes. *J. Am. Chem. Soc.* **2007**, *129*, 210−217.

(32) Truesdell, K. A.; Crosby, G. A. Observation of a novel low-lying excited state in zinc(II) complexes. *J. Am. Chem. Soc.* **1985**, *107*, 1787−1788.

(33) Crosby, G. A.; Highland, R. G.; Truesdell, K. A. Spectroscopic properties of $(nd)^{10}$ transition metal complexes. *Coord. Chem. Rev.* **1985**, *64*, 41−52.

(34) Jordan, K. J.; Wacholtz, W. F.; Crosby, G. A. Structural dependence of the luminescence from bis(substituted benzenethiolato)(2,9-dimethyl-1,10-phenanthroline)zinc(II) complexes. *Inorg. Chem.* **1991**, *30*, 4588−4593.

(35) Highland, R.; Crosby, G. Determination of the activation barrier to energy transfer from $^3\pi\pi^*$ to charge transfer levels via steady-state and transient luminescence measurements on bis(4-chlorothiophenol)(1,10-phenanthroline)zinc(II). *Chem. Phys. Lett.* **1985**, *119*, 454−458.

(36) Highland, R. G.; Brummer, J. G.; Crosby, G. A. Redistribution of excitation energy between nonequilibrated electronic excited levels of zinc(II) complexes. *J. Phys. Chem. A* **1986**, *90*, 1593−1598.

(37) Galin, A.; Razskazovsky, Y.; Mel'nikov, M. Photophysical properties of mixed-ligand complexes (ArS)2ZnPhen with interligand charge-transfer excited states: influence of substituents in the arylthiolate ligand. *J. Photochem. Photobiol., A* **1993**, *72*, 35−40.

(38) Mrózek, O.; Gernert, M.; Belyaev, A.; Mitra, M.; Janiak, L.; Marian, C. M.; Steffen, A. Ultra-long Lived Luminescent Triplet Excited States in Cyclic (Alkyl)(amino)carbene Complexes of Zn(II) Halides. *Chem.—Eur. J.* **2022**, *28*, No. e202201114.

(39) Lüdtke, N.; Kuhnt, J.; Heil, T.; Steffen, A.; Marian, C. M. Revisiting LLCT phosphorescence emission from zinc(II) diimine bis-thiolate complexes: It's actually TADF. *ChemPhotoChem* **2022**, *6*, No. e202200142.

(40) Wang, R.; Deng, L.; Fu, M.; Cheng, J.; Li, J. Novel Zn^{II} complexes of 2-(2-hydroxyphenyl)benzothiazoles ligands: electroluminescence and application as host materials for phosphorescent organic light-emitting diodes. *J. Mater. Chem.* **2012**, *22*, 23454−23460.

(41) Dumur, F. Zinc complexes in OLEDs: An overview. *Synth. Met.* **2014**, *195*, 241−251.

(42) Bizzarri, C.; Spuling, E.; Knoll, D. M.; Volz, D.; Bräse, S. Sustainable metal complexes for organic light-emitting diodes (OLEDs). *Coord. Chem. Rev.* **2018**, *373*, 49−82.

(43) Mahoro, G. U.; Fernandez-Cestau, J.; Renaud, J.-L.; Coto, P. B.; Costa, R. D.; Gaillard, S. Recent Advances in Solid-State Lighting Devices Using Transition Metal Complexes Exhibiting Thermally Activated Delayed Fluorescent Emission Mechanism. *Adv. Opt. Mater.* **2020**, *8*, No. 2000260.

(44) Sakai, Y.; Sagara, Y.; Nomura, H.; Nakamura, N.; Suzuki, Y.; Miyazaki, H.; Adachi, C. Zinc complexes exhibiting highly efficient

thermally activated delayed fluorescence and their application to organic light-emitting diodes. *Chem. Commun.* **2015**, *51*, 3181−3184.

(45) Berezin, A. S.; Vinogradova, K. A.; Krivopalov, V. P.; Nikolaenkova, E. B.; Plyusnin, V. F.; Kupryakov, A. S.; Pervukhina, N. V.; Naumov, D. Y.; Bushuev, M. B. Excitation-Wavelength-Dependent Emission and Delayed Fluorescence in a Proton-Transfer System. *Chem.—Eur. J.* **2018**, *24*, 12790−12795.

(46) Xiong, J.; Li, K.; Teng, T.; Chang, X.; Wei, Y.; Wu, C.; Yang, C. Dinuclear ZnII Complexes Exhibiting Thermally Activated Delayed Fluorescence and Luminescence Polymorphism. *Chem.—Eur. J.* **2020**, *26*, 6887−6893.

(47) Goswami, B.; Feuerstein, T. J.; Yadav, R.; Lebedkin, S.; Boden, P. J.; Steiger, S. T.; Niedner-Schatteburg, G.; Gerhards, M.; Kappes, M. M.; Roesky, P. W. Thermally activated delayed fluorescence and phosphorescence quenching in iminophosphonamide copper and zinc complexes. *Chem.—Eur. J.* **2021**, *27*, 15110−15119.

(48) Nelson, D. J.; Nolan, S. P. Quantifying and understanding the electronic properties of N-heterocyclic carbenes. *Chem. Soc. Rev.* **2013**, *42*, 6723−6753.

(49) Back, O.; Henry-Ellinger, M.; Martin, C. D.; Martin, D.; Bertrand, G. ^{31}P NMR Chemical Shifts of Carbene-Phosphinidene Adducts as an Indicator of the π-Accepting Properties of Carbenes. *Angew. Chem., Int. Ed.* **2013**, *52*, 2939−2943.

(50) Mrózek, O.; Mitra, M.; Hupp, B.; Belyaev, A.; Lüdtke, N.; Wenger, O.; Marian, C. M.; Steffen, A. An Air- and Moisture-Stable Zinc(II) Carbene Dithiolate Dimer Showing Thermally Activated Delayed Fluorescence and Dexter Energy Transfer. *Chem.−Eur. J., Int. Ed.*, under revision, 2022.

(51) Mrózek, O.; Mitra, M.; Belyaev, A.; Putscher, M.; Guhl, J.; Marian, C. M.; Steffen, A. Trigonal Coordinated Zinc(II) Complexes Combine Efficient TADF and Circularly Polarized Luminescence. in preparation, 2022.

(52) Frisch, M. J.; Trucks, G. W.; Schlegel, H. B.; Scuseria, G. E.; Robb, M. A.; Cheeseman, J. R.; Scalmani, G.; Barone, V.; Petersson, G. A.; Nakatsuji, H.; Li, X.; Caricato, M.; Marenich, A. V.; Bloino, J.; Janesko, B. G.; Gomperts, R.; Mennucci, B.; Hratchian, H. P.; Ortiz, J. V.; Izmaylov, A. F.; Sonnenberg, J. L.; Williams-Young, D.; Ding, F.; Lipparini, F.; Egidi, F.; Goings, J.; Peng, B.; Petrone, A.; Henderson, T.; Ranasinghe, D.; Zakrzewski, V. G.; Gao, J.; Rega, N.; Zheng, G.; Liang, W.; Hada, M.; Ehara, M.; Toyota, K.; Fukuda, R.; Hasegawa, J.; Ishida, M.; Nakajima, T.; Honda, Y.; Kitao, O.; Nakai, H.; Vreven, T.; Throssell, K.; Montgomery, J. A., Jr.; Peralta, J. E.; Ogliaro, F.; Bearpark, M. J.; Heyd, J. J.; Brothers, E. N.; Kudin, K. N.; Staroverov, V. N.; Keith, T. A.; Kobayashi, R.; Normand, J.; Raghavachari, K.; Rendell, A. P.; Burant, J. C.; Iyengar, S. S.; Tomasi, J.; Cossi, M.; Millam, J. M.; Klene, M.; Adamo, C.; Cammi, R.; Ochterski, J. W.; Martin, R. L.; Morokuma, K.; Farkas, O.; Foresman, J. B.; Fox, D. J. *Gaussian16*, revision A.03; Gaussian Inc.: Wallingford, CT, 2016.

(53) Von Arnim, M.; Ahlrichs, R. Performance of Parallel TURBOMOLE for Density Functional Calculations. *J. Comput. Chem.* **1998**, *19*, 1746−1757.

(54) Furche, F.; Ahlrichs, R. Adiabatic Time-Dependent Density Functional Methods for Excited State Properties. *J. Chem. Phys.* **2002**, *117*, 7433−7447.

(55) Hirata, S.; Head-Gordon, M. Time-dependent density functional theory within the Tamm-Dancoff approximation. *Chem. Phys. Lett.* **1999**, *314*, 291−299.

(56) Figgen, D.; Rauhut, G.; Dolg, M.; Stoll, H. Energy-Consistent Pseudopotentials for Group 11 and 12 Atoms: Adjustment to Multi-Configuration Dirac−Hartree−Fock Data. *Chem. Phys.* **2005**, *311*, 227−244.

(57) Schäfer, A.; Horn, H.; Ahlrichs, R. Fully Optimized Contracted Gaussian Basis Sets for Atoms Li to Kr. *J. Chem. Phys.* **1992**, *97*, 2571−2577.

(58) Lee, C.; Yang, W.; Parr, R. G. Development of the Colle-Salvetti Correlation-Energy Formula into a Functional of the Electron Density. *Phys. Rev. B* **1988**, *37*, 785−789.

(59) Becke, A. D. A New Mixing of Hartree-Fock and Local Density-Functional Theories. *J. Chem. Phys.* **1993**, *98*, 1372−1377.

(60) Heil, A.; Marian, C. M. DFT/MRCI-R2018 study of the photophysics of the zinc(ii) tripyrrindione radical: non-Kasha emission? *Phys. Chem. Chem. Phys.* **2019**, *21*, 19857−19867.

(61) Cancès, E.; Mennucci, B.; Tomasi, J. A new integral equation formalism for the polarizable continuum model: Theoretical background and applications to isotropic and anisotropic dielectrics. *J. Chem. Phys.* **1997**, *107*, 3032.

(62) Mennucci, B.; Cancès, E.; Tomasi, J. Evaluation of Solvent Effects in Isotropic and Anisotropic Dielectrics and in Ionic Solutions with a Unified Integral Equation Method: Theoretical Bases, Computational Implementation, and Numerical Applications. *J. Phys. Chem. B* **1997**, *101*, 10506.

(63) Ahlrichs, R.; Bär, M.; Häser, M.; Horn, H.; Kölmel, C. Electronic Structure Calculations on Workstation Computers: The Program System Turbomole. *Chem. Phys. Lett.* **1989**, *162*, 165−169.

(64) TURBOMOLE V6.6 2014, a development of University of Karlsruhe and Forschungszentrum Karlsruhe GmbH, 1989-2007, TURBOMOLE GmbH, since 2007. Available from http://www.turbomole.com.

(65) Hättig, C.; Hellweg, A. Unpublished. Available from the TURBOMOLE Basis Set Library.

(66) Weigend, F.; Häser, M.; Patzelt, H.; Ahlrichs, R. RI-MP2: optimized auxiliary basis sets and demonstration of efficiency. *Chem. Phys. Lett.* **1998**, *294*, 143−152.

(67) Grimme, S.; Waletzke, M. A Combination of Kohn-Sham Density Functional Theory and Multi-Reference Configuration Interaction Methods. *J. Chem. Phys.* **1999**, *111*, 5645−5655.

(68) Marian, C. M.; Heil, A.; Kleinschmidt, M. The DFT/MRCI Method. *WIREs Comput. Mol. Sci.* **2019**, *9*, No. e1394.

(69) Heil, A.; Kleinschmidt, M.; Marian, C. M. On the performance of DFT/MRCI Hamiltonians for electronic excitations in transition metal complexes: The role of the damping function. *J. Chem. Phys.* **2018**, *149*, No. 164106.

(70) Kleinschmidt, M.; Tatchen, J.; Marian, C. M. Spin-Orbit Coupling of DFT/MRCI Wavefunctions: Method, Test Calculations, and Application to Thiophene. *J. Comput. Chem.* **2002**, *23*, 824−833.

(71) Kleinschmidt, M.; Marian, C. M. Efficient Generation of Matrix Elements for One-Electron Spin-Orbit Operators. *Chem. Phys.* **2005**, *311*, 71−79.

(72) Etinski, M.; Tatchen, J.; Marian, C. M. Time-Dependent Approaches for the Calculation of Intersystem Crossing Rates. *J. Chem. Phys.* **2011**, *134*, No. 154105.

(73) Etinski, M.; Tatchen, J.; Marian, C. M. Thermal and Solvent Effects on the Triplet Formation in Cinnoline. *Phys. Chem. Chem. Phys.* **2014**, *16*, 4740−4751.

(74) Kleinschmidt, M.; Tatchen, J.; Marian, C. M. SPOCK.CI: A Multireference Spin-orbit Configuration Interaction Method for Large Molecules. *J. Chem. Phys.* **2006**, *124*, No. 124101.

(75) Jabłoński, M. Theoretical Study of N-Heterocyclic-Carbene−ZnX_2 (X = H, Me, Et) Complexes. *Materials* **2021**, *14*, No. 6147.

(76) Englman, R.; Jortner, J. The energy gap law for radiationless transitions in large molecules. *Mol. Phys.* **1970**, *18*, 145−164.

(77) Föller, J.; Ganter, C.; Steffen, A.; Marian, C. M. Computer-aided design of luminescent linear N-heterocyclic carbene copper(I) pyridine complexes. *Inorg. Chem.* **2019**, *58*, 5446−5456.

Electronic Supplementary Information
for
Finding new design principles of OLED emitters through theoretical investigations of Zn(II) carbene complexes

Nora Lüdtke,[†] Andreas Steffen,[*,‡] and Christel M. Marian[*,†]

†Institute of Theoretical and Computational Chemistry, Heinrich-Heine-University Düsseldorf, Universitätsstr. 1, D-40225 Düsseldorf, Germany

‡Faculty of Chemistry and Chemical Biology, TU Dortmund University, Otto-Hahn-Str. 6, D-44227 Dortmund, Germany

E-mail: Andreas.Steffen@tu-dortmund.de; Christel.Marian@hhu.de

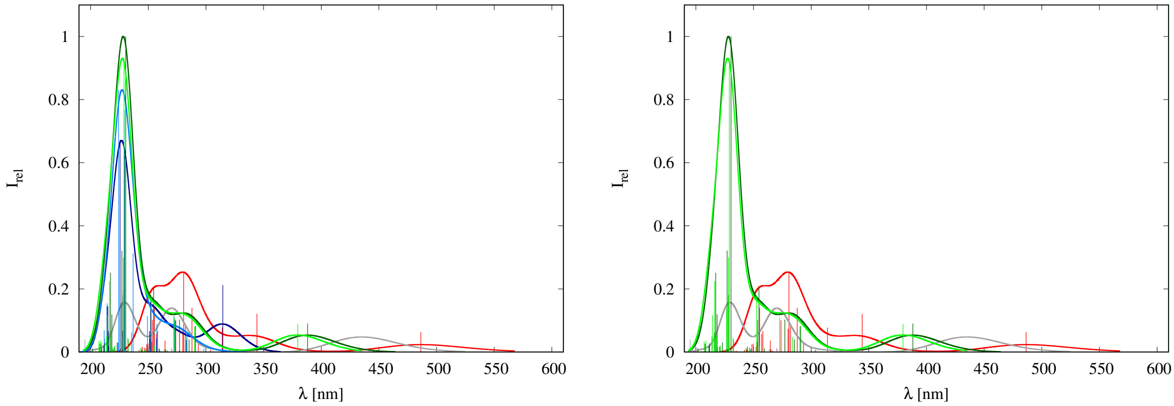

(a) All regarded compounds (b) Compounds **1-S$_2$**, **1-S$_2^{Me}$**, **1-O$_2$** and **2-S$_2$**

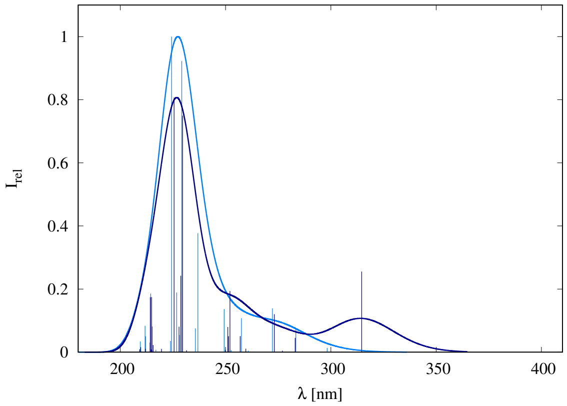

(c) Compound **3-S$_2^{\parallel}$**and **3-S$_2^{\perp}$**

Figure S1: Calculated singlet absorption spectra of compounds **1-S$_2$** (green), (dark-green), **1-O$_2$** (grey), **2-S$_2$** (red), **3-S$_2^{\parallel}$** (light-blue) and **3-S$_2^{\perp}$** (blue) in THF. In (a) and (b) the intensity of the absorption is normalized to the absorption maximum of complex . In (c) the different absorption spectra of complex **3-S$_2^{\parallel}$** and **3-S$_2^{\perp}$** are shown and normalized to the absorption maximum of **3-S$_2^{\parallel}$**.

Table S1: DFT/MRCI excitation energies (ΔE/eV) of complex $\mathbf{3\text{-}S_2^{\parallel}}$ and $\mathbf{3\text{-}S_2^{\perp}}$ in THF at various molecular geometries. The DFT/MRCI energy of the S_0 state at the DFT-optimized S_0 minimum geometry of $\mathbf{3\text{-}S_2^{\parallel}}$ in a polarizable THF environment serves as common origin. 0–0 energies including zero-point vibrational energy corrections are given in parentheses.

state	optimized geometry					
	$S_0\mathbf{3\text{-}S_2^{\perp}}$	$S_0\mathbf{3\text{-}S_2^{\parallel}}$	S_{LMCT}	T_{LMCT}	$T_{LC}(dithiol)$	$T_{LC}(NHC)$
S_0	0.00	0.02	0.56	0.58	0.93	0.44
S_{LLCT}	3.94	4.18	2.75 (**2.68**)	3.01	4.72	4.34
$S_{LC}(dithiol)$	4.38	4.40	4.62	4.72	4.33	5.03
T_{LLCT}	3.79	4.11	2.64	2.79 (**2.74**)	4.67	4.21
$T_{LC}(dithiol)$	3.78	3.83	3.91	4.01	3.15 (**3.05**)	4.26
$T_{LC}(NHC)$	4.08	4.58	4.34	5.47	4.98	3.62 (**3.46**)

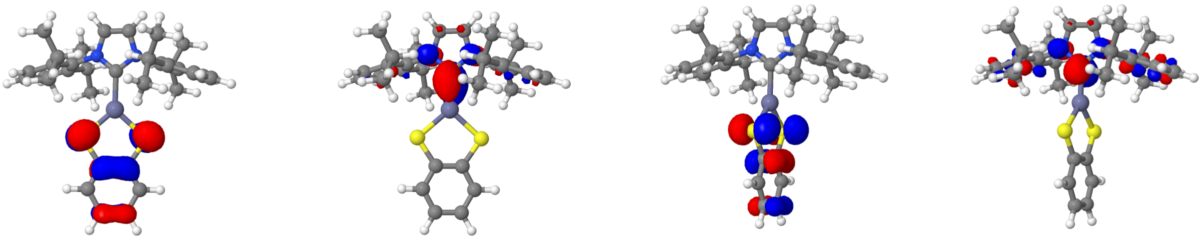

HOMO @ S_0 of $\mathbf{3\text{-}S_2^{\parallel}}$ LUMO @ S_0 of $\mathbf{3\text{-}S_2^{\parallel}}$ HOMO @ S_0 of $\mathbf{3\text{-}S_2^{\perp}}$ LUMO @ S_0 of $\mathbf{3\text{-}S_2^{\perp}}$

Figure S2: HOMO and LUMO orbitals of the NHC-Zn-Thiophenol complex $\mathbf{3\text{-}S_2^{\parallel}}$ and $\mathbf{3\text{-}S_2^{\perp}}$ in THF at the respective optimized ground state geometries.

Paper IV

Chemistry–A European Journal
Research Article
doi.org/10.1002/chem.202203980

Chemistry Europe
European Chemical Societies Publishing

www.chemeurj.org

An Air- and Moisture-stable Zinc(II) Carbene Dithiolate Dimer Showing Fast Thermally Activated Delayed Fluorescence and Dexter Energy Transfer Catalysis**

Ondřej Mrózek,[a] Mousree Mitra,[a] Bejamin Hupp,[a] Andrey Belyaev,[a] Nora Lüdtke,[b] Dorothee Wagner,[c] Cui Wang,[c] Oliver S. Wenger,[c] Christel M. Marian,*[b] and Andreas Steffen*[a]

Abstract: A dimeric Zn^{II} carbene complex featuring bridging and chelating benzene-1,2-dithiolate ligands is highly stable towards air and water. The donor-Zn-acceptor structure leads to visible light emission in the solid state, solution and polymer matrices with λ_{max} between 577–657 nm and, for zinc(II) complexes, unusually high radiative rate constants for triplet exciton decay of up to $k_r = 1.5 \times 10^5$ s^{-1} at room temperature. Variable temperature and DFT/MRCI studies show that a small energy gap between the $^{1/3}$LL/LMCT states of only 79 meV is responsible for efficient thermally activated delayed fluorescence (TADF). Time-resolved luminescence and transient absorption studies confirm the occurrence of long-lived, dominantly ligand-to-ligand charge transfer excited states in solution, allowing for application in Dexter energy transfer photocatalysis.

Introduction

Photoactive complexes of the 3d elements are currently being intensively investigated[1–6] with regard to their potential to either substitute or complement more precious 4d/5d transition metal complexes in photonic applications, where triplet excitons need to be harvested. The exploitation scenarios include, for example, sensors,[7] imaging,[8] organic light emitting devices (OLEDs),[9,10] stimuli-responsive materials,[11] as well as photocatalysis[5,12–14] for high-value products. Besides the argument of relative costs of the metals, one of the major driving forces for this development is certainly also the desire to understand the spin dynamics and various luminescence phenomena, and to discover new photoreactions. Ultimately, the breadth of findings will lead to the formulation of structure-property relationships, allowing for control of the photophysical and -chemical properties for a given application scenario. For many of the first-row transition metal complexes in their d^1 to d^9 electron configuration, an important intellectual challenge to realize room-temperature luminescence is the occurrence of metal-centred (MC) d–d* states,[15] which can be populated thermally from the initial excited states of charge transfer (CT) character and often lead to undesired non-radiative decay. Strategies to overcome this problem are to increase the ligand field splitting[16,17] or manipulate the energy of CT states[18] by judicious choice of the ligand sphere.

An alternative is to employ metal centres in their d^0 or d^{10} electron configuration.[10,18–23] This approach provides the additional advantage of various coordination spheres of the same metal centre being accessible, which greatly influences the nature, energy and reactivity of the excited states. Extensive work on trigonally and linearly coordinated Cu^I compounds, in particular, has shown that very efficient triplet state decay can be obtained either by phosphorescence,[20,24–26] or thermally activated delayed fluorescence (TADF).[10,21,27–29] For this, the ideal molecular structure should allow for the formation of low-energy ligand-to-ligand charge transfer (LLCT) states with some metal-to-ligand (ML)CT admixture to mediate spin-orbit coupling (SOC). While Cu^I is beneficially redox-active, the high oxidation potential of Zn^{II} forbids the formation of MLCT states. In addition, the majority of photoactive zinc(II) complexes is homoleptically coordinated, and thus fluorescent from ligand-centred (^{1}LC) states.[30–32]

---

[a] Dr. O. Mrózek, M. Mitra, Dr. B. Hupp, Dr. A. Belyaev, Prof. Dr. A. Steffen
Department of Chemistry and Chemical Biology
TU Dortmund University
Otto-Hahn-Str. 6
44227 Dortmund (Germany)
E-mail: andreas.steffen@tu-dortmund.de

[b] N. Lüdtke, Prof. Dr. C. M. Marian
Institute of Theoretical and Computational Chemistry
Heinrich Heine University Düsseldorf
40225 Düsseldorf (Germany)
E-mail: Christel.Marian@hhu.de

[c] D. Wagner, Dr. C. Wang, Prof. Dr. O. S. Wenger
Department of Chemistry
University of Basel
4056 Basel (Switzerland)

[**] A previous version of this manuscript has been deposited on a preprint server (https://doi.org/10.26434/chemrxiv-2022-j0rbs)

Supporting information for this article is available on the WWW under https://doi.org/10.1002/chem.202203980

However, a class of heteroleptically coordinated [ZnX$_2$(phen)] (phen = 1,10-phenanthroline; X = halides, thiolates) has been reported to exhibit rare, but very weak phosphorescence at room temperature from ^{3}LLCT/^{3}LC(phen) states.[33] We recently refined this analysis by extensive theoretical and experimental studies, showing that, in fact, TADF occurs from $^{1/3}$LLCT states with a very small energy gap $\Delta E(S_1\text{-}T_1)$, although non-radiative deactivation is dominant.[34] A similar behaviour was described for a zinc(II) iminophosphonamide complex by Roesky et al.[35] Adachi and co-workers reported TADF from a homoleptically coordinated Zn^{II} compound, albeit low radiative rate constants of only $k_r = 2.6\times10^4$ s^{-1} from intra-ligand $^{1/3}$(IL)CT states were found.[36]

These rare examples show that there is indeed potential to exploit zinc(II) complexes for triplet exciton harvesting via TADF, and we thus followed the strategy of preparing donor-M-acceptor structures to enter $^{1/3}$LLCT states to ensure high k_r. As a first foray into this field, we recently employed an electrophilic cyclic alkyl(amino)carbene (cAAC) as acceptor site for Zn^{II} halides, with the latter acting as donors. The obtained dimers [Zn$_2$Cl$_2$(μ-Cl)$_2$(^{Me}cAAC)$_2$] feature triplet ^{3}XCT/LE excited states with ultra-long lifetimes up to several milliseconds, but undesired photo-induced conformational transformation as well as further decomposition processes at room temperature involving the Zn–X bonds was observed.[37] In order to enhance the stability and foster the formation of low-energy LLCT excited states, we now focused on chelating benzene-1,2-dithiolate (bdt) as a redox-active donor for the {Zn(^{Me}cAAC)} acceptor motif.

Results and Discussion

The reaction of two equivalents disodium benzene-1,2-dithiolate (Na$_2$bdt) with [Zn$_2$Cl$_2$(μ-Cl)$_2$(^{Me}cAAC)$_2$][37] in THF solution occurs with a fast color change from colorless to yellow and simultaneous precipitation of NaCl (Figure 1). After work-up, crystallization using a CH$_2$Cl$_2$/*n*-pentane mixture afforded yellow single crystals of **Zn1** in 74% isolated yield. X-ray diffraction analysis revealed a centrosymmetric, dimeric arrangement, in which the bdt units each bind with one sulfur solely to one zinc(II) ion and bridge the two {Zn(^{Me}cAAC)} fragments with the other (Figure 1).

Although a similar coordination mode of bdt was reported for electron-deficient Zn^{II} complexes bearing *N*,*N*-chelating ligands,[38,39] it is unprecedented in the context of carbene compounds, and we find that the Zn-S^{bridging} distances are slightly shorter by ~0.07 Å for **Zn1**. The Zn–C^{carbene} bond length of 2.0575(13) Å is very similar to the value found for [Zn$_2$Cl$_2$(μ-Cl)$_2$(^{Me}cAAC)$_2$] of 2.0547(17) Å. We note that the dimeric structure of **Zn1** is maintained in solution as the ^{1}H and ^{13}C{^{1}H} NMR spectra show only one set of sharp signals.

The μ_2,k^2-bonding mode of the bdt ligands is a key feature of the molecular structure and provides enhanced steric protection of the Zn–C(carbene) bond of **Zn1** in comparison to the chloride bridged congener[37], which is highly photolabile at room temperature even in the solid state, and highly sensitive

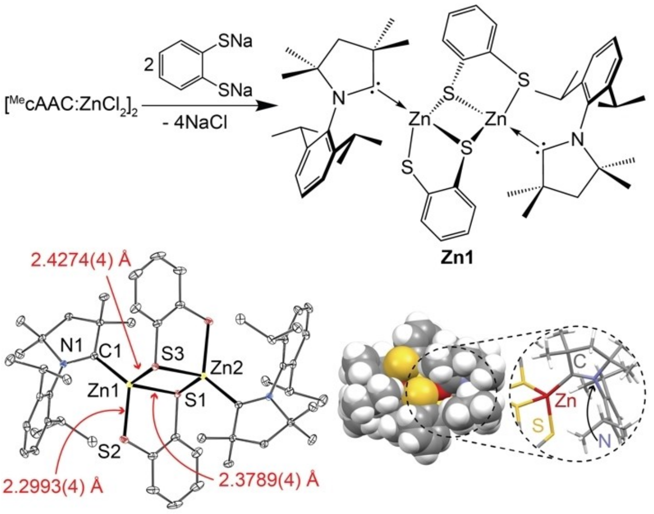

Figure 1. Synthesis and crystal structure of **Zn1**. Thermal ellipsoids are drawn at the 30% probability level and hydrogens are omitted for clarity. Selected bond lengths (Å) and angles ( ): Zn1-C1 2.0575(13); Zn1-S1 2.3789(4); Zn1-S2 2.2993(4); Zn1-S3 2.4274(4); C1-Zn1-S1 115.47(4); C1-Zn1-S2 125.36(4); C1-Zn1-S3 119.58(4); Zn1-S1-Zn2 80.83(1); S1-Zn1-S3 99.17(1).

towards oxygen and moisture. In contrast, **Zn1** is remarkably photostable not only in the solid state, but more importantly also in dry and de-oxygenated, or aerated and wet CD$_2$Cl$_2$ solution (Figure S6 in Supporting Information). Notably, no protonation of ^{Me}cAAC or bdt ligands was observed in the presence of water, which is surprising as carbene complexes are typically prone to hydrolysis even in the presence of traces of moisture in organic solvents. TGA/DSC measurements indicate good thermal stability as single-crystalline **Zn1** decomposes only above 210 C by dissociation of one ^{Me}cAAC ligand after first liberating 2 equivalents of co-crystallized solvent (Figure S5).

Cyclic voltammetry (CV) on **Zn1** performed in acetonitrile using the ferrocene/ferrocenium couple as a reference revealed a series of irreversible oxidation events within the potential range of 0.2–1.5 V (Figure S7) that we assign to consecutive oxidations of the thiolate moieties. As a consequence, thiyl radicals can be formed that have a strong tendency to dimerize to give disulfide species,[40] which can easily dissociate from the zinc(II) centers and thus explain the irreversible character of the oxidative events. In addition, we observed a fully reversible reduction wave at −2.35 V associated with the reduction of the ^{Me}cAAC ligand as shown by DFT calculations (Figure 2).

The UV/vis absorption spectra of **Zn1** in CH$_2$Cl$_2$ solution display a broad low-energy band with $\lambda_{max} = 374$ nm (ε = 3,600 M^{-1} cm^{-1}), which stems from bdt(π)→^{Me}cAAC(π^*_{CN}) LLCT excitations with LMCT admixture according to our DFT/MRCI calculations (Figures 2 and 3). In the inversion-symmetric minimum nuclear arrangement of the electronic ground state, only the $S_0 \rightarrow S_2$ and $S_0 \rightarrow S_3$ transitions, both of $^1A_g \rightarrow {}^1A_u$ type, carry nonvanishing but small electric dipole oscillator strengths of 0.02 and 0.05, respectively, which are in line with the observed weak absorption. Vibronic interactions, which lift the

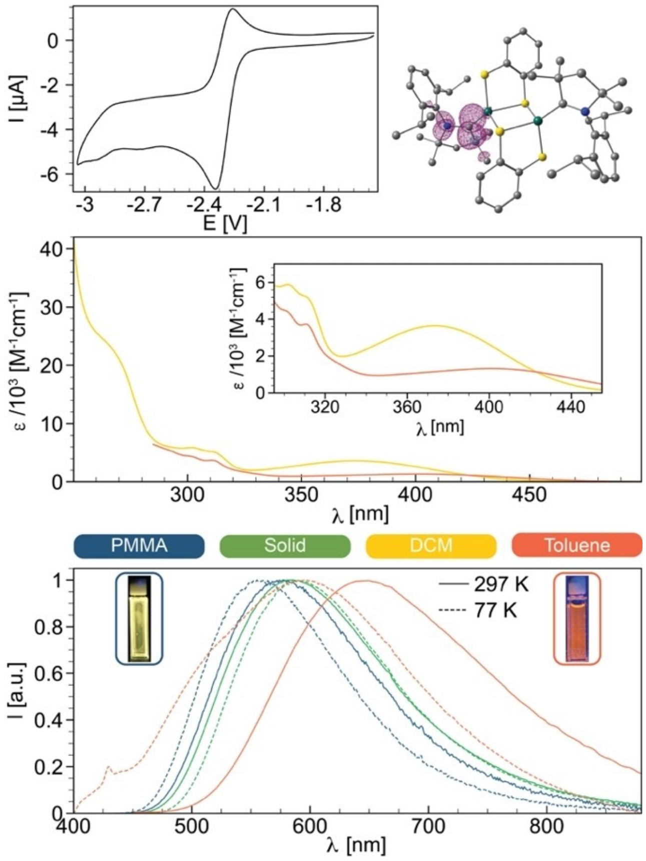

Figure 2. Top: CV vs. Fc/Fc$^+$ in CH_3CN using an Ag reference electrode (left) and calculated spin density (right) of the radical anion **Zn1**$^-$. Middle: absorption spectra of **Zn1** in CH_2Cl_2 (yellow) and toluene (orange). Bottom: emission spectra of **Zn1** in PMMA, solid state, CH_2Cl_2 and toluene at 297 (solid lines) and 77 K (dashed lines).

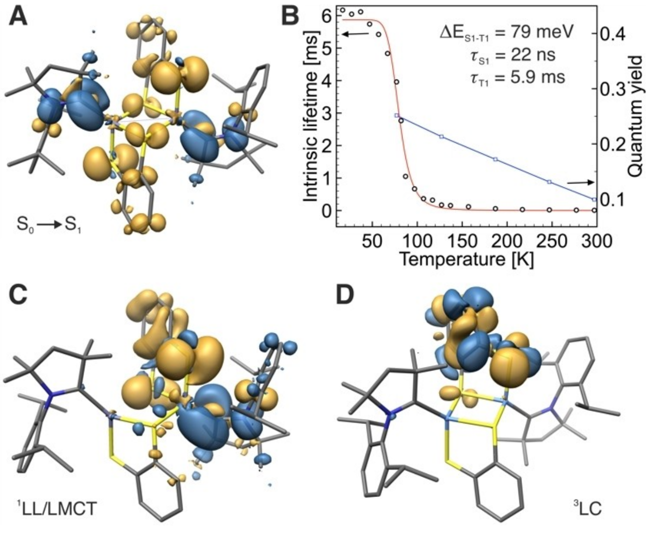

Figure 3. DFT/MRCI difference densities (isovalue ±0.0015) of the $S_0 \rightarrow S_1$ absorption (A), and of the optimized ^{1}LL/LMCT (C) and ^{3}LC (D) states of **Zn1** in THF. Areas losing electron density upon electronic excitation from the ground state are shown in gold, areas gaining electron density in blue. Experimental TADF fit of **Zn1** in PMMA (B).

symmetry selection rules, are expected to lend intensity to the $S_0 \rightarrow S_1$ and $S_0 \rightarrow S_4$ transitions as well, thus broadening the band in the low-energy regime. The high-energy region of the spectrum shows a series of additional absorptions including rather broad bands centred at 306 (structured, $\varepsilon \sim 5{,}500\ M^{-1}\,cm^{-1}$), 267 ($\varepsilon = 23{,}000\ M^{-1}\,cm^{-1}$) and 243 nm ($\varepsilon = 37{,}600\ M^{-1}\,cm^{-1}$), respectively. The first transition, calculated at 301 nm in THF, originates from an intra-ligand (IL)CT on bdt involving sulfur lone-pair orbitals as donors and the benzene π system as acceptor (Figure S25). The band with $\lambda_{max} = 267$ nm consists of several strong transitions with varying LLCT and ILCT contributions. Here, charge is transferred from sulfur lone pairs to π* orbitals of the ^{Me}cAAC ligand or of the benzene unit of btd. At the blue edge of this band, the first bdt→Rydberg transition, involving 3d shells of the sulfur atoms, is encountered in the DFT/MRCI spectrum. Complex **Zn1** further features additional strong and high-energy absorptions shown as two narrow bands at 248 and 236 nm ($\varepsilon \sim 53{,}000\ M^{-1}\,cm^{-1}$) that can be assigned to LC transitions of $\pi \rightarrow \pi^*$ character localized at the bdt unit (Figure S26). The absorption features in toluene solution are very similar, but λ_{max} of the lowest energy band shifts bathochromically by 27 nm (1,800 cm^{-1}) due to the lower solvent polarity in comparison to CH_2Cl_2 (see below), which is beneficial for utilization of **Zn1** in photocatalysis.

Upon photoexcitation ($\lambda_{ex} = 360$–480 nm), broad luminescence with $\lambda_{max} = 648$ nm is observed in de-aerated CH_2Cl_2 at room temperature, albeit with low quantum yield $\phi_{PL} = 0.02$ (Figure 2 and Table 1). The observed emission lifetime of 135 ns gives rise to $k_r = 1.5 \times 10^5\ s^{-1}$, indicative of triplet states being involved.[6,20–26] However, k_r is too fast for phosphorescence as SOC mediated by the zinc and sulfur atoms would be too small, and thus we assign the emission to TADF. We note a minor negative solvatochromic shift in toluene by 164 cm^{-1}, that might be related to the centrosymmetric nature of **Zn1** in its ground state. In both solvents, large Stokes shifts of 9,700–11,300 cm^{-1} are caused by unhindered geometry relaxation in the S_1 and T_1 state accompanied by substantial nuclear displacements and localization of the CT excitation on one side of the complex according to our calculations (Figure 3C). Consequently, facile vibrational relaxation S_1/T_1S_0 is possible, explaining the low ϕ_{PL} and short τ. This structural distortion is

Table 1. Photophysical data for **Zn1** in solid state, solutions, and polymeric matrices.

Medium	T [K]	λ_{max} [nm]	τ [ns][a]	Φ_{PL}	k_r [s^{-1}][b]	k_{nr} [s^{-1}][c]
solid	297	585	472	0.02	4.2×10^4	2.1×10^6
	77	587	170×10^3	0.06	35.2	552
crystals	297	644	97	>0.01	–	–
	77	639	260×10^3	0.01	38.5	3810
DCM	297	650	135	0.02	1.5×10^5	7.3×10^6
	77	551	316×10^3	–	–	–
Toluene	297	657	194	0.02	1.0×10^5	5.1×10^6
	77	596	641×10^3	–	–	–
PS	297	585	444	0.02	4.5×10^4	2.2×10^6
	77	580	927×10^3	0.08	86.3	993
PMMA	297	577	741	0.10	1.4×10^5	1.2×10^6
	77	558	987×10^3	0.25	253.0	760

[a] amplitude average lifetime, [b] $k_r = \phi_{PL}/\tau$, [c] $k_{nr} = (1-\phi_{PL})/\tau$.

hindered in the solid state or in polystyrene (PS) matrix, and thus the emission shifts hypsochromically to $\lambda_{max} = 585$ nm (Table 1). Interestingly, **Zn1** in PMMA matrix (10 wt-%) shows an even larger hypsochromic shift of 1,946 cm^{-1} compared to CH_2Cl_2 solution to $\lambda_{max} = 577$ nm. In addition to the enhanced rigidity (see above), the polar environment stabilizes the polar ground state of **Zn1** with negatively charged bdt ligands and positively charged $Zn^{II}/^{Me}$cAAC, further increasing the energy gap $\Delta E(S_1\text{-}S_0)$. These effects lead to greatly enhanced $\phi_{PL} = 0.10$ while maintaining the high k_r. In order to shed light on the assumed TADF mechanism, we performed detailed variable-temperature (VT) measurements in PMMA, in which **Zn1** exhibits the most efficient luminescence (Figures 2 and 3). Upon lowering the temperature to 77 K, the yellow emission shifts hypsochromically by ca. 20 nm due to further rigidification, with a concomitant increase of τ to 987 µs. The intrinsic radiative lifetimes $\tau_{rad} = 1/k_r$ between 7–297 K can be fitted to a three-states kinetic model (Figure 3B) according to Equation (1):

$$\tau_{rad} = \frac{3 + \exp\left[-\frac{\Delta E(S_1-T_1)}{k_B T}\right]}{3k_{fl} + k_{ph} \cdot \exp\left[-\frac{\Delta E(S_1-T_1)}{k_B T}\right]} \quad (1)$$

providing an estimated $\Delta E(S_1\text{-}T_1) = 79$ meV (637 cm^{-1}), which is in excellent agreement with the DFT/MRCI energy difference at the S_1 minimum in THF of 90 meV (726 cm^{-1}). The small energy gap and long lifetime of the T_1 state of ca. 6 ms (calc. 32 ms) are beneficial for efficient rISC, and in combination with the estimated short $\tau(S_1) = 22$ ns, efficient TADF is enabled.

An anomalous hypsochromic shift of the emission in CH_2Cl_2 by ca. 100 nm upon cooling to 77 K is observed (Table 1), which appears to originate from a population of a different excited state. In addition to the ^{3}LLCT state, we find a higher-lying minimum on the T_1 potential energy surface that is of ^{3}LC(dbt) nature (Figure 3D and Figure S31). The involvement of the sulfur atoms in the excitation mediates SOC (64 cm^{-1}, Table S9), resulting in phosphorescence with $\tau_{rad} = 22$ ms according to the calculations.

Transient absorption (TA) studies of **Zn1** in toluene (Figure 4) confirm that internal conversion and ISC leading to the formation of the final ^{3}LL/LMCT state, that is involved in the TADF process, occur on a timescale faster than our instrument response of 10 ns. The TA spectrum shows in general a positive absorbance change over the whole spectral range with a drop in optical density at $\lambda_{abs} = 390$ and 320 nm, which coincides with overlapping ground state absorption. The decays of the excited state absorption (ESA) at $\lambda_{abs} = 348$ and 440 nm were fitted monoexponentially and yielded lifetimes of 370 and 354 ns, respectively, which is in the range of the recorded luminescence lifetimes.

The population of triplet excited states, of which the broad emission covers an energy range from 2.48-1.60 eV, with associated long lifetimes of hundreds of nanoseconds in solution suggests that **Zn1** may be employed in photocatalytic transformations as triplet sensitizer, similar to two recently reported Zn(II) complexes with dark (non-emissive) triplet excited states.[41] Fulfilling another important prerequisite for photocatalysis, the continuous irradiation of **Zn1** for one hour with high-power 450 nm LEDs revealed excellent photostability by maintaining 96% and 99% of the original absorbance in toluene and THF, respectively (Figure S24). The photo-isomerization (*E*)-stilbene→(*Z*)-stilbene requires the population of the organic T_1 state at 2.2 eV, of which sensitization with our zinc(II) complex appears feasible. Indeed, 2 mol-% of **Zn1** in degassed toluene give 93% conversion after four hours of irradiation, which is faster than found for the standard $[Ru(bpy)_3]^{3+}$ that requires 5 mol-% and 8 h.[42] Control experiments under identical conditions but without **Zn1** showed no formation of (*Z*)-stilbene (Figure S25), highlighting the suitability of our zinc(II) complex for photocatalytic transformations.

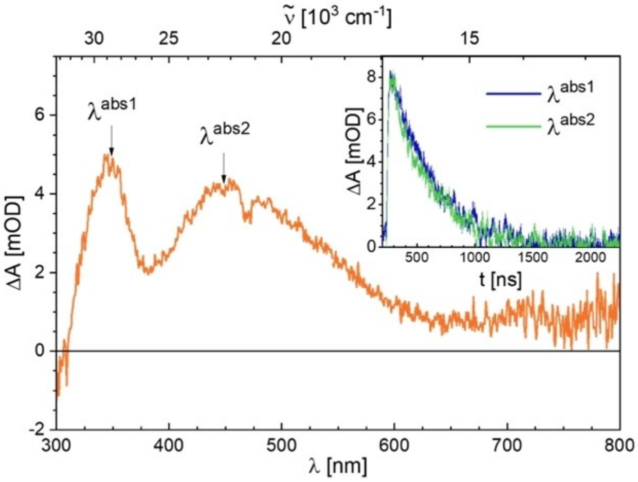

Figure 4. Transient absorption spectrum of **Zn1** in de-aerated toluene at 293 K, recorded at 10 ns time delay upon excitation at 420 nm with laser pulse energy of 15 mJ. The spectrum was recorded with an integration time of 100 ns after the indicated delay time. The inset shows the decays of the excited state absorption (ESA) signals at 348 nm (blue trace) and 440 nm (green trace).

Conclusions

In conclusion, a new type of dimeric Zn^{II}-based emitter in the yellow to orange region of the electromagnetic spectrum, with a donor-M-acceptor motif by employing an electron-rich thiolate ligand in combination with an electrophilic carbene ligand, exhibits $^{1/3}$LLCT states suitable for efficient TADF with high k_r. The visible light absorption, for carbene complexes astonishing stability towards air and water, in combination with the observation of long-lived triplet states in solution renders the complex suitable for Dexter energy transfer photocatalysis. Overall, these promising first results clearly show that Zn^{II}-based photoactive complexes bear great potential as serious alternatives to traditional 4d and 5d transition metal compounds employed in devices and photochemistry.

Experimental Section

General considerations: All operations were performed under an argon atmosphere by using conventional Schlenk-line techniques or glovebox. The solvents were dried using Technology Inc. Pure-Solv system or standard methods, and were degassed and stored over activated 4 Å molecular sieves. Dimeric [Zn_2(μ-$Cl)_2(Cl)_2(^{Me}$cAAC$)_2$][37] and benzene-1,2-dithiol[43,44] (for details see below) were prepared according to established procedures. All other starting materials were available commercially and were used without further purification. ^{1}H, ^{13}C{^{1}H} APT, ^{1}H–^{13}C HSQC, ^{1}H–^{13}C HSMB, ^{1}H–^{1}H COSY and ^{1}H–^{15}N HMBC NMR spectra were measured at 300 K on Bruker 500 Avance or Bruker 600 Avance spectrometers. The chemical shifts are given in ppm relative to residual signals of the respective solvent [^{1}H, ^{13}C: CD_2Cl_2 (5.32, 53.84 ppm); C_6D_6 (7.16, 128.06)]. Cyclic voltammetry measurements were performed on a Gamry Instruments Reference [600] potentiostat with three electrodes cell configuration (working electrode: Pt-disk, counter electrode: Pt-wire, reference electrode: silver wire separated by Vycor tip). Redox potentials are referenced to the ferrocene/ferrocenium couple and ^{n}Bu_4NBF_4 was used (100 mM solution) as supporting electrolyte. TGA/DSC data were recorded using a STA650 instrument (TA instruments, USA) with a heat rate of 10 C/min and under constant flow of nitrogen gas.

All photophysical measurements were performed in dry and deaerated solutions. In the case of polymeric matrices, the respective polymer (PMMA or PS) was weighted into a vial together with 10 wt% of **Zn1**. Subsequently, the mixture was dissolved in DCM, the solution was added to a spectroscopic cuvette, and the solvent was slowly evaporated to form a thin layer (film) of **Zn1** in the matrix. The remaining solvent molecules were evaporated by keeping the film under a low vacuum for 12 h. The solid-state measurements were performed either in single-crystalline form (sample denoted as 'crystals') or, to remove co-crystallized molecules of solvent, single-crystals were ground and dried under vacuum for 24 h (sample denoted as 'solid'). Optical absorption spectroscopy was performed using an Agilent Cary 5000 spectrophotometer using standard 1 cm path length quartz cells. Excitation and emission spectra were recorded on an Edinburgh Instrument FLS1000 spectrometer, equipped with a 450 W Xenon arc lamp, double monochromators for the excitation and emission pathways, and a red-sensitive photomultiplier (PMT-980) as a detector. The excitation and emission spectra were corrected using the standard corrections supplied by the manufacturer for the excitation source's spectral power and the detector's sensitivity. Quantum yields in solution were measured using an FLS1000 spectrometer equipped with an integrating sphere (N-M01), and the quantum yield of solid samples and polymeric matrices were measured using an integrating cryosphere (Microstat N2) from Oxford Instruments. The luminescence lifetimes were measured using a μF2 pulsed 60 W Xenon microsecond flashlamp, with a repetition rate of 100 Hz and a multichannel scaling (MCS) module or with VPLEDs (383.8 nm with 1.1 mW or 449.6 nm with 37 mW), with 100 ns pulse width and an MCS module, depending on the time range. The emission was collected at a right angle to the excitation source. The low-temperature experiments were performed using liquid nitrogen-cooled OptistatDN-V cryostat from Oxford Instruments or 4 K cryostat (CS204SI-FMX-1SS) from Advanced Research System equipped with a closed cycle water-cooled helium compressor.

An LP920-KS apparatus from Edinburgh Instruments was employed for nanosecond transient absorption spectroscopy. Excitation was performed by a frequency-tripled Nd:YAG laser (Quantel Brilliant b, ca. 10 ns pulse width and ca. 10 mJ output) equipped with an OPO from Opotek (excitation wavelength set to 420 nm with ca. 15 mJ output). A beam expander (GBE02-A from Thorlabs) was used to ensure homogeneous excitation. Detection of transient absorption spectra occurred on an iCCD camera (Andor), whereas kinetics at a single wavelength were recorded using a photomultiplier tube. Samples were prepared in toluene (50 μM), degassed by rigorous bubbling with dry Ar, and checked for photodegradation via UV/VIS in regular intervals over the course of the measurements.

Preliminary picosecond transient absorption studies with sub-nanosecond time resolution were performed using a TRASS instrument from Hamamatsu and a mode-locked picosecond Nd:YAG laser (model PL2251B-10-SH-TH with PRETRIG option) as an excitation source. The laser pulse duration was ~30 ps and the pulse frequency was 10 Hz. The third harmonic (355 nm) was used for excitation of the sample, however, significant decomposition was observed over the course of the measurement, presumably due to the high energy (both pulse energy and wavelength) of the excitation source.

Computational Methods: For all geometry optimizations the Gaussian 16 program was used.[45] The ground state geometries were optimized with Kohn–Sham density functional theory (DFT).[46] For the optimization of the singlet excited state geometries the time dependent DFT (TDDFT)[47] was used and for the excited triplet state geometries the Tamm-Dancoff approximation (TDA)[48] to TDDFT was chosen. The 10-mdf 6 s5p3d basis set with defpp-ecp was used for the zinc atoms[49] and for sulfur the def2-SVPD basis was chosen.[50] For all other atoms the def-SV(P) basis set was used.[50] As functional BH-LYP functional was chosen for all calculations.[51,52] A THF environment was mimicked via the polarizable continuum model (PCM).[53,54] To examine the excitation energies and oscillator strengths of the spin allowed transitions, DFT/MRCI calculations were carried out.[55,56] As Hamiltonian, the redesigned R2018 was selected and 30 singlet and 30 triplet roots were calculated. For the DFT/MRCI calculations, the point charges of the Gaussian 16 calculations were extracted. With the SPOCK program, the spin-orbit coupling matrix elements (SOCMEs) were obtained.[57,58]

Synthetic Procedures

$C_6H_4S_2H_2$ (H_2bdt): 5 mL of benzenethiol (49 mmol) were added dropwise to a mixture of *n*-BuLi (103 mmol, 2.5 M, 41 mL) and TMEDA (54 mmol, 8.1 mL) in 40 mL of *n*-pentane at −78 C. The mixture was allowed to slowly warm to room temperature and stirred overnight. Then the solution was again cooled to −78 C and octasulfur (49 mmol) was added dropwise. The mixture was stirred at −78 C for two hours and overnight at room temperature, followed by slow addition of 10 mL of water. The quenched mixture was poured into diluted hydrochloric acid and extracted with Et_2O (3×50 mL). Organic layers were combined, dried over anhydrous $MgSO_4$ and evaporated to dryness using rotavapor. The crude product was vacuum distilled (55 C, 0.2 mbar) to give 1.4 mL (24%) of colorless liquid. ^{1}H NMR (500 MHz, C_6D_6): 7.96 (m, 2H), 6.65 (m, 2H), 3.35 (s, 2H). ^{13}C NMR (125 MHz, C_6D_6): 131.4 (s, 2 C), 130.9 (s, 2 C), 126.4 (s, 2 C).

$C_6H_4S_2Na_2$ (bdt): 337 mg (14 mmol) of NaH was dispersed in 20 mL of THF and 1.1 g (7.7 mmol) of benzene-1,2-dithiol in 10 mL of THF was added dropwise. After complete addition, the mixture was stirred for one hour at 60 C and then overnight at room temperature. After filtration, the remaining white solid was washed with additional portion of THF (2×15 mL) and the product was vacuum-dried for 4 h at 60 C. Yield: 942 mg (5.0 mmol, 72 %) of white powder.

[(^{Me}cAAC)Zn(k*S*:μ^2*S*-PhS$_2$)$_2$Zn(^{Me}cAAC)] (Zn1): 47 mg of (250 mmol) disodium benzene-1,2-dithiolate (**bdt**) was mixed with 100 mg (119 mmol) of [(^{Me}cAAC)(Cl)Zn(μ-Cl)$_2$Zn(Cl)(^{Me}cAAC)] in 7 mL of THF and the resulting mixture was stirred overnight at room temperature. After that, the solvents were vacuum-evaporated, and the solid residue was extracted with DCM (3x5 mL). The combined organic fractions were concentrated by vacuum evaporation to a final volume of 3 mL and crystallization was induced by gas phase diffusion of n-pentane. The obtained single-crystals were collected, washed with cold THF (2 mL), *n*-pentane (2×5 mL) and vacuum dried. Yield: 86 mg (73.5 %, 86 mmol) of yellow crystalline material. CHNS analysis calcd for $C_{53}H_{72}N_2S_4ZnCl_2$: C, 59.7; H, 6.8; N, 2.6. Found: C, 59.8; H, 7.1; N, 2.62. ^{1}H NMR (600 MHz, CD_2Cl_2): δ [ppm] = 7.53 (t, $^3J(^1H,^1H) = 7.8$ Hz, 2H, H^4, $C_6H_3{}^iPr_2$), 7.39 (m, 4H, $C_6H_4S_2$), 7.35 (d, $^3J(^1H,^1H) = 7.8$ Hz, 4H, $H^{3,5}$, $C_6H_3{}^iPr_2$), 6.69 (m, 4H, $C_6H_4S_2$), 2.77 (sept, $^3J(^1H,1H) = 6.7$ Hz, 4H, CH^{iPr}), 2.17 (s, 4H, $-CH_2-$), 1.57 (s, 12H, $(CH_3)_2$), 1.48 (s, 12H, $(CH_3)_2$), 1.32 (d, $^3J(^1H,1H) = 6.7$ Hz, 12H, $CH_3{}^{iPr}$), 1.23 d, $^3J(^1H,^1H) = 6.7$ Hz, 12H, $CH_3{}^{iPr}$). ^{13}C NMR (125 MHz, CD_2Cl_2): δ [ppm] = 243.8 (s, 2 C, $C^{carbene}$), 145.2 (s, 4 C, $C^{2,6}$, *Dipp*), 144.4 (s, 4 C, $C^{1,2}$, *Ph*S$_2$), 133.9 (s, 2 C, C^1, *Dipp*), 130.9 (s, 2 C, C^4, *Dipp*), 130.6 (s, 4 C, *Ph*S$_2$), 126.1 (s, 4 C, $C^{3,5}$, *Dipp*), 122.3 (s, 4 C, *Ph*S$_2$), 84.5 (s, 2 C, $NCC^{carbene}$), 55.2 (s, 2 C, $NC(CH_3)_2$), 49.9 (s, 2 C, $-CH_2-$), 29.5 (s, 4 C, $C(CH_3)_2$), 29.4 (s, 4 C, $CH(CH_3)_2$, Dipp), 28.1 (s, 4 C, $C(CH_3)_2$), 27.3 (s, 4 C, $CH(CH_3)_2$, Dipp), 23.9 (s, 4 C, $CH(CH_3)_2$, Dipp). ^{15}N (60 MHz, CD_2Cl_2): δ [ppm] = -141.86 ppm.

Deposition Number 2189606 (for **Zn1**) contains the supplementary crystallographic data for this paper. These data are provided free of charge by the joint Cambridge Crystallographic Data Centre and Fachinformationszentrum Karlsruhe Access Structures service.

Acknowledgements

This work was supported by Deutsche Forschungsgemeinschaft [DFG, Priority Program SPP 2102 “Light-controlled reactivity of metal complexes” (MA 1051/18-1 and STE 1834/7-1)]. We are also grateful to the DFG for funding of major research equipment (INST 212/430-1 FUGG and INST 212/455-1 FUGG). A.B. is grateful to Alexander von Humboldt Foundation for a Research Fellowship grant for Postdoctoral Research. C.W. acknowledges the Deutsche Forschungsgemeinschaft (DFG, German Research Foundation) for the funding (WA 5012/1-1). Open Access funding enabled and organized by Projekt DEAL.

Conflict of Interest

The authors declare no conflict of interest.

Data Availability Statement

The data that support the findings of this study are available in the supplementary material of this article.

Keywords: carbenes · luminescence · photocatalysis · TADF · zinc

[1] C. Förster, K. Heinze, *Chem. Soc. Rev.* **2020**, *49*, 1057–1070.
[2] O. S. Wenger, *J. Am. Chem. Soc.* **2018**, *140*, 13522–13533.
[3] C. B. Larsen, O. S. Wenger, *Chem. Eur. J.* **2018**, *24*, 2039–2058.
[4] C. Wegeberg, O. S. Wenger, *JACS Au* **2021**, *1*, 1860–1876.
[5] B. M. Hockin, C. Li, N. Robertson, E. Zysman-Colman, *Catal. Sci. Technol.* **2019**, *9*, 889–915.
[6] A. Steffen, B. Hupp, in Comprehensive Coordination Chemistry III (Eds.: E. C. Constable, G. Parkin, L. Que Jr), Elsevier, Oxford, **2021**, pp. 466–502.
[7] O. S. Wenger, *Chem. Rev.* **2013**, *113*, 3686–3733.
[8] Q. Zhao, C. Huang, F. Li, *Chem. Soc. Rev.* **2011**, *40*, 2508–2524.
[9] C. Bizzarri, E. Spuling, D. M. Knoll, D. Volz, S. Bräse, *Coord. Chem. Rev.* **2018**, *373*, 49–82.
[10] R. Hamze, J. L. Peltier, D. Sylvinson, M. Jung, J. Cardenas, R. Haiges, M. Soleilhavoup, R. Jazzar, P. I. Djurovich, G. Bertrand, M. E. Thompson, *Science* **2019**, *363*, 601–606.
[11] J. X. Wang, C. Li, H. Tian, *Coord. Chem. Rev.* **2021**, *427*, 213579.
[12] J.-H. Shon, D. Kim, M. D. Rathnayake, S. Sittel, J. Weaver, T. S. Teets, *Chem. Sci.* **2021**, *12*, 4069–4078.
[13] C. K. Prier, D. A. Rankic, D. W. C. MacMillan, *Chem. Rev.* **2013**, *113*, 5322–5363.
[14] D. M. Arias-Rotondo, J. K. McCusker, *Chem. Soc. Rev.* **2016**, *45*, 5803–5820.
[15] J. K. McCusker, *Science* **2019**, *363*, 484–488.
[16] P. Chábera, Y. Liu, O. Prakash, E. Thyrhaug, A. El Nahhas, A. Honarfar, S. Essén, L. A. Fredin, T. C. B. Harlang, K. S. Kjær, K. Handrup, F. Ericson, H. Tatsuno, K. Morgan, J. Schnadt, L. Häggström, T. Ericsson, A. Sobkowiak, S. Lidin, P. Huang, S. Styring, J. Uhlig, J. Bendix, R. Lomoth, V. Sundström, P. Persson, K. Wärnmark, *Nature* **2017**, *543*, 695–699.
[17] S. Otto, M. Grabolle, C. Förster, C. Kreitner, U. Resch-Genger, K. Heinze, *Angew. Chem. Int. Ed.* **2015**, *54*, 11572–11576; *Angew. Chem.* **2015**, *127*, 11735–11739.
[18] S. B. Vittardi, R. T. Magar, B. R. Schrage, C. J. Ziegler, E. Jakubikova, J. J. Rack, *Chem. Commun.* **2021**, *57*, 4658–4661.
[19] Y. Zhang, T. S. Lee, J. M. Favale, D. C. Leary, J. L. Petersen, G. D. Scholes, F. N. Castellano, C. Milsmann, *Nat. Chem.* **2020**, *12*, 345–352.
[20] M. Gernert, U. Müller, M. Haehnel, J. Pflaum, A. Steffen, *Chem. Eur. J.* **2017**, *23*, 2206–2216.
[21] M. Gernert, L. Balles-Wolf, F. Kerner, U. Müller, A. Schmiedel, M. Holzapfel, C. M. Marian, J. Pflaum, C. Lambert, A. Steffen, *J. Am. Chem. Soc.* **2020**, *142*, 8897–8909.
[22] R. Hamze, S. Shi, S. C. Kapper, D. S. Muthiah Ravinson, L. Estergreen, M.-C. Jung, A. C. Tadle, R. Haiges, P. I. Djurovich, J. L. Peltier, R. Jazzar, G. Bertrand, S. E. Bradforth, M. E. Thompson, *J. Am. Chem. Soc.* **2019**, *141*, 8616–8626.
[23] A. M. T. Muthig, M. Krumrein, J. Wieland, M. Gernert, F. Kerner, J. Pflaum, A. Steffen, *Inorg. Chem.* **2022**, *61*, 14833–14844.
[24] V. A. Krylova, P. I. Djurovich, B. L. Conley, R. Haiges, M. T. Whited, T. J. Williams, M. E. Thompson, *Chem. Commun.* **2014**, *50*, 7176–7179.
[25] B. Hupp, C. Schiller, C. Lenczyk, M. Stanoppi, K. Edkins, A. Lorbach, A. Steffen, *Inorg. Chem.* **2017**, *56*, 8996–9008.
[26] B. Hupp, J. Nitsch, T. Schmitt, R. Bertermann, K. Edkins, F. Hirsch, I. Fischer, M. Auth, A. Sperlich, A. Steffen, *Angew. Chem. Int. Ed.* **2018**, *57*, 13671–13675; *Angew. Chem.* **2018**, *130*, 13860–13864.
[27] J. Nitsch, F. Lacemon, A. Lorbach, A. Eichhorn, F. Cisnetti, A. Steffen, *Chem. Commun.* **2016**, *52*, 2932–2935.
[28] A. Ruduss, B. Turovska, S. Belyakov, K. A. Stucere, A. Vembris, K. Traskovskis, *Inorg. Chem.* **2022**, *61*, 2174–2185.
[29] R. Tang, S. Xu, T.-L. Lam, G. Cheng, L. Du, Q. Wan, J. Yang, F.-F. Hung, K.-H. Low, D. L. Phillips, C.-M. Che, *Angew. Chem. Int. Ed.* **2022**, *61*, e202203982.
[30] S. Bestgen, C. Schoo, B. L. Neumeier, T. J. Feuerstein, C. Zovko, R. Köppe, C. Feldmann, P. W. Roesky, *Angew. Chem. Int. Ed.* **2018**, *57*, 14265–14269; *Angew. Chem.* **2018**, *130*, 14461–14465.

[31] R. Sakamoto, T. Iwashima, J. F. Kögel, S. Kusaka, M. Tsuchiya, Y. Kitagawa, H. Nishihara, *J. Am. Chem. Soc.* **2016**, *138*, 5666–5677.
[32] J. F. Kögel, S. Kusaka, R. Sakamoto, T. Iwashima, M. Tsuchiya, R. Toyoda, R. Matsuoka, T. Tsukamoto, J. Yuasa, Y. Kitagawa, T. Kawai, H. Nishihara, *Angew. Chem. Int. Ed.* **2016**, *55*, 1377–1381; *Angew. Chem.* **2016**, *128*, 1399–1403.
[33] K. A. Truesdell, G. A. Crosby, *J. Am. Chem. Soc.* **1985**, *107*, 1787–1788.
[34] N. Lüdtke, J. Kuhnt, T. Heil, A. Steffen, C. M. Marian, *ChemPhotoChem* **2022**, *7*, e202200142.
[35] B. Goswami, T. J. Feuerstein, R. Yadav, S. Lebedkin, P. J. Boden, S. T. Steiger, G. Niedner-Schatteburg, M. Gerhards, M. M. Kappes, P. W. Roesky, *Chem. Eur. J.* **2021**, *27*, 15110–15119.
[36] Y. Sakai, Y. Sagara, H. Nomura, N. Nakamura, Y. Suzuki, H. Miyazaki, C. Adachi, *Chem. Commun.* **2015**, *51*, 3181–3184.
[37] O. Mrózek, M. Gernert, A. Belyaev, M. Mitra, L. Janiak, C. M. Marian, A. Steffen, *Chem. Eur. J.* **2022**, *28*, e202201114.
[38] K. Halvorsen, G. A. Crosby, W. F. Wacholtz, *Inorg. Chim. Acta* **1995**, *228*, 81–88.
[39] D. M. Hatch, W. F. Wacholtz, J. T. Mague, *Acta Crystallogr. Sect. C* **2003**, *59*, m452-m453.
[40] M. Borsari, M. Cannio, G. Gavioli, *Electroanalysis* **2003**, *15*, 1192–1197.
[41] J. A. Kübler, B. Pfund, O. S. Wenger, *JACS Au* **2022**, *2*, 2367–2380.
[42] M. M. Floes-Leonar, C. R. Azpilcueta, C. Amador-Bedolla, S. S. Rozenel, *J. Photochem. Photobiol. A* **2021**, *414*, 113224.
[43] P. S. Nejman, B. Morton-Fernandez, N. Black, D. B. Cordes, A. M. Slawin, P. Kilian, J. D. Woollins, *J. Organomet. Chem.* **2015**, *776*, 7–16.
[44] D. M. Giolando, K. Kirschbaum, *Synthesis* **1992**, 451–452.
[45] Gaussian 16, Revision A.03, M. J. Frisch, G. W. Trucks, H. B. Schlegel, G. E. Scuseria, M. A. Robb, J. R. Cheeseman, G. Scalmani, V. Barone, G. A. Petersson, H. Nakatsuji et al., 2016; Gaussian Inc. Wallingford CT.
[46] M. Von Arnim, R. Ahlrichs, *J. Comput. Chem.* **1998**, *19*, 1746–1757.
[47] F. Furche, R. Ahlrichs, *J. Chem. Phys.* **2002**, *117*, 7433–7447.
[48] S. Hirata, M. Head-Gordon, *Chem. Phys. Lett.* **1999**, *314*, 291–299.
[49] D. Figgen, G. Rauhut, M. Dolg, H. Stoll, *Chem. Phys.* **2005**, *311*, 227–244.
[50] A. Schäfer, H. Horn, R. Ahlrichs, *J. Chem. Phys.* **1992**, *97*, 2571–2577.
[51] C. Lee, W. Yang, R. G. Parr, *Phys. Rev. B* **1988**, *37*, 785–789.
[52] A. D. Becke, *J. Chem. Phys.* **1993**, *98*, 1372–1377.
[53] E. Cancès, B. Mennucci, J. Tomasi, *J. Chem. Phys.* **1997**, *107*, 3032.
[54] B. Mennucci, E. Cancès, J. Tomasi, *J. Phys. Chem. B* **1997**, *101*, 10506.
[55] S. Grimme, M. Waletzke, *J. Chem. Phys.* **1999**, *111*, 5645–5655.
[56] C. M. Marian, A. Heil, M. Kleinschmidt, *WIREs Comput. Mol. Sci.* **2019**, *9*, e1394.
[57] M. Kleinschmidt, J. Tatchen, C. M. Marian, *J. Comput. Chem.* **2002**, **23**, 824–833.
[58] M. Kleinschmidt, C. M. Marian, *Chem. Phys.* **2005**, *311*, 71–79.

Manuscript received: December 20, 2022
Accepted manuscript online: January 13, 2023
Version of record online: ■■, ■■

RESEARCH ARTICLE

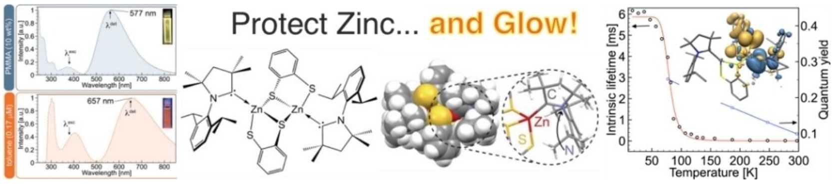

Steric protection of the Zn-Carbene bond by a bridging coordination mode of 1,2-dithiolate ligands leads to air- and moisture-stable complexes. Efficient TADF with high radiative rate constants at room temperature is observed from $^{1/3}$LL/LMCT states according to variable temperature, transient absorption and DFT/MRCI studies. Application in Dexter energy transfer catalysis is demonstrated, exemplifying the potential of this new class of abundant 3d photoactive systems.

Dr. O. Mrózek, M. Mitra, Dr. B. Hupp, Dr. A. Belyaev, N. Lüdtke, D. Wagner, Dr. C. Wang, Prof. Dr. O. S. Wenger, Prof. Dr. C. M. Marian, Prof. Dr. A. Steffen**

1 – 8

An Air- and Moisture-stable Zinc(II) Carbene Dithiolate Dimer Showing Fast Thermally Activated Delayed Fluorescence and Dexter Energy Transfer Catalysis

Chemistry–A European Journal

Supporting Information

An Air- and Moisture-stable Zinc(II) Carbene Dithiolate Dimer Showing Fast Thermally Activated Delayed Fluorescence and Dexter Energy Transfer Catalysis

Ondřej Mrózek, Mousree Mitra, Bejamin Hupp, Andrey Belyaev, Nora Lüdtke, Dorothee Wagner, Cui Wang, Oliver S. Wenger, Christel M. Marian,* and Andreas Steffen*

Table of Contents

NMR Spectra

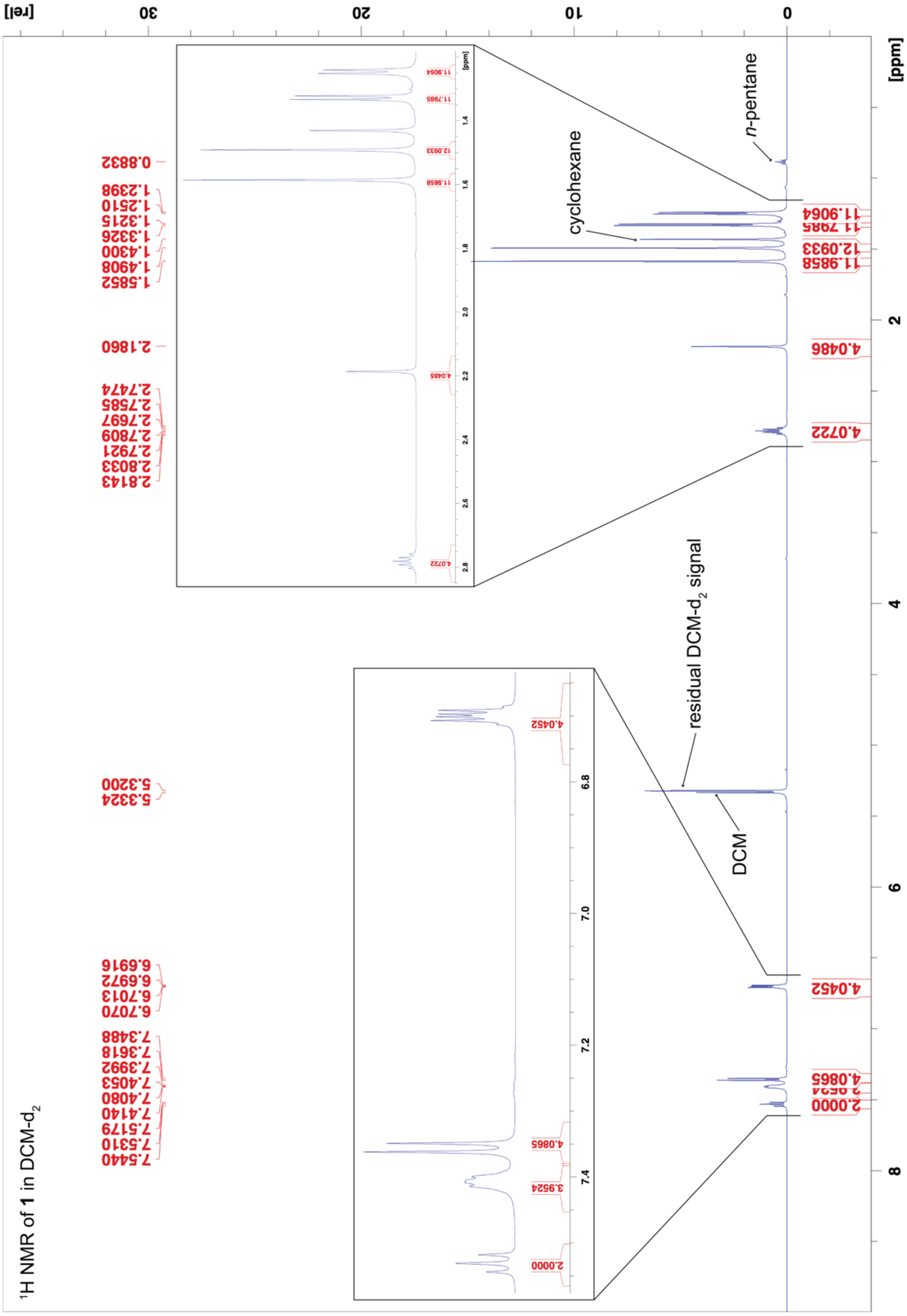

Figure S1. ^{1}H NMR spectrum of **Zn1** in DCM-d_2. The residual molecules of cyclohexane and *n*-pentane are impurities presented in deuterated solvents while DCM is a crystal solvent presented in crystal lattice, which was evidenced by X-ray diffraction and elemental analysis.

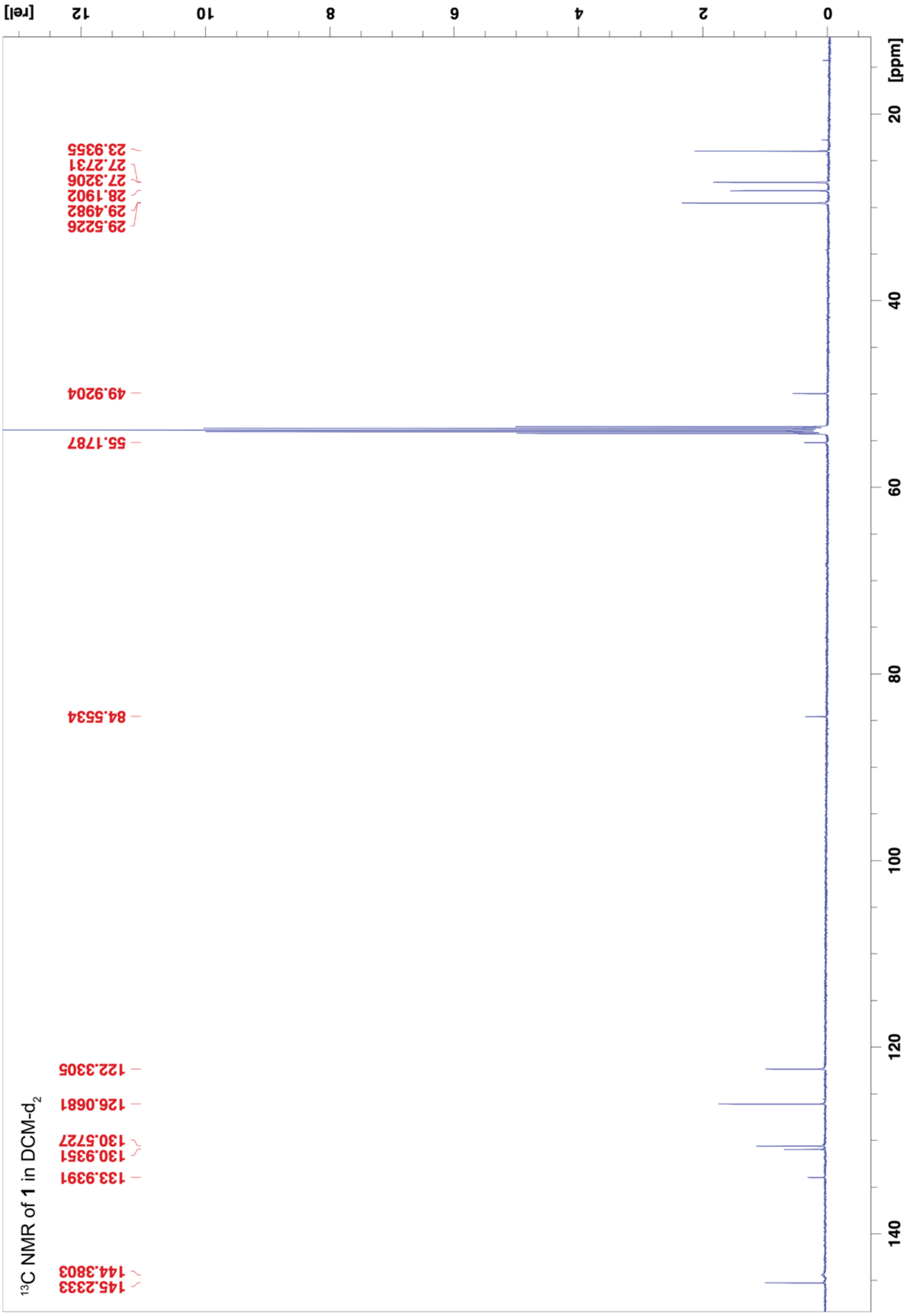

Figure S2. ^{13}C NMR spectrum of **Zn1** in DCM-d_2.

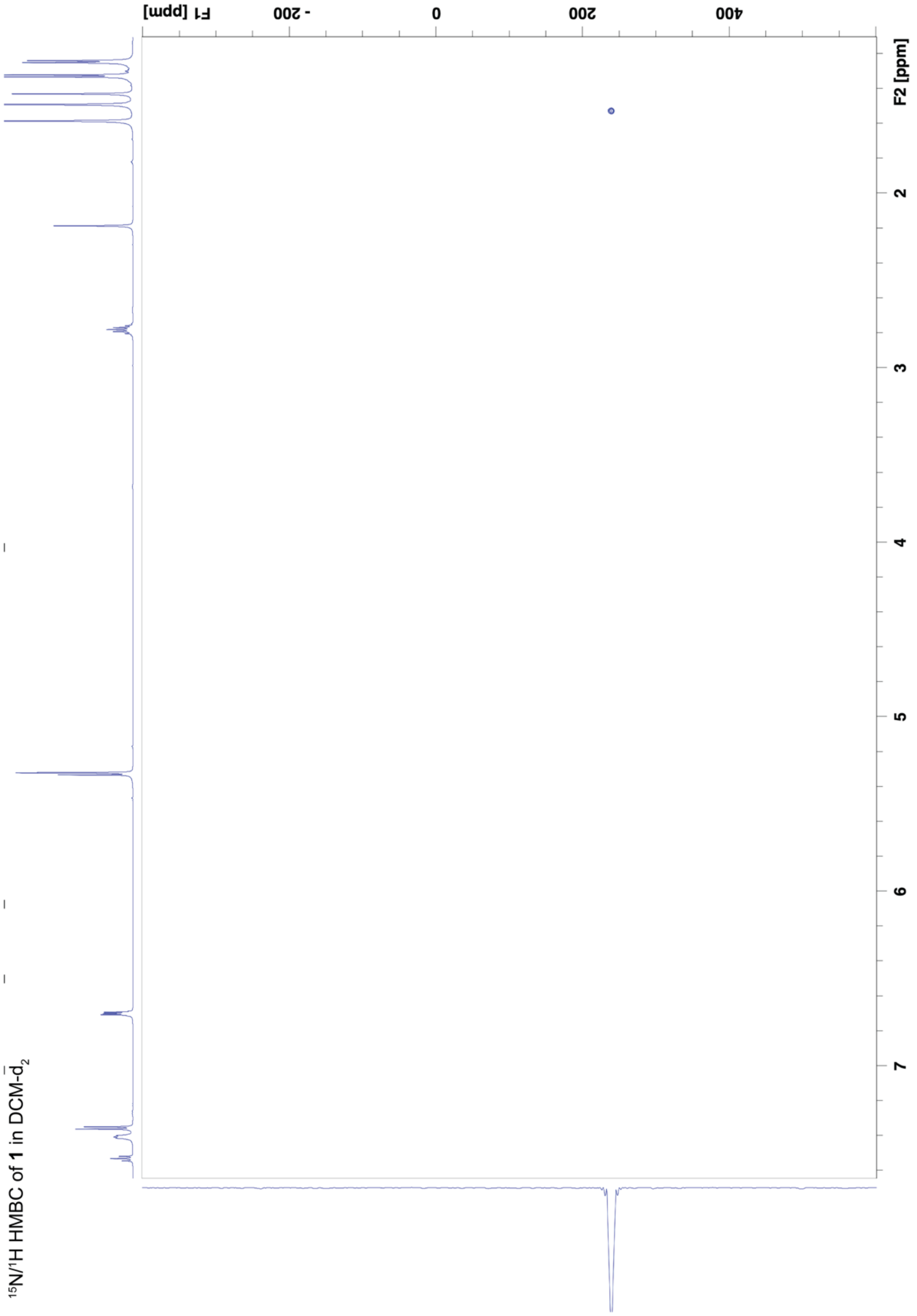

Figure S3. $^{15}N/^{1}H$ HMBC spectrum of **Zn1** in DCM-d_2. δ = 239.9 ppm (NH_3 reference scale) = -141.86 ppm (CH_3NO_2 reference scale).

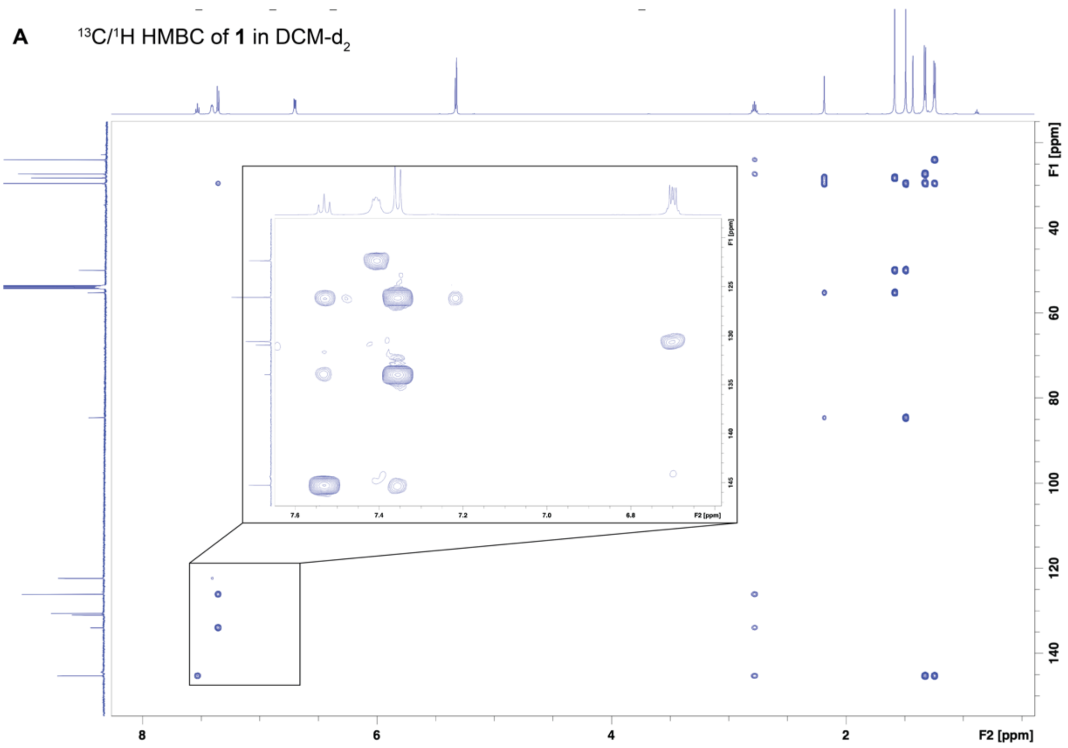

A ^{13}C/^{1}H HMBC of **1** in DCM-d_2

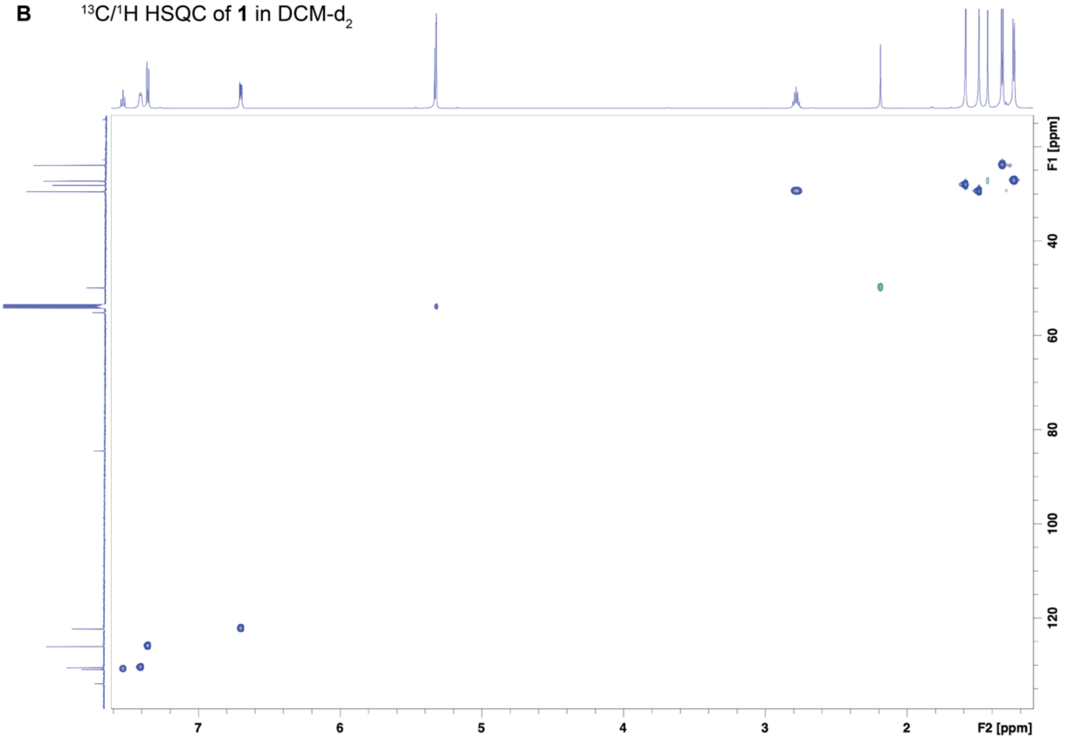

B ^{13}C/^{1}H HSQC of **1** in DCM-d_2

Figure S4. ^{13}C/^{1}H HMBC (**A**) and ^{13}C/^{1}H HSQC (**B**) spectra of **Zn1** in DCM-d_2.

Thermogravimetry analysis

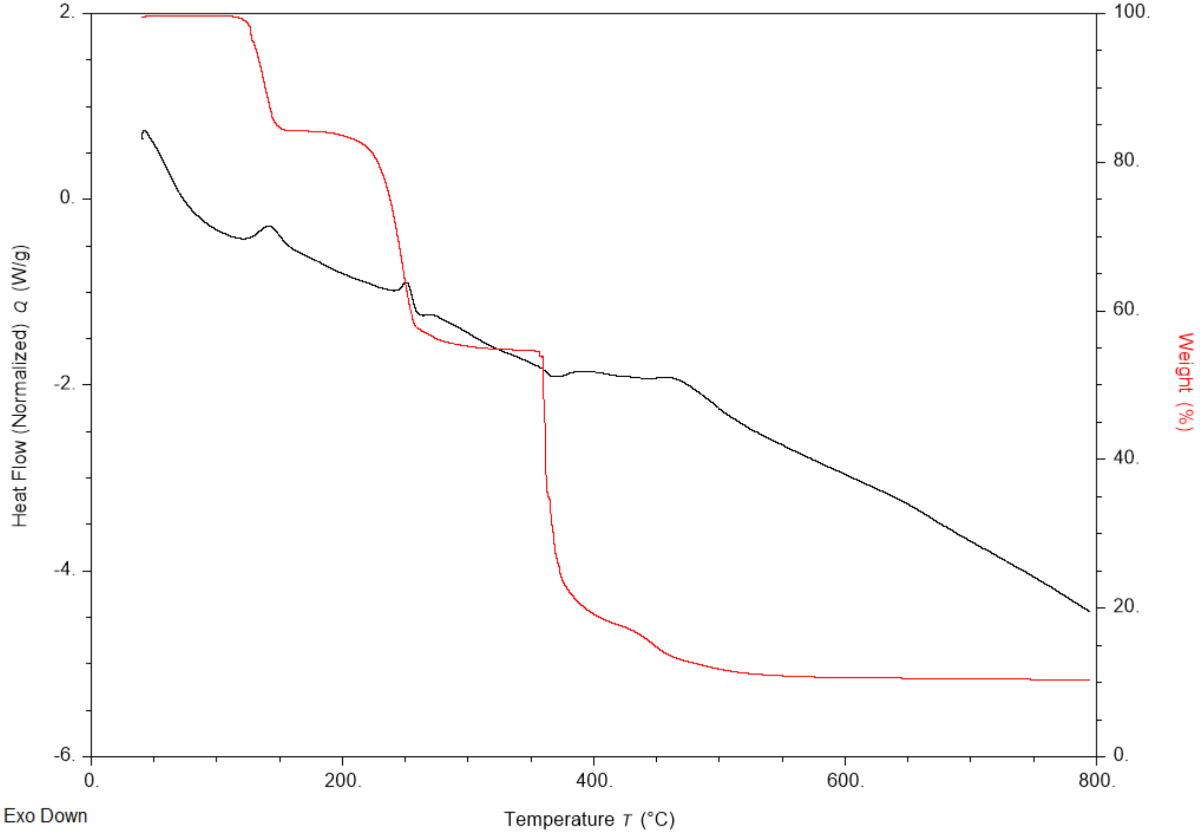

Figure S5. TGA/DSC data for compound **Zn1** in single crystalline form.

Stability Towards Water and Oxygen

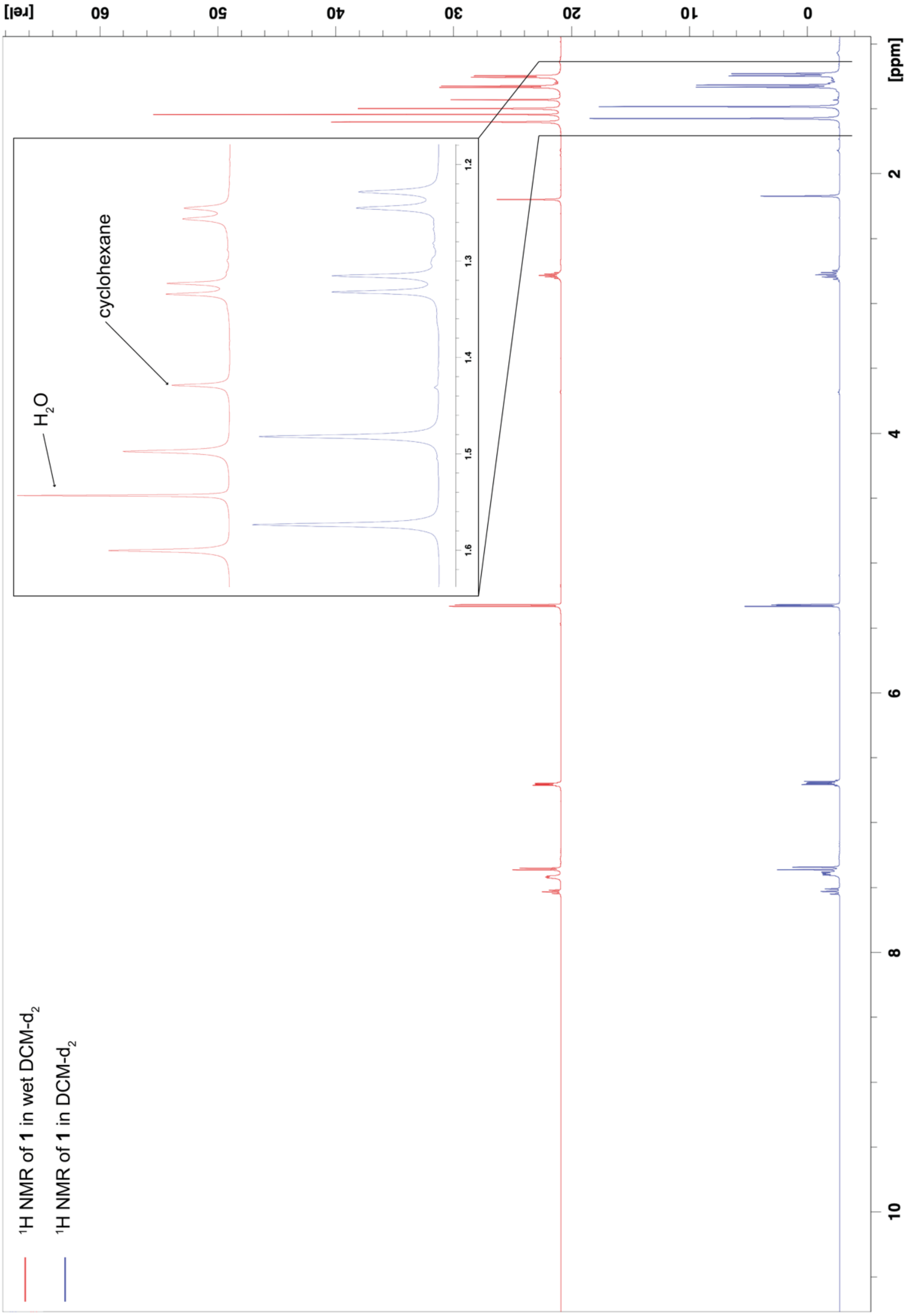

Figure S6. ^{1}H NMR spectra of **Zn1** in wet (red) and dry/degassed (blue) DCM-d$_2$. Spectra, showing no formation of protonated ^{Me}cAAC or bdt species, were recorded after four hours of dissolution of complex in wet, air-saturated solvent.

X-ray Crystallography

The crystals of **Zn1** were immersed in a film of NVH or perfluoropolyether oil, mounted on a polyimide microloop (MicroMounts of MiTeGen) and transferred to stream of cold nitrogen (Bruker Kryoflex2), and measured at a temperature of 100 K. The X-ray diffraction data was collected on a Bruker D8 diffractometer with a CMOS Photon 100 and multilayer optics monochromated MoKα (0.71073Å) radiation (INCOATEC microfocus sealed tube). The frames were integrated with the Bruker SAINT software package using a narrow-frame algorithm. The APEX3 v2018.7-0 program package was used for cell refinements and data reductions. The structure was solved using intrinsic phasing methods,[1,2] refined and visualized with the OLEX2-1.3 program.[3] A semiempirical absorption correction (SADABS) was applied to all data. All non-hydrogen atoms were refined anisotropically. Hydrogen atoms were included in structure factors calculations. All Hydrogen atoms were assigned to idealised geometric positions. The unit cell of the 1 contains disordered solvent molecules of dichloromethane which has been treated as a diffuse contribution to the overall scattering without specific atom positions by SQUEEZE/PLATON.[4] The crystallographic details are summarized in Table 1. CCDC 2189606 contain the supplementary crystallographic data for this paper.

Table S1. Crystal data and structure refinement for **Zn1**.

Identification code	**Zn1**
CCDC number	**2189606**
Empirical formula	$C_{52}H_{70}N_2S_4Zn_2$
Formula weight	982.08
Temperature/K	100.0
Crystal system	triclinic
Space group	P-1
a/Å b/Å c/Å α/° β/° γ/°	10.4251(2) 11.4928(3) 12.4597(3) 104.1850(10) 91.9470(10) 96.1930(10)
Volume/Å^3	1436.05(6)
Z	1
ρ_{calc}g/cm^3	1.136
μ/mm^{-1}	1.012
F(000)	520.0
Crystal size/mm^3	0.307 × 0.156 × 0.14
Radiation	MoKα (λ = 0.71073)
2Θ range for data collection/°	5.058 to 51.998
Index ranges	$-12 \leq h \leq 12$, $-14 \leq k \leq 14$, $-14 \leq l \leq 15$
Reflections collected	29910
Independent reflections	5624 [R_{int} = 0.0234, R_{sigma} = 0.0168]
Data/restraints/parameters	5624/0/279
Goodness-of-fit on F^2	1.059
Final R indexes [I>=2σ (I)]	R_1 = 0.0235, wR_2 = 0.0642
Final R indexes [all data]	R_1 = 0.0246, wR_2 = 0.0650
Largest diff. peak/hole / e Å^{-3}	0.33/-0.42

(a) $R_1 = \sum||F_o|-|F_c||/\sum|F_o|$; $wR_2 = [\sum[w(F_o^2-F_c^2)^2/\sum[(wF_o^2)^2]]^{1/2}$; $w = 1/[\sigma^2(F_o^2)+(aP)^2+bP]$, where $P = (F_o^2+2F_c^2)/3$

(b) GooF = $S = [[\sum w(F_o^2-F_c^2)^2]/(m-n)]^{1/2}$, where m = number of reflexes and n = number of parameters

216

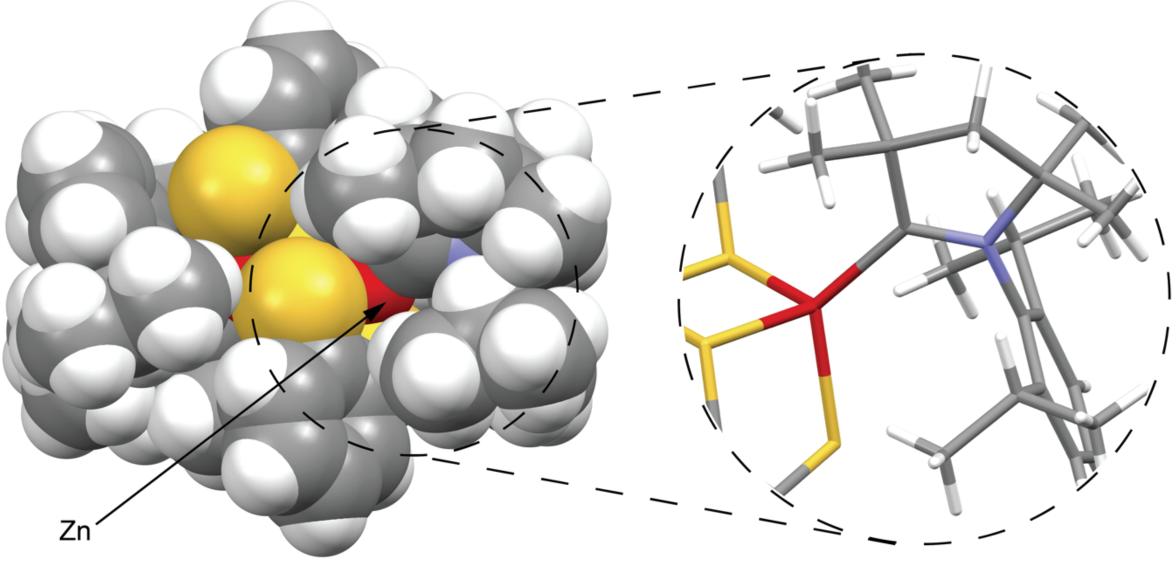

Figure S7. Space-filling showing steric protection of Zn–C^{carbene} bond.

Cyclic Voltammetry

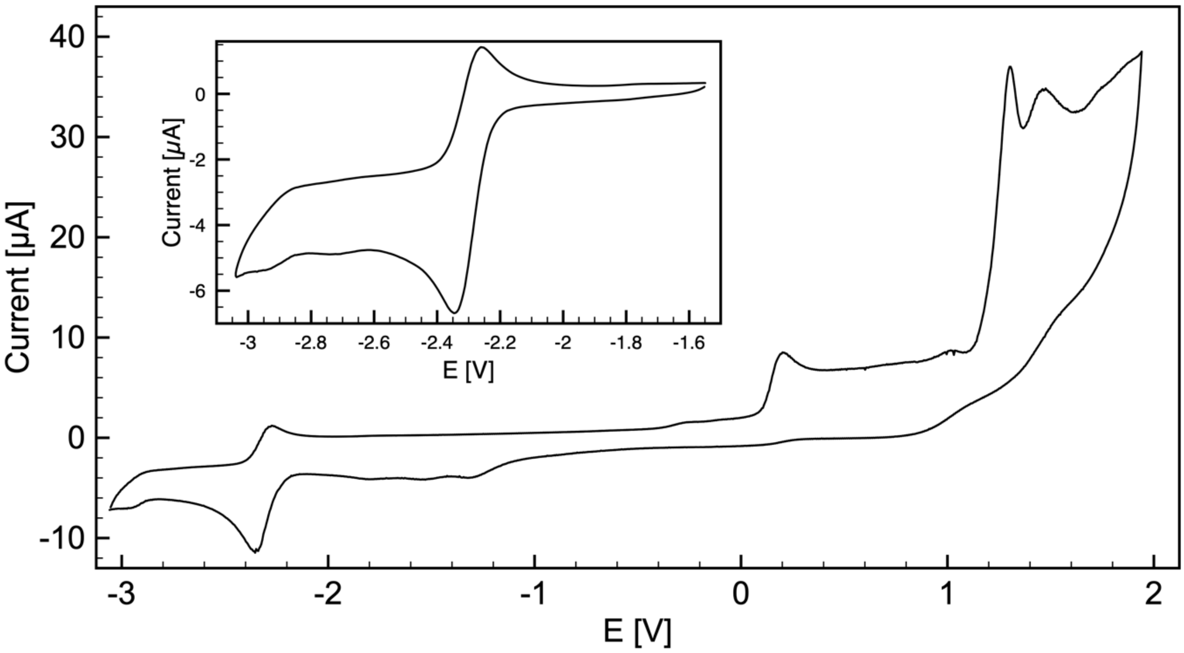

Figure S8. Cyclic voltammetry of **Zn1** in CH_3CN using ferrocene/ferrocenium couple as a reference (scan rate 100 mV/s, 100 mM $^{n}Bu_4NBF_4$, Pt-disk working electrode). Inset: detail of reversible reduction.

Photophysical Measurements

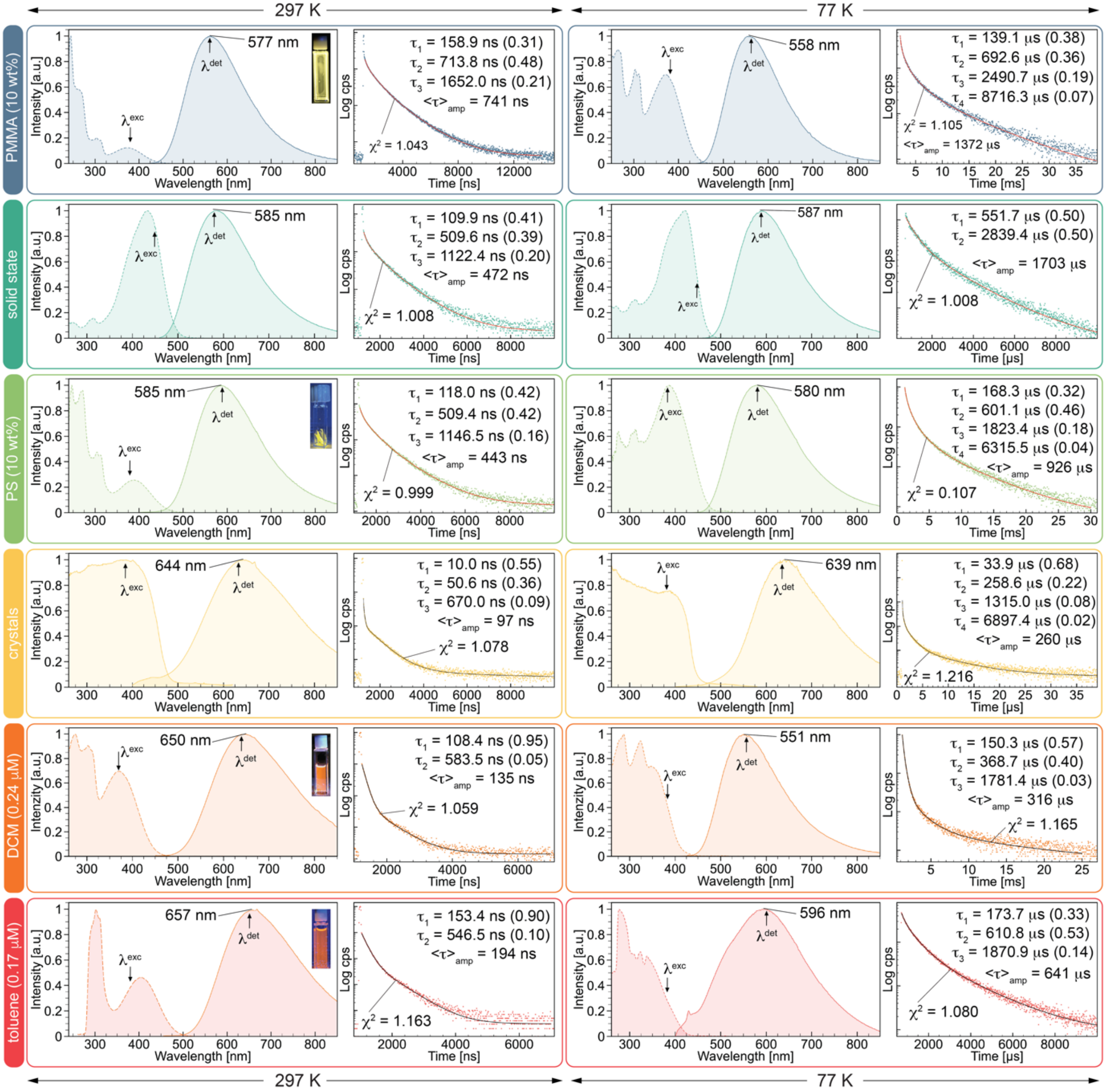

Figure S9. Summary of photophysical data of **Zn1** in different media.

Emission and Excitation Spectra at 297 and 77 K.

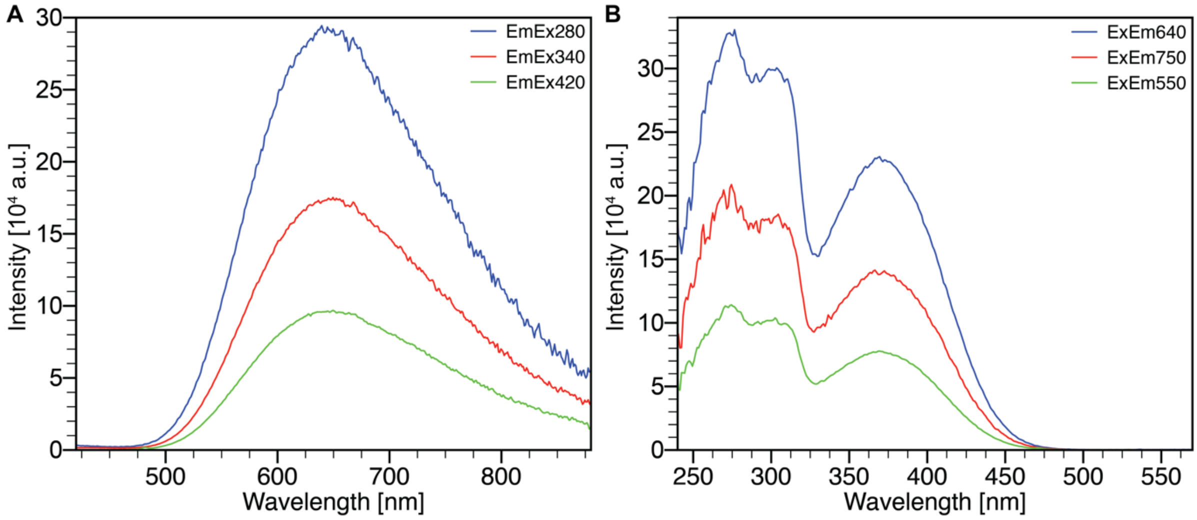

Figure S10. Emission (**A**) and excitation maps (**B**) of **Zn1** in DCM (2.4 × 10^{-5} M) at 297K.

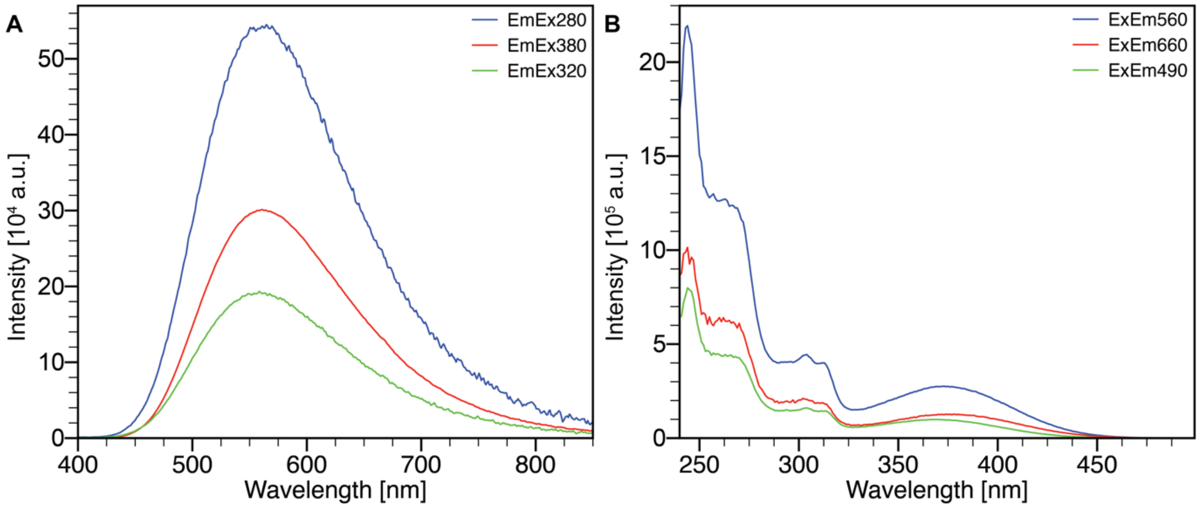

Figure S11. Emission (**A**) and excitation map (**B**) of **Zn1** in PMMA matrix (10wt%) at 297K.

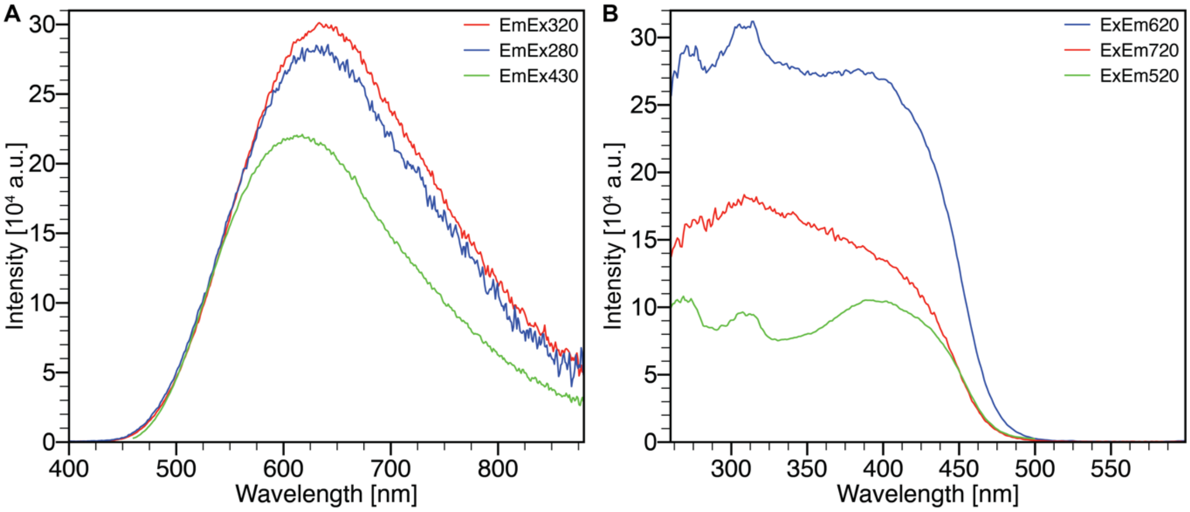

Figure S12. Emission (**A**) and excitation map (**B**) of **Zn1** in solid state at 297K.

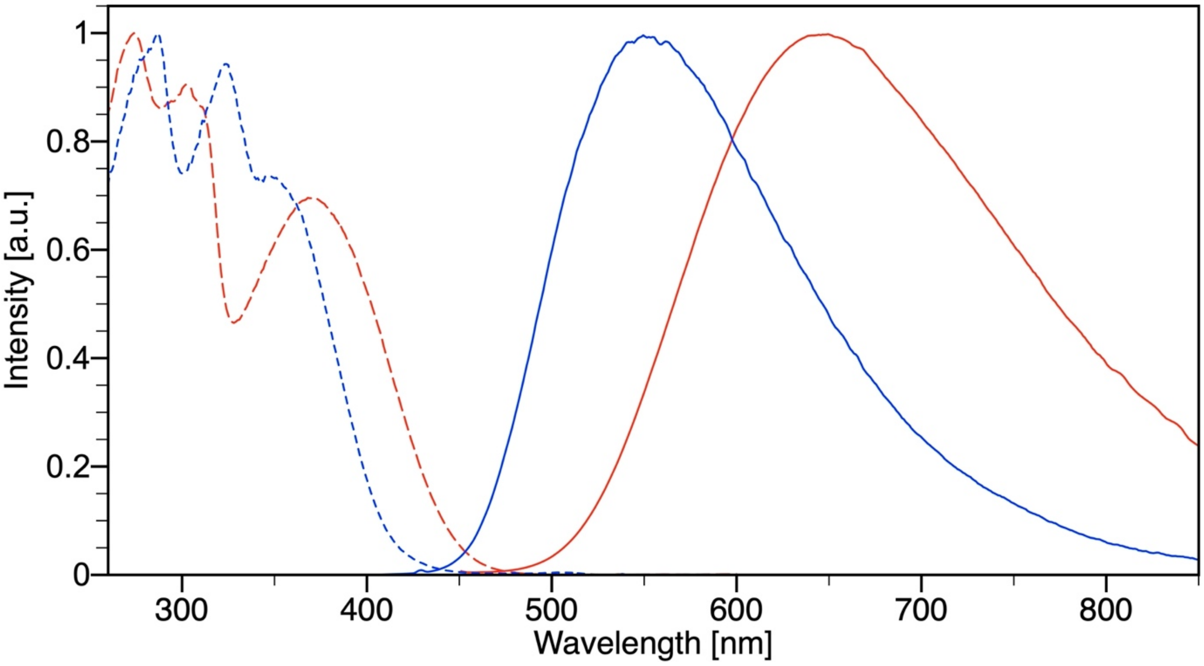

Figure S13. Comparison of emission and excitation profiles on **Zn1** in DCM at 297K (red) and 77K (blue).

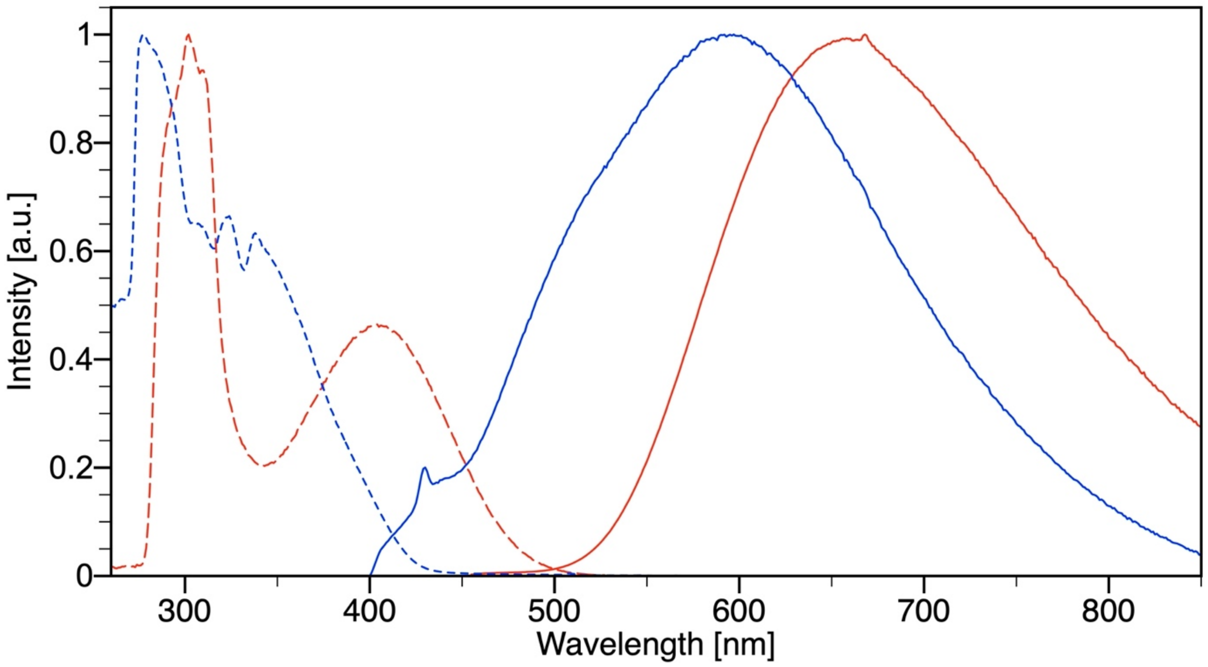

Figure S14. Comparison of emission and excitation profiles on **Zn1** in toluene at 297K (red) and 77K (blue).

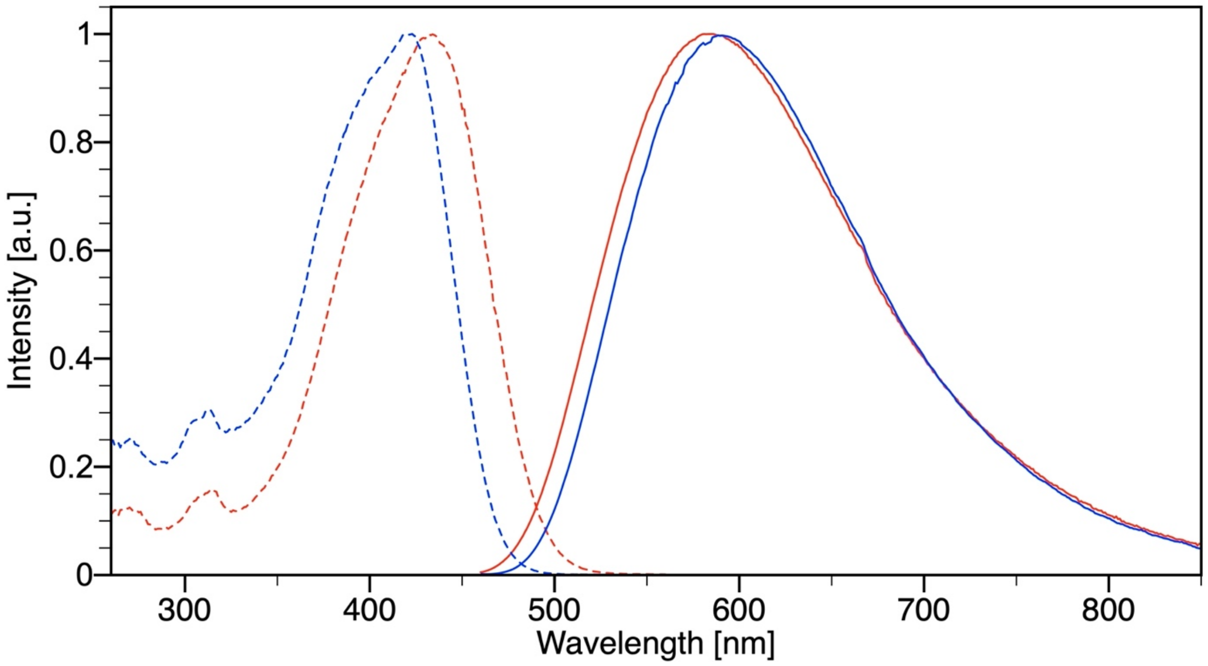

Figure S15. Comparison of emission and excitation profiles on **Zn1** in solid-state at 297K (red) and 77K (blue).

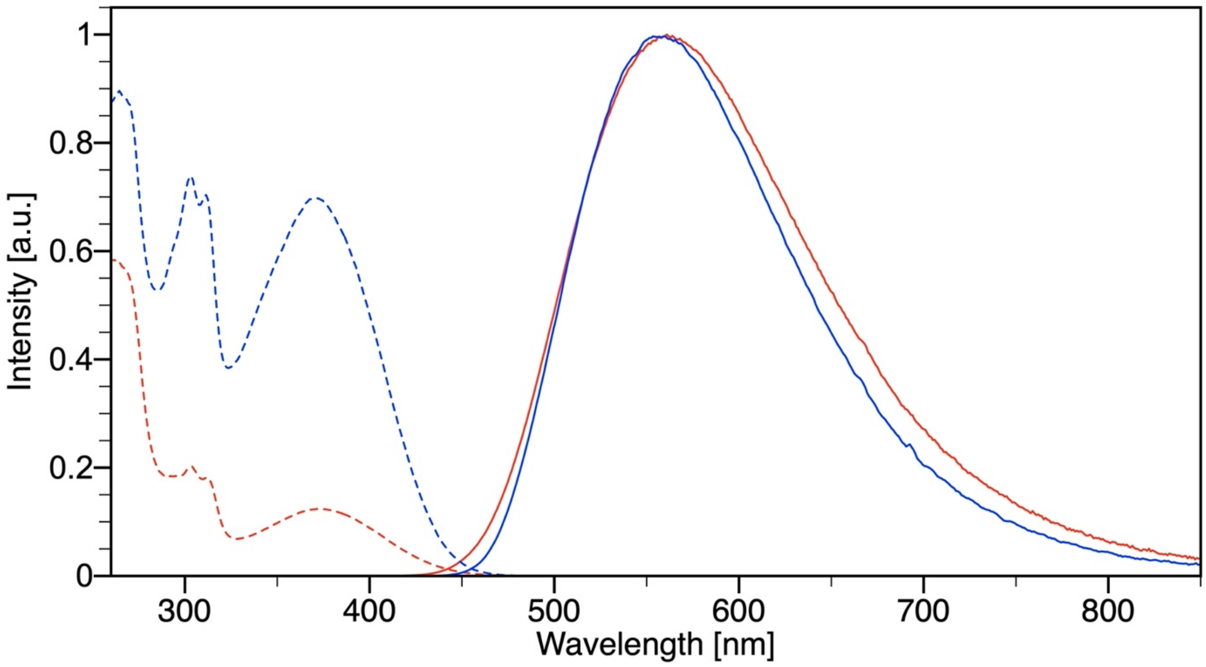

Figure S16. Comparison of emission and excitation profiles on **Zn1** in PMMA (10 wt%) at 297K (red) and 77K (blue).

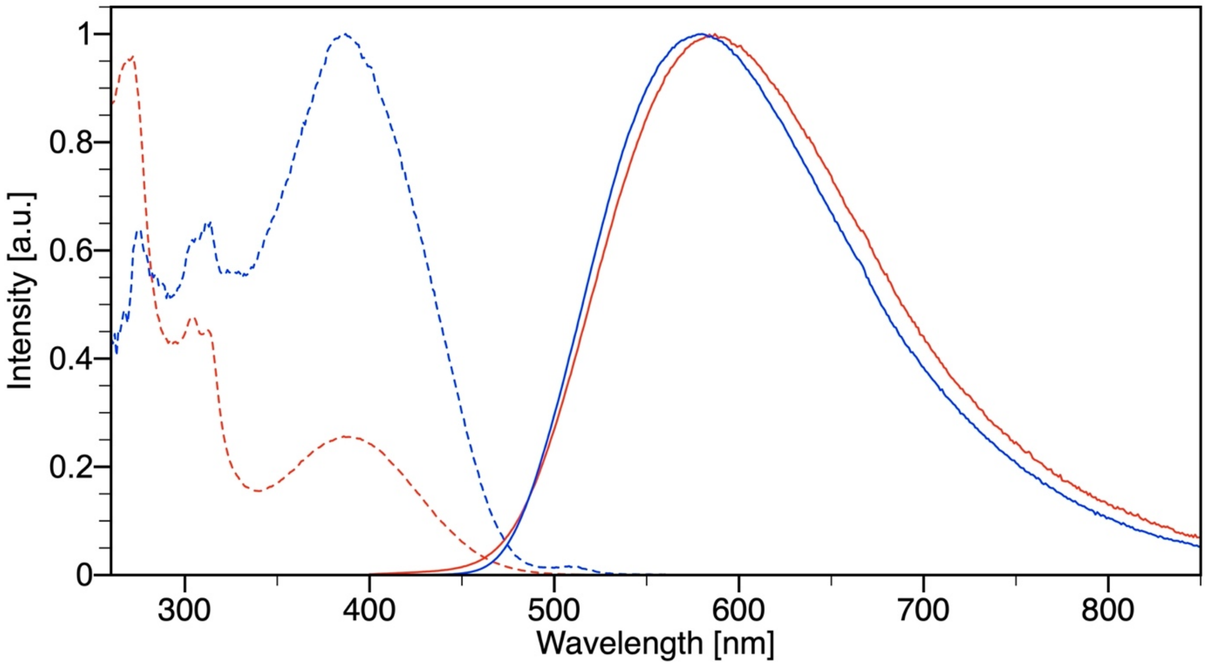

Figure S17. Comparison of emission and excitation profiles on **Zn1** in PS (10 wt%) at 297K (red) and 77K (blue).

Lifetime Measurements at room temperature

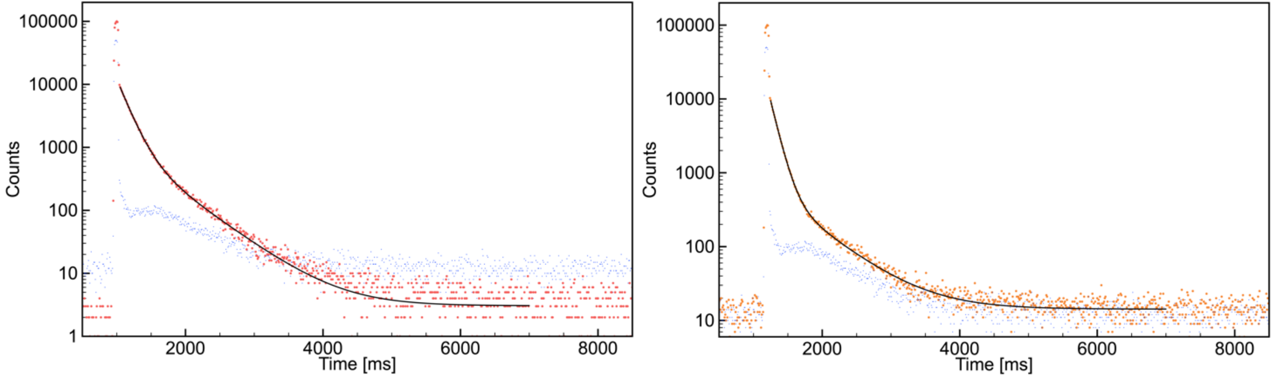

Figure S18. Luminescence decay and IRF (blue dots) obtained for **Zn1** in DCM (blue dots, 2.4 × 10^{-5} M) and toluene (orange dots, 1.7 × 10^{-5} M) solution at room temperature after 450 nm excitation (VPL) and biexponential fits (DCM: red curve, χ^2 = 1.059; toluene: black curve, χ^2 = 1.163) of the data.

Table S2 Parameters of biexponential fit of photoluminescence decay of **Zn1** in DCM.

	LT [ns]	**pre-exponential factors**	**Rel. %**	**<τ>$_{amp}$ [ns]**	**<τ>$_{int}$ [ns]**
		DCM solution			
τ_1	108.4±0.7	9726.4	76.01	134.8±1.1	222.4±4.3
τ_2	583.5±9.1	570.6	23.99		
		Toluene solution			
τ_1	153.4±1.2	8556.8	70.69	194.38±1.7	268.6±3.9
τ_2	546.5±6.8	995.9	29.31		

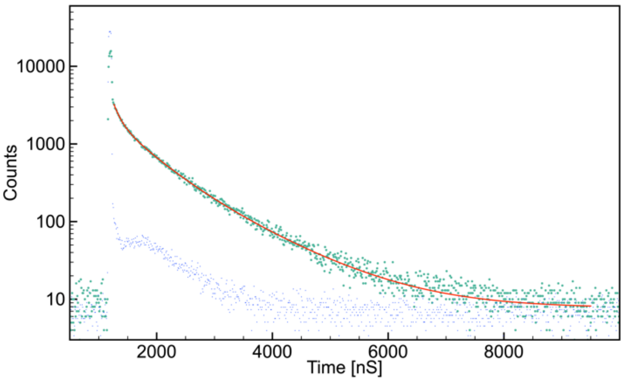

Figure S19. Luminescence decay and IRF (blue dots) obtained for **Zn1** in solid state (green dots) at room temperature after 450 nm excitation (VPL) and triexponential fit (black curve, χ^2 = 1.008).

Table S3 Parameters of triexponential fit of photoluminescence decay of **Zn1** in solid state.

	LT [ns]	**pre-exponential factors**	**Rel. %**	**<τ>$_{amp}$ [ns]**	**<τ>$_{int}$ [ns]**
τ_1	109.9±7.7	1375.5	9.44		
τ_2	509.6±38.0	1325.9	42.2	472.4±27.9	768.5±41.9
τ_3	1122.4±48.7	691.1	48.4		

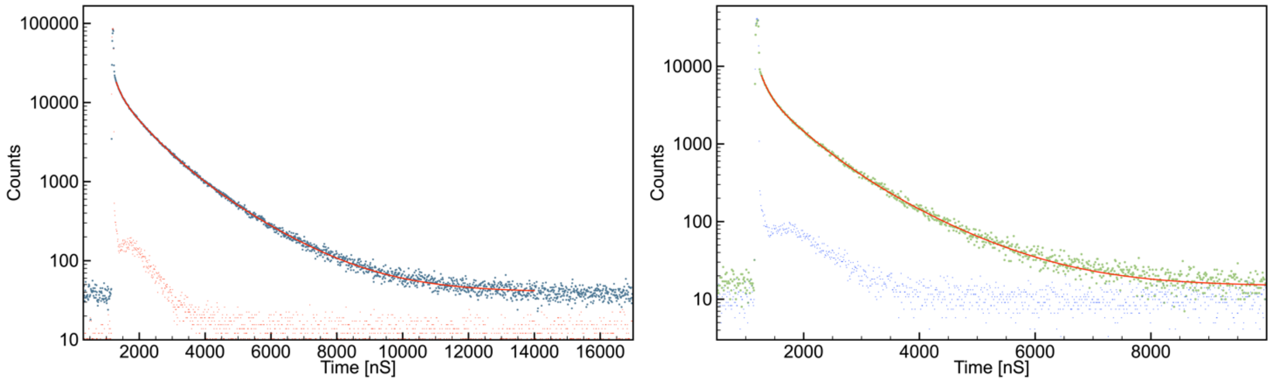

Figure S20. Luminescence decay obtained for **Zn1** in PMMA (blue dots, 10 wt%) and PS (green dots, 10 wt%) with IRF (red and blue dots, respectively) at room temperature after 380 nm excitation (VPLED) and triexponential fit (PMMA: black curve, χ^2 = 1.043, PS black curve, χ^2 = 0.999).

Table S4 Parameters of biexponential fit of photoluminescence decay of **Zn1** in PMMA and PS matrix (10 wt%).

	LT [ns]	**pre-exponential factors**	**Rel. %**	**<τ>$_{amp}$ [ns]**	**<τ>$_{int}$ [ns]**
		PMMA			
τ_1	158.9±5.4	5678.6	6.57		
τ_2	713.8±14.5	8936.6	46.46	741.4±12.4	1117.9±17.3
τ_3	1652.0±20.9	3902.7	46.96		
		PS			
τ_1	118.0±5.1	3364.7	11.25		
τ_2	509.4±21.2	3344.6	48.24	443.86±16.5	723.5±27.9
τ_3	1146.5±35.6	1248.1	40.52		

Lifetime Measurements at 77K

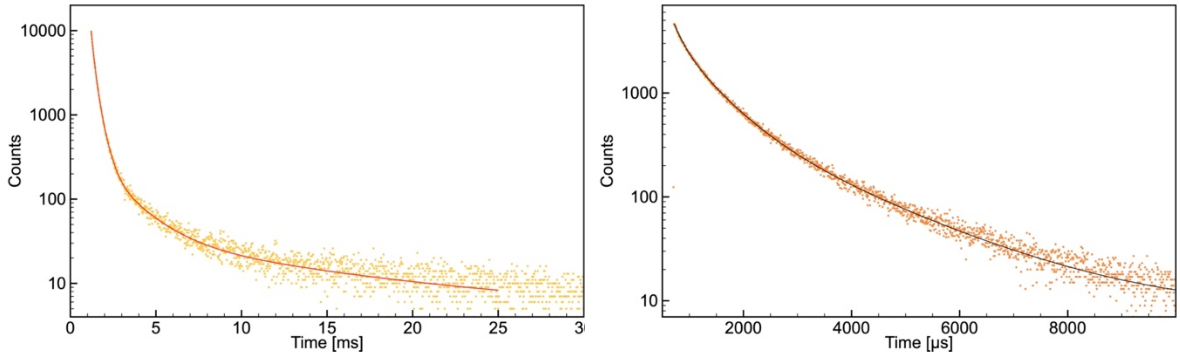

Figure S21. Luminescence decay obtained for **1** in DCM (blue dots, 2.4 × 10^{-5} M) and toluene (orange dots, 1.7 × 10^{-5} M) at 77 K after 380 nm excitation (VPL) and biexponential fits (DCM: red curve, χ^2 = 1.165; toluene: black curve, χ^2 = 1.163) of the data.

Table S5 Parameters of fit of photoluminescence decay of **Zn1** in DCM and toluene, respectively.

	LT [µs]	**pre-exponential factors**	**Rel. %**	**$<\tau>_{amp}$ [µs]**	**$<\tau>_{int}$ [µs]**
		DCM			
τ_1	150.3±4.0	5682.6	26.94	316.5±8.8	1707.0±360.1
τ_2	368.7±8.9	4033.7	46.94		
τ_3	1781.4±83.6	260.9	14.67		
τ_4	10769.7±1645.7	44.7	11.44		
		Toluene			
τ_1	173.7±4.4	1537.4	9.06	641.2±8.4	1086.5±16.5
τ_2	610.8±8.8	2413.4	50.04		
τ_3	1870.9±23.0	644.1	40.09		

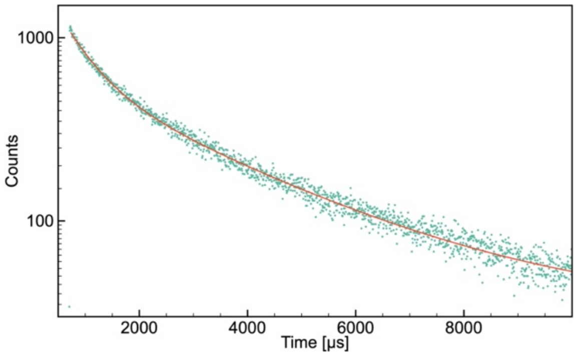

Figure S22. Luminescence decay obtained for **Zn1** in solid state (green dots) at room temperature after 450 nm excitation (VPL) and triexponential fit (red curve, χ^2 = 1.063).

Table S6 Parameters of biexponential fit of photoluminescence decay of **Zn1** in solid state.

	LT [ns]	**pre-exponential factors**	**Rel. %**	**<τ>$_{amp}$ [ns]**	**<τ>$_{int}$ [ns]**
τ_1	551.7±8.4	513.1	16.08	1703.4±16.1	2471.5±26.5
τ_2	2839.4±27.4	520.2	83.9		

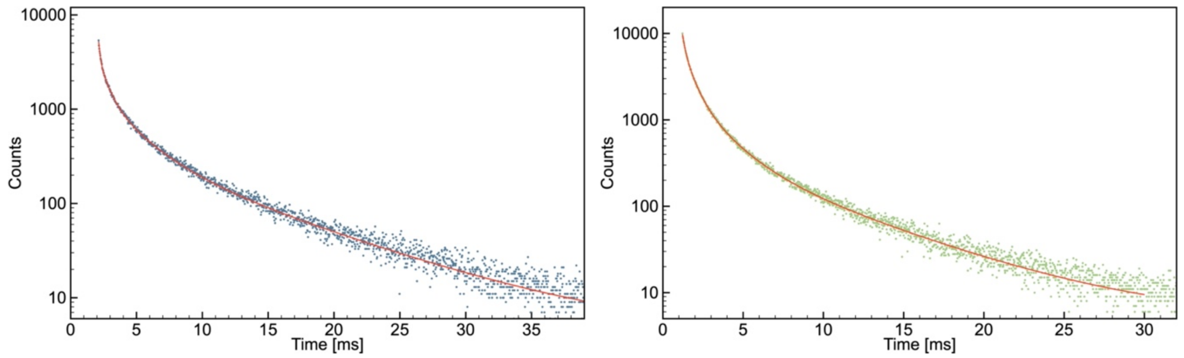

Figure S23. Luminescence decay obtained for **Zn1** in PMMA (blue dots, 10 wt%) and PS (green dots, 10 wt%) at 77K after 380 nm excitation (VPLED) and fit (PMMA: black curve, χ^2 = 1.043, PS black curve, χ^2 = 0.999).

Table S7 Parameters of multiexponential fit of photoluminescence decay of **Zn1** in PMMA and PS matrix (10 wt%).

	LT [ns]	**pre-exponential factors**	**Rel. %**	**<τ>$_{amp}$ [ns]**	**<τ>$_{int}$ [ns]**
		PMMA			
τ_1	139.1±5.2	1973.2	3.80	1372.1±27.9	4723.0±107.6
τ_2	692.6±21.8	1914.4	18.37		
τ_3	2490.7±67.3	1021.4	35.24		
τ_4	8716.3±141.7	352.8	42.60		
		PS			
τ_1	168.3±7.1	3090.8	11.25	926.74±20.3	2650.4±71.5
τ_2	601.1±18.1	4529,0	48.24		
τ_3	1823.4±52.8	1778.8	40.52		
τ_4	6315.5±117.9	412.7	40.52		

Photostability

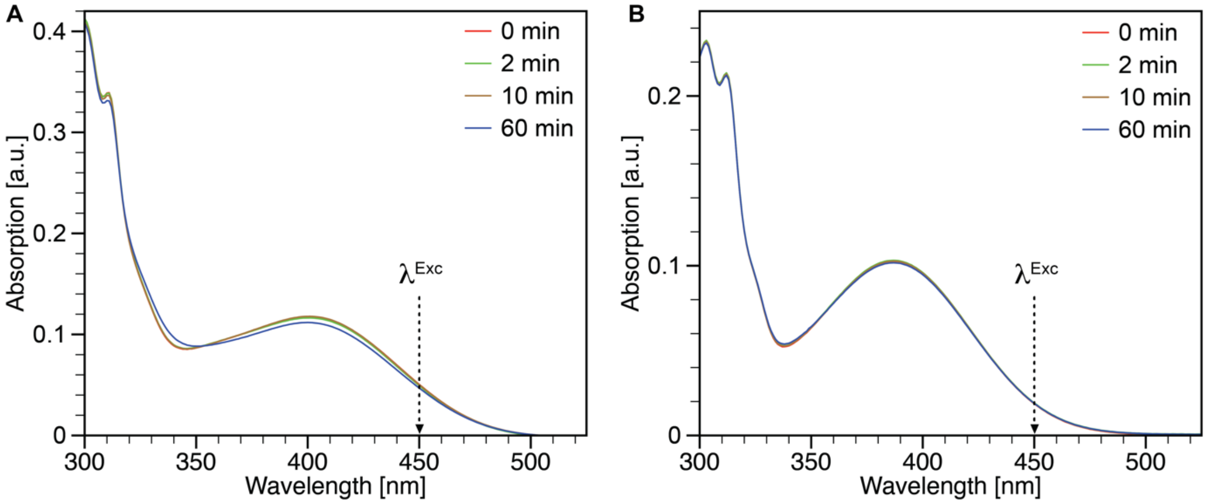

Figure S24. Photostability of **Zn1** under continuous 450 nm irradiation (18W EvoluChem™ LED) in various solvents. **A**: toluene (1.7 × 10^{-5} M), B: THF (3.6 × 10^{-5} M). Absorbance monitored at 402 (toluene) and 387 nm (THF): the 96% and 99% of original absorbance after 1 hour of irradiation in toluene and THF, respectively, showing excellent photostability of **Zn1** for photocatalytic application.

Photo-isomerization of (*E*)-stilbene

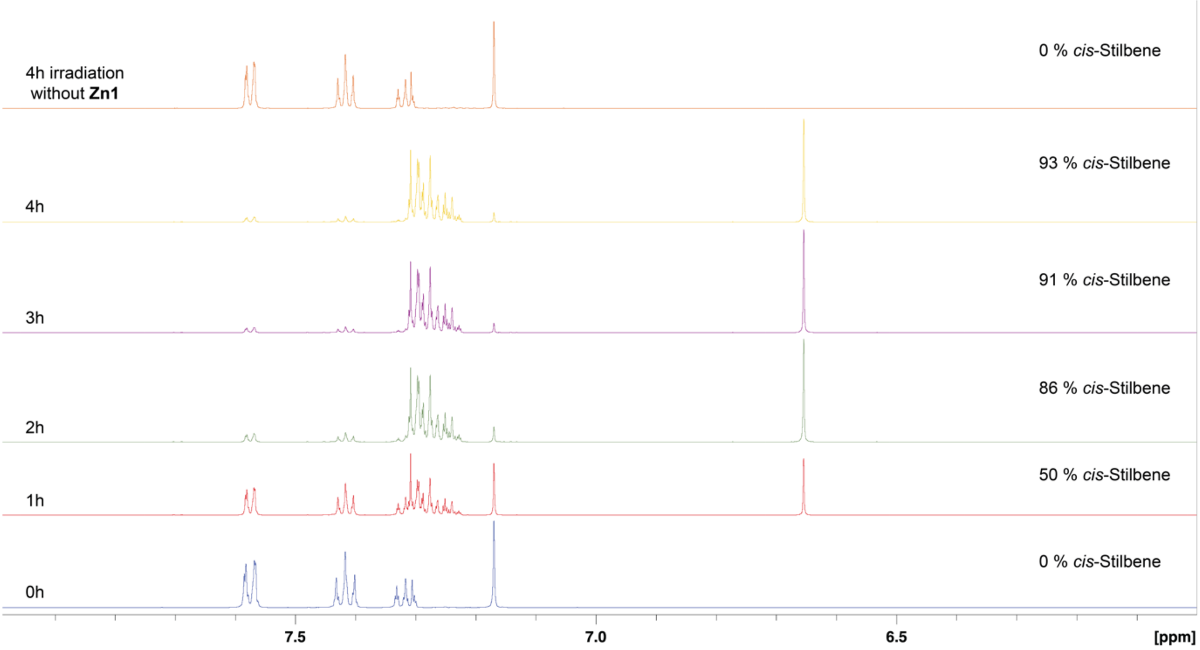

Figure S25. Photo-induced isomerization (*E*)-stilbene → (*Z*)-stilbene monitored by ^{1}H NMR spectroscopy using toluene-d$_8$ solution containing 2 mM of **Zn1** and 50 mM of (*E*)-stilbene. Irradiation source: 450 nm, 18W EvoluChem™ LED. Top (orange) spectrum: reference experiment using identical condition but without **Zn1** photocatalyst

Computational Methods and Technical Details

For all geometry optimizations the Gaussian 16 program was used.[5] The ground state geometries were optimized with Kohn-Sham density functional theory (DFT).[6] For the optimization of the singlet excited state geometries the time dependent DFT (TDDFT)[7] was used and for the excited triplet state geometries the Tamm-Dancoff approximation (TDA)[8] to TDDFT was chosen. The 10-mdf 6s5p3d basis set with defpp-ecp was used for the zinc atoms[9] and for sulfur the def2-SVPD basis was chosen.[10] For all other atoms the def-SV(P) basis set was used.[10] As functional BH-LYP functional was chosen for all calculations.[11,12] A THF environment was mimicked via the polarizable continuum model (PCM).[13,14] To examine the excitation energies and oscillator strengths of the spin allowed transitions DFT/MRCI calculations, were carried out.[15,16] As Hamiltonian the redesigned R2018 was selected and 30 singlet and 30 triplet roots were calculated. For the DFT/MRCI calculations, the point charges of the Gaussian 16 calculations were extracted. With the SPOCK program the spin-orbit coupling matrix elements (SOCMEs) were obtained.[17,18]

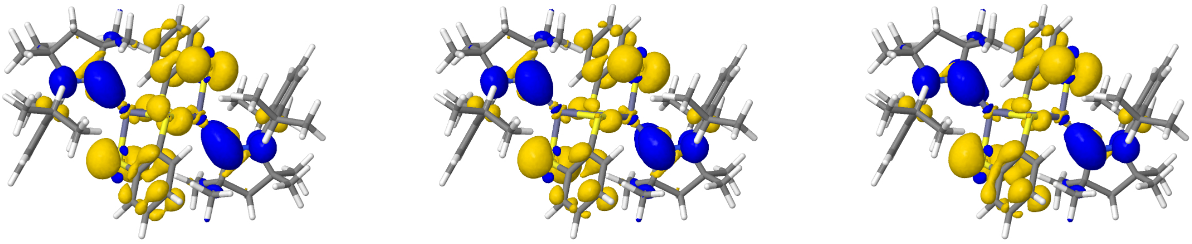

S_1, 380 nm
f(L) = 0.00

S_2, 364 nm
f(L) = 0.02

S_3, 339 nm
f(L) = 0.05

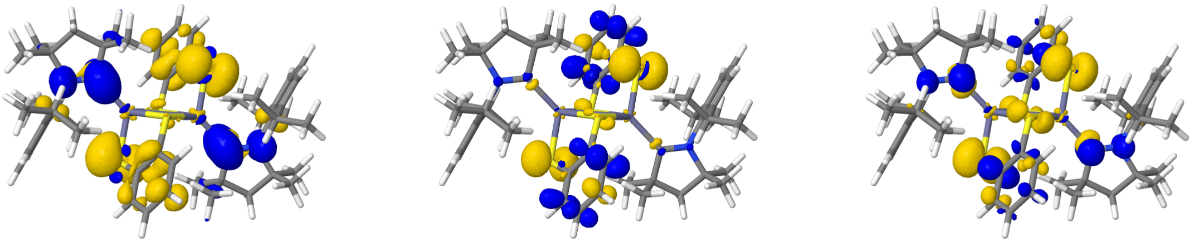

S_4, 329 nm
f(L) = 0.00

S_5, 301 nm
f(L) = 0.06

S_{12}, 276 nm
f(L) = 0.12

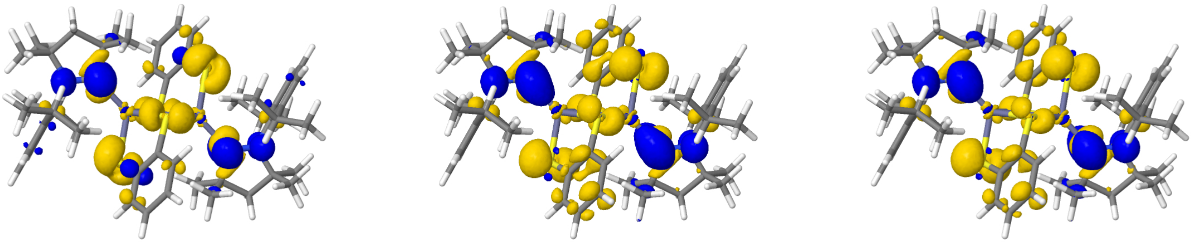

S_{14}, 272 nm
f(L) = 0.18

T_1, 394 nm

T_2, 381 nm

Figure S26: DFT/MRCI difference densities, excitation energies and oscillator strengths of the relevant excitations of complex **Zn1** in THF at the optimized S_0 geometry. Areas losing electron density upon electronic excitation from the ground-state are shown in gold, areas gaining electron density in blue.

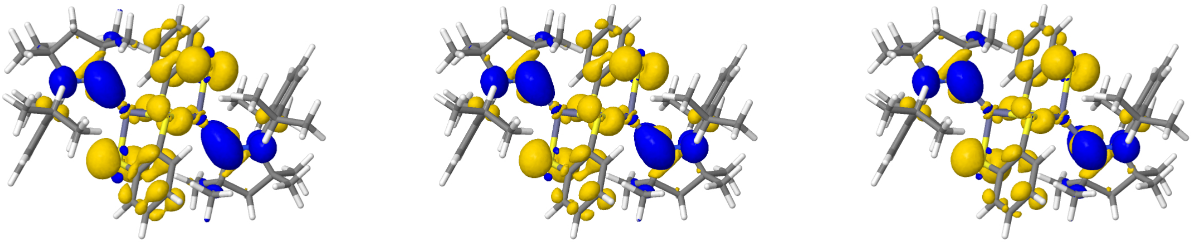

S_1 @ S_0 T_1 @ S_0 T_2 @ S_0

Figure S27: DFT/MRCI difference densities of the S_1, T_1 and T_2 state of complex **Zn1** in THF at the optimized S_0 geometry. For color codes, see Figure S26.

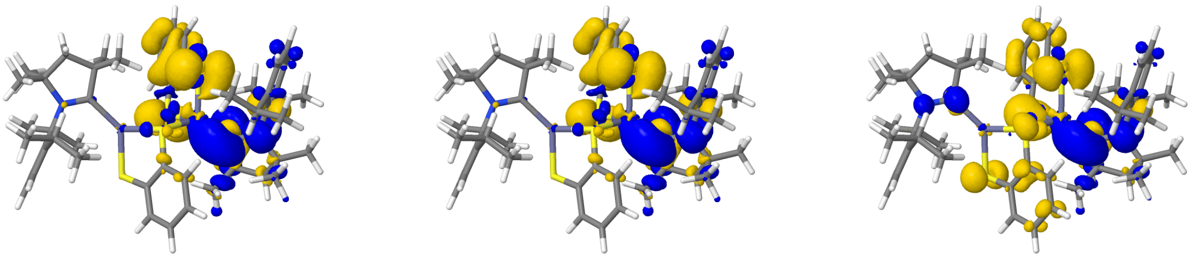

S_1 @ S_{LLCT} T_1 @ S_{LLCT} T_2 @ S_{LLCT}

Figure S28: DFT/MRCI difference densities of the S_1, T_1 and T_2 state of complex **Zn1** in THF at the optimized S_{LLCT} geometry. For color codes, see Figure S26.

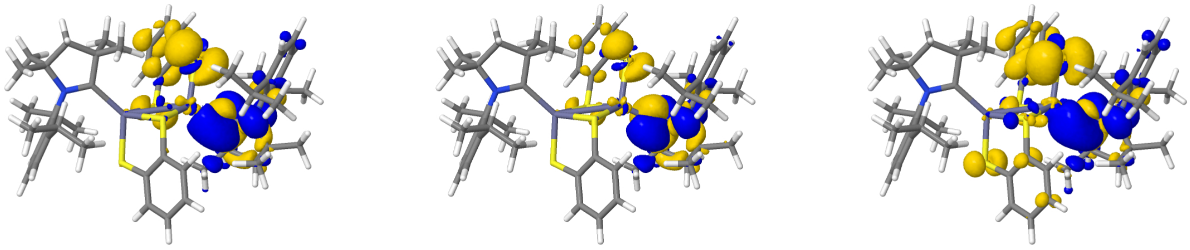

S_1 @ S_{LLCT} T_1 @ S_{LLCT} T_2 @ S_{LLCT}

Figure S29: DFT/MRCI difference densities of the S_1, T_1 and T_2 state of complex **Zn1** in THF at the optimized $T_{LL/LMCT}$ geometry. For color codes, see Figure S26.

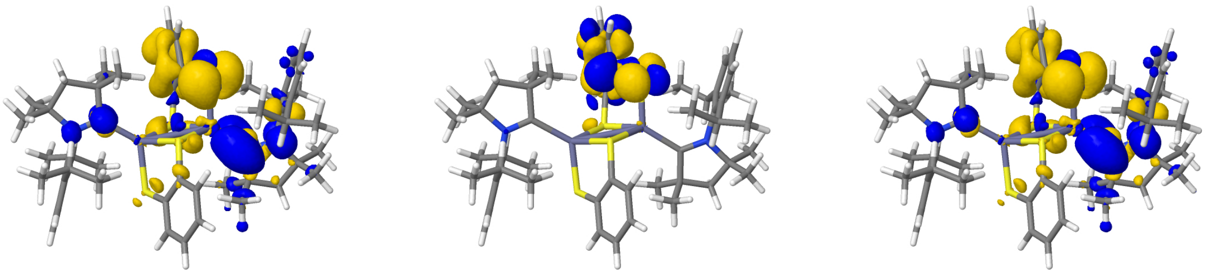

S_1 @ T_{LC} T_1 @ T_{LC} T_2 @ T_{LC}

Figure S30: DFT/MRCI difference densities of the S_1, T_1 and T_2 state of complex **Zn1** in THF at the optimized T_{LC} geometry. For color codes, see Figure S26.

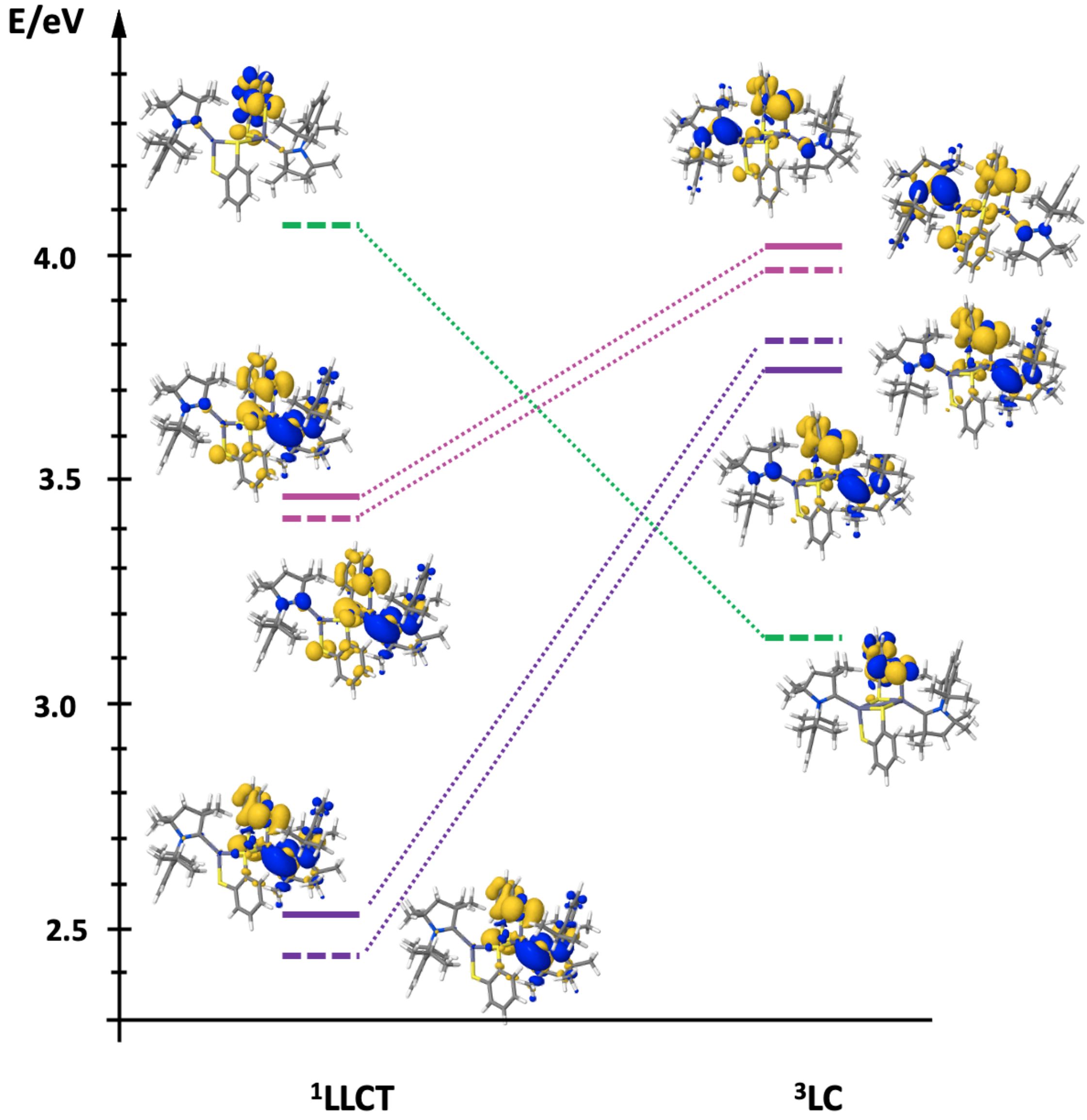

Figure S31: DFT/MRCI excitation energies and difference densities of the complex **Zn1** in THF calculated with DFT/MRCI at the optimized ^{1}LLCT and ^{3}LC geometries. The DFT/MRCI energy of the S_0 state at the DFT-optimized S_0 minimum geometry in a polarizable THF environment serves as common origin. Dashed lines represent triplet states and solid lines represent singlet states. The following color codes have been used: violet and pink LLCT ($\pi_{\mathrm{dtb}} \rightarrow \pi^*_{\mathrm{carb}}$) and green LC ($\pi_{\mathrm{thiol}} \rightarrow \pi^*_{\mathrm{thiol}}$). For color codes of the difference densities, see Figure S26.

Table S8: DFT/MRCI excitation energies (ΔE/eV) of **Zn1** in THF at various molecular geometries. The DFT/MRCI energy of the S$_0$ state at the DFT-optimized S$_0$ minimum geometry in a polarizable THF environment serves as common origin. 0–0 energies including zero-point vibrational energy corrections are given in parentheses.

state	optimized geometry			
	S$_0$	S$_{\mathrm{LLCT}}$	T$_{\mathrm{LL/LMCT}}$	T$_{\mathrm{LC(thiol)}}$
S$_0$	0.00	0.70	1.21	0.80
S$_{\mathrm{LLCT}}$	3.26	2.53 (**2.45**)	3.31	3.81
S$'_{\mathrm{LLCT}}$	3.41	3.46	4.15	4.01
T$_{\mathrm{LLCT}}$	3.15	2.44	2.76 (**2.66**)	3.74
T$'_{\mathrm{LLCT}}$	3.25	3.42	4.00	3.96
T$_{\mathrm{LC(thiol)}}$	3.55	4.06	4.83	3.15 (**3.04**)
T$'_{\mathrm{LC(thiol)}}$	3.56	4.19	4.85	4.21

Table S9: SOMEs [cm^{-1}] computed at the optimized geometries.

optimized geometry	$\langle$ T$_1$| $\hat{H}_{SO}$| S$_1$ $\rangle$			$\sum$ (SOCMEs)^2
	x	y	z	
S$_{\mathrm{LLCT}}$	0.84	0.09	1.67	3.49
T$_{\mathrm{LL/LMCT}}$	-2.63	-1.77	2.60	16.79
T$_{\mathrm{LC(thiol)}}$	3.41	2.43	-6.79	63.69

Table S10: Cartesian coordinates of the optimized S$_0$ geometry of complex **Zn1**.

atom	x	y	z
Zn	3.277080	5.187227	5.375498
S	5.052022	5.584904	6.964482
S	1.739072	5.018962	7.140121
N	2.042695	7.101935	3.304992
C	0.810124	7.171588	4.064042
C	-1.378341	6.351943	4.595452

Continued on next page

Table S10: Cartesian coordinates of the optimized S_0 geometry of complex **Zn1**.

atom	x	y	z
H	-2.170353	5.622504	4.466207
C	-1.560763	7.394619	5.484417
H	-2.491235	7.484013	6.036061
C	-0.195848	6.209138	3.870705
C	4.205396	6.632268	2.674919
C	-0.542590	8.309578	5.685567
H	-0.681597	9.105677	6.408451
C	-0.064040	4.994859	2.964178
H	0.886979	5.059891	2.436402
C	0.660679	8.219788	4.992097
C	2.673573	5.749378	8.448344
C	3.710792	7.812977	1.822405
H	4.141351	8.744656	2.202618
H	4.003230	7.721673	0.773362
C	3.079251	6.411092	3.666529
C	1.755505	9.222056	5.327354
H	2.564811	9.103114	4.606977
C	4.415129	5.363106	1.840719
H	3.515200	5.065720	1.295162
H	4.721329	4.523711	2.467284
H	5.208363	5.546060	1.107354
C	2.192462	7.854217	1.985252
C	4.060162	5.993168	8.384993

Continued on next page

Table S10: Cartesian coordinates of the optimized S_0 geometry of complex **Zn1**.

atom	x	y	z
C	-0.036134	3.694806	3.772777
H	0.787513	3.678728	4.491266
H	0.091167	2.838606	3.099614
H	-0.971348	3.550038	4.325405
C	2.355774	8.942977	6.706196
H	1.601835	9.046708	7.494965
H	3.164076	9.654101	6.915087
H	2.762894	7.931536	6.770531
C	5.510306	6.975061	3.396801
H	6.267681	7.255251	2.655042
H	5.893342	6.122381	3.966306
H	5.380805	7.818605	4.083851
C	1.456561	7.117274	0.868870
H	1.787278	6.083845	0.752858
H	1.647319	7.638295	-0.074498
H	0.377684	7.123967	1.038820
C	1.273002	10.672415	5.248199
H	0.783401	10.894522	4.294888
H	2.123219	11.354982	5.361519
H	0.562653	10.902803	6.049852
C	1.996592	6.106074	9.623220
C	-1.177647	4.924856	1.915411
H	-2.149919	4.726725	2.380185

Continued on next page

Table S10: Cartesian coordinates of the optimized S_0 geometry of complex **Zn1**.

atom	x	y	z
H	-0.978773	4.108590	1.211257
H	-1.268378	5.852215	1.341470
C	4.703832	6.589527	9.472945
H	5.770424	6.779905	9.404390
C	1.656200	9.277109	2.037824
H	0.590601	9.303836	2.284126
H	1.779987	9.719960	1.044136
H	2.202085	9.903079	2.743753
C	2.649982	6.681968	10.700092
C	4.016214	6.931840	10.626484
Zn	5.484894	3.121619	6.680555
S	3.710026	2.723944	5.091603
S	7.022997	3.289808	4.915975
N	6.719237	1.206675	8.751007
C	7.951794	1.136828	7.991956
C	10.140493	1.955967	7.460761
H	10.932687	2.685182	7.590150
C	10.322720	0.913311	6.571729
H	11.253210	0.823727	6.020146
C	8.957992	2.099004	8.185445
C	4.556611	1.676608	9.381117
C	9.304345	-0.001397	6.370454
H	9.443212	-0.797487	5.647534

Continued on next page

Table S10: Cartesian coordinates of the optimized S_0 geometry of complex **Zn1**.

atom	x	y	z
C	8.826461	3.313170	9.092167
H	7.875553	3.248121	9.620145
C	8.101053	0.088642	7.063856
C	6.088461	2.559507	3.607713
C	5.051076	0.495819	10.233603
H	4.620376	-0.435794	9.853392
H	4.758682	0.587149	11.282657
C	5.682769	1.897665	8.389493
C	7.006023	-0.913378	6.728540
H	6.196726	-0.794289	7.448903
C	4.347068	2.945784	10.215331
H	5.247063	3.243057	10.760843
H	4.040935	3.785216	9.588784
H	3.553850	2.762915	10.948734
C	6.569398	0.454390	10.070720
C	4.701865	2.315748	3.671057
C	8.798435	4.613328	8.283739
H	7.974695	4.629474	7.565353
H	8.671211	5.469443	8.957027
H	9.733569	4.758183	7.731002
C	6.405848	-0.634127	5.349697
H	7.159785	-0.737992	4.560942
H	5.597399	-1.345070	5.140762

Continued on next page

Table S10: Cartesian coordinates of the optimized S_0 geometry of complex **Zn1**.

atom	x	y	z
H	5.998940	0.377402	5.285396
C	3.251639	1.333989	8.659263
H	2.494244	1.053878	9.401034
H	2.868685	2.186715	8.089776
H	3.381024	0.490438	7.972201
C	7.305432	1.191239	11.187070
H	6.974912	2.224738	11.303023
H	7.114560	0.670299	12.130460
H	8.384309	1.184332	11.017135
C	7.488206	-2.363844	6.807681
H	7.977696	-2.586083	7.761018
H	6.637848	-3.046224	6.694290
H	8.198556	-2.594353	6.006065
C	6.765418	2.202867	2.432805
C	9.940316	3.382983	10.140683
H	10.912491	3.581107	9.675699
H	9.741666	4.199177	10.844983
H	10.031129	2.455548	10.714488
C	4.058163	1.719486	2.583070
H	2.991567	1.529136	2.651624
C	7.105514	-0.968560	10.018044
H	8.171130	-0.995365	9.771823
H	6.981608	-1.411517	11.011671

Continued on next page

Table S10: Cartesian coordinates of the optimized S_0 geometry of complex **Zn1**.

atom	x	y	z
H	6.559630	-1.594395	9.311990
C	6.112002	1.627064	1.355902
C	4.745761	1.377231	1.429502
H	7.833702	2.386670	2.376415
H	6.672079	1.366246	0.462735
H	4.220112	0.917782	0.598169
H	4.541845	7.391356	11.457791
H	2.089889	6.942830	11.593237
H	0.928311	5.922250	9.679609

Table S11: Cartesian coordinates of the optimized S_{LLCT} geometry of complex **Zn1**.

atom	x	y	z
Zn	-1.9997000	0.3548000	0.1491300
S	-0.0900200	1.1660800	-0.9398700
S	-1.9953000	2.0091500	1.7183100
N	-4.7128000	-0.5639200	-0.7094900
C	-5.3005800	0.4959400	0.0894900
C	-6.2280900	1.2697300	2.1605700
H	-6.4914200	1.1015400	3.1988800
C	-6.4801200	2.5047600	1.5923700
H	-6.9493600	3.2886600	2.1781200
C	-5.6285600	0.2426300	1.4346700
C	-3.1569000	-1.9890200	-1.6366600

Continued on next page

Table S11: Cartesian coordinates of the optimized S_{LLCT} geometry of complex **Zn1**.

atom	x	y	z
C	-6.1046700	2.7460600	0.2834800
H	-6.2708700	3.7296400	-0.1415700
C	-5.3150500	-1.0529700	2.1689000
H	-4.9226700	-1.7714000	1.4507600
C	-5.5001600	1.7616000	-0.4941600
C	-0.8318000	3.1028200	0.9533200
C	-4.4921000	-2.2199500	-2.3652700
H	-4.4448600	-1.7755400	-3.3636500
H	-4.7172100	-3.2817800	-2.4915300
C	-3.4418100	-0.8017500	-0.7486100
C	-5.0362100	2.1492800	-1.8909400
H	-4.6343600	1.2617400	-2.3817500
C	-2.7630300	-3.1735400	-0.7426500
H	-3.5591400	-3.4506600	-0.0451000
H	-1.8665400	-2.9463100	-0.1597700
H	-2.5474500	-4.0439600	-1.3720100
C	-5.5718400	-1.5101200	-1.5419900
C	-0.0356900	2.7618700	-0.1563000
C	-4.2263200	-0.8454800	3.2263200
H	-3.2996600	-0.4596300	2.7915500
H	-3.9966400	-1.7978500	3.7184300
H	-4.5505400	-0.1386400	3.9983000
C	-3.9002100	3.1755100	-1.8306400

Continued on next page

Table S11: Cartesian coordinates of the optimized S$_{LLCT}$ geometry of complex **Zn1**.

atom	x	y	z
H	-4.2408200	4.1178300	-1.3867400
H	-3.5380400	3.3925500	-2.8423600
H	-3.0555600	2.8171900	-1.2360400
C	-2.0216100	-1.6940400	-2.6176900
H	-1.9103700	-2.5383700	-3.3076100
H	-1.0655000	-1.5544500	-2.1021900
H	-2.2275900	-0.7966600	-3.2111400
C	-6.3551000	-2.4648100	-0.6469800
H	-5.7100800	-3.0823800	-0.0190600
H	-6.9369300	-3.1352900	-1.2868300
H	-7.0570900	-1.9226100	-0.0092500
C	-6.1741900	2.6928100	-2.7592000
H	-7.0293400	2.0120300	-2.7979700
H	-5.8191200	2.8521100	-3.7839100
H	-6.5331700	3.6577100	-2.3843800
C	-0.7016400	4.3899600	1.4912300
C	-6.5537300	-1.6754300	2.8183300
H	-6.9248400	-1.0577900	3.6435700
H	-6.3043800	-2.6590400	3.2326200
H	-7.3743300	-1.8063100	2.1063300
C	0.8476700	3.7081400	-0.6838600
H	1.4535100	3.4334300	-1.5412300
C	-6.5602900	-0.7613500	-2.4223400

Continued on next page

Table S11: Cartesian coordinates of the optimized S$_{LLCT}$ geometry of complex **Zn1**.

atom	x	y	z
H	-7.2713900	-0.1777800	-1.8302500
H	-7.1295900	-1.4990800	-2.9970300
H	-6.0609700	-0.1035600	-3.1350000
C	0.1781100	5.3171400	0.9594700
C	0.9599800	4.9765700	-0.1393600
Zn	1.6903200	-0.2050100	0.2941900
S	0.2224300	-1.4708300	1.7395900
S	1.7617700	-2.1168600	-1.1556300
N	4.5435600	0.6884800	0.3732500
C	4.9874400	-0.2263100	-0.6237200
C	5.3262600	-0.8375300	-2.9382600
H	5.2441500	-0.6015100	-3.9945100
C	5.8743600	-2.0477000	-2.5580700
H	6.2247200	-2.7510100	-3.3077200
C	4.8652200	0.0808000	-1.9929400
C	3.4477300	1.2127600	2.4050500
C	5.9664200	-2.3586700	-1.2106100
H	6.3905900	-3.3132900	-0.9165900
C	4.2293100	1.3636900	-2.4961300
H	3.8699200	1.9132300	-1.6257800
C	5.5346500	-1.4700300	-0.2303000
C	1.1218100	-3.3297500	-0.1305300
C	4.9045200	1.7295600	2.4253100

Continued on next page

Table S11: Cartesian coordinates of the optimized S$_{LLCT}$ geometry of complex **Zn1**.

atom	x	y	z
H	5.5321800	1.0363200	2.9956000
H	4.9942100	2.7107900	2.9019600
C	3.3508200	0.5030500	1.0571900
C	5.6722300	-1.8851700	1.2251600
H	5.4596800	-1.0103500	1.8371700
C	2.4332700	2.3535500	2.5592900
H	2.5268200	3.1028300	1.7694300
H	1.4086200	1.9673300	2.5181800
H	2.5625800	2.8561500	3.5276500
C	5.3869400	1.7545000	0.9666500
C	0.4701000	-3.0567100	1.1195700
C	3.0168100	1.0865300	-3.3879900
H	2.2726400	0.4734700	-2.8706300
H	2.5318800	2.0285600	-3.6724400
H	3.3031700	0.5702700	-4.3118900
C	4.6464000	-2.9549200	1.6036800
H	4.7927400	-3.8713100	1.0183200
H	4.7405200	-3.2158000	2.6653900
H	3.6284900	-2.5951700	1.4295800
C	3.2158500	0.2373400	3.5684700
H	3.3560500	0.7430300	4.5343000
H	2.1970400	-0.1644300	3.5431500
H	3.9091400	-0.6089000	3.5231600

Continued on next page

Table S11: Cartesian coordinates of the optimized S$_{LLCT}$ geometry of complex **Zn1**.

atom	x	y	z
C	5.1081400	3.1233100	0.3317400
H	4.0360200	3.3322400	0.2859600
H	5.5855400	3.9129400	0.9239000
H	5.5117300	3.1817700	-0.6819200
C	7.0856600	-2.3568700	1.5748500
H	7.8439500	-1.6197700	1.2881900
H	7.1687400	-2.5242700	2.6556300
H	7.3366000	-3.3018700	1.0795900
C	1.2388700	-4.6821700	-0.5493500
C	5.2370800	2.2451600	-3.2382700
H	5.5653500	1.7708700	-4.1711300
H	4.7869500	3.2112400	-3.4978400
H	6.1309100	2.4386800	-2.6356900
C	-0.0178300	-4.1537000	1.8725800
H	-0.5060600	-3.9458800	2.8181900
C	6.8784100	1.4676000	0.8516600
H	7.1987200	1.4275100	-0.1950200
H	7.4404300	2.2697500	1.3432300
H	7.1517200	0.5238900	1.3297600
C	0.7527400	-5.7133100	0.2057100
C	0.1165300	-5.4443600	1.4359500
H	1.7331000	-4.8808200	-1.4937300
H	0.8589000	-6.7368200	-0.1379600

Continued on next page

Table S11: Cartesian coordinates of the optimized S$_{LLCT}$ geometry of complex **Zn1**.

atom	x	y	z
H	-0.2655000	-6.2622900	2.0378200
H	1.6516900	5.6933300	-0.5706900
H	0.2499200	6.3065100	1.4009900
H	-1.3135800	4.6585400	2.3465400

Table S12: Cartesian coordinates of the optimized T$_{LL/LMCT}$ geometry of complex **Zn1**.

atom	x	y	z
Zn	-1.7825400	0.2305400	0.1745700
S	-0.0506000	1.3726300	-1.1190300
S	-1.8997700	2.0202500	1.6473000
N	-4.5609200	-0.4954200	-0.7612300
C	-5.1215000	0.5157500	0.1145200
C	-6.0134300	1.1899200	2.2349000
H	-6.2593000	0.9716200	3.2682300
C	-6.2733800	2.4510000	1.7320800
H	-6.7308900	3.2058800	2.3636000
C	-5.4269100	0.1982500	1.4502300
C	-3.0535200	-1.8260200	-1.8844100
C	-5.9225500	2.7546200	0.4287800
H	-6.0956500	3.7572300	0.0539100
C	-5.1002500	-1.1288500	2.1180500
H	-4.6938200	-1.8038200	1.3652800
C	-5.3347800	1.8068800	-0.4044900

Continued on next page

Table S12: Cartesian coordinates of the optimized T$_{LL/LMCT}$ geometry of complex **Zn1**.

atom	x	y	z
C	-0.8125900	3.1869100	0.8902300
C	-4.4181600	-1.9702700	-2.5800000
H	-4.4134700	-1.4007700	-3.5143400
H	-4.6500300	-3.0082600	-2.8311100
C	-3.2925500	-0.7368600	-0.8614800
C	-4.9019100	2.2506800	-1.7942100
H	-4.5655800	1.3736600	-2.3482900
C	-2.6265900	-3.1092700	-1.1589800
H	-3.3769000	-3.4527800	-0.4408000
H	-1.6864800	-2.9659400	-0.6216600
H	-2.4773800	-3.9047900	-1.8974000
C	-5.4567800	-1.3739500	-1.6283800
C	-0.0302300	2.9307900	-0.2516200
C	-4.0216700	-0.9549200	3.1919700
H	-3.1110700	-0.5024200	2.7900600
H	-3.7543400	-1.9302200	3.6156400
H	-4.3776600	-0.3203300	4.0114200
C	-3.7085600	3.2067700	-1.7197800
H	-3.9728600	4.1286200	-1.1890000
H	-3.3841100	3.4806800	-2.7308100
H	-2.8615400	2.7544600	-1.1982100
C	-1.9595800	-1.4233700	-2.8756300
H	-1.9000100	-2.1759600	-3.6705700

Continued on next page

Table S12: Cartesian coordinates of the optimized T$_{LL/LMCT}$ geometry of complex **Zn1**.

atom	x	y	z
H	-0.9779100	-1.3681100	-2.3933500
H	-2.1748000	-0.4553800	-3.3413400
C	-6.1537500	-2.4302400	-0.7758900
H	-5.4527200	-3.0618600	-0.2270600
H	-6.7397600	-3.0764800	-1.4366600
H	-6.8437100	-1.9694400	-0.0655500
C	-6.0398700	2.8968100	-2.5883300
H	-6.9336300	2.2662800	-2.6198500
H	-5.7173400	3.0822700	-3.6194000
H	-6.3282200	3.8626000	-2.1589600
C	-0.7260500	4.4618300	1.4689500
C	-6.3320900	-1.7994000	2.7320800
H	-6.7163300	-1.2235500	3.5813200
H	-6.0690400	-2.7961700	3.1046000
H	-7.1481200	-1.9120600	2.0119400
C	0.7845100	3.9393400	-0.7731100
H	1.3724600	3.7267100	-1.6602700
C	-6.5244200	-0.5808600	-2.3665000
H	-7.1957500	-0.0603500	-1.6771100
H	-7.1256200	-1.2852600	-2.9505200
H	-6.0971500	0.1408600	-3.0632800
C	0.0927500	5.4496100	0.9494700
C	0.8554600	5.1915400	-0.1844500

Continued on next page

Table S12: Cartesian coordinates of the optimized T$_{LL/LMCT}$ geometry of complex **Zn1**.

atom	x	y	z
Zn	1.3505200	-0.1680200	0.0802300
S	-0.1869100	-1.1347100	1.6214200
S	1.7008300	-2.1840700	-0.9869100
N	4.3774600	0.5198400	0.2935900
C	4.9959500	-0.3608000	-0.6514700
C	5.4814600	-0.9640200	-2.9336800
H	5.3895300	-0.7735200	-3.9977500
C	6.2021800	-2.0627800	-2.5039900
H	6.6738100	-2.7238400	-3.2246100
C	4.8586300	-0.1053800	-2.0289700
C	3.2897200	0.8317800	2.4491600
C	6.3123300	-2.3177300	-1.1477300
H	6.8710800	-3.1863800	-0.8162300
C	4.0496800	1.0532200	-2.5832600
H	3.5585400	1.5458200	-1.7433700
C	5.7253900	-1.4810300	-0.2028500
C	0.9294600	-3.2692200	0.1709900
C	4.6326700	1.6107200	2.3581400
H	5.4163500	1.0365700	2.8620300
H	4.5691100	2.5818700	2.8572600
C	3.2881700	0.2036700	1.0552400
C	5.8771600	-1.8319000	1.2651300
H	5.5262800	-0.9800000	1.8450200

Continued on next page

Table S12: Cartesian coordinates of the optimized T$_{LL/LMCT}$ geometry of complex **Zn1**.

atom	x	y	z
C	2.1136800	1.7806100	2.7008800
H	2.0357500	2.5586100	1.9379300
H	1.1649500	1.2356800	2.7232200
H	2.2398500	2.2700300	3.6742100
C	5.0024000	1.7586100	0.8643300
C	0.1198700	-2.8424100	1.2438200
C	2.9463600	0.5820900	-3.5328700
H	2.2808200	-0.1374800	-3.0461700
H	2.3379300	1.4352400	-3.8541100
H	3.3592000	0.1105000	-4.4320100
C	5.0001300	-3.0298700	1.6369700
H	5.3165800	-3.9296600	1.0955900
H	5.0737600	-3.2409700	2.7108300
H	3.9490400	-2.8429300	1.3937600
C	3.3077800	-0.2103500	3.5701900
H	3.4049600	0.2865200	4.5435800
H	2.3730900	-0.7817700	3.5727600
H	4.1377900	-0.9139400	3.4634600
C	4.4007100	3.0306400	0.2664400
H	3.3084700	3.0026200	0.2692800
H	4.7204200	3.8988700	0.8531800
H	4.7359600	3.1842500	-0.7617800
C	7.3313100	-2.0776900	1.6711900

Continued on next page

Table S12: Cartesian coordinates of the optimized T$_{LL/LMCT}$ geometry of complex **Zn1**.

atom	x	y	z
H	7.9762200	-1.2348300	1.3976400
H	7.3985400	-2.2163900	2.7567400
H	7.7415900	-2.9786500	1.2015700
C	1.1273100	-4.6471700	-0.0041700
C	4.9438000	2.0816300	-3.2806800
H	5.4032600	1.6576300	-4.1816100
H	4.3565800	2.9559800	-3.5863100
H	5.7539300	2.4276900	-2.6299600
C	-0.4519700	-3.7994400	2.0901100
H	-1.0663100	-3.4587400	2.9176000
C	6.5098700	1.7676400	0.6608700
H	6.7728500	1.8299400	-0.3995100
H	6.9273200	2.6464000	1.1650300
H	6.9844100	0.8776800	1.0819000
C	0.5420500	-5.5804700	0.8325400
C	-0.2549500	-5.1551800	1.8915000
H	1.7558200	-4.9790900	-0.8243200
H	0.7128700	-6.6391300	0.6626400
H	-0.7158600	-5.8748200	2.5607700
H	1.4973100	5.9570800	-0.6086900
H	0.1304300	6.4236900	1.4279200
H	-1.3243900	4.6696300	2.3503400

Table S13: Cartesian coordinates of the optimized T$_{LC}$ geometry of complex **Zn1**.

atom	x	y	z
Zn	3.264888	5.158651	5.287666
S	5.065323	5.550241	6.861546
S	1.752453	5.007947	7.074022
N	1.988639	7.103378	3.282818
C	0.813814	7.241011	4.119714
C	-1.376252	6.533728	4.787565
H	-2.207305	5.840630	4.716863
C	-1.457841	7.596278	5.668267
H	-2.350319	7.738483	6.269439
C	-0.244283	6.322648	4.002169
C	4.048989	6.468226	2.483800
C	-0.386837	8.462719	5.798434
H	-0.445545	9.273317	6.516249
C	-0.212880	5.079648	3.125652
H	0.705172	5.093609	2.539036
C	0.769081	8.305672	5.038928
C	2.708114	5.722735	8.375072
C	3.567312	7.659854	1.640225
H	4.103879	8.564295	1.943084
H	3.749424	7.514444	0.572402
C	3.008347	6.358699	3.578553
C	1.931792	9.252293	5.297768
H	2.690770	9.081597	4.534456

Continued on next page

Table S13: Cartesian coordinates of the optimized T$_{LC}$ geometry of complex **Zn1**.

atom	x	y	z
C	4.061159	5.160928	1.680441
H	3.092059	4.945546	1.221335
H	4.335299	4.313243	2.310383
H	4.803879	5.239852	0.879065
C	2.078389	7.828292	1.942478
C	4.095755	5.953232	8.298461
C	-0.179001	3.804992	3.974077
H	0.671628	3.794812	4.660502
H	-0.099726	2.924872	3.325138
H	-1.092454	3.701405	4.570728
C	2.595508	8.954349	6.643186
H	1.895444	9.103400	7.473233
H	3.450179	9.624108	6.797077
H	2.954863	7.924226	6.694072
C	5.440147	6.719613	3.067377
H	6.145324	6.913850	2.250515
H	5.803973	5.852333	3.627481
H	5.443606	7.591047	3.731845
C	1.179737	7.153444	0.909521
H	1.412706	6.097006	0.767163
H	1.317304	7.658575	-0.051546
H	0.126963	7.247259	1.185620
C	1.523275	10.725358	5.227456

Continued on next page

Table S13: Cartesian coordinates of the optimized T$_{LC}$ geometry of complex **Zn1**.

atom	x	y	z
H	0.995911	10.964936	4.298877
H	2.413173	11.362608	5.287574
H	0.870105	11.000182	6.063042
C	2.047476	6.078436	9.559520
C	-1.390453	5.015607	2.149389
H	-2.339438	4.875397	2.678814
H	-1.266537	4.165120	1.469005
H	-1.479426	5.922598	1.543821
C	4.758811	6.531824	9.384223
H	5.826519	6.711208	9.305320
C	1.672804	9.292725	2.026395
H	0.639279	9.411793	2.364519
H	1.746019	9.720379	1.021127
H	2.330662	9.870986	2.675661
C	2.718941	6.638681	10.633427
C	4.087491	6.872075	10.547927
Zn	5.496363	3.097432	6.646739
S	3.759997	2.694837	4.997384
S	7.151109	3.232744	4.958774
N	6.676642	1.184653	8.739241
C	7.949032	1.159774	8.045254
C	10.146691	2.036318	7.660929
H	10.913824	2.778596	7.852108

Continued on next page

Table S13: Cartesian coordinates of the optimized T$_{LC}$ geometry of complex **Zn1**.

atom	x	y	z
C	10.402763	1.018241	6.761806
H	11.365451	0.959983	6.263955
C	8.920677	2.139171	8.316826
C	4.475418	1.599256	9.271113
C	9.417605	0.088321	6.480705
H	9.615405	-0.687403	5.749467
C	8.708579	3.333569	9.234393
H	7.732439	3.235744	9.708429
C	8.174501	0.136345	7.104787
C	6.179254	2.946183	3.556439
C	4.953623	0.415789	10.128972
H	4.559086	-0.518093	9.716758
H	4.611454	0.486614	11.164476
C	5.642803	1.856323	8.337473
C	7.127135	-0.886704	6.689205
H	6.271980	-0.796558	7.359361
C	4.205854	2.853000	10.112173
H	5.075084	3.157244	10.701934
H	3.912734	3.696779	9.484780
H	3.383819	2.645587	10.806173
C	6.478511	0.404640	10.036679
C	4.842711	2.290044	3.667008
C	8.690010	4.644241	8.442883

Continued on next page

Table S13: Cartesian coordinates of the optimized T$_{LC}$ geometry of complex **Zn1**.

atom	x	y	z
H	7.912996	4.644986	7.674072
H	8.494802	5.486281	9.117653
H	9.652896	4.825045	7.951736
C	6.606093	-0.608776	5.278105
H	7.410665	-0.678665	4.536962
H	5.837197	-1.343902	5.011562
H	6.168191	0.388416	5.196524
C	3.209902	1.242484	8.488339
H	2.427552	0.936817	9.193146
H	2.834339	2.095706	7.914333
H	3.385703	0.411586	7.796208
C	7.148156	1.130156	11.200933
H	6.790988	2.153794	11.325389
H	6.925763	0.583579	12.122617
H	8.233482	1.148348	11.080431
C	7.641917	-2.325472	6.782260
H	8.080829	-2.546758	7.760011
H	6.818015	-3.028111	6.611758
H	8.403767	-2.527555	6.021317
C	6.891089	2.763938	2.287905
C	9.761660	3.416201	10.342828
H	10.752037	3.645944	9.934337
H	9.503649	4.216866	11.045675

Continued on next page

Table S13: Cartesian coordinates of the optimized T$_{LC}$ geometry of complex **Zn1**.

atom	x	y	z
H	9.845545	2.483338	10.908733
C	4.460033	1.380366	2.711605
H	3.499154	0.881824	2.811159
C	7.041366	-1.007664	9.979935
H	8.118327	-1.011507	9.787744
H	6.874913	-1.475424	10.955832
H	6.542426	-1.625347	9.233170
C	6.466282	1.876461	1.361086
C	5.256025	1.119679	1.578947
H	7.792831	3.348147	2.120797
H	7.015812	1.744876	0.432900
H	4.931872	0.390003	0.844950
H	4.627204	7.318263	11.377441
H	2.171382	6.899369	11.534342
H	0.978068	5.905216	9.626187

References

(1) Sheldrick, G. M. *SHELXT* – Integrated space-group and crystal-structure determination. *Acta Crystallogr. Sect. A* **2015**, *71*, 3–8.

(2) Sheldrick, G. M. Crystal structure refinement with *SHELXL*. *Acta Crystallogr. Sect. C* **2015**, *71*, 3–8.

(3) Dolomanov, O. V.; Bourhis, L. J.; Gildea, R. J.; Howard, J. A. K.; Puschmann, H. *OLEX2*: a complete structure solution, refinement and analysis program. *J. Appl. Crystallogr.* **2009**, *42*, 339–341.

(4) Spek, A. L. *PLATON* SQUEEZE: a tool for the calculation of the disordered solvent contribution to the calculated structure factors. *Acta Crystallogr. Sect. C* **2015**, *71*, 9–18.

(5) Frisch, M. J. et al. Gaussian 16, Revision A.03. 2016; Gaussian Inc. Wallingford CT.

(6) Von Arnim, M.; Ahlrichs, R. Performance of Parallel TURBOMOLE for Density Functional Calculations. *J. Comput. Chem.* **1998**, *19*, 1746–1757.

(7) Furche, F.; Ahlrichs, R. Adiabatic Time-Dependent Density Functional Methods for Excited State Properties. *J. Chem. Phys.* **2002**, *117*, 7433–7447.

(8) Hirata, S.; Head-Gordon, M. Time-dependent density functional theory within the Tamm–Dancoff approximation. *Chem. Phys. Lett.* **1999**, *314*, 291–299.

(9) Figgen, D.; Rauhut, G.; Dolg, M.; Stoll, H. Energy-Consistent Pseudopotentials for Group 11 and 12 Atoms: Adjustment to Multi-Configuration Dirac–Hartree–Fock Data. *Chem. Phys.* **2005**, *311*, 227–244.

(10) Schäfer, A.; Horn, H.; Ahlrichs, R. Fully Optimized Contracted Gaussian Basis Sets for Atoms Li to Kr. *J. Chem. Phys.* **1992**, *97*, 2571–2577.

(11) Lee, C.; Yang, W.; Parr, R. G. Development of the Colle-Salvetti Correlation-Energy Formula into a Functional of the Electron Density. *Phys. Rev. B* **1988**, *37*, 785–789.

(12) Becke, A. D. A New Mixing of Hartree-Fock and Local Density-Functional Theories. *J. Chem. Phys.* **1993**, *98*, 1372–1377.

(13) Cancès, E.; Mennucci, B.; Tomasi, J. A new integral equation formalism for the polarizable continuum model: Theoretical background and applications to isotropic and anisotropic dielectrics. *J. Chem. Phys.* **1997**, *107*, 3032.

(14) Mennucci, B.; Cancès, E.; Tomasi, J. Evaluation of Solvent Effects in Isotropic and Anisotropic Dielectrics and in Ionic Solutions with a Unified Integral Equation Method: Theoretical Bases, Computational Implementation, and Numerical Applications. *J. Phys. Chem. B* **1997**, *101*, 10506.

(15) Grimme, S.; Waletzke, M. A Combination of Kohn–Sham Density Functional Theory and Multi-Reference Configuration Interaction Methods. *J. Chem. Phys.* **1999**, *111*, 5645–5655.

(16) Marian, C. M.; Heil, A.; Kleinschmidt, M. The DFT/MRCI Method. *WIREs Comp. Mol. Sci.* **2019**, *9*, e1394.

(17) Kleinschmidt, M.; Tatchen, J.; Marian, C. M. Spin-Orbit Coupling of DFT/MRCI Wavefunctions: Method, Test Calculations, and Application to Thiophene. *J. Comput. Chem.* **2002**, *23*, 824–833.

(18) Kleinschmidt, M.; Marian, C. M. Efficient Generation of Matrix Elements for One-Electron Spin–Orbit Operators. *Chem. Phys.* **2005**, *311*, 71–79.